Semiconductors, Vol. 34, No. 7, 2000, pp. 741–745. Translated from Fizika i Tekhnika Poluprovodnikov, Vol. 34, No. 7, 2000, pp. 769–773.
Original Russian Text Copyright © 2000 by Galiev, Kaminskiĭ, Mokerov, Nevolin, Saraĭkin, Slepnev.

ATOMIC STRUCTURE AND NONELECTRONIC PROPERTIES OF SEMICONDUCTORS

Investigation of Distribution and Redistribution of Silicon in Thin Doped Gallium-Arsenide Layers Grown by Molecular Beam Epitaxy on Substrates with (100), (111)Ga, and (111)As Orientations

G. B. Galiev*, V. É. Kaminskiĭ*, V. G. Mokerov*, V. K. Nevolin,**
V. V. Saraĭkin*, and Yu. V. Slepnev*

** Institute of Radio Engineering and Electronics, Russian Academy of Sciences, Mokhovaya ul. 11, Moscow, 103907 Russia*
e-mail:mok@mail.cplire.ru
*** Moscow Institute of Electronic Engineering (Technical University), Moscow, 103498 Russia*

Submitted November 12, 1999; accepted for publication November 16, 1999

Abstract—The distribution of silicon in GaAs was investigated by secondary-ion mass spectrometry (SIMS) before and after the thermal annealing of thin doped GaAs layers grown by molecular beam epitaxy on substrates with (100), (111)Ga, and (111)As orientations. The surface relief pattern of the grown epitaxial films was studied by atomic-force microscopy both inside and outside the ion-etching crater developed during the SIMS analysis. Features of the surface relief inside the crater are revealed for various orientations. Changes observed in the shape of doping profiles are explained both by the features of the development of the surface relief during the ion etching accompanying the SIMS analysis and by an accelerated diffusion of Si over the growth defects. © *2000 MAIK "Nauka/Interperiodica".*

1. INTRODUCTION

Up until now, silicon has remained a basic impurity used for doping the epilayers of III–V compounds grown by molecular beam epitaxy (MBE). Depending on the growth conditions and the substrate orientation, silicon as an amphoteric impurity can occupy sites in Ga and As sublattices. In gallium arsenide with the (100) substrate orientation, silicon occupies a site predominantly in the Ga sublattice forming the *n*-type epilayers. On substrates that have the (111)Ga orientation, both compensated epilayers and *n* or *p* epilayers [1–5] can be obtained, depending on substrate temperature and also on the ratio γ between the arsenic and gallium fluxes ($\gamma = P_{As}/P_{Ga}$, where P_{As} and P_{Ga} are the partial pressures of arsenic and gallium in the growth area).

In manufacturing the devices, the abruptness of the substrate–epilayer barrier and the distribution of impurities in the epilayer are very important. Whereas the behavior of silicon in the gallium sublattice Si_{Ga} for GaAs(100) during the growth and following the thermal annealing is studied in detail [6–12], virtually no such data have been published on the silicon-doped GaAs epilayers grown on substrates with (111)Ga and (111)As orientations.

The purpose of this study was to investigate the distributions of silicon in the GaAs epilayers grown on substrates with the (100), (111)Ga, and (111)As orientations during growth and after thermal annealing.

2. EXPERIMENTAL PROCEDURE

The structures under investigation were grown by MBE on semi-insulating GaAs substrates with (100), (111)Ga, and (111)As orientations for $\gamma = 28$ and a growth temperature of $T_G = 600°C$. The value of γ was chosen from considerations that the epilayers on the (111)Ga and (111)As substrates are found for these γ to be nearly compensated and with a specular surface [3]; i.e., the Si atoms occupy both As and Ga sites in the GaAs crystal lattice. To provide identical technological conditions, all three samples were grown in the same technological process. These conditions were achieved by cementing together the three substrates with various orientations on a common molybdenum sample holder using indium, which ensured identical growth conditions for all the samples. After a buffer layer ~0.5 μm thick was grown, we grew three silicon-doped layers to a thickness of ~320 Å separated by undoped layers 640 Å thick; the thickness of the top undoped layer amounted to 1280 Å. Schematically, the structure of the samples under investigation is shown in Fig. 1. When forming the doped layers, we set the silicon source at a temperature that enabled us to provide a concentration of conduction electrons in the GaAs(100) epilayer of $n_e \simeq 10^{18}$ cm^{-3}. The silicon-concentration depth profiles $N_{Si}(x)$ were measured by a CAMECA IMS-4F setup for secondary-ion mass spectrometry (SIMS). Here, we

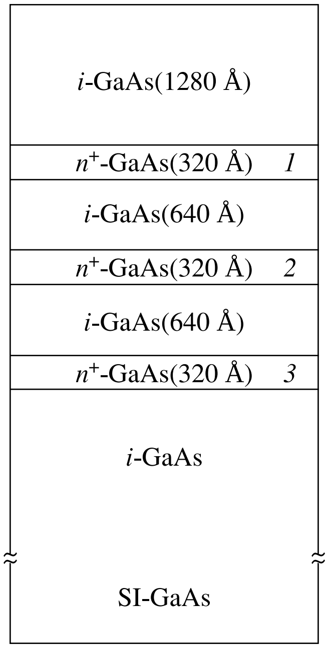

Fig. 1. Schematic representation of the cross section for the samples under investigation. *1–3* are the silicon-doped regions.

used the oxygen ions O_2^+ with an energy $E_p = 5$ keV as the primary beam. The scanned area amounted to 250×250 μm^2, and the silicon secondary ions were collected from the central part of the scanned area of 60×60 μm^2 with the mass resolution of 5000. The surface roughness of the sample inside and outside the ion-etching crater following SIMS analysis was measured using a P7-SPMLS-MDT (HT-MDT company) atomic-force microscope (AFM) under the tamping-mode conditions. A scanned area amounted to ~10000×10000 nm^2. The subsequent annealing of the samples for investigating the Si redistribution was carried out in the growth chamber of the MBE system in the arsenic flow at an annealing temperature $T_a = 750$°C for 1 h and at an arsenic pressure $P_{\mathrm{As}} \simeq 10^{-5}$ Torr.

3. RESULTS OF MEASUREMENTS AND DISCUSSION

In Figs. 2 and 3, we show the results of measurements of $N_{\mathrm{Si}}(x)$ for the samples under investigation before (Fig. 2) and following (Fig. 3) annealing at T_a = 750°C for 1 h. Numbers *1*, *2*, and *3* denote the silicon-doped layers beginning at the surface. Figures 2 and 3 show that a high content of silicon is observed in the surface region. For annealed samples, this region expands and the Si content increases there. Moreover, modifications in the $N_{\mathrm{Si}}(x)$ curves are different for different orientations. For the three samples before annealing, $N_{\mathrm{Si}}(1) \geq N_{\mathrm{Si}}(2) \geq N_{\mathrm{Si}}(3)$, which is characteristic of SIMS measurements of doping profiles. This is associated with special features of the SIMS, in particular, with the so-called mixing effect [10, 11]. (Henceforth, $N_{\mathrm{Si}}(1)$, $N_{\mathrm{Si}}(2)$, and $N_{\mathrm{Si}}(3)$ are peak values of silicon concentration in doped regions *1*, *2*, and *3*, respectively, according to Fig. 1.) Figure 3 shows that the situation is different for the annealed samples; namely, $N_{\mathrm{Si}}(1) < N_{\mathrm{Si}}(2) < N_{\mathrm{Si}}(3)$ for the (100) and (111)Ga orientations and $N_{\mathrm{Si}}(1) > N_{\mathrm{Si}}(2) > N_{\mathrm{Si}}(3)$ for the (111)As orientation.

In Table 1, we list the values of a full width at half-maximum (FWHM) of the $N_{\mathrm{Si}}(x)$ peaks for the samples under investigation before and after annealing; the profiles $N_{\mathrm{Si}}(x)$ for these samples are shown in Figs. 2 and 3. We denote the FWHM values of the corresponding doped layers (according to Fig. 1) by the symbols $\Delta_{00}(1, 2, 3)$, $\Delta_{0A}(1, 2, 3)$, and $\Delta_{0B}(1, 2, 3)$ before annealing and by the symbols $\Delta_{a0}(1, 2, 3)$, $\Delta_{aA}(1, 2, 3)$, and $\Delta_{aB}(1, 2, 3)$ after annealing for the (100), (111)Ga, and (111)As orientations, respectively. From these data, the FWHM values for peaks *1*, *2*, and *3* are seen to be related before annealing as $\Delta_{00}(1) < \Delta_{00}(2) < \Delta_{00}(3)$ and $\Delta_{0B}(1) < \Delta_{0B}(2) < \Delta_{0B}(3)$ for the (100) and (111)As orientations and as $\Delta_{0A}(1) \approx \Delta_{0A}(2) \approx \Delta_{0A}(3)$ for the (111)Ga orientation.

First, we consider the situation for the (100) and (111)As orientations before annealing. In this case, we can explain a broadening of the doping profiles for layers *2* and *3* compared with layer *1* by special features of

Table 1

	Orientation								
	(100)			(111)Ga			(111)As		
Numbers of layers	1	2	3	1	2	3	1	2	3
Designation of FWHM before annealing	$\Delta_{00}(1)$	$\Delta_{00}(2)$	$\Delta_{00}(3)$	$\Delta_{0A}(1)$	$\Delta_{0A}(2)$	$\Delta_{0A}(3)$	$\Delta_{0B}(1)$	$\Delta_{0B}(2)$	$\Delta_{0B}(3)$
Value of FWHM in Å before annealing	350	364	376	350	350	350	475	575	650
Designation of FWHM after annealing at T = 750°C	$\Delta_{a0}(1)$	$\Delta_{a0}(2)$	$\Delta_{a0}(3)$	$\Delta_{aA}(1)$	$\Delta_{aA}(2)$	$\Delta_{aA}(3)$	$\Delta_{aB}(1)$	$\Delta_{aB}(2)$	$\Delta_{aB}(3)$
Value of FWHM in Å after annealing at T = 750°C	440	440	420	374	385	385	–	–	660

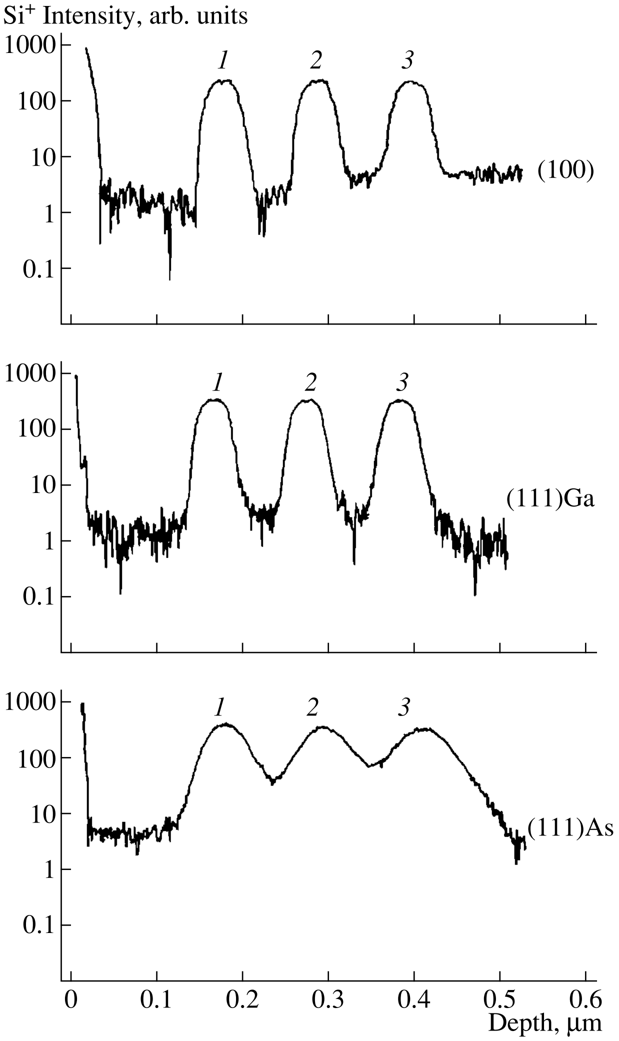

Fig. 2. Silicon depth profiles $N_{\mathrm{Si}}(x)$ measured by the SIMS for the samples grown on the substrates with the (100), (111)Ga, and (111)As orientations before annealing.

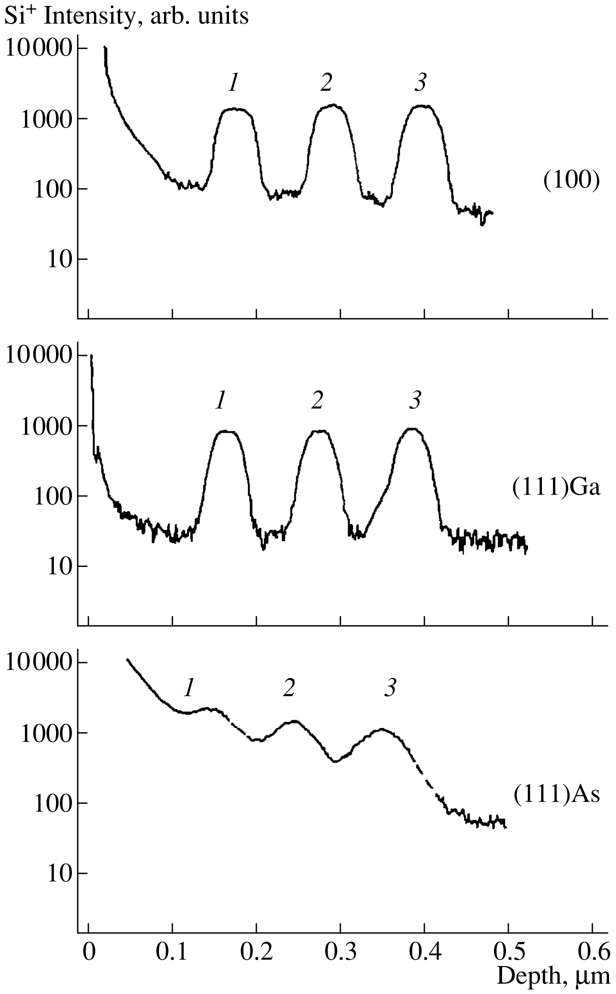

Fig. 3. Silicon depth profiles $N_{\mathrm{Si}}(x)$ measured by the SIMS for the studied samples grown on the substrates with the (100), (111)Ga, and (111)As orientations after annealing.

the SIMS method, i.e., by the “mixing” effect and (or) by the development of a surface relief during the ion etching. Furthermore, the broadening of the doping profiles, i.e., an increase in Δ(2) and Δ(3) for the layers lying below the sample surface, can be induced by the Si diffusion during the growth, because layers *2* and *3* are at $T = T_G$ for a longer time than is layer *1*. Such results were found in [10] for the δ-doped layers. However, in our case, the annealing of the grown structures at $T_a = 750°C$ for 60 min did not result in a significant broadening of profiles. Therefore, for unannealed samples with the (100) and (111)As orientations, the change in δ is more likely related to the development of a surface profile during the SIMS measurements of $N_{\mathrm{Si}}(x)$. In Table 2, we give the data of the AFM measurements of the values $R_{\max}$, R_{mean}, R_a, and R_q. (Here, $R_{\max}$ is the maximum deviation from a mean value, R_{mean} is the mean value, R_a is the surface roughness, and R_q is the rms deviation.) We note a significant distinction in the FWHM values for the (100) and (111)As orientations; in particular, $\Delta_{00} < \Delta_{0B}$ for all the layers (Table 1). A comparison of the data for these samples (see Tables 1, 2) suggests that the distinction between the FWHM values is associated most likely with both the primary roughness and the development of the surface relief during the ion etching. In particular, we have $R_a \simeq 0.9$ for the (100) orientation, whereas $R_a \simeq 14$ for the (111)As orientation.

In contrast with the (100) and (111)As orientations, the FWHM values for the (111)Ga orientation are virtually identical for all three layers before annealing (Table 1); at the same time, the changes in $R_{\max}$, R_a, and R_q within the crater are considerably larger compared with the data for the (100) orientation. We explain this result by the different development of the surface relief for various orientations during the ion etching, which

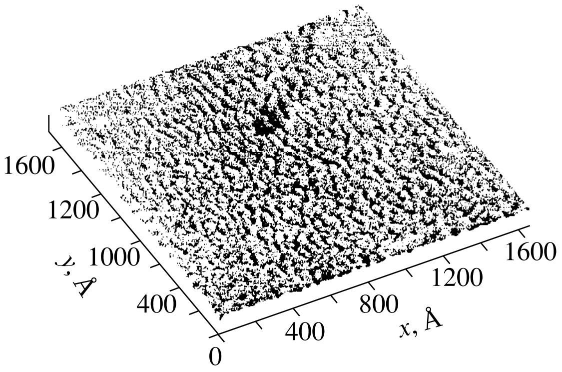

Fig. 4. AFM image of the initial surface within the ion-etching crater for a sample grown on the substrate with the (100) orientation.

accompanies the SIMS analysis. In Figs. 4 and 5, we show the AFM images of the surfaces outside (Fig. 4) and inside (Fig. 5) the ion-etching crater for the samples with (100) and (111)Ga orientations (we present here the image only for one sample, since the images of the surfaces outside the crater for all three samples under investigation do not radically differ from one another). Figure 5 shows that the surface relief for the (111)Ga orientation following the ion etching represents an almost periodic structure of alternating peaks and valleys with a height of ≃120 Å. We note that no such surface relief is observed for the (100) and (111)As orientations following ion etching.

The GaAs surface relief similar to that found by us for the (111)Ga orientation was observed [13] in the ion-etching crater formed during the SIMS analysis; the authors referred to such irregularities as “ripples.” In [13], the origination conditions, the parameters of the ripple irregularities, and their modifications were investigated in detail as functions of energy and the angle of incidence of the primary ion beam (O_2^+). In our case, as in [13], the ripple irregularities appear in the ion-etching crater only for the sample with the (111)Ga orientation. Since, in all our SIMS measurements, the angle of incidence and the primary-beam energy were identical, the origination of ripples was likely associated with features of the interaction between the primary ion beam and the GaAs surface of the (111)Ga orientation. Here, the Si-ion yield in the SIMS analysis is probably averaged over a thickness of the ripple-amplitude span (~120 Å in our case). In turn, this fact is responsible for a weak depth dependence of the broadening of the profiles.

Let us consider the data for the samples upon annealing. As shown in Fig. 3, the FWHM values, along with the shape of the $N_{\mathrm{Si}}(x)$ curves, change upon annealing. In particular, maximum changes in the FWHM values for Si-doped regions *1*, *2*, and *3* before and after annealing amount to $\Delta_{a0}(1) - \Delta_{00}(1) \simeq 90$ Å for the (100) orientation. For the (111)Ga orientation, these changes are insignificant and amount to $\Delta_{aA}(3) - \Delta_{0A}(3) \simeq 30$ Å. An increase in the FWHM for the (100) orientation can be explained by Si diffusion during annealing. The observed insignificant increase in the FWHM for the (111)Ga orientation can be explained by the diffusion and, as was noted above, also by the origination of the ripple irregularities during the ion etching during the SIMS analysis and by the features of the secondary-ion emission from such a surface. We failed to determine the changes in FWHM values after annealing (except peak *3*) for the sample with the (111)As orientation owing to a strong modification in the $N_{\mathrm{Si}}(x)$ curves.

In conclusion, we consider a change in the $N_{\mathrm{Si}}(x)$ shape for the surface region. The presence of an initially high content of silicon in a thin surface region for the silicon-doped deep GaAs epilayers was observed in many studies (for example, [6, 9, 10]). Some authors do not consider this region; however, according to [9], a high Si content in an initially undoped region does not represent an actual high concentration of silicon in the GaAs lattice sites and more closely resembles the Si inclusions at the defect-growth sites. It is this phenomenon that was observed, through a microscope, by the authors. In our case, this phenomenon is also pronounced during the SIMS analysis in the ion-image mode, in which these Si inclusions are visible as luminous spots in the region under analysis. A pronounced drift of silicon to the surface after annealing for the sample grown on a substrate with the (111)As orientation can be explained by an accelerated diffusion of Si over the growth defects, because this surface turns out

Table 2

	Orientation					
	(100)		(111)Ga		(111)As	
	Outside the crater	Inside the crater	Outside the crater	Inside the crater	Outside the crater	Inside the crater
R_{max}, nm	20	27	23	140	139	160
R_{mean}, nm	4.9	10.79	7.8	58	79	74
R_a, nm	0.9	3.47	1.7	30	14	17
R_q, nm	1.29	4.3	2.27	36	19	21

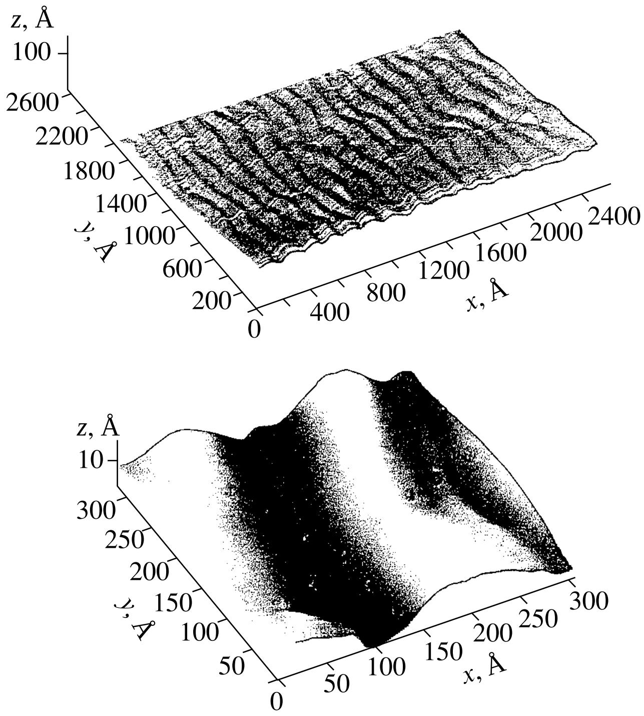

Fig. 5. AFM image of the surface inside the ion-etching crater for a sample grown on the substrates with the (111)Ga orientation (a magnified fragment of the surface is shown below).

to be the most imperfect under the given growth conditions.

4. CONCLUSION

Thus, we can draw the following conclusions from the results of the investigation reported above.

(1) For an identical value of γ, the surface roughness is different for the epilayers grown on substrates with the (100), (111)Ga, and (111)As orientations. In particular, for $\gamma = 28$, the surface is most perfect for the (100) orientation (with the smallest R_a value) and least perfect for the (111)As orientation (with the largest R_a value).

(2) When measuring the surface roughness by the AFM method, we found that the relief of the GaAs surface with the (111)Ga orientation, in contrast to the (100) and (111)As orientations, evolves during the SIMS analysis in the form of ripple irregularities. It was shown that such a feature in the development of a relief can reduce the SIMS depth resolution, especially in measuring the impurity profiles in thin and ultrathin layers.

(3) We assume that an observed increase in the content of silicon in the surface region of the samples upon annealing is associated with an accelerated Si diffusion over the defects.

REFERENCES

1. W. I. Wang, E. E. Méndez, T. S. Kuan, and L. Esaki, Appl. Phys. Lett. **47**, 826 (1985).
2. F. Piazza, L. Pavesi, M. Henin, and D. Johnston, Semicond. Sci. Technol. **7**, 1504 (1992).
3. V. G. Mokerov, G. B. Galiev, Yu. V. Slepnev, and Yu. V. Khabarov, Fiz. Tekh. Poluprovodn. (St. Petersburg) **32**, 1320 (1998) [Semiconductors **32**, 1175 (1998)].
4. Y. Okano, H. Seto, H. Katahama, *et al.*, Jpn. J. Appl. Phys. **28**, L151 (1989).
5. Y. Kadoya, A. Sato, and H. Kano, J. Cryst. Growth **111**, 280 (1991).
6. Ph. Jansen, M. Meuris, M. van Rossum, and G. Borgs, J. Appl. Phys. **68**, 3766 (1990).
7. E. F. Schubert, J. B. Stark, T. H. Chiu, and B. Tell, Appl. Phys. Lett. **53**, 293 (1988).
8. K. H. Lee, D. A. Stevenson, and M. D. Deal, J. Appl. Phys. **68**, 4008 (1990).
9. L. Pavesi, N. H. Ky, and J. D. Ganiere, J. Appl. Phys. **71**, 2225 (1992).
10. R. B. Beall, J. B. Clegg, and J. J. Harris, Semicond. Sci. Technol. **3**, 612 (1988).
11. A.-M. Lanzillotto, M. Santos, and M. Shayegan, Appl. Phys. Lett. **55**, 1445 (1989).
12. M. E. Greiner and J. F. Gibbons, Appl. Phys. Lett. **44**, 750 (1984).
13. A. Ishitani, A. Karen, Y. Nakagawa, *et al.*, in *Proceedings of SIMS VIII Conference* (Amsterdam, The Netherlands, 1991), p. 315.

Translated by V. Bukhanov

Semiconductors, Vol. 34, No. 7, 2000, pp. 746–754. Translated from Fizika i Tekhnika Poluprovodnikov, Vol. 34, No. 7, 2000, pp. 774–782.

ELECTRONIC AND OPTICAL PROPERTIES OF SEMICONDUCTORS

The Magnetoresistance of Compensated Ge:As at Microwave Frequencies in the Vicinity of the Metal–Insulator Phase Transition

A. I. Veĭnger, A. G. Zabrodskiĭ, and T. V. Tisnek

Ioffe Physicotechnical Institute, Russian Academy of Sciences, Politekhnicheskaya ul. 26,
St. Petersburg, 194021 Russia

e-mail: anatoly.veinger@pop.ioffe.rssi.ru

Submitted December 30, 1999; accepted for publication December 30, 1999

Abstract—The magnetoresistance of heavily doped Ge:As near the metal–insulator phase transition has been studied both on the metal and insulator sides of the transition. Measurements were made at microwave frequencies using a noncontact technique of electron spin resonance. The field and temperature dependences of the magnetoresistance derivative in metallic samples reveal two main features of the phenomenon: a negative magnetoresistance at weak fields, due to the weak localization effect, and a positive magnetoresistance at strong fields, arising from the electron–electron interaction in the diffusion channel. Only a weak negative magnetoresistance with a characteristic low-field behavior is observed in insulating samples. The results are compared with the theory of quantum corrections. © *2000 MAIK "Nauka/Interperiodica".*

1. INTRODUCTION

Theoretical and experimental studies of the magnetoresistance (MR) of doped semiconductors show that its origin is different on the metal and insulator sides of the metal–insulator (MI) phase transition. The quantum correction theory is valid on the metal side of the transition [1, 2]. The theory deals with three main phenomena: electron wave function interference at self-crossing trajectories (weak localization processes), coherent interaction of electrons during their diffusion (interaction in the diffusion channel), and short-term Cooper pairing of electrons (interaction in the Cooper channel). On the insulator side of the transition, other mechanisms are invoked in the case of strongly localized carrier transport, taking into account the scattering of a tunneling carrier by impurities [3], wave-function shrinkage [3], narrowing of the impurity band in a magnetic field [4], and spin-related effects [5–7]. Hence, it is no wonder that most of the experimental studies of the MR in doped semiconductors are restricted to one or the other side of the MI phase transition.

The goal of this paper is to trace the transition from the MR mechanisms characteristic of free electrons in heavily doped semiconductors to those effective for localized electrons in the insulating state of the semiconductor. The MI transition was initiated by introducing a compensating Ga impurity into the metallic Ge:As by its neutron doping. A very sensitive and high-precision noncontact measurement technique based on electron spin resonance (ESR) spectroscopy, proposed in our previous work [8], was used. The method makes it possible to measure the MR at microwave frequencies simultaneously with taking ESR spectra of the same sample [9] and, thus, to take into account the possible effect of the spin properties of a semiconductor on its MR.

2. EXPERIMENTAL TECHNIQUE AND RESULTS

A set of compensated Ge:As samples was produced by means of the dosed introduction of a compensating Ga impurity into a heavily doped Ge:As with an initial As concentration of 5.75×10^{17} cm^{-3} by neutron transmutation doping.[1] The degree of compensation depended on the neutron integrated flux. An advantage of the technique is that the arrangement of the transmuted donors and acceptors is random, so correlation effects in their distribution are negligible. The samples investigated had electron concentrations n within the range from 5.75×10^{17} to 7×10^{16} cm^{-3}, depending on the neutron integrated flux. A Varian E-112 EPR spectrometer operating at 10 GHz with an ESR-9 flow-through cryostat (Oxford Instruments) was employed.

---

[1] In neutron-induced doping of germanium by transmutation of its ^{70}Ge and ^{74}Ge isotopes, acceptor (Ga) and donor (As) impurities are introduced in a ratio of about 3 : 1, together with a small amount of deep doubly charged Se donors arising from the ^{76}Ge isotope. The procedure for fabricating the sets of Ge:As samples for studying the MI transition was described in detail in [10, 11].

It enabled measurements in a wide temperature range from 3 to 300 K.

The resistivity of five Ge:As samples is shown as a function of temperature in Fig. 1 reproduced from [11]. The metallic conduction disappears (MI transition occurs) somewhere in between the fourth and fifth samples. (The temperature dependence of the sixth sample, compensated to the greatest extent, was not measured.) Some parameters of the investigated samples are listed in the table.

The MR measurement technique we proposed is based on recording changes in the microwave-cavity Q-factor with an applied magnetic field (dQ/dH) in an ESR spectrometer [8]. In its turn, the cavity Q-factor may change not only as a result of changes in the energy absorption by spins, as in the case of ESR, but also for some other reasons. One of these may be a change in the sample resistivity in a magnetic field, with $dQ/dH \propto d\sigma/dH$ (where σ is the sample conductivity) for high-resistivity samples and $dQ/dH \propto dR/dH$ (where R is the sample resistance) for low-resistivity samples. In our case, the resistance of all the investigated samples was fairly low; thus, the microwave absorption was proportional to the sample resistance.

We note that a microwave measurement differs fundamentally from the dc one in two aspects. First, a microwave field penetrates into a sample only as deep as the skin-effect layer. Thus, all results obtained refer only to this layer and not to the bulk. Second, the microwave absorption in an ESR spectrometer is measured in a cavity and changes in the cavity Q-factor affect the magnitude of the effect.

The dependence of this derivative on the magnetic field, measured for five samples at different temperatures, is shown in Fig. 2. The magnetic field is plotted on the abscissa, and the derivative of microwave absorption, on the ordinate, in relative units calculated by a procedure common to all the samples. The procedure was as follows. A volume in which microwave absorption occurs was determined for each sample as a product of the sample surface area S and the skin depth δ calculated using the data shown in Fig. 1. Then, the magnitude A_n of the derivative, found experimentally for each of the samples, was divided by this volume. Thus, we obtained the derivative A_{dn} of the magnetoresistance per unit volume at a given magnetic field.

In order to monitor cavity Q-factor changes, we used as a marker the background ESR line ($g = 2$) (not shown in Fig. 2) arising from cryostat components. The amplitude A_{bg} of this line, measured at a fixed temperature, is proportional to the cavity Q and depends only on it, since the concentration of paramagnetic centers in the cryostat components remains unchanged during all measurements. The width of this line is constant too. That is why, in order to record the Q variation between the samples, it suffices to divide A_{dn} by the ratio of the background line amplitude for a given sample and a sample for which A_{dn} is assumed to be unity. For convenience, we took for unit amplitude the positive derivative of the microwave absorption of an uncompensated sample 1 in a magnetic field $H = 14$ kOe within the temperature range of 3.4–3.8 K. Thus, the twice-normalized (to sample volume and cavity Q-factor) derivative of the absorption is written as

$$A_{dn} = (A_n/S\delta)(A^0_{bg}/A_{bg}). \tag{1}$$

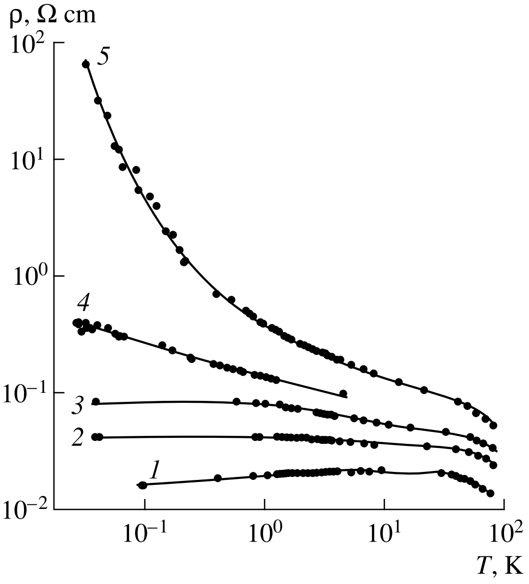

Fig. 1. Temperature dependence for the five investigated Ge:As samples; the main parameters are listed in the table. The curve numbers coincide with the sample numbers in the table.

As can be seen from Fig. 2, both the field and temperature dependences of the MR change with the increasing degree of compensation when the electron concentration approaches the MI critical point and goes beyond. The dependences for sample 6, practically coinciding with those for sample 5, are not shown. The following features are noticeable in the field dependence of the derivative of the microwave absorption. The derivative is negative at a low temperature in weak fields; i.e., a negative MR is observed. In strong fields,

Parameters of investigated samples of compensated Ge:As

Sample no.	n, 10^{17} cm^{-3}	N_D, 10^{17} cm^{-3}	N_A, 10^{17} cm^{-3}	$K = N_A/N_D$
1	5.75	5.75	0	0
2	4.5	6.28	1.78	0.28
3	4.15	6.43	2.28	0.35
4	3.85	6.56	2.71	0.41
5	3.3	6.80	3.50	0.51
6	0.7	7.90	7.21	0.91

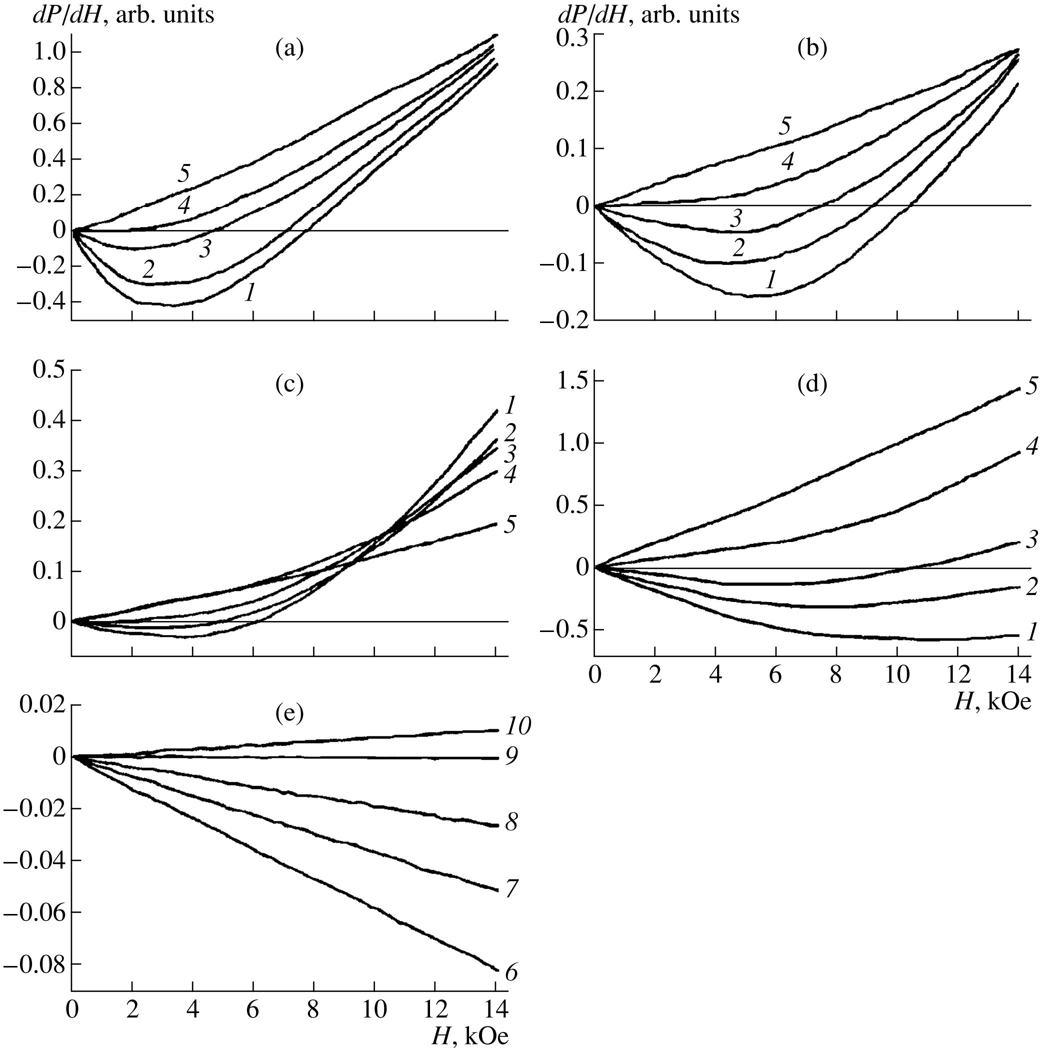

Fig. 2. Derivative of the microwave absorption vs. the magnetic field for the five investigated samples at different temperatures. Samples: (a) 1, (b) 2, (c) 3, (d) 4, and (e) 5. Curves in the plots correspond to the following temperatures T: (a–d) (samples 1–4) (*1*) 3.2, (*2*) 3.5, (*3*) 4.0, (*4*) 6.0, and (*5*) 15.0 K; (e) (sample 5): (*6*) 3–10, (*7*) 20, (*8*) 50, (*9*) 80, and (*10*) 100 K.

the derivative becomes positive, which must weaken the negative MR and eventually lead to a change in its sign. The positive derivative linearly increases with the field. At higher temperatures, the negative part of the derivative vanishes and it becomes positive for any field. On the insulator side of the MI transition, the derivative magnitude is smaller than that on the metal side throughout the investigated field range. However, the derivative remains negative up to higher temperatures and changes linearly with the field.

3. DISCUSSION OF RESULTS

3.1. Dimensionality of the Magnetoresistance Effect

It is known [1, 2] that quantum corrections to conductivity depend on the effective sample dimensionality determined by the ratio of the sample thickness to the electron dephasing length L_φ. In the case of microwave measurements, the sample thickness is to be substituted by the skin depth δ, since only this part of the sample interacts with the electromagnetic field. The dimensionality of the effect can be estimated for the original metallic sample 1 (with the lowest resistivity). Using the well-known formula for the skin depth as a function of the material's conductivity and data from Fig. 1, we obtain $\delta = 0.07$ mm.

On the other hand, in the case of weak localization leading to a negative MR [2], analysis of the field dependences yields a simple estimate of L_φ. The essence of this method is as follows. The dephasing length is related to the characteristic magnetic field H_φ by

$$H_\varphi = \hbar c/4eD\tau_\varphi, \qquad (2)$$

where D is the electron diffusion coefficient; τ_φ is the characteristic dephasing time, $L_\varphi = (D\tau_\varphi)^{1/2}$; and other notation is conventional. In weak fields $H \ll H_\varphi$, the MR for two-dimensional (2D, $d = 2$) and three-dimensional (3D, $d = 3$) systems [1, 2] is proportional to H^2:

$$\Delta\rho/\rho \propto -H^2, \quad d\rho/dH \propto -H. \tag{3}$$

In strong fields $H \gg H_\varphi$, these dependences are different for $d = 2$ and 3. For example, in the 2D case,

$$\Delta\rho/\rho \propto -\ln H, \quad d\rho/dH \propto -H^{-1}, \tag{4}$$

and in the 3D case,

$$\Delta\rho/\rho \propto -H^{1/2}, \quad d\rho/dH \propto -H^{-1/2}. \tag{5}$$

A comparison of (4) and (5) with relations (3) shows that, for $H \approx H_\varphi$, the derivative $d\rho/dH$ has a minimum. It can be seen from Fig. 2a that $H_\varphi \approx 4$ kOe at $T = 3.2$ K. This yields for the dephasing length

$$L_\varphi = (D\tau_\varphi)^{1/2} = (\hbar c/4eH_\varphi)^{1/2} \approx 2 \times 10^{-6}\ \text{cm} \ll \delta. \tag{6}$$

It follows from (6) that the skin depth exceeds the dephasing length by four orders of magnitude even in the lowest resistivity sample, so that all the samples remain 3D in the microwave range.

3.2. Field Dependence of the Magnetoresistance

The field dependences of the MR for three samples (1, 2, and 3) that are the farthest from the MI transition point are qualitatively similar. At weak fields, the derivative of the microwave absorption is negative and linear in the field. This corresponds to (3) with weak localization in low magnetic fields. The derivative passes through a minimum with the field increasing to several kilooersteds, and then a transition to a positive MR is observed at higher fields. Generally speaking, neither of the two formulas (4) and (5) describe the behavior of the negative MR in this region. The positive MR observed at high enough fields is quadratic (and the derivative, linear) in the field.

There are mechanisms leading to the positive MR that is quadratic in field. Among these is, in the first place, the classical Lorentzian MR

$$\Delta\rho/\rho = (\mu H)^2, \quad d\rho/dH \propto H, \tag{7}$$

where μ is the electron mobility. In the case of heavy doping and, consequently, degenerate electron gas, the MR decreases abruptly by a factor of $(kT/\varepsilon_F)^2$:

$$\Delta\rho/\rho = (\pi^2/3)r(kT/\varepsilon_F)^2(\mu H)^2, \tag{8}$$

where r is the exponent in the energy dependence of the carrier momentum relaxation time, and ε_F is the Fermi energy.

Effects leading to an anomalous positive MR are known in the theory of quantum corrections to conductivity for degenerate semiconductors. The first of these effects stems from the interaction between electron spins in their diffusion (interaction in the diffusion channel). The corresponding characteristic magnetic field H_S is determined by setting the Zeeman splitting $g\mu_B H$ (g is the Lande factor and μ_B is the Bohr magneton) equal to the electron temperature kT:

$$H_S = kT/g\mu_B. \tag{9}$$

At $T = 3.2$ K, we obtain $H_S \approx 30$ kOe.

Thus, throughout the entire investigated range of magnetic fields, we have $H \ll H_S$. In this case,

$$\Delta\rho/\rho = (0.053/2\sqrt{2})(g\mu_B H/kT)^2(kT/D\hbar)^{1/2} \tag{10}$$

and

$$d\rho/dH \propto H. \tag{11}$$

The second mechanism is associated with fluctuation pairing of electrons (interaction in the Cooper channel). The corresponding characteristic field H_C is given by

$$\begin{aligned} H_C &= (\pi ckT)/(2De) = H_\varphi(2\pi kT\tau_\varphi/\hbar) \\ &= H_\varphi(2\pi kTL_\varphi^2/D\hbar), \end{aligned} \tag{12}$$

which yields, in view of the values $L_\varphi = 2 \times 10^{-6}$ cm [see (6)] and $D = 0.16$ cm^2 s^{-1} determined from the resistance of sample 1, $H_C = 60H_\varphi$. Thus, for this mechanism, too, $H \ll H_C$ in the entire investigated range of fields and

$$\begin{aligned} \Delta\rho/\rho &= 0.053(D\hbar/kT)^{3/2}(eH/\hbar c)^2, \\ d\rho/dH &\propto H. \end{aligned} \tag{13}$$

Comparing (8), (10), and (13), we can see that all three mechanisms give the same magnetic-field dependence, but the classical and quantum mechanisms produce different temperature dependences of the MR. While for the first mechanism the magnitude of the effect must grow with temperature, it decreases for the other two mechanisms. That is why it is appropriate to analyze the experimental temperature dependences of the MR.

First of all, we separate the effects responsible for the negative and positive MR. This can be easily done, since the effects are additive; i.e., each of them affects the resistivity independently. In order to discriminate the positive MR effect, we find the slope of the derivative at high fields, where it increases linearly with the field, and extrapolate it to the origin at this angle. The obtained straight line describes the uncombined positive MR. To determine the empirical field dependence of the negative MR, this straight line is to be subtracted from the overall experimental dependence.

Such a procedure was carried out for each of the three least compensated samples (1, 2, and 3) at every temperature. As a result, we obtained two sets of the positive and negative MR field dependences at different temperatures for each of the samples. For sample 1,

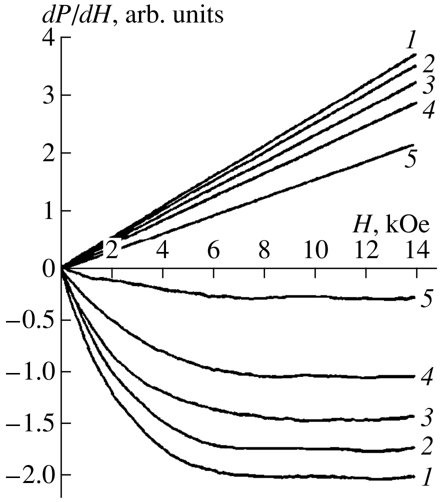

Fig. 3. Separated field dependences of the derivatives of the negative and positive magnetoresistance for sample 1 at different temperatures. The line numbers correspond to the temperatures in Fig. 2a.

these are shown in Fig. 3. Other samples exhibit qualitatively similar dependences. The magnitude of the derivative of the negative MR signal increases linearly with field in weak fields and saturates in strong fields. This means that the negative MR is quadratic in field in the former case and is linear in the latter. Such behavior in high fields is inconsistent with the quantum correction theory, which predicts [see (5)] that the negative MR must increase in these fields in proportion to $H^{1/2}$, i.e., the derivative must decrease as $H^{-1/2}$. Nevertheless, the above estimate of L_φ remains valid, but, as can be seen from our data, in this case, H_φ should mean the field at which there occurs a transition from the linear increase of the derivative to its saturation.

For sample 4 (the nearest to the MI transition point), such a separation is impossible, since, as can be seen from Fig. 2, the derivative shows no linear rise with the field at low temperatures even in the strongest fields. However, the MR field dependence is qualitatively similar to those for the first three samples.

In samples 5 and 6 with the carrier density lower than the critical value, the low-temperature MR (hopping conduction over impurities) remains negative and the magnitude of its derivative grows linearly in the entire field range. No transition to positive MR at low temperatures is observed in these samples, while, as the temperature increases, a transition to positive MR occurs at the liquid-nitrogen temperature where the classical transport of free carriers is dominant. Mention should also be made of a significant decrease in the magnitude of the effect on the insulator side of the MI transition.

Thus, the following conclusions can be made on analyzing the MR field dependence.

(i) On the metal side of the MI transition, up to the critical point, the MR field dependence for n-Ge:As is a sum of the negative and positive MRs.

(ii) The derivative of the positive MR increases linearly with field in the entire investigated field range (the resistivity increases quadratically).

(iii) The derivative of the negative MR is linear in the field in weak fields and saturates in stronger fields (with resistivity quadratic and linear, respectively).

3.3. Temperature Dependence of Magnetoresistance

As follows from (8), (10), and (13), the temperature dependences of the field derivatives of the positive MR must be of the same type as those of the functions themselves, i.e., the derivative must increase with temperature in the classical case and decrease in the case of quantum corrections.

To elucidate the temperature dependence of the negative MR, we give complete expressions for this effect in the 3D case. For $H \ll H_\varphi$, we have

$$\Delta\rho/\rho = -(1/6)(D\tau_\varphi)^{3/2}(eH/\hbar c)^2, \tag{14}$$

and, in the case of $H \gg H_\varphi$, we have

$$\Delta\rho/\rho = -[0.605(eH/\hbar c)^{1/2} - (D\tau_\varphi)^{-1/2}]. \tag{15}$$

From (14) and (15) it follows that the temperature dependence of the negative MR in weak fields is determined by the temperature dependence of $L_\varphi = (D\tau_\varphi)^{1/2}$. As a rule, the dephasing time in 3D semiconductors approximately coincides with the characteristic electron–electron interaction time in disordered conductors, τ_{ee}, and, therefore, it must decrease with increasing temperature in proportion to $T^{-3/2}$. The diffusion coefficient can be assumed to be temperature-independent in this temperature range.

Thus, the magnitude of this effect must decrease with increasing temperature in weak fields and be temperature-independent in strong fields. Indeed, as can be seen from Fig. 3, the slope of the derivative of MR decreases with increasing temperature for weak fields and is temperature-independent for strong fields.

In Fig. 4a, the slope of the derivative of the negative MR in weak fields is shown as a function of temperature for the three least compensated metallic samples and insulator sample 5. It can be seen that, for metallic samples at low temperature, the dependence has a power-law form

$$d\rho/dH \propto T^{-\alpha}, \tag{16}$$

where $\alpha \approx 1.25$.

As follows from (14), the theory yields $\alpha = 9/4$ in the case where the dephasing time is determined by the electron–electron interaction. It can also be supposed that the dephasing time in our samples 1–3 is determined to some extent by the time of electron momentum relaxation via electron–phonon scattering, for which $\tau_{ph} \propto T^{-1}$. Substitution of this expression into (14) yields $\alpha = 1$. Hence, a conclusion can be made that the dephasing time is in the range between τ_{ee} and τ_{ph} but is closer to the former and shifts somewhat toward the latter when the MI transition point is approached in the course of compensation.

It follows from (2) that H_φ must shift towards stronger fields with increasing temperature. An analysis of the field dependences shown in Fig. 3 demonstrates that such a shift does occur. With the temperature increasing from 3.2 to 8 K, H_φ increases from 2.7 to 4 kOe; i.e., $H_\varphi \simeq T^{1/2}$. However, at higher temperatures, H_φ decreases again. This is probably due to the lower measurement accuracy at high temperatures.

A comparison of the temperature dependences for the positive component of the MR for samples 1–3 (Fig. 4b) with theoretical formulas (8), (10), and (13) shows that for all the three samples the derivative of the MR decreases with increasing temperature at low temperatures and starts to increase only upon heating to above 40 K (see the curve for sample 1 in Fig. 4b). Therefore, the positive MR becomes classical (Lorentzian) only at a high temperature, when the electron gas becomes nondegenerate, and remains anomalous at a low temperature, which must be the consequence of a quantum interaction between electrons in the diffusion or Cooper channels. In both cases, this leads to the following temperature dependence:

$$d\rho/dH \propto T^{-\alpha}, \quad (17)$$

with $\alpha = 3/2$.

The experimental values of α for the obtained linear approximations are smaller than those predicted by theory in the low-temperature limit, being about 0.9. Since the temperature appears explicitly in formulas (10) and (13), it is difficult to explain the discrepancy between the experimental and theoretical temperature dependences on their basis. The close resemblance of the field and temperature dependences of MR in the case of interaction between electrons in the diffusion and Cooper channels makes it difficult to choose one of them judging from the results obtained. However, a comparison of the characteristic fields for these mechanisms [see (9) and (12)] shows that the effect due to the interaction in the diffusion channel must be more pronounced.

3.4. Effect of Compensation

Figure 5 shows the derivatives of the negative MR and anomalous positive MR as functions of the magnetic field for all the investigated samples at the lowest temperature of 3.2 K where these effects are the most pronounced. At this temperature, the anomalous positive MR can be clearly observed only for the three least compensated samples. The anomalous positive MR in samples 2 and 3 is substantially smaller than that in sample 1 and is not observed at all in sample 5. Therefore, we can suppose that at a low temperature this effect contributes only slightly to the overall MR field dependence. This is why only unseparated experimental dependences are shown in Fig. 5 for samples 4 and 5.

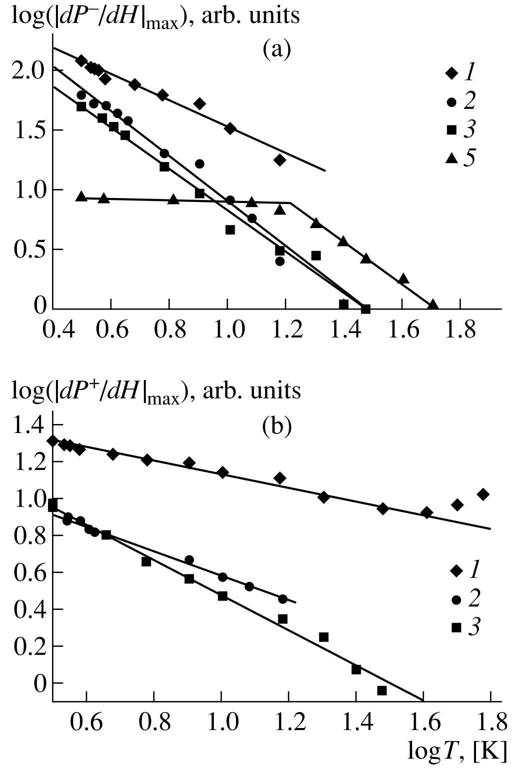

Fig. 4. Temperature dependences of (a) the maximum magnitudes of the negative magnetoresistance for samples 1, 2, 3, and 5 and (b) the positive magnetoresistance in a magnetic field of 14 kOe for samples 1, 2, and 3.

It can be seen from Fig. 5 that, as the compensation becomes stronger and the MI transition is approached, both the negative MR and the anomalous positive MR decrease, with the effects becoming less pronounced even at low levels of compensation K and depending on this parameter only slightly at medium levels of compensation. The further weakening of the negative MR effect occurs beyond the MI transition point on its insulator side, so that, in the insulating sample 5, this effect is almost 1.5 orders of magnitude weaker compared with the uncompensated metallic sample 1.

The simultaneous weakening of both the effects upon compensation presumably indicates that the compensation reduces the coherence length, which determines the quantum corrections. Only two parameters determine the coherence length: the diffusion coefficient and a characteristic time equal to the dephasing time in the case of a negative MR and to the interaction time in the case of an anomalous positive MR. It is

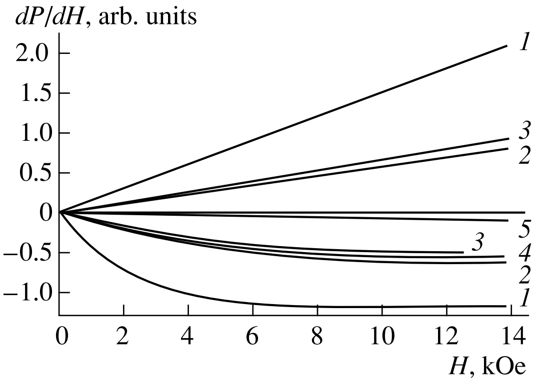

Fig. 5. Field dependences of the derivatives of the negative and positive magnetoresistance at a temperature of 3.2 K and different compensation levels. Curve numbers correspond to sample numbers in the table.

obvious that the introduction of charged donors and acceptors must reduce the momentum relaxation time, which determines the diffusion coefficient and directly affects the dephasing time, as shown above. However, it seems rather strange that the coherence length decreases mainly and rather abruptly for low compensation levels and only slightly (or not at all) for medium compensation levels.

3.5. Magnetoresistance of Insulating Samples

For sufficiently high compensation levels, the carrier density becomes smaller than the critical value for the MI transition to occur under dc conditions and the Fermi level shifts down below the percolation level (samples 5 and 6). Under these conditions, free carriers exist only in small limited regions of a sample, in which the fluctuating conduction-band bottom drops down below the Fermi level [12]. In dc measurements, the current through such a sample is limited by high-resistivity regions in which the Fermi level lies above the percolation level. In measurements at sufficiently high frequencies, a capacitive current flows through the high-resistivity regions and these do not contribute to the total resistance of the sample. The resistance is determined by the regions with free carriers, i.e., by those in which the Fermi level lies above the conduction-band bottom. Therefore, unlike the metallic samples where the Fermi level lies above the percolation level in the entire sample, in the case of the insulating samples dc and high-frequency measurements furnish information about different regions of a sample, with high and low resistivity, respectively. As a result, the MR in insulating samples shows different types of behavior under dc and microwave conditions. This is confirmed by comparison of our results with the data reported in [13], where a linear field dependence of the MR was observed in heavily doped samples.

It can be seen from Figs. 4a and 5 that the following MR features are observed in insulating samples under microwave conditions. As before, a negative MR is observed, but with a slope of the field dependence of the derivative an order of magnitude smaller than that in compensated but metallic samples. A quadratic field dependence of the negative MR persists over the entire range of the investigated fields. The temperature dependence of the MR changes: it becomes field-independent at low temperatures and tends to the form characteristic of compensated metallic samples at higher temperatures. A comparison of Figs. 4 and 1 shows that a transition from one type of behavior to the other occurs in the temperature range where the power-law conductivity–temperature relation characteristic of the MI transition region changes to the exponential one. In other words, the increasing carrier density in the conduction band makes the sample resistance insensitive to the conduction-band bottom fluctuations.

If we use, as before, the quantum correction theory for explaining the mechanism of appearance of a negative MR at microwave frequencies, it follows from Fig. 5 that the formation of isolated regions with free carriers leads to a dramatic increase in the characteristic magnetic field H_φ. In accordance with (2), this must occur because of a decrease in the dephasing length as a result of either the diffusion coefficient becoming smaller or the dephasing time becoming shorter. The increase in the scattering probability with increasing degree of compensation must lead to a reduction of both the parameters, but its influence on the latter is presumably stronger.

The quantum correction theory predicts that, with one of the sample dimensions decreasing (transition to 2D mode), the probability that closed trajectories appear increases owing to electron reflection from the sample boundaries. However, as follows from the presented results, passing to small regions leads in our case to a lower probability of closed trajectory appearance because of the decrease in the dephasing length.

One of the possible reasons for such MR behavior in isolated regions with low resistivity could be a transition from the metal conductivity to hopping over states within the Coulomb gap. Naturally, both the diffusion coefficient and the dephasing time decrease as a result. The mechanisms of the quantum correction theory, characteristic of metallic samples, are not operable at all in this case.

Another possibility of dephasing length shortening as a result of the MI transition is the following. In the bulk of the conducting region, a carrier with the energy above the Fermi level moves freely, but it can be captured with high probability at the boundary by a donor without phonon emission. Dephasing occurs in this case and the corresponding characteristic length is determined by the time of diffusion through the low-resistivity region rather than by the dephasing time.

Accurate quantitative estimates are difficult to obtain, but the temperature independence of the negative MR at low temperatures supports this model.

It is interesting that the negative MR of sample 6 exhibits a behavior similar to that of the less compensated sample 5. This fact can also be explained in terms of the formation of isolated low-resistivity regions. With the degree of compensation becoming larger, the number of such regions decreases while their internal structure is preserved. Therefore, the response of a structure of this kind to the magnetic field must remain qualitatively the same.

Thus, some features of the negative MR measured at microwave frequencies in compensated insulating samples are associated with the existence of isolated conducting regions.

4. CONCLUSION

(I) The MR effects remain 3D in the MI transition region at microwave frequencies, even though the skin effect substantially reduces the absorbing volume of the samples. The decrease in the absorbing volume is compensated for by a large increase in sensitivity.

(II) The field dependence of the MR in metallic samples demonstrates the presence of two effects, negative and positive MR, with comparable magnitudes. The effects can be separated because of the fundamentally different types of behavior exhibited by the resistivity in a strong magnetic field.

(III) The field dependence of the negative MR has two characteristic regions: at weak fields the derivative of the MR is linear in the magnetic field, which corresponds to a quadratic decrease of the resistivity, while at high fields the derivative of the MR is constant; i.e., the resistance decreases linearly with the increasing field. The latter dependence contradicts the weak-localization mechanism in the quantum correction theory predicting a square-root dependence of the MR at high fields.

(IV) The field dependence of the positive MR remains quadratic over the entire investigated range of fields.

(V) The magnitude of the negative MR decreases in weak fields following a power law with exponent $\alpha \approx 1.25$. This behavior conforms qualitatively to the weak-localization mechanism if we assume that the dephasing time lies between the electron-momentum relaxation times associated with the electron–electron and electron–phonon interactions and that the compensation shifts somewhat the dephasing time from the former to the latter.

(VI) The temperature dependence of the positive MR also shows power-law behavior. The fact that the effect becomes less pronounced with increasing temperature suggests that the anomalous positive MR, most likely associated with the interaction between electrons in the diffusion channel, manifests itself in this case. However, the exponent $\alpha \approx 0.9$ remains smaller than the value predicted by the quantum correction theory for this mechanism ($\alpha = 3/2$).

(VII) If the degree of compensation increases and the MI transition is approached, both the magnitude of the negative MR and the anomalous positive MR at a low temperature decrease. The former becomes less pronounced so that it is impossible to distinguish it in a “pure” form near the transition and further calculate the negative MR. The transition from a quadratic to a linear negative MR shifts toward higher fields. These effects indicate that the coherence length decreases with increasing compensation.

(VIII) The negative MR in compensated insulating samples is preserved, but the field dependence becomes purely quadratic, the magnitude of the effect decreases, and its temperature dependence can be separated into two regions. At low temperatures the MR is temperature independent, while at higher temperatures it tends to a dependence similar to that in compensated samples.

(IX) In insulating heavily compensated samples, the field and temperature dependences do not change with the increasing degree of compensation, since the negative MR measured at microwave frequencies reflects the behavior of electrons inside the isolated regions. Only the concentration of such regions decreases with the increasing degree of compensation, while the electron gas properties inside each region are preserved.

5. ACKNOWLEDGMENTS

We thank the participants of the scientific seminar of the Laboratory of Non-Equilibrium Processes, Ioffe Physicotechnical Institute, for their helpful participation in discussions.

The work was supported by the Russian Foundation for Basic Research (project no. 98-02-17353).

REFERENCES

1. B. L. Altshuler and A. G. Aronov, in *Modern Problems in Condensed Matter Sciences*, Vol. 10: *Electron–Electron Interaction in Disordered Systems*, Ed. by L. Efros and M. Pollak (North-Holland, New York, 1985), p. 1.
2. T. A. Polyanskaya and Yu. V. Shmartsev, Fiz. Tekh. Poluprovodn. (Leningrad) **23** (1), 3 (1989) [Sov. Phys. Semicond. **23**, 1 (1989)].
3. B. I. Shklovskii and B. Z. Spivak, in *Hopping Transport in Solids*, Ed. by M. Pollak and B. Shklovskii (North-Holland, New York, 1991), p. 271.
4. M. E. Reikin, J. Czingon, Qin-Yi Ye, *et al.*, Phys. Rev. B **45**, 6015 (1992).

5. N. V. Agrinskaya, V. I. Kozub, and D. V. Shamshur, Zh. Éksp. Teor. Fiz. **107**, 2063 (1995) [JETP **80**, 1142 (1995)].
6. H. L. Zhao, B. Z. Spivak, M. P. Gelfand, and S. Feng, Phys. Rev. B **44**, 10760 (1991).
7. A. Kurobe and H. J. Kamamura, Proc. Phys. Soc. Jpn. **51**, 1904 (1982).
8. A. I. Veĭnger, A. G. Zabrodskiĭ, T. V. Tisnek, and Zh. Biskupski, Fiz. Tekh. Poluprovodn. (St. Petersburg) **32**, 557 (1998) [Semiconductors **32**, 497 (1998)].
9. A. I. Veĭnger, A. G. Zabrodskiĭ, and T. V. Tisnek, Fiz. Tekh. Poluprovodn. (St. Petersburg) **34** (2000) (in press) [Semiconductors **34**, 45 (2000)].
10. A. G. Zabrodskiĭ, Fiz. Tekh. Poluprovodn. (Leningrad) **14**, 1130 (1980) [Sov. Phys. Semicond. **14**, 670 (1980)].
11. A. G. Zabrodskiĭ and K. N. Zinov'eva, Zh. Éksp. Teor. Fiz. **86**, 727 (1984) [Sov. Phys. JETP **59**, 425 (1984)].
12. B. I. Shklovskiĭ and A. L. Éfros, *Electronic Properties of Doped Semiconductors* (Nauka, Moscow, 1979; Springer-Verlag, New York, 1984).
13. A. N. Ionov and I. S. Shlimak, in *Hopping Transport in Solids*, Ed. by M. Pollak and B. Shklovskii (Elsevier North-Holland, 1991), p. 397.

Translated by S. Ktitorov

Semiconductors, Vol. 34, No. 7, 2000, pp. 755–758. Translated from Fizika i Tekhnika Poluprovodnikov, Vol. 34, No. 7, 2000, pp. 783–786.
Original Russian Text Copyright © 2000 by Gurevich, Logvinov, Espejo, Titov, Meriuts.

ELECTRONIC AND OPTICAL PROPERTIES OF SEMICONDUCTORS

The Role of Nonequilibrium Carriers in Linear Charge Transport (Ohm's Law)

Yu. G. Gurevich*, G. N. Logvinov*, G. Espejo*, O. Yu. Titov, and A. Meriuts*****
** Depto. De Fisica, CINVESTAV-I. P. N. Apdo. Postal 14–740, Mexico 07000, D. F. Mexico*
*** CICATA-I. P. N., Jose Sirob # 10, Col. Alameda, Santiago de Queretaro, Qro., 76040 México*
**** Kharkov Polytechnical University, Kharkov, 310002 Ukraine*

Submitted January 20, 2000; accepted for publication January 25, 2000

Abstract—The charge transport in a bipolar semiconductor to a metal wire was studied in a linear approximation with respect to the electric field. It is shown that both electrons and holes in general are nonequilibrium carriers in an arbitrarily weak electric field. Therefore, the consideration of surface and bulk recombination is necessary for the correct description of electrical conductivity. The spatial distributions of quasi-Fermi levels for electrons and holes are obtained in the quasi-neutrality approximation, and the general expression for a bipolar semiconductor conductivity is derived. This conductivity depends strongly not only on the transport of electrons and holes but also on the surface- and bulk-recombination rates. The criteria of low and high rates of recombination are determined; it is shown that a commonly used expression for the conductivity of a bipolar semiconductor is valid only at high rates of surface and/or bulk recombination. *© 2000 MAIK "Nauka/Interperiodica".*

INTRODUCTION

In considering an electric current in a homogeneous electron or hole semiconductor the well-known expressions [1]

$$\mathbf{j}_{n,\,p} = -\sigma_{n,\,p}\nabla\varphi \qquad (1)$$

are typically used; here, $\mathbf{j}_{n,\,p}$ are the densities of electron and hole currents, $\sigma_{n,\,p}$ are the electron and hole conductivities, and φ is the electric potential.

If the applied voltage is low, the $\sigma_{n,\,p}$ is independent of the voltage (a linear theory, Ohm's law) and is determined by the equilibrium concentrations of the majority carriers (n_0 or p_0). In this case, the chemical potentials of electrons μ_n^0 and holes μ_p^0 and their concentrations are related by the known expressions

$$\mu_n^0 = -\varepsilon_g - \mu_p^0, \qquad (2)$$

$$n_0 p_0 = n_i^2, \qquad (3)$$

where ε_g is the energy gap width, and n_i is the concentration of carriers in an intrinsic semiconductor.

In a bipolar semiconductor, the expression (1) describes the electron and hole components of an electric current. In the context of the theory linear with respect to the field, the expressions (1) and (2) can be rewritten in a form also suitable for an inhomogeneous semiconductor,

$$\mathbf{j}_{n,\,p} = -\sigma_{n,\,p}\nabla\tilde{\varphi}(x), \qquad (4)$$

where $\tilde{\varphi}(x) = \varphi(x) - (1/e)\mu_n^0$ is the electrochemical potential and $(-e)$ is the electron charge.

It should be emphasized that an effective electric field $\nabla\tilde{\varphi}$ appearing in the expressions for the currents $\mathbf{j}_n$ and $\mathbf{j}_p$ is the same. Therefore, the total current in a bipolar superconductor is defined by

$$\mathbf{j}_0 = -(\sigma_n + \sigma_p)\nabla\tilde{\varphi}(x). \qquad (5)$$

It should be pointed out that in obtaining (4) no boundary conditions were imposed either on the currents or on the potentials. Therefore, one may conclude that the expressions (4) determine the currents in an infinite semiconducting medium.

In actual situations, a semiconductor always has finite dimensions and is connected to an external power source by means of metallic wires. In this case, the process of a current flow in bipolar semiconductors differs radically from that described above. Indeed, the holes, in contrast with electrons, cannot be transferred from a semiconductor into a metal because of their absence in a metal (the circuit is opened at the contacts $x = \pm a$). Therefore, the holes should accumulate at one of the sample ends, provided the bulk and surface recombination processes in a semiconductor are not taken into account. As a result, the hole concentration at this contact exceeds an equilibrium value, whereas it becomes lower at the other contact. This means that nonequilibrium holes appear in a semiconductor (in the absence of recombination) even in the context of a linear theory. As is well known [2], the appearance of nonequilibrium carriers results in the necessity to introduce quasi-

Fermi levels $\tilde{\varphi}_n(x) = \varphi(x) - (1/e)\mu_n(x)$ and $\tilde{\varphi}_p(x) = \varphi(x) + (1/e)\mu_p(x)$. In this case, relations (2) and (3) for $\mu_n(x)$ and $\mu_p(x)$ do not hold. This means that, if one neglects the recombination processes, the electrons and holes are generally the nonequilibrium carriers even in an arbitrarily low electric field.

As a result, electrons and holes move in different effective electric fields $\nabla\tilde{\varphi}_n$ and $\nabla\tilde{\varphi}_p$ ($\nabla\tilde{\varphi}_n \neq \nabla\tilde{\varphi}_p$), and, instead of (5), we must write

$$\mathbf{j}_0 = -\sigma_n\nabla\tilde{\varphi}_n(x) - \sigma_p\nabla\tilde{\varphi}_p(x). \tag{6}$$

Formula (6) indicates that, in the absence of recombination, the electrical conductivity of a bipolar semiconductor is not reduced to the expression

$$\sigma = \sigma_n + \sigma_p \tag{7}$$

and the calculation of electrical conductivity requires the consideration of a spatial distribution of electron and hole quasi-Fermi levels.

It is clear that, in actual situations, there always exists a bulk and surface recombination. If the rates of at least one of them are sufficiently high, the excess concentration of holes in the near-surface regions vanishes and the conventional formula (7) becomes applicable.

However, one should bear in mind that it is impossible *a priori* to formulate the criterion for the recombination rates sufficient for relation (7) to hold.

The purpose of this study is to provide a solution to this problem and to develop the general concepts of the charge transport as a linear electric transport of nonequilibrium carriers in a bipolar semiconductor for arbitrary recombination rates.

MAIN EQUATIONS OF THE PROBLEM

As mentioned in the Introduction, in order to calculate the electrical conductivity of a bipolar semiconductor it is necessary to know the spatial variations of the electron and hole quasi-Fermi levels. They are determined from the coordinate dependences of nonequilibrium concentrations of electrons and holes and from the distribution of the electric potential. The electric potential is not a linear function of coordinates, because a semiconductor becomes inhomogeneous in the presence of nonequilibrium carriers.

To find the quasi-Fermi levels, one must solve the following system of equations:

$$\operatorname{div}\mathbf{j}_n = eR_n, \tag{8}$$

$$\operatorname{div}\mathbf{j}_p = -eR_p, \tag{9}$$

$$\nabla\varphi(x) = 4\pi e(\delta n - \delta p). \tag{10}$$

Here, δn and δp are the concentrations of nonequilibrium electrons and holes, and $R_{n,p}$ are the rates of electron and hole recombination.

The correct theory of recombination (see [3]) suggests that R_n is identically equal to R_p, and for all recombination mechanisms in linear approximation we have

$$R_n = R_p = R = \frac{\delta n}{\tau_n} + \frac{\delta p}{\tau_p}. \tag{11}$$

The values of τ_n and τ_p in (11) are the material parameters having the dimension of time, but they are not the lifetimes of electrons and holes. However, when the condition of quasi-neutrality holds [4] ($r_d^2 \ll a^2$, where r_d is the Debye radius and a is the sample length), as often takes place, then the nonequilibrium electron and hole concentrations are equal ($\delta n = \delta p$) and the lifetime τ common to electrons and holes comes into existence:

$$\frac{1}{\tau} = \frac{1}{\tau_n} + \frac{1}{\tau_p}. \tag{12}$$

From [3] it follows that $\tau_n/\tau_p = p_0/n_0$; therefore, the lifetime of nonequilibrium carriers can be represented as

$$\tau = \tau_n\frac{p_0}{n_0 + p_0}. \tag{13}$$

As is well known [4], the use of Poisson equation (10) in the quasi-neutrality approximation becomes unnecessary. However, the electric potential at the boundary displays jumplike changes.

Equations (8)–(10) should be complemented with the boundary conditions. They were formulated in [5]. For the one-dimensional problem, the boundary conditions have the form

$$j_p(x = \pm a) = \pm eR_s, \tag{14}$$

$$j_n(x = \pm a) = j_0 - eR_s, \tag{15}$$

$$\begin{aligned} j_0 = {} & \pm\sigma_n^s[\varphi_s(\pm a) - \varphi_m(\pm a)] \\ & \mp\frac{\sigma_n^s}{e}[\mu_n(\pm a) - \mu_m] \pm \frac{\sigma_n^s}{e}\Delta\varepsilon_c. \end{aligned} \tag{16}$$

Here, the indices s and m refer to a semiconductor and to a metal, σ_n^s is the surface electron conductivity of a semiconductor, $\Delta\varepsilon_c$ is the energy gap between the bottom of the conduction band of a semiconductor and the bottom of the conduction band of a metal [5], and φ_s and φ_m are the electric potentials in a semiconductor and in a metal.

The quantity R_s in (14), (15) is the rate of surface recombination of nonequilibrium carriers. By analogy with a bulk recombination, the rate of the surface recombination can be represented as [3]

$$R_s = S_n\delta n + S_p\delta p, \tag{17}$$

where S_n and S_p are the parameters characterizing the properties of the contacts. When the quasi-neutrality conditions ($\delta n = \delta p$) are satisfied, a rate of surface recombination common to electrons and holes can be introduced:

$$S = S_n + S_p; \tag{18}$$

then,

$$R_s = S\delta n. \tag{19}$$

The boundary conditions (14) and (15) account for the fact that holes are present only in a semiconductor, and electrons, both in a semiconductor and in a metal.

QUASI-FERMI LEVELS AND THE CONDUCTIVITY OF A BIPOLAR SEMICONDUCTOR

Let us assume that the potential in a metal at the contact $x = -a$ is $\varphi_m(x = -a) = 0$ and at the contact $x = +a$ is $\varphi(x = +a) = U$.

The electric and chemical potentials of a semiconductor can be represented in the following form:

$$\varphi(x) = \varphi_0 + \delta\varphi(x), \tag{20}$$

$$\mu_n(x) = \mu_n^0(T) + \delta\mu_n(x), \tag{21}$$

$$\mu_p(x) = -\varepsilon_g - \mu_n^0(T) + \delta\mu_p(x). \tag{22}$$

Here, φ_0 is the contact potential difference; and $\delta\varphi(x)$, $\delta\mu_n(x)$, and $\delta\mu_p(x)$ are unknown additions, which account for the deviations of the corresponding quantities from the equilibrium values in the electric field.

It can be readily shown that

$$\delta n(x) = \frac{n_0}{T}\delta\mu_n(x), \tag{23}$$

$$\delta p(x) = \frac{p_0}{T}\delta\mu_p(x), \tag{24}$$

$$\delta\mu_p(x) = \frac{n_0}{p_0}\delta\mu_n(x). \tag{25}$$

In view of (6), continuity equations (8) and (9) can be rewritten as

$$-\sigma_n\frac{d^2[\delta\tilde{\varphi}_n(x)]}{dx^2} = \frac{e\delta n}{\tau}, \tag{26}$$

$$\sigma_p\frac{d^2[\delta\tilde{\varphi}_p(x)]}{dx^2} = \frac{e\delta n}{\tau}, \tag{27}$$

where $\delta\tilde{\varphi}_{n,\,p}(x) = \delta\varphi(x) \mp (1/e)\delta\mu_{n,\,p}(x)$ are the quasi-Fermi levels in the presence of an electric current in a circuit.

Solving the system of equations (26) and (27) and taking into account (23)–(25) and the boundary conditions (14)–(16), we obtain

$$\delta\tilde{\varphi}_{n,\,p}(x) = \frac{U}{2} - \frac{j_0}{\sigma_n + \sigma_p} \mp \frac{1}{e}A\frac{\sigma_p}{\sigma_n + \sigma_p}\frac{n_0 + p_0}{p_0}\sinh(\lambda x), \tag{28}$$

where

$$A = j_0\frac{ep_0}{\sigma_n\lambda(n_0 + p_0)}[\cosh(\lambda a) + S_n\tau_n\lambda\sinh(\lambda a)]^{-1},$$

$$\lambda^2 = \frac{e^2 n_0}{T\tau_n}\frac{\sigma_n + \sigma_p}{\sigma_n\sigma_p}.$$

The quantity λ^{-1} has the meaning of a diffusion length in a bipolar semiconductor.

The electrical conductivity of a bipolar semiconductor with account taken of the contacts is defined by the expression

$$\sigma = \left[\frac{1}{\sigma_n^s a} + \frac{1}{\sigma_n + \sigma_p} \times \frac{\cosh(\lambda a) + (\sigma_p/\lambda a\sigma_n + S_n\tau_n\lambda)\sinh(\lambda a)}{\cosh(\lambda a) + S_n\tau_n\lambda\sinh(\lambda a)}\right]^{-1}. \tag{29}$$

From (28) it is evident that, in the presence of a current, a single Fermi level really splits into two quasi-levels. Their difference is given by

$$\delta\tilde{\varphi}_n(x) - \delta\tilde{\varphi}_p(x) = ej_0\frac{\sinh(\lambda x)}{\sigma_n\lambda[\cosh(\lambda a) + S_n\tau_n\lambda\sinh(\lambda a)]}. \tag{30}$$

From (30) it follows that this difference becomes greater with an increase in the current and a decrease in the rates of the surface and bulk recombination (decrease in S_n and increase in τ_n). On the contrary, the difference between the quasi-Fermi levels vanishes at extremely high rates of surface and/or bulk recombination.

The term $1/a\sigma_n^s$ in (29) represents the conductivity of contacts. Therefore, the quantity

$$\sigma_s = \left[\frac{1}{\sigma_n + \sigma_p} \times \frac{\cosh(\lambda a) + (\sigma_p/\lambda a\sigma_n + S_n\tau_n\lambda)\sinh(\lambda a)}{\cosh(\lambda a) + S_n\tau_n\lambda\sinh(\lambda a)}\right]^{-1} \tag{31}$$

is the electrical conductivity of a bipolar semiconductor. This value depends strongly not only on the electron and hole conductivities but, like the quasi-Fermi levels, also on the rates of surface and bulk recombination. In the case of a high-rate surface and/or volume recombination, $S \gg S_0$, $S_0 = [(n_0 + p_0)/(\sigma_n + \sigma_p)](T\sigma_p^2/e^2 a n_0 p_0)$ and/or $\tau_n \ll \tau_0$, $\tau_0 = (e^2 n_0 a/T)[(\sigma_n + \sigma_p)/(\sigma_n \sigma_p)$, we have

$$\sigma_s = \sigma_n + \sigma_p, \tag{32}$$

which coincides with the known expression (7). In the case of low-rate surface and bulk recombination ($S \ll S_0$ and $\tau_n \gg \tau_0$), we have

$$\sigma_s = \sigma_n. \tag{33}$$

In the case of low-rate surface recombination, the conductivity of a bipolar semiconductor is defined solely by the electron subsystem. The holes are not involved in the process of charge transport, which supports the qualitative arguments given in the Introduction.

We note that the condition for a low-rate bulk recombination $\tau_n \gg \tau_0$ can be rewritten as $\lambda a \ll 1$; i.e., the bulk recombination is ineffective when the sample length is smaller than the diffusion length. The condition for smallness of the surface recombination $S \ll S_0$ can be rewritten as

$$S \ll \frac{l}{a} v_T, \tag{34}$$

where l is a free path length of the carriers and v_T is their mean thermal velocity.

CONCLUSION

Criterion (34) is in good agreement with the qualitative estimates given in [6]. As shown in [7], in n-$\mathrm{Cd}_x\mathrm{Hg}_{1-x}\mathrm{Te}$ epilayers, the rate of surface recombination at room temperature is $S \sim 10^3$ cm/s. Since $v_T \sim 10^7$ cm/s and $l \sim 10^{-5}$–10^{-6} cm [2], the surface recombination (from the standpoint of the occurrence of nonequilibrium carriers) becomes ineffective if [see (34)] $2a \ll 10^{-2}$ cm. If, in addition, the condition $2a \ll \lambda^{-1}$ is satisfied, the nonequilibrium carriers will play a decisive role in the process of electrical conductivity. In conclusion, it should be mentioned that the necessity of taking into account the nonequilibrium carriers in linear problems of charge transport is not limited by the bipolar conductivity in semiconductors. A similar situation was encountered in studies of thermoelectric phenomena in bipolar semiconductors [8]. Furthermore, in the context of linear theory, an increase in the mobility of colloidal particles in highly concentrated suspensions in the presence of an electric field is observed, although the mechanism of such an increase is entirely different (see [9])

ACKNOWLEDGMENT

This work was supported in part by CONACyT, Mexico.

REFERENCES

1. A. I. Ansel'm, *Introduction to the Theory of Semiconductors* (Nauka, Moscow, 1978).
2. V. L. Bonch-Bruevich and S. G. Kalashnikov, *The Physics of Semiconductors* (Nauka, Moscow, 1977).
3. I. N. Volovichev, G. Espejo, Yu. G. Gurevich, *et al.*, Phys. Rev. B (in press).
4. V. P. Silin and A. A. Rukhadze, *Electromagnetic Properties of Plasma and Plasmalike Media* (Atomizdat, Moscow, 1961).
5. Yu. G. Gurevich, J. Thermoelectr., No. 2, 5 (1997).
6. É. I. Rashba, Z. S. Gribnikov, and V. Ya. Kravchenko, Usp. Fiz. Nauk **119** (1), 3 (1976) [Sov. Phys. Usp. **19**, 361 (1976)].
7. P. A. Borodovskiĭ, A. F. Buldigin, and V. S. Varavin, Fiz. Tekh. Poluprovodn. (St. Petersburg) **32**, 1076 (1998) [Semiconductors **32**, 963 (1998)].
8. Yu. G. Gurevich, O. Yu. Titov, G. N. Logvinov, and O. I. Ljubimov, Phys. Rev. B **51**, 6999 (1995).
9. J. M. Méndez-Alcaraz and O. Alarcon-Waess, *A New Theoretical Approach for the Electrophoretic Mobility of Charged Colloidal Particles in Concentrated Suspension* (in press).

Translated by A. V. Zalesskii

Semiconductors, Vol. 34, No. 7, 2000, pp. 759–762. Translated from Fizika i Tekhnika Poluprovodnikov, Vol. 34, No. 7, 2000, pp. 787–790.
Original Russian Text Copyright © 2000 by Ivlev, Gatskevich.

ELECTRONIC AND OPTICAL PROPERTIES OF SEMICONDUCTORS

Liquid Phase Reflectivity under Conditions of Laser-Induced Silicon Melting

G. D. Ivlev and E. I. Gatskevich

Institute of Electronics, Belarussian Academy of Sciences, Minsk, 220090 Belarus

Submitted January 24, 2000; accepted for publication January 27, 2000

Abstract—Dynamics of liquid silicon reflectivity at the wavelength of 0.63 μm is investigated under conditions of single-pulse heating of the semiconductor surface with ultraviolet radiation of an ArF excimer laser. The dependence of the reflectivity at the instant of maximum heating of the surface on the power density of the laser pulse is found. It is shown that the temperature-related reduction in reflectivity is most pronounced if the surface is overheated well above the equilibrium boiling point for silicon. The possible overheating of the liquid phase close to the ablation energy threshold is about 1500 K. © *2000 MAIK "Nauka/Interperiodica".*

It is known that laser-induced silicon melting is accompanied by an increase in silicon reflectivity R by a factor of about 2. The dynamics of reflectivity is investigated by optical probing of the irradiated surface with a typical probe wavelength of $\lambda = 0.63$ μm [1, 2]. An increase in R is conditioned by a semiconductor crystal–liquid metal [3] phase transition. The front of the phase transition, which is initiated by nanosecond laser heating of Si at the irradiation energy density W below the ablation threshold W_a, propagates into a single crystal for 1 μm beneath the surface. During melting, the peak temperature T_p of the liquid phase surface can considerably exceed [4] the equilibrium point T_m = 1685 K of the crystal–melt phase transition. In this case, the temperature gradient in a liquid layer reaches a value of about 10^7 K/m; i.e., the state of the liquid phase is far from the thermodynamic equilibrium.

The molten-silicon reflectivity R_m (the equilibrium state of the melt) should decrease both during laser heating and during a quasi-static increase in temperature T, because the rate of electron–phonon collisions in a skin layer increases, which causes the variation in the complex refractive index $\tilde{n} = n + i\kappa = f(\lambda, T)$. The spectral dependence $\tilde{n}(\lambda)$ for the wavelength range of 0.4–1 μm remained nearly unchanged when the temperature was varied from the equilibrium melting point T_m for Si to a value 200 K above the melting point [5]. The dependence $R_m(T)$ for $\lambda = 0.63$ μm was later determined experimentally [6] upon heating the silicon melt up to $T = 1950$ K. Upon heating, the decrease in R_m was 0.02% per degree Celsius. Experimental data on optical parameters of the Si melt at $T \geq 2000$ K are absent from the literature.

The behavior of R_m during nanosecond laser heating of liquid Si has been investigated in only a few studies [1, 2, 4] that have been devoted precisely to this aspect of laser irradiation. Experiments [1, 2] were carried out according to the two-pulse technique of Si heating by the first or second harmonic of the Nd:YAG laser emission. The liquid phase formation was initiated by the first pulse with a small W_1 excess above the Si melting threshold W_m. After a short delay Δt, the melt was heated by the second pulse with a varied energy density W_2. According to the opinion of the authors of [2], the advantage of this experimental procedure is that the effect of the second pulse, which heats the melt surface, can be analyzed in more detail compared to a single-pulse irradiation.

According to [1], the optical parameters of the melt $\tilde{n}$ and R_m at $\lambda = 0.63$ μm remained constant during the second pulse, although the calculated temperature T_p approached the equilibrium boiling point for Si T_b = 2900 K at the highest experimental value W_2. On the other hand, the reversible variation in R_m at the same wavelength in an identical experiment [2] was clearly pronounced even at temperatures below T_b (but ≥2000 K), which were found from the measurements of $R_m(W_2)$ using the Drude model. It was later found (using the methods of optical pyrometry and R_m measurements at $\lambda = 1.06$ μm [4]) that the temperature-related decrease in reflectivity under conditions of the single-pulse irradiation with a ruby laser was clearly observable only at overheating of the liquid phase, i.e., at $T_p > T_b$.

The above discrepancies, as well as the lack of knowledge about optical properties of the overheated silicon melt, have stimulated new experiments. The

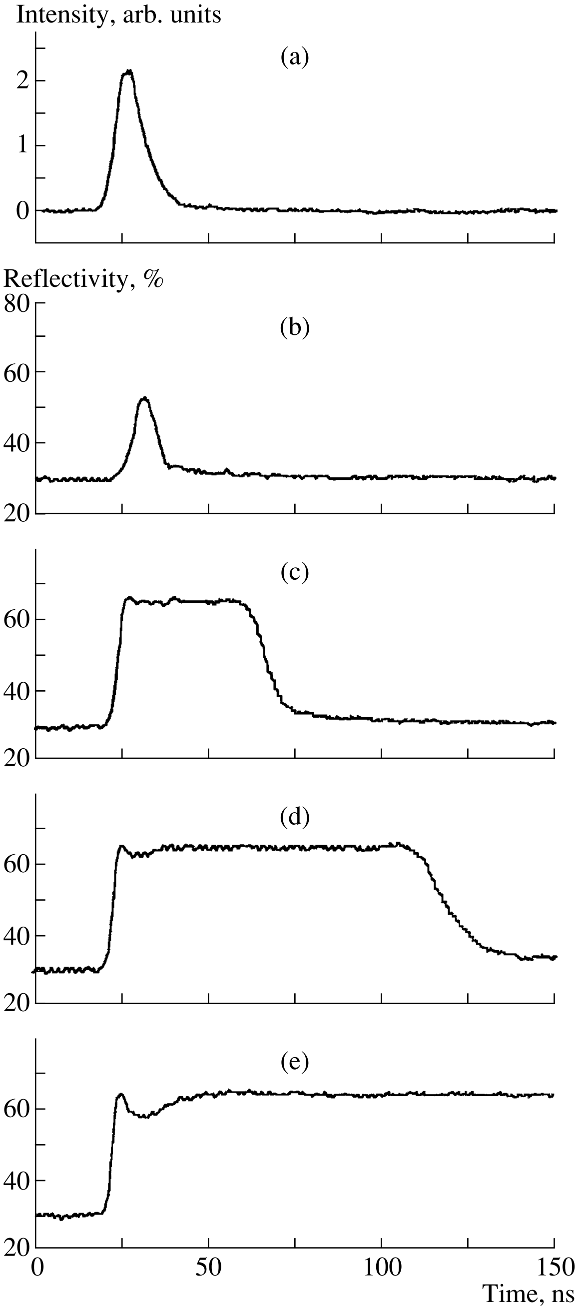

Fig. 1. (a) Shape of the laser pulse irradiating the silicon surface and time dependences of the reflectivity R_m at λ = 0.63 μm for energy densities of (b) 0.64, (c) 1.3, (d) 1.5, and (e) 2.2 J/cm^2.

purpose of this study is to investigate the dynamics of the liquid-phase reflectivity during Si melting upon exposure to single-pulse ultraviolet (UV) radiation of an excimer laser.

Wafers of a KDB-10 silicon (p-Si:B, ρ = 10 Ω cm) with the surface orientation (111), which were mechanically and chemically polished, were irradiated in experimental conditions according to [7] using an EMG 100 ArF excimer laser with a wavelength of 0.19 μm and a half-height pulse width of τ = 10–12 ns. The p polarized probe beam of a helium–neon laser (λ = 0.63 μm) was focused to a spot of ~50 μm at the center of the irradiated zone; the angle of incidence was 30°. The probe radiant flux reflected from the sample was detected using a silicon photodiode with a transient-response rise time of 1 ns. The output signal of the photodiode, which was provided with an interference filter for λ = 0.63 μm, was fed to the input of a TS 8123 storage oscilloscope with a passband of 100 MHz (rise time 3.5 ns).

According to the data obtained, an increase in R, which is related to Si melting, is observed for W > 0.6 J/cm^2 (Fig. 1). An increase in the energy density to 0.75 J/cm^2 causes R to increase to the value of R_m that corresponds to the optical parameters of the melt. The probe radiation reflectivity from a liquid phase does not vary in the W range from 0.8 to 1.3–1.4 J/cm^2. Thus, on reaching the maximum, the reflectivity remains constant until the process of epitaxial crystallization is completed. For energy densities $W \geq 1.5$ J/cm^2, reversible variation of R_m during the laser pulse is observed, which is associated with heating the melt surface. The reflectivity initially increases to the maximum, is decreased by a certain quantity ΔR, and increases again due to cooling of the liquid phase, whose temperature is tens of degrees below T_m during crystallization [8]. The quantity ΔR substantially rises with an increase in W to 2.2 J/cm^2 (W_a = 2.3–2.4 J/cm^2) when the higher peak temperature of the surface is reached.

A silicon single crystal with a mechanically and chemically polished surface is characterized by the refractive index $\tilde{n}$ = 3.88 + 0.02i at T = 300 K at λ = 0.63 μm [9]. The reflectivity R_c = 29.7% corresponds to these values n and κ for the p polarization of the beam and an angle of incidence of 30° [10]. According to the results of measurements, $R_m = 2.2R_c$; i.e., the quantity R_m somewhat exceeds 65%. This value is in good agreement with the experimental data [2], in which the angle of incidence, polarization, and wavelength were the same. However, Si was heated by exposure to two laser pulses of equal width (7 ns) with a radiation wavelength of 0.53 μm (Δt = 28 ns). The dependence of reflectivity on the laser-pulse energy density at the instant of reaching the reflectivity minimum, which was obtained by us (Fig. 2), is similar to the dependence $R_m(W_2)$ reported in [2]. Once the irradiation energy is close to the damage threshold of the silicon surface, the value of R_m at the instant of maximum heating of the liquid phase decreases by 8% and by almost 10% in experimental conditions [2], under which, judging from the data, the threshold value $W_2 = W_a$ was ~2 J/cm^2.

Once the Si surface was heated using a single-pulse radiation of a ruby laser [4] (τ = 80 ns), the relatively weak reversible variation in the reflectivity of the melt for the *p*-polarized probe beam ($\lambda = 1.06$ μm), whose angle of incidence on the sample surface was 45°, was observed only on heating the surface to a temperature of several hundred degrees above T_b ($W_a = 6.4$ J/cm^2). Thus, according to the results of pyrometric measurements, $T_p = 3400$ K at $W = 5.8$ J/cm^2 (overheating by ~500 K). In this case, ΔR amounted to only 2.5%. It should be larger at $\lambda = 0.63$ μm. In this case, according to our estimation, ΔR should be 3–3.5%. However, this value is still substantially lower than the above maximum values of ΔR. According to the data (Fig. 2) taken from [2], the calculated temperature of 3400 K corresponds to $\Delta R = 3\%$. This temperature coincides with the experimental T_p value mentioned above. However, the energy density $W_2 = 1.2$ J/cm^2, at which such heating of the melt surface is possible, is still rather low compared to $W_a = 2$ J/cm^2.

This means that the surface is overheated by much more than 500 K at an energy density close to W_a in experimental conditions [2]. Melt overheating is precisely the factor that leads to a pronounced decrease in the melt reflectivity. Actually, at calculated temperatures below 2600 K, $\Delta R = 0$. In the T_p range from 2600 K to T_b, ΔR is as small as 2% (Fig. 2), and, for $W \longrightarrow W_a$ ($T_p > T_b$), it approaches 10%. Assuming that ΔR increases proportionally to the difference $T_p - T_b$ (3% per 500 K), we estimate the possible overheating at about 1500 K. This refers equally to our experimental conditions with the single-pulse laser heating of the Si surface.

Using the results of pyrometric measurements [4], we can demonstrate that no temperature dependence of $\tilde{n}$ and R_m was revealed in study [1], where the dynamics of optical parameters for the two-pulse laser irradiation of silicon was investigated, because the melt surface was not heated to at least 2900 K in this experiment. For the maximum value $W_2 = 4$ J/cm^2 in the second pulse ($\tau_2 = 70$ ns, $\lambda_2 = 1.06$ μm, and $\Delta t = 20$ ns) and the energy density $W_1 = 0.8$ J/cm^2 in the first pulse ($\tau_1 = 50$ ns and $\lambda_1 = 0.53$ μm), the duration of the combined irradiation was the same as the value in the experiment [4] with a ruby laser ($\tau = 80$ ns).

The total energy density $W' = W_1 + W_2 = 4.8$ J/cm^2 corresponds to $T_p = 2850$ K according to the empirical formula $T_p = a + bW^2$ ($a = 1648$ K and $b = 52.3$ K cm^4/J^2). This formula is sufficiently accurate for description of the dependence $T_p(W)$ in the range $W = 1$–6 J/cm^2 [4]. However, it is necessary to take into account the difference in reflectivities of the laser radiation from the melt, i.e., the nonequivalency of the experimental conditions for the energy balance of the pulse exposure. It can be found from the spectral dependence $\tilde{n}(\lambda)$ for liquid Si [5] that $R_m = 73\%$ at $\lambda = 0.53$ and 0.69 μm, and $R_m = 76\%$ at $\lambda = 1.06$ μm. Thus, the absorptivity $1 - R_m$ at $\lambda = 1.06$ μm (23%) is 4% less than at $\lambda = 0.69$ μm.

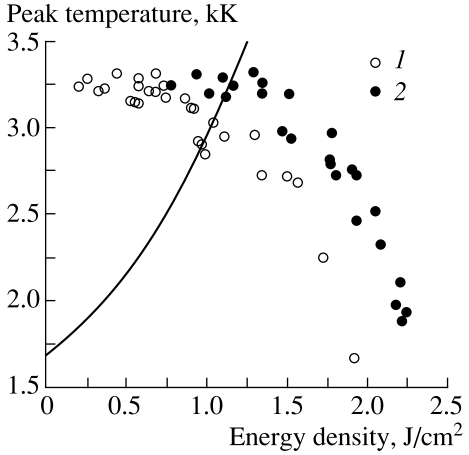

Fig. 2. Silicon melt reflectivity on attaining the minimum of R_m in relation to the quantities (*1*) W_2 and (*2*) W. The calculated curve $T_p(W_2)$ obtained by solving the heat conduction equation and the experimental points *1* are taken from [2].

Introducing the corresponding correction to the quantity W_2, which should be decreased by 15%, and determining T_p for the new value $W' = 4.2$ J/cm^2, we find that the attainable temperature of the Si surface was lower than 2600 K. For this reason, the authors of [1] observed no variations in the probe radiation reflection from the melt.

In conclusion, we note that the observed decrease in the silicon reflectivity in conditions of the pulse laser heating becomes more pronounced with overheating of the liquid phase above the equilibrium boiling point of the melt. A decrease in the pulse width from ~10^{-7} s to 10^{-8} s permits one to increase the possible overheating of the melt surface several times because of a substantial increase in the heating rate. The variation in the optical parameters of the melt with its transition to the metastable liquid state is clearly observed for both two-pulse and single-pulse laser heating of the Si surface by both visible and UV radiation. The temperature dependence of reflectivity of the melt for the thermodynamic stability region of the liquid state manifests itself solely beginning from the temperatures close to the equilibrium boiling point of silicon.

ACKNOWLEDGMENTS

We thank V. Chab for the opportunity to perform the experiment with an excimer laser.

REFERENCES

1. G. M. Gusakov, A. A. Komarnitskii, and A. S. Em, Phys. Status Solidi A **107**, 261 (1988).
2. J. Boneberg, O. Yavas, B. Mierswa, and P. Leiderer, Phys. Status Solidi B **174**, 295 (1992).

3. A. R. Regel’ and V. M. Glazov, *Physical Properties of Electronic Melts* (Nauka, Moscow, 1980).
4. G. D. Ivlev and E. I. Gatskevich, Fiz. Tekh. Poluprovodn. (St. Petersburg) **30**, 2097 (1996) [Semiconductors **30**, 1093 (1996)].
5. K. M. Shvarev, B. A. Baum, and P. V. Gel’d, Fiz. Tverd. Tela (Leningrad) **16**, 3246 (1974) [Sov. Phys. Solid State **16**, 2111 (1974)].
6. M. O. Lampert, J. M. Koebel, and P. Siffert, J. Appl. Phys. **52**, 4975 (1981).
7. G. Ivlev, E. Gatskevich, V. Chab, *et al.*, Appl. Phys. Lett. **75**, 498 (1999).
8. G. D. Ivlev and E. I. Gatskevich, Appl. Surf. Sci. **143**, 265 (1999).
9. V. I. Gavrilenko, A. M. Grekhov, D. B. Karbushyan, and V. G. Litovchenko, *Optical Properties of Semiconductors* (Naukova Dumka, Kiev, 1987).
10. A. P. Prishivalko, *Reflection of Light from Absorbing Media* (Akad. Nauk BSSR, Minsk, 1963).

Translated by N. Korovin

Semiconductors, Vol. 34, No. 7, 2000, pp. 763–767. Translated from Fizika i Tekhnika Poluprovodnikov, Vol. 34, No. 7, 2000, pp. 791–795.
Original Russian Text Copyright © 2000 by Venger, Gasan-zade, Strikha, Staryĭ, Shepel'skiĭ.

Far Infrared Stimulated and Spontaneous Radiation in Uniaxially Deformed Zero-Gap $Hg_{1-x}Cd_xTe$

E. F. Venger, S. G. Gasan-zade, M. V. Strikha, S. V. Staryĭ, and G. A. Shepel'skiĭ

Institute of Semiconductor Physics, National Academy of Sciences of Ukraine, Kiev, 252028 Ukraine

Submitted January 24, 2000; accepted for publication January 27, 2000

Abstract—Stimulated radiation in the range of 80–100 μm was observed in uniaxially stressed zero-gap $Hg_{1-x}Cd_xTe$ ($x = 0.10$–0.14) under conditions of impact ionization by an electric field. The abrupt increase in emission occurs under the threshold values of elastic strain and electric-field strength and is followed by an abrupt increase in the current in the sample. The field and deformation dependences of spontaneous radiation are also determined. The mechanism of the effect observed is suggested taking into account the transformation of energy bands and impurity acceptor levels by the uniaxial elastic stress. © *2000 MAIK "Nauka/Interperiodica".*

INTRODUCTION

Studies of stimulated radiation in the far infrared (IR) range (that corresponds to THz frequencies) have been performed during the last decade in a lightly doped *p*-Ge. In this case, the population inversion was produced in the crossed electric and magnetic fields, and the optical transitions occurred between degenerate subbands of light and heavy holes (see review [1]). Observation of intense stimulated radiation in the uniaxially stressed *p*-Ge was reported in [2]. Uniaxial stress induces the transformation of the energy spectrum of holes (both free and bound by acceptors) and, in particular, results in a significant splitting of the energy levels. The authors of [2] recently identified the peaks of stimulated radiation on the basis of spectral studies and theoretical calculations; they related these peaks to optical transitions via the resonance acceptor states [3].

In this paper, we report for the first time the observation of the intense far IR radiation in the uniaxially-stressed zero-gap *p*-type $Hg_{1-x}Cd_xTe$ semiconductor under the condition of impact ionization by a strong electric field.

Under the condition of uniaxial stress, a significant transformation of the energy spectrum of the zero-gap semiconductor occurs [4, 5]. It consists in the formation of the stress-dependent energy gap between the *c* and *v* bands for $k = 0$ and also the loop of extrema in the *v* band for $k_\perp = k_c$ (see Fig. 1). Here, $k_\parallel$ and $k_\perp$ are the wave vectors in the longitudinal and transverse direction with respect to the axis of strain (for the isotropic band spectrum), and k_c is the wave vector in the side extremum of the *v* band. The transformation of the energy spectrum of zero-gap semiconductor clearly manifests itself in the features of galvanomagnetic phenomena in the uniaxially stressed crystal [6, 7].

The transitions in the far IR range between the strain-split subbands of zero-gap semiconductors were studied theoretically in [8]. The possibility of negative absorption under quasi-equilibrium population inversion for electron–hole pairs was discussed; this population inversion is described by the Fermi distribution in the *c* and *v* bands. This mechanism can be effected by injection or under optical pumping; however, the threshold carrier concentration calculated for the stimulated radiation mode seemed to be rather high.

Another mechanism of population inversion in the case of uniaxially-deformed zero-gap $Hg_{1-x}Cd_xTe$ is proposed in this paper. Under the conditions of impact ionization induced by the applied external electric field, a distribution of high-energy electrons appears in the *c* band, whereas the holes are localized near the extremum of the *v* band. Due to the transformation of impurity states by the uniaxial stress, the lower split acceptor level intersects the top of the *v* band and the contribution of indirect interband radiative transitions to recombination sharply increases. As a result, the realization of the stimulated radiation mode seems possible.

EXPERIMENT

Samples of zero-gap *p*-type $Hg_{1-x}Cd_xTe$ ($x = 0.10$–0.14) with the concentration of electrically active impurities $N_A - N_D = 6 \times 10^{15}$–$2 \times 10^{16}$ cm^{-3} (at 77 K) were studied. Special attention was given to sample preparation with strictly parallel faces. Deviation from the parallelism did not exceed 1′–1.5′. The elastic stress *P* and electric field *E* were applied along two crystallographic directions [100] and [112]. The field intensity up to $E < 60$ V/cm with a pulse duration of about 1 μs was applied using indium contacts formed at the narrow sample sides at a distance of 3–5 mm. The length

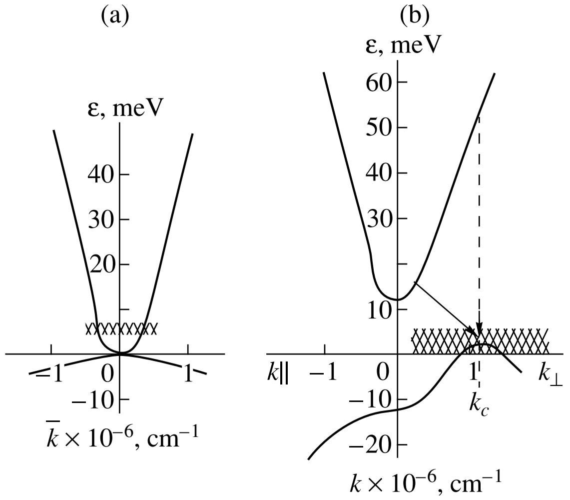

Fig. 1. Transformation of the energy spectrum of zero-gap $Hg_{1-x}Cd_xTe$ ($x = 0.14$) under the uniaxial deformation at $T = 4.2$ K. $P =$ (a) 0 and (b) 2.5 kbar, **P** ∥ [001]. The arrows indicate the direct and indirect radiative transitions.

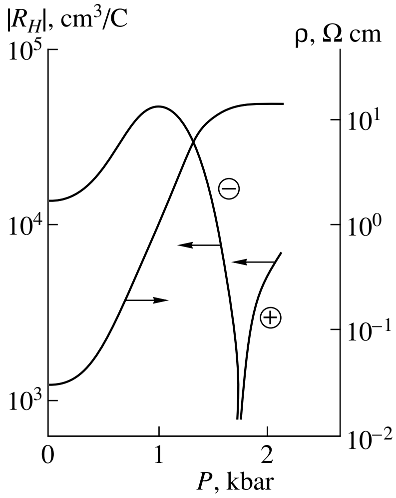

Fig. 2. Deformation dependences of electrical resistivity ρ and Hall coefficient R_H for $Hg_{1-x}Cd_xTe$ with $x \simeq 0.14$, $T = 4.2$ K. The Hall coefficient is measured for $H = 5$ kOe.

of the samples along the compression axis was 6–8 mm, their cross-sectional area was 0.5–0.8 mm^2.

The value of the applied elastic stress was in the range of $P = 0$–3 kbar. The measurements were carried out at the liquid-helium temperature. The radiation was detected with a Ge(Ga) photodetector with the maximum sensitivity at the wavelength of radiation of 100 μm.

Dependence of the resistivity ρ and Hall coefficient R_H for $Hg_{1-x}Cd_xTe$ samples on the uniaxial stress P in a weak constant electric field is shown in Fig. 2. The sharp changes of ρ and R_H have a simple explanation. In the absence of elastic stress, the valence and conduction bands of a zero-gap semiconductor are degenerate at the point $k = 0$. Acceptor states form an impurity band at the energy distance $E_A = 5$–6 meV above the top of the valence band and, thus, turn out to be in the conduction band, i.e., become resonance states. In this case, the Fermi level is pinned in the acceptor band $E_F = E_A$.

The donors, as follows from numerous low-temperature experiments, remain ionized in $Hg_{1-x}Cd_xTe$ up to the lowest temperature. Therefore, the conduction of the zero-gap p-$Hg_{1-x}Cd_xTe$ sample is defined at low temperatures by free electrons with the concentration $n = (eR_H)^{-1}$ rather than by holes. In the sample under study, $n = (2$–$3) \times 10^{15}$ cm^{-3}. The electron mobility determined from the relation $\mu_n = |R_H/\rho|$ is equal to 6×10^5 cm^2/(V s) for the given case. The negative sign of R_H is indicative of the electron type of conduction in crystals under such conditions. With uniaxial stress applied, the acceptor level follows the top of the valence band and falls in the energy gap produced by a deformation (see Fig. 1). In this case, the electrons freeze out at the acceptor states. As a result, the free electron concentration exponentially decreases, which leads to the sharp changes of ρ and R_H observed experimentally.

The dependences of spontaneous radiation intensity I in the far IR range (the wavelength about 100 μm) and of the current J through the sample on the intensity of the pulsed electric field under various values of elastic stress are shown in Fig. 3. All the measurements were performed for the intensities of the electric field that exceeded the breakdown threshold for shallow impurities. For $E = 3$–5 V/cm, practically all the electrons frozen previously at acceptor states are excited due to the impurity breakdown and, thus, are found again in the conduction band.

A significant enhancement of the current and spontaneous radiation intensity with an increase in the electric field occurs in the range of slight elastic deformations (0–0.5 kbar), in which case the superlinearity of curves $I(E)$ and $J(E)$ is observed even for $E > 10$ V/cm. The superlinearity becomes especially noticeable for $E = 40$–50 V/cm. The dependence observed can be explained by an increase in the free electron concentration. Actually, in the absence of the energy gap, an intrinsic concentration of carriers n_i in the zero-gap semiconductor increases with the electric field as $n_i \propto E^{3/2}$. A certain contribution to the shape of the curve $J(E)$ can be made by the field dependence of mobility $\mu_n(E)$. In the case of scattering by the ionized impurities, $\mu_n \propto E_F^{3/2}$, whereas, under the significant heating of electrons, $\mu_n \propto T_e^{3/2}$ (T_e is an effective electron temperature). In the range of large elastic stresses, the factor of enhancement of the intrinsic concentration becomes insignificant owing to the large energy gap

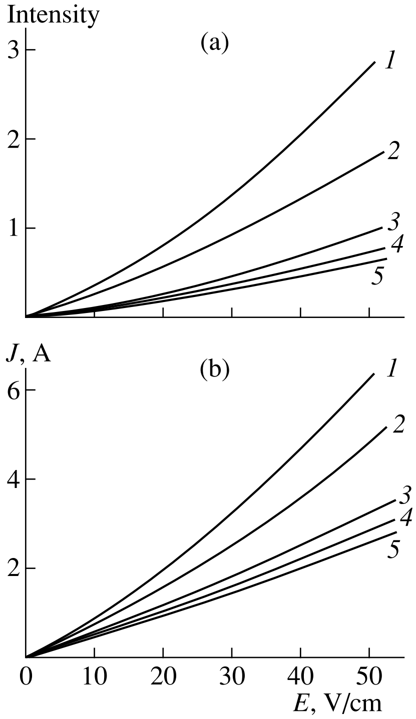

Fig. 3. Dependence of (a) spontaneous radiation intensity and (b) electric current on the intensity of electric field E for deformation induced by P = (*1*) 0 and 0.5, (*2*) 1.0, (*3*) 1.5, (*4*) 2.0, (*5*) 2.5 kbar; $\mathbf{P} \parallel [001]$, $T = 4.2$ K. The sample is the same as in Fig. 2.

between the bands (for $P = 2.5$ kbar, $E_g \approx 25$ meV) produced by the deformation and the position of the resonance acceptor level in this gap (Fig. 1). Therefore, a slight nonlinearity of $I(E)$ and $J(E)$ is determined here only by a weak dependence $\mu_n(E)$.

It is of interest to note that, in the region of $P > 1.5$ kbar, sharp peaks are observed in the curves of radiation intensity dependences $I(E)$; these peaks are observed only during the strain increase. They do not manifest themselves under steady-state conditions. Under subsequent effects of elastic deformation, the positions of radiation peaks on the deformation scale and their intensity change. In this case, no abrupt changes in the dependences of electric current $J(E)$ are observed. The radiation peaks observed can be explained by the break-away of dislocation in the electric breakdown during the action of uniaxial stress. The nature of these peaks will not be discussed further owing to the lack of experimental data.

Under the threshold values of elastic deformation and the electric field ($P = 2.5$–2.7 kbar, $E = 50$–55 V/cm) within the range of photodetector sensitivity, a sharp (by about 3 orders of magnitude) enhancement of radiation intensity is observed (Fig. 4). The abrupt increase in radiation is followed by a current increase, which, however, is much weaker: by no more than 4–6 times. The dependences observed turned out to be reversible and repeated under the subsequent application of P or E. The presence of a threshold in the P and E values, a large intensity of a signal, a correlation between these thresholds in the current and radiation signals, and the decisive role of the parallelism of the faces and the surface state of a crystal for the radiation to be observed indicate that this radiation is stimulated. A sharp enhancement of the current arising simultaneously with the appearance of stimulated radiation implies that band-to-band impact ionization plays a significant role in this process.

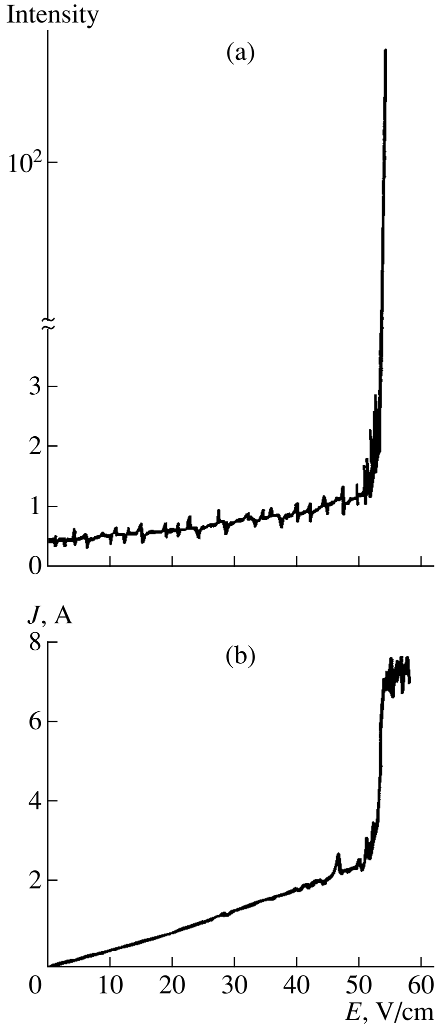

Fig. 4. The abrupt increase in (a) radiation intensity and (b) electric current for $Hg_{1-x}Cd_xTe$ for $P = 2.5$ kbar, $\mathbf{P} \parallel [001]$, $T = 4.2$ K. The sample is the same as in Fig. 2.

THEORY: DISCUSSION OF EXPERIMENTAL RESULTS

Taking into account the features of the energy band structure of an uniaxially-deformed zero-gap semiconductor, we consider the possible optical transitions responsible for the radiation in the far IR spectral

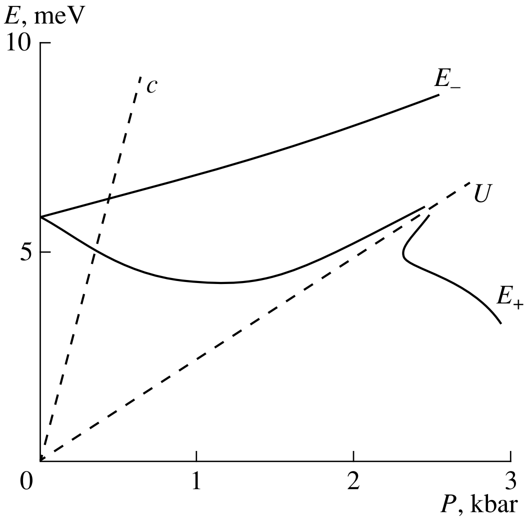

Fig. 5. Transformation of the band spectrum and acceptor level in the zero-gap $Hg_{1-x}Cd_xTe$ with $x = 0.14$ (according to [6]) induced by the elastic deformation.

region (photon energy of about 10 meV). It is noteworthy first of all that, for the elastic stresses $P \geq 2.5$ kbar in $Hg_{1-x}Cd_xTe$ with compositions $x = 0.10$–0.15, the energies on the order of 60–80 meV [7] correspond to direct transitions between the c band and the top of v band (see Fig. 1). Therefore, when considering the radiation spectra observed in our experiments for elastic stresses exceeding 1 kbar, we should take into account only the radiative transitions from the conduction band to the levels of the acceptor type (the momentum conservation law in this case is “removed” due to the smeared acceptor wave function in the momentum space).

In this case, the probability of electron transition from the state ($c\sigma p$, where σ is a spin index and p is the quasi-momentum) to the acceptor state (a) is defined by the known corollary to the Kubo formula (see, e.g., [9])

$$\tau_R^{-1}(cp) = \frac{(2\pi e)^2}{\varepsilon V}\sum_{q\mu}\omega_q^{-1}\sum_{\sigma'}\left|(c\sigma p\left|\hat{V}e_{q\mu}\right|a\sigma')\right|^2 \times \delta(E_{cp} - E_A - \eta\omega_q)[1 - f(E_A)]. \qquad (1)$$

Here, q and μ are the wave vector and polarization index of the photon emitted (with frequency ω_q and polarization unit vector $e_{q\mu}$), V is the normalization volume, ε is the dielectric constant (we assume it to be isotropic), $\hat{V}$ is the velocity operator, $f(E)$ is the electron distribution function, and E_{cp} is the electron energy spectrum. The last bracketed term in (1) describes the probability of occupation of the acceptor state by a hole.

Then, we substitute the acceptor wave function in the form of expansion in the free hole functions ($v\sigma'p'$)

$$\varphi_{a\sigma'} = \frac{1}{\sqrt{V}}\sum_{p'} C_{p'}^{V\sigma'}\varphi_{V\sigma'p'} \qquad (2)$$

in the matrix element in (1).

Thus, the problem of finding of the radiative transition rate is virtually reduced to the problem of determining the expansion coefficients $C_{p'}^{V}$. These coefficients can be calculated in the context of the zero-radius potential model, which was used in the case of a uniaxially deformed semiconductor [10].

We do not present the details of calculations, which are rather cumbersome in this case, and note only that the expansion coefficients $C_{p'}^{V}$ in expression (2) are proportional to

$$C_{p'}^{V} \propto \frac{1}{E_{Vp} - E_A} \qquad (3)$$

(this expression is the general consequence of the Coster–Slater model). Therefore, when the top of the valence band is intersected by the lowest split acceptor level, the singularity appears in the matrix element in expression (1).

Dependence of the position of acceptor energy levels on the deformation is shown in Fig. 5 and is taken from [6]. For a stress of $P = 2.5$ kbar, the lowest split state (state E^+) intersects the top of the v band and becomes a resonance level instead of a localized one. Due to dependence (3), the matrix element in expression (1) sharply increases in this case. Under conditions of impact ionization, the resonance states in the elastic stress range indicated turn out to be occupied by holes. Therefore, the intensity of radiative transitions sharply increases.

The mechanism of optical transitions under consideration can account for the appearance of intense radiation with a photon energy of about 10 meV. Additional studies are necessary for more detailed consideration of the nature of the radiative mechanism. First in priority should be the determination of the spectral distribution of the radiation observed and the form of the nonequilibrium distribution function for charge carriers under impact ionization.

ACKNOWLEDGMENTS

We are grateful to I.V. Altukhov and M.S. Kagan for providing us with the opportunity to take measurements and to F.T. Vas’ko for his fruitful participation in discussion of experimental results.

REFERENCES

1. A. A. Andronov, Fiz. Tekh. Poluprovodn. (Leningrad) **21**, 1153 (1987) [Sov. Phys. Semicond. **21**, 701 (1987)].

2. I. V. Altukhov, M. S. Kagan, and V. P. Sinis, Pis'ma Zh. Éksp. Teor. Fiz. **47**, 136 (1988) [JETP Lett. **47**, 164 (1988)].
3. I. V. Altukhov, M. S. Kagan, K. A. Korolev, *et al.*, Zh. Éksp. Teor. Fiz. **115**, 89 (1999) [JETP **88**, 51 (1999)].
4. A. V. Germanenko and G. M. Minkov, Phys. Status Solidi B **184**, 9 (1994).
5. E. V. Bakhanova and F. T. Vas'ko, Fiz. Tverd. Tela (Leningrad) **32**, 86 (1990) [Sov. Phys. Solid State **32**, 47 (1990)].
6. F. T. Vas'ko, S. G. Gasan-zade, V. A. Romaka, and G. A. Shepel'skiĭ, Pis'ma Zh. Éksp. Teor. Fiz. **41**, 100 (1985) [JETP Lett. **41**, 120 (1985)].
7. A. V. Germanenko, G. M. Min'kov, E. L. Rumyantsev, and O. É. Rut, Zh. Éksp. Teor. Fiz. **94** (8), 242 (1988) [Sov. Phys. JETP **67**, 1654 (1988)].
8. E. V. Bahanova, M. V. Strikha, and F. T. Vasko, Phys. Status Solidi B **164**, 157 (1991).
9. E. V. Bakhanova and F. T. Vas'ko, Pis'ma Zh. Tekh. Fiz. **13**, 1520 (1987) [Sov. Tech. Phys. Lett. **13**, 638 (1987)].
10. F. T. Vas'ko and M. V. Strikha, Fiz. Tekh. Poluprovodn. (Leningrad) **24**, 1227 (1990) [Sov. Phys. Semicond. **24**, 773 (1990)].

Translated by T. Galkina

Semiconductors, Vol. 34, No. 7, 2000, pp. 768–774. Translated from Fizika i Tekhnika Poluprovodnikov, Vol. 34, No. 7, 2000, pp. 796–802.

ELECTRONIC AND OPTICAL PROPERTIES OF SEMICONDUCTORS

Hysteresis of Magnetoresistance in Neutron-Transmutation-Doped Ge in the Region of Hopping Transport over the Coulomb-Gap States

A. G. Andreev, S. V. Egorov, A. G. Zabrodskiĭ, R. V. Parfen'ev, and A. V. Chernyaev

Ioffe Physicotechnical Institute, Russian Academy of Sciences, ul. Politekhnicheskaya 26,
St. Petersburg, 194021 Russia

Submitted January 25, 2000; accepted for publication January 27, 2000

Abstract—The phenomenon of hysteresis of magnetoresistance in neutron-transmutation-doped Ge:Ga in the region of hopping transport over the Coulomb-gap states was observed and studied experimentally. The hysteresis is accompanied by an abrupt decrease in the resistivity in a magnetic field of about 800 Oe after a preliminary magnetization of the samples in the fields exceeding 1 kOe. The relative magnitude of the resistivity jump increases with decreasing temperature. This effect is observed on the insulator side of the metal–insulator transition, which occurs for a Ga concentration of 1.85×10^{17} cm^{-3}. The main special features of the observed phenomenon were studied, and plausible explanations of this phenomenon are offered. © *2000 MAIK "Nauka/Interperiodica".*

1. INTRODUCTION

Neutron-transmutation-doped (NTD) Ge:Ga is a *p*-type compensated semiconductor in which a metal–insulator transition occurs for the concentration of the dominant neutron-transmutation-introduced Ga impurity equal to 1.85×10^{17} cm^{-3} [1]. The conditions for variable-range hopping (VRH) over the states of the Coulomb gap $g = g_0(E - E_F)^2$ in the impurity band of Ga acceptor states in the vicinity of the Fermi energy are satisfied on the insulator side of the metal–insulator transition at sufficiently low temperatures $T \leq 1$ K [2, 3]. A square-law positive magnetoresistance observed under the above conditions in moderate magnetic fields is due to the fact that an external magnetic field compresses the hole wave function in the plane perpendicular to the field and thus diminishes the probability of the hops [4]. A study of the field and temperature dependences of the positive magnetoresistance in the NTD Ge:Ga made it possible [3] to verify the existence of the Coulomb gap and evaluate the localization radius *a* of a hole bound by the impurity. According to [1], the localization radius diverges and the Coulomb gap vanishes exactly at the critical point of the metal–insulator transition; this point is determined from the vanishing of the low-temperature limit of the electrical conductivity σ(0) on the metal side of the transition. In addition, study of magnetoresistance in the NTD Ge:Ga in the range of fairly low fields at ultralow temperatures revealed the phenomenon of magnetoresistance hysteresis [5], which had not been observed previously. In this paper, we report the results of studying this phenomenon.

2. EXPERIMENTAL

We studied a series of NTD Ge:Ga samples (the technology for preparation of the NTD Ge samples has been described elsewhere [2]). The degree of compensation (the degree of the acceptor-band occupancy) of this material depended somewhat on the neutron spectrum [6] and amounted to 35% in the case under consideration. The range of doping with the neutron-transmutation-introduced Ga impurity (see table) was defined by the reactor-neutron integrated flux and

Table

Serial no. of the sample	Concentration Ga, 10^{17} cm^{-3}	kT_0, meV	The magnitude of the magnetoresistance jump, %	H_c, Oe
1	0.45	5.16	4.75	600
2	0.71	2.95	10	740
3	0.91	1.73	6	830
4	1.05	1.19	5	740
5	1.3	0.42	1	750
6	1.8	0.08	–	–
7	2.3	–	–	–

amounted to 4.5×10^{16}–2.3×10^{17} cm^{-3}. Figure 1 illustrates the temperature dependences of resistivity of the studied samples in the temperature range characteristic of the VRH transport within the Coulomb gap. It follows from the analysis of temperature dependence of activation energy (see [7]) that the hopping transport occurs at sufficiently low temperatures $T \leq 1$ K (the transition temperature is indicated with vertical segments at the curves), in which case the resistivity follows the law

$$\rho(T) = \rho_0 \exp\left(\frac{T_0}{T}\right)^{1/2}, \qquad (1)$$

where the parameter $T_0 \propto g_0^{-1/3} a$ (the values of kT_0 are listed in the table).

The samples to be studied were cut in the (111) plane. The measurements were performed in the temperature range of 0.4–2.2 K and mostly in the transverse configuration ($\mathbf{H} \perp \mathbf{J}$), i.e., $\mathbf{H} \parallel [111]$. The magnetic-field strength was varied in the range from −10 kOe to +10 kOe, with the sweep rate being equal to $v = 1.5$–20 kOe/min.

3. HYSTERESIS OF MAGNETORESISTANCE IN THE NTD Ge:Ga SAMPLES

Figure 2 shows the typical magnetoresistance curves for samples 2 and 3 at $T = 0.45$ K and for the sweep rate of 3.6 kOe/min.[1] For $H \geq 5$ kOe, the aforementioned positive-magnetoresistance effect is observed for both the forward (points *1–2–3–4* in the magnetoresistance curve) and the return (*4–5–6–1*) sweep runs. Under lower fields, a small-magnitude negative magnetoresistance effect is observed in the course of the forward and return runs to points *2* and *5*. In addition, after the change in the magnetic-field orientation during the forward run in the interval of *2–3* in the field of $H_c = 600$ Oe, the effect of a nonequilibrium abrupt decrease in resistivity by several percent of the resistivity in the zero field is observed; this decrease is followed by relaxation of the resistivity to the equilibrium value for $H \cong 5$ kOe. This effect is not observed in the course of the return run in the interval of *4–5* for the same field; however, it can be observed again if the magnetic-field polarity is reversed in the interval of *5–6*.

According to the measurements, an abrupt decrease in resistivity occurs only after the sample is subjected to a field higher than 2 kOe, with subsequent reversal of the field sign. The dependence of the shape of the magnetoresistance curve on the magnetic history of the sample suggests that we deal with a magnetoresistance hysteresis.

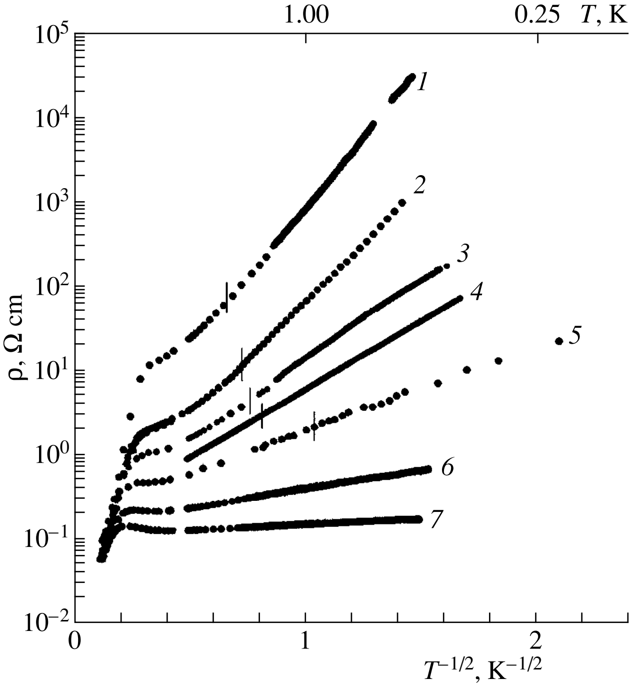

Fig. 1. Temperature dependences of resistivity of the NTD Ge:Ga samples with alloyed In contacts for N_{Ga} = (*1*) 0.45×10^{17}, (*2*) 0.71×10^{17}, (*3*) 0.91×10^{17}, (*4*) 1.05×10^{17}, (*5*) 1.3×10^{17}, (*6*) 1.8×10^{17}, and (*7*) 2.3×10^{17} cm^{-3}. Vertical segments indicate the high-temperature limit of the VRH transport for the samples in which this transport was observed.

The temperature dependence of the magnetoresistance-jump magnitude $\Delta\rho$ relative to its value $\rho(0)$ in the zero field is shown in Fig. 3 for a constant sweep rate. It can be seen that the resistivity jump vanishes at temperatures higher than about 0.7 K, which corresponds to the high-temperature limit of the VRH transport. The jump is clearly pronounced at $T \leq 0.6$ K, and, in certain cases, its magnitude can be as large as ~10% in sample 2 at $T = 0.4$ K. Thus, the hysteresis emerges precisely when the VRH transport becomes dominant and then becomes rapidly more pronounced with decreasing temperature.

We observed the hysteresis described above in the NTD Ge:Ga samples on the insulator side of the transition alone. Figure 4 shows the dependences of the magnetoresistance-jump magnitude and the critical magnetic field H_c (determined from the maximum in the derivative $d\rho/dH$) on the doping level N_{Ga}. It can be seen that the jump magnitude increases initially with increasing Ga concentration and then attains a maximum (~10%) in the vicinity of $N_{Ga} = 7 \times 10^{16}$ cm^{-3}; the latter value amounts to about 40% of the critical concentration $N_c = 1.85 \times 10^{17}$ cm^{-3} for the metal–insulator

---

[1] The samples with concentration corresponding to sample 2 in the table were of two types: with gold and indium contacts. Henceforth, unless otherwise stated, the data reported refer to the sample with gold contacts.

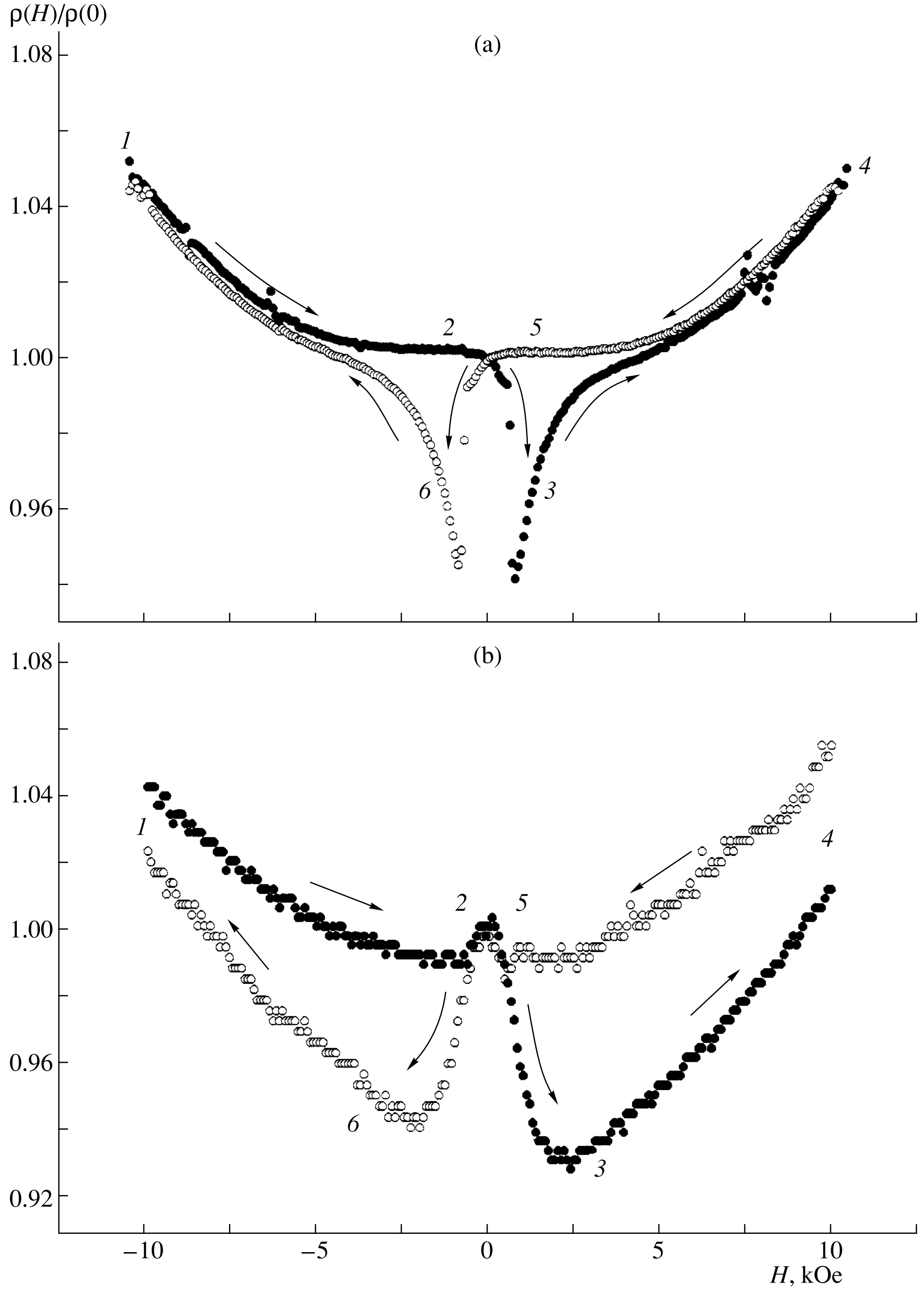

Fig. 2. Magnetoresistance of samples (a) 2 and (b) 3 at $T = 0.45$ K and for $v = 3.6$ kOe/min. The arrows indicate the direction of the sweep run, with the shaded symbols corresponding to the forward run and the unshaded symbols corresponding to the return run. The resistivity in the zero magnetic field ρ(0) of samples 2 and 3 at the above temperature is 1090 and 114 Ω cm, respectively.

transition. As the doping level increases further, the magnetoresistance jump diminishes and vanishes for $N_{\mathrm{Ga}} = 1.8 \times 10^{17}$ cm^{-3}, which coincides with N_c. The measured values of the critical field H_c for $v = 3.6$ kOe/min and for the field varying from –10 kOe to +10 kOe are shown in Fig. 4 and are listed in the table. It can be seen that the value of H_c increases only slightly with increasing Ga concentration.

Figure 5 shows the magnetoresistance curves measured for several field-sweep rates. It can be seen that an increase in the sweep rate causes the negative magnetoresistance jump and the subsequent dip in the magnetoresistance curve to become less abrupt; in addition, the relaxation in the region of high fields becomes slower. Figure 6 shows the dependences of the jump magnitude and the value of the critical magnetic field on the field-sweep rate v. Both of these dependences exhibit a minimum for the same sweep rate equal to about 10 kOe/min.

Studies have shown that the magnetoresistance hysteresis (including the characteristic minimum) described above is virtually independent of the value of the measurement current and the orientation of **H** (be it transverse or longitudinal) relative to the current direction.

The probe and current contacts to the NTD Ge:Ga samples under investigation were typically prepared by alloying In, which is in its superconducting state at $T \leq$ 3.4 K. The superconductivity of In is destroyed by a field of H_c = 290 Oe at T = 0.4 K; thus, the behavior of the In contact cannot account for the magnetoresistance jump that is observed under much higher fields. In order to verify this, we also prepared normal (Au) contacts to one of the samples. A comparison of the magnetoresistance behavior in the samples with superconducting (In) and nonsuperconducting (Au) contacts (Fig. 7) shows the pattern is qualitatively the same in both cases. This confirms the above conclusion that the destruction of superconductivity of In contacts cannot account for the observed hysteresis in magnetoresistance.

4. DISCUSSION

The observed abrupt decrease in resistivity of the NTD p-Ge sample in the course of its magnetization reversal can be caused by a release of heat by an ensemble of localized, magnetically ordered charge carriers (in the case under consideration, by holes in the impurity band) in the critical field H_c. In this case, each localized hole is assigned a magnetic dipole moment, which interacts with the surrounding charge carriers and with an external magnetic field. The Ge:Ga resistivity depends exponentially on temperature, decreases abruptly for $H = H_c$, and then relaxes slowly to the equilibrium values of $\rho(H)$. On the basis of temperature dependences of resistivity of the samples and the size and mass of the latter, we can calculate the amount of energy per unit mass $\Delta Q/m$, which is released in the sample and corresponds to a given change in temperature, using the formula

$$\Delta Q/m = c\Delta T, \qquad (2)$$

where c is the specific heat of Ge at 0.45 K (5.47×10^{-5} J/(kg K)) and m is the mass of the sample.

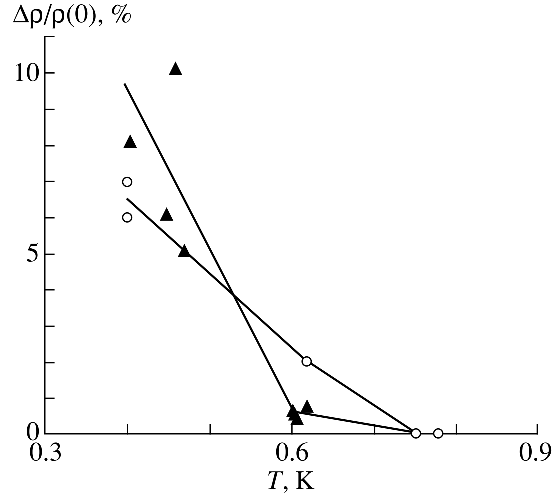

Fig. 3. The temperature dependences of the magnetoresistance-jump magnitude for samples 2 (shaded symbols) and 3 (unshaded symbols); v = 3.6 kOe/min.

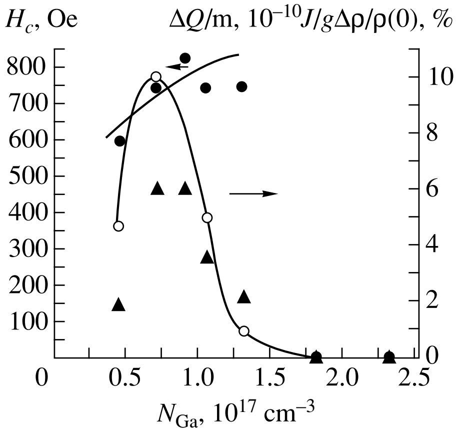

Fig. 4. Relative magnitude of the resistivity jump (unshaded circles), the critical field H_c (shaded circles), and the specific heat $\Delta Q/m$ released in the sample (shaded triangles) in relation to the Ga concentration N_{Ga}.

The values of $\Delta Q/m$ calculated according to formula (2) are shown in Fig. 4 in relation to the Ga impurity concentration N_{Ga}. It can be seen that the peak in the $\Delta Q/m$ (N_{Ga}) curve coincides approximately with the largest magnitude of the resistivity jump observed. Thus, the physical processes responsible for the energy release and, correspondingly, the magnetoresistance hysteresis are most intense in the Ga concentration range from $N_c/4$ to $N_c/2$, where the magnitude of the resistivity jump is largest.

In addition, in order to verify experimentally the hypothesis that the hysteresis has a thermal origin, we measured the magnetoresistance of the sample whose heat exchange with the thermostat was reduced by a stearin coating. It was expected that the rate of heat removal from the sample would be lowered and the relaxation to the equilibrium would be slowed owing to the emergence of additional thermal mass in cooling. It can be seen from Fig. 8 that the minimum in the magnetoresistance curve for the thermally insulated sample

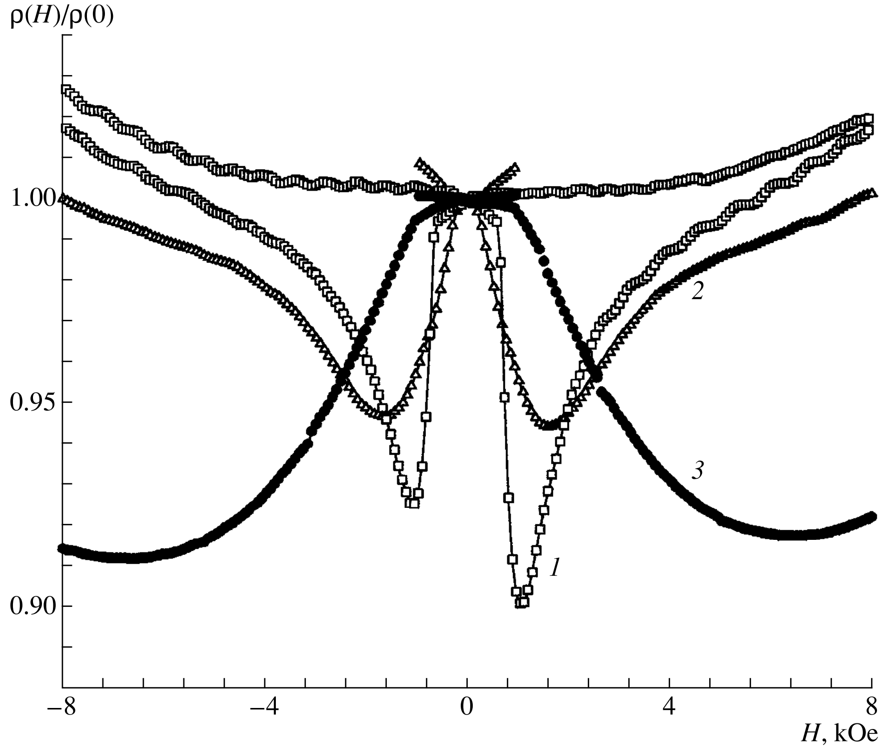

Fig. 5. The influence of the rate of the magnetic-field sweep *v* on the hysteresis curve for sample 2; *v* = (*1*) 3.6 (0.43 K), (*2*) 10.8 (0.43 K), and (*3*) 27 (0.475 K) kOe/min.

is indeed broader and the magnitude of the magnetoresistance jump is smaller.

We note that hysteresis is not observed in the case of free holes (in the vicinity of the metal–insulator transition and in the metallic state; see Fig. 4). On the other hand, the hysteresis effect becomes less pronounced when we pass to a more sparse ensemble of holes away from the metal–insulator transition. The former of the above two facts may indicate that the charge carriers should be localized in order to observe the hysteresis. The latter fact suggests that the concentration of localized magnetic dipoles should be sufficiently high; i.e., a certain threshold interaction is possible.

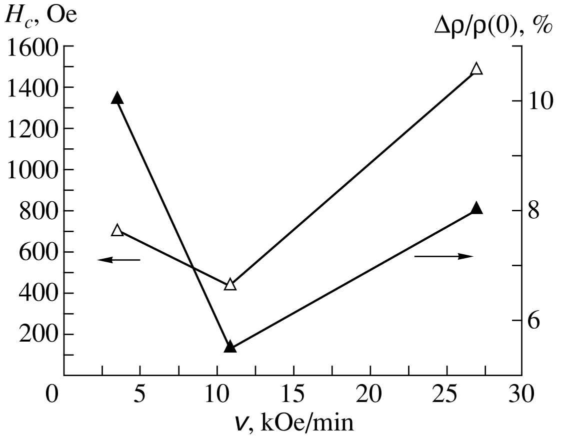

Fig. 6. The influence of the magnetic-field sweep rate on the relative magnitude of the resistivity jump $\Delta\rho/\rho(0)$ and on the critical field H_c for the magnetoresistance jump in sample 2. The range of variation in H is from –10 kOe to +10 kOe.

The question now arises as to the origin of the aforementioned magnetic moments and to the causes of the heat release in the ensemble of these moments. We offer several plausible schemes.

These magnetic moments are magnetic dipole moments of holes bound by neutral donors. Such a charge configuration of the acceptor A^0 implies that a single hole is bound by an acceptor. In a magnetizing field, the dipoles in this system acquire a prevalent orientation, which causes, on average, the sample to become magnetized. The originated configuration is retained if the magnetic field is switched off; this is due to a significant hole–hole interaction. Further, the field decreases to zero and reverses its sign. The existing configuration corresponds now to the population inversion of magnetic levels and is nonequilibrium. Eventually, a transition to equilibrium configuration occurs in the critical field and is accompanied with the reorientation of dipoles and the release of heat.

The second hypothesis is not related to reorientation in the ensemble of localized charge carriers. It is known

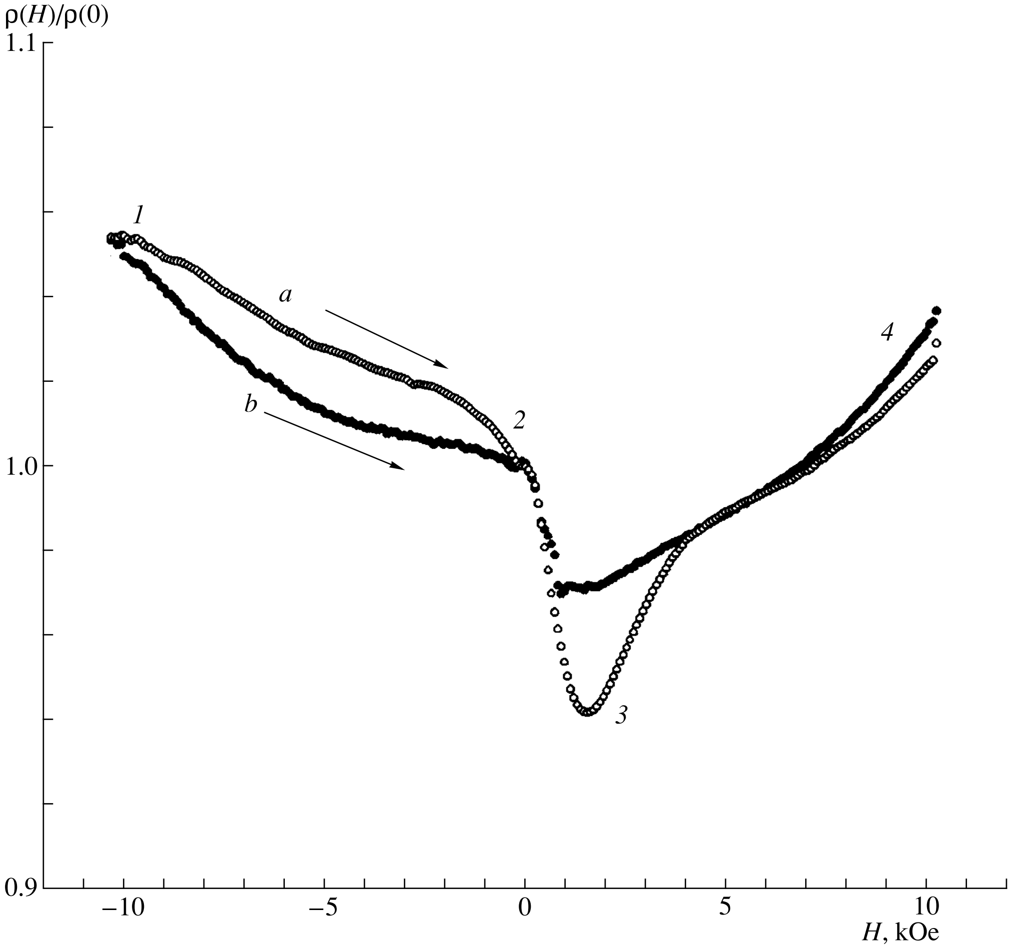

Fig. 7. Magnetoresistance of the NTD Ge:Ga samples with $N_{Ga} = 7.1 \times 10^{16}$ cm^{-3} (*a*) ($T = 0.45$ K and $\rho(0) = 1090$ Ω cm) with Au contacts prepared by thermal compression and (*b*) similar samples with the alloyed In contacts ($T = 0.43$ K and $\rho(0) = 1640$ Ω cm). The magnetic-field sweep rate is $v = 3.6$ kOe/min; the direction of variation of the magnetic field is indicated by arrows and numbers.

that, in the state of equilibrium, the holes localized in *p*-Ge are distributed over two charge states of acceptors: A^+, in which case there are two holes at a single acceptor, and A^0, in which case there is a single bound hole. It is also known that the binding energy of the state A^0 is lower than the binding energy of the state A^+ (the center with negative correlation energy). In a strong magnetizing field, a nonequilibrium redistribution of holes over the acceptor charge states A^0 and A^+ may occur, so that the latter state becomes favored. Such an excess population of the states A^+ is statistically nonequilibrium. In this case, the experimentally observed abrupt decrease in resistivity may be explained by heating in the course of transition from a statistically nonequilibrium state with an excess of A^+ centers to the equilibrium state. Such a transition is accompanied by heating of the material, because an excess fraction of A^+ centers should be transferred to the state A^0. This is accompanied by a release of heat, since the binding energy of the A^+ center is higher than that of the A^0 center.

We should mention another possible explanation based on ferromagnetism emerging in a system with a density of states that exhibits peaks on both sides of the Fermi level [8]. In the case under consideration, such a density of states appears in the impurity band, with the Coulomb gap being located at the Fermi level.

5. THE MAIN RESULTS AND CONCLUSIONS

We detected a hysteresis of magnetoresistance under conditions of VRH transport over the states in the Coulomb gap in the NTD Ge:Ga samples. This hysteresis manifests itself in the course of magnetization reversal of the sample and consists in an abrupt decrease in resistivity in a field of ~700 Oe with subsequent relaxation of resistivity to the equilibrium values.

The magnitude of the resistivity jump increases with decreasing temperature; this jump is observed in a limited range of doping levels on the insulator side of the metal–insulator transition.

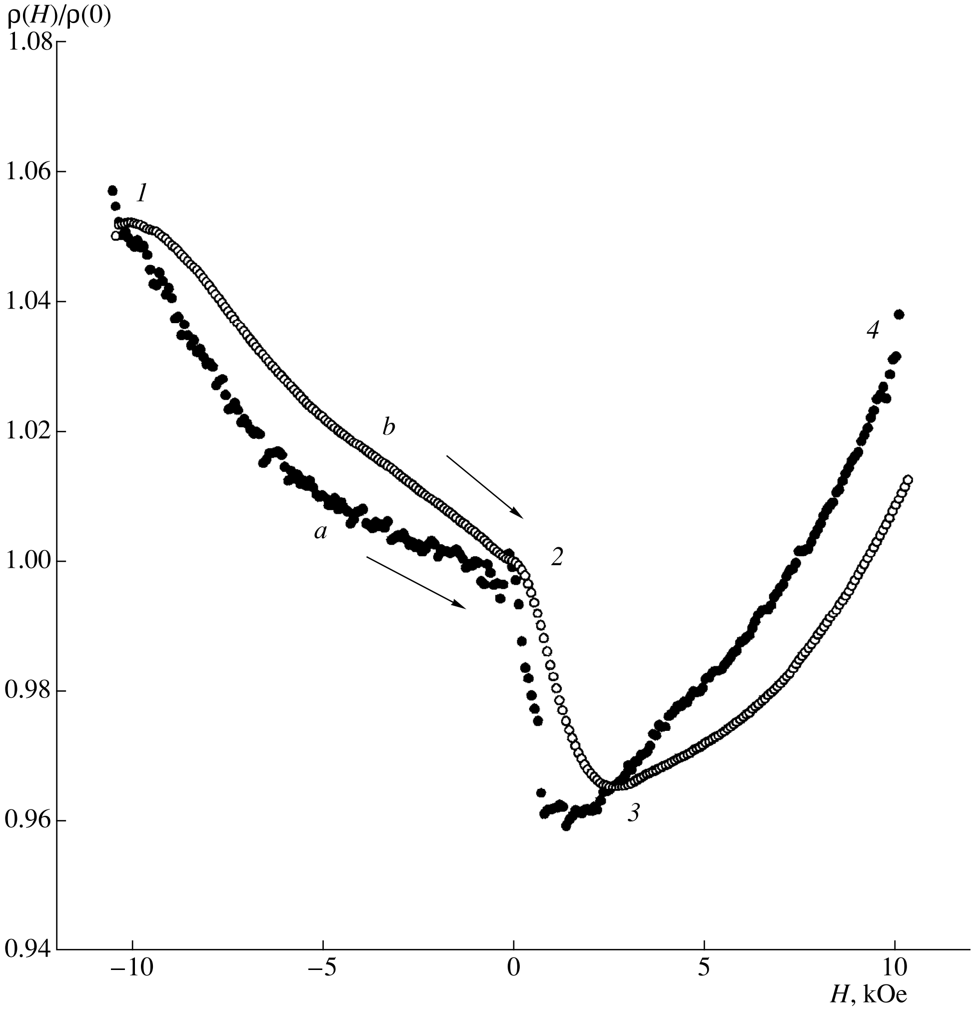

Fig. 8. Magnetoresistance of the NTD Ge:Ga samples with $N_{Ga} = 7.1 \times 10^{16}$ cm^{-3} for (*a*) the uncoated sample ($T = 0.43$ K and $\rho(0) = 1640\ \Omega$ cm) and (*b*) the sample coated with stearin ($T = 0.45$ K and $\rho(0) = 1167\ \Omega$ cm); $v = 10.8$ kOe/min.

We suggested several plausible explanations for the phenomenon observed; these explanations are based on the thermal origin of the resistivity jump, which is verified experimentally.

ACKNOWLEDGMENTS

We thank N.S. Averkiev for his fruitful participation in discussion of the results.

This study was supported by the Russian Foundation for Basic Research, project no. 98-02-17353.

REFERENCES

1. A. G. Zabrodskii, A. G. Andreev, and S. V. Egorov, Phys. Status Solidi **205**, 61 (1998).
2. A. G. Zabrodskiĭ, A. G. Andreev, and M. V. Alekseenko, Fiz. Tekh. Poluprovodn. (Leningrad) **26**, 431 (1992) [Sov. Phys. Semicond. **26**, 244 (1992)].
3. A. G. Zabrodskiĭ and A. G. Andreev, Pis'ma Zh. Éksp. Teor. Fiz. **58**, 809 (1993) [JETP Lett. **58**, 756 (1993)].
4. B. I. Shklovskiĭ and A. L. Éfros, *Electronic Properties of Doped Semiconductors* (Nauka, Moscow, 1979; Springer-Verlag, New York, 1984).
5. A. G. Andreev, S. V. Egorov, A. G. Zabrodskiĭ, *et al.*, in *Proceedings of the XXXI Conference on Low Temperature Physics* (Moscow, 1998), p. 44.
6. A. G. Zabrodskiĭ and M. V. Alekseenko, Fiz. Tekh. Poluprovodn. (St. Petersburg) **28**, 168 (1994) [Semiconductors **28**, 101 (1994)].
7. A. G. Zabrodskiĭ and K. N. Zinov'eva, Zh. Éksp. Teor. Fiz. **86**, 727 (1984) [Sov. Phys. JETP **59**, 425 (1984)].
8. M. Shimizu, Proc. Phys. Soc. **84**, 397 (1963); **86**, 147 (1965).

Translated by A. Spitsyn

Semiconductors, Vol. 34, No. 7, 2000, pp. 775–780. Translated from Fizika i Tekhnika Poluprovodnikov, Vol. 34, No. 7, 2000, pp. 803–808.
Original Russian Text Copyright © 2000 by Vexler, Grekhov, Shulekin.

SEMICONDUCTOR STRUCTURES, INTERFACES, AND SURFACES

The Role of Impact Ionization in the Formation of Reverse Current–Voltage Characteristics of Al–SiO_2–*n*-Si Tunnel Structures

M. I. Vexler, I. V. Grekhov, and A. F. Shulekin*
Ioffe Physicotechnical Institute, Russian Academy of Sciences, ul. Politekhnicheskaya 26, St. Petersburg, 194021 Russia
**e-mail: shulekin@pop.ioffe.rssi.ru*

Submitted December 28, 1999; accepted for publication December 29, 1999

Abstract—Physical processes responsible for the reverse current–voltage (*I*–*V*) characteristics of Al–SiO_2–*n*-Si structures with 1.2–3.2-nm-thick SiO_2 and a silicon doping level of 10^{14}–10^{18} cm^{-3} were analyzed. A new model describing the evolution of the hot-electron energy in structures of this kind is suggested. The roles played by Auger ionization and impact ionization are differentiated. The turn-on voltages of a tunnel MOS structure are studied both theoretically and experimentally. The turn-on voltage is shown to decrease with increasing oxide layer thickness. *© 2000 MAIK “Nauka/Interperiodica”.*

INTRODUCTION

It is well known that a reverse-biased metal–oxide–semiconductor (MOS) structure with an oxide thickness of less than 3 nm can act as a tunnel-emitter bipolar transistor [1, 2]. Among the advantages of such a device are the small inversion-base transit time, the absence of limitations on diminishing the emitter size, and a relatively simple fabrication procedure [2]. In addition, recent experiments have shown that tunnel-thin SiO_2 layers can be used as a gate insulator for MOSFETs [3]. This finding stimulated interest in the physics of the operation of ultrathin MOS structures on the whole.

Previously, primary attention in the study of tunnel Al–SiO_2–*n*-Si MOS structures was focused on the range of low (several volts) applied biases *V* [1, 2, 4], mainly with regimes with low (about 1 V) voltage *U* applied to the insulator considered. In only few works [4, 5] has emphasis been placed on the range of higher *U*, namely, voltages corresponding to the occurrence of Auger ionization initially induced by hot electrons injected into the semiconductor. The Auger recombination was found to be responsible for the positive feedback in the structure and for the *S*-shaped reverse current–voltage (*I*–*V*) characteristic [4, 6, 7]. Nevertheless, no attempts have yet been made to study systematically the possible role of impact ionization in the space-charge region (SCR), which may be of fundamental importance at high biases *V*.

This study was aimed at (i) revealing the physical factors that determine the appearance of the reverse *I*–*V* characteristics of Al–SiO_2(1–3nm)–*n*-Si structures, (ii) determining the turn-on voltage V_{sw}, and (iii) clarifying the role of impact ionization in the behavior of these structures.

MODEL

In Al–SiO_2–*n*-Si structures (in contrast to many other combinations of materials, e.g., the case of a gold electrode), electron injection into silicon must occur at any reverse bias *V* exceeding the Fermi level depth Φ in the band gap of the Si bulk (Fig. 1). The left- and right-hand barriers (χ_m and χ_e, Fig. 1) have nearly equal heights, so that, even at nearly zero voltage *U* applied to the insulator, there is no substantial hindrance to electron transport from the Fermi level of the metal.

Theoretically, the electron current must exceed the hole current by a factor of 100 or more (see, e.g., [1]), but, in practice, the difference may be smaller [2, 6]. To describe the evolution of the electron energy in a tunnel MOS structure, the following model can be proposed.

The injected electrons are initially monoenergetic, with any electron possessing an energy $E_{in} = qU - (\chi_m - \chi_e)$ at the Si–SiO_2 interface and gaining some additional energy ΔE in ballistic transit through the inversion layer. The quantity ΔE is assumed equal to the contribution of the inversion layer charge to the surface potential ψ_s and is defined as $\Delta E = q^2 N_s z_{inv}/\varepsilon_0\varepsilon_s$, where z_{inv} denotes the average distance of holes from the interface and N_s is their two-dimensional (2D) density.

Electron energy relaxation occurs even outside the inversion region and does so in two stages. In the first stage, the average electron energy decreases from E_{eff} to some value $\langle E\rangle$ determined by the maximum field in the SCR ($\langle E\rangle$ is lower than E_g, but may substantially exceed kT). This occurs at a typical distance from the interface on the order of the phonon emission length λ_{ph} (6–10 nm). Since the carrier motion during optical phonon emission is highly chaotic, this distance (unlike $\langle E\rangle$) depends only slightly on the field in the SCR.

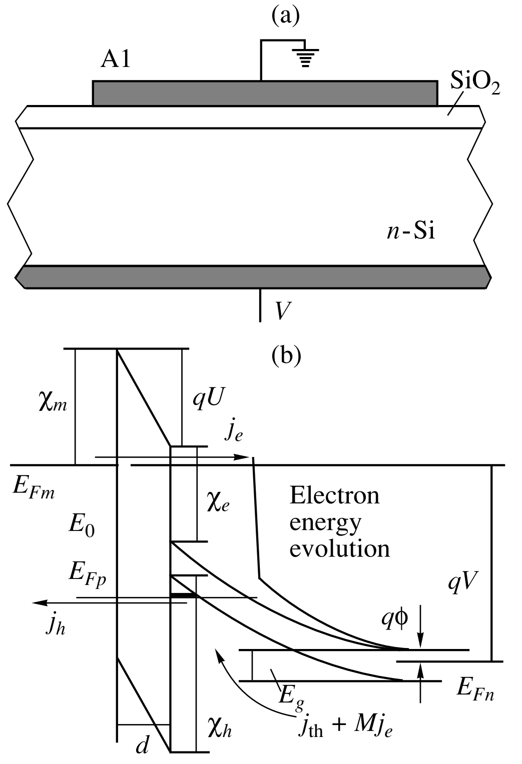

Fig.1. (a) Tunnel MOS structure; (b) band diagram for a reverse-biased structure (for designations, see text).

Therefore, the quantity $E_{eff} = (E_{in} + \Delta E)$ controls the characteristics of the first stage of relaxation, and, in particular, the quantum yield of Auger ionization *P*.

In the second stage, electrons are completely thermalized by the gradual loss of their energy that occurs while passing through the SCR (on the average, from $\langle E \rangle$ to *kT*). In this case, electrons are kept hot for a relatively long time by the SCR field and can cause impact ionization of silicon, with quantum yield γ depending on the depletion region width *w* and its doping level N_d (as in a *p*–*n* junction). In this case, the initial carrier energy E_{eff} has no effect on γ. With allowance made for both ionization effects, the multiplication factor for electrons $M = (1 + P(E_{eff}))(1 + \gamma(w, N_d)$.

From the quantum-mechanical standpoint, elementary processes of Auger and impact ionization are identical, but, in the phenomenological approach, we find it reasonable to distinguish between these two processes, as was done above. By the Auger process, we mean the generation of electron–hole pairs by initially hot (injected) electrons in the course of their energy relaxation, and, by impact ionization, we mean generation of these pairs by electrons heated in a strong field.

The Auger generation in tunnel MOS structures has been discussed in detail elsewhere [4–7]. The new concept of this study consists in considering the impact ionization and also the fact that, during the aforementioned first stage of thermalization, the electron motion is highly chaotic. For low E_{eff} (less than 3–4 eV), the dependence $P(E_{eff})$ can be determined on the basis of published data on the energy loss rates for ionization τ_{ii}^{-1} and for phonon emission τ_{ph}^{-1} (with energy $\hbar\omega_0$ ascribed to phonons) in the form

$$P(E_{eff}) = w_{ii}(E_{eff}) + \sum_{i=1} w_{ii}(E_{eff} - i\hbar\omega_0) \times \prod_{j=0}^{i-1} (1 - w_{ii}(E_{eff} - j\hbar\omega_0)), \qquad (1)$$

where $w_{ii}(E_e) = (1 + \tau_{ph}^{-1}(E_e)/\tau_{ii}^{-1}(E_e))^{-1}$. The expression for γ is derived by approximate integration of the well-known ionization coefficient $\alpha_{ii} = a_0\exp(-b_0/F(z))$, where *F* is the field, over the SCR:

$$\gamma = a_0 q N_d w^2 b_0^{-1} \varepsilon_0^{-1} \varepsilon_s^{-1} \exp(-b_0\varepsilon_0\varepsilon_s/qN_d w). \qquad (2)$$

The electron and hole tunnel currents are calculated by the formulas

$$j_e = 3q[\chi_m - qU/2]\pi^{-1}\hbar^{-1}d^{-2}\theta_e(E_{Fm}), \qquad (3)$$

$$j_h = qE_0 N_s h^{-1}\theta_h(E_0), \qquad (4)$$

where θ_e and θ_h are the tunneling probabilities for electrons and holes, respectively [1, 7, 8], and E_0 is the ground level for holes in the inversion layer. In any mode of operation of a tunnel MOS structure, the balance equation for supply and loss of minority carriers must be satisfied:

$$j_h + j_{diff} = j_e(M - 1) + j_{th}, \qquad (5)$$

where $j_{th} = qwG$ is the thermal current determined by the generation rate *G*, and j_{diff} is the diffusion current of holes from the Si–SiO_2 interface into the bulk of Si [1]; the latter current is important only for $U \sim V$. All the terms appearing in (5) depend on *V* and *U*.

The following parameter values were adopted: $T = 300$ K, $E_g = 1.12$ eV, $\varepsilon_s = 11.9$, $\varepsilon_I = 3.9$, $G = 10^{22}$ s^{-1} m^{-3}; $a_0 = 4.05 \times 10^5$ cm^{-1}, $b_0 = 1.0 \times 10^6$ V/cm (obtained from data reported in [9]), $\tau_{ii}^{-1}/\tau_{ph}^{-1} = (E_e - E_g)^{4.2}/655$, $\hbar\omega_0 = 0.063$ eV (according to [10]; E_e is in eV), $\chi_m = 3.17$ eV, $\chi_e = 3.15$ eV, $\chi_h = \chi_e + E_g$, $m_I = 0.3m_0$ (both for electrons and for holes in SiO_2), effective heavy-hole masses are $m_z = 0.746m_0$ and $m_\perp = 0.549m_0$ for (111)Si, and $m_z = 0.291m_0$ and $m_\perp = 0.433m_0$ for (100)Si, (as in our previous study [8]). We do not discuss here methods for calculating the energy band structure for a tunnel MOS structure and such parameters as z_{inv}, E_0, and *w*, because the appropriate methods are well known [7, 8, 11].

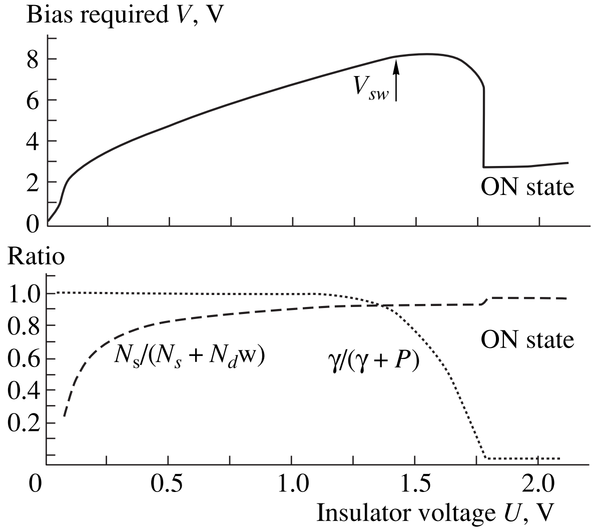

Fig. 2. Calculated biases V to be applied to the structure to produce an insulator voltage U. $N_d = 10^{16}$ cm^{-3}, $d = 2.5$ nm, (100) orientation. The dashed line represents the relative contribution of the inversion layer charge to the oxide field ($N_s/(N_s + N_d w)$); the dotted line represents the relative contribution of the impact ionization to the supply of holes ($\gamma/(\gamma + P)$).

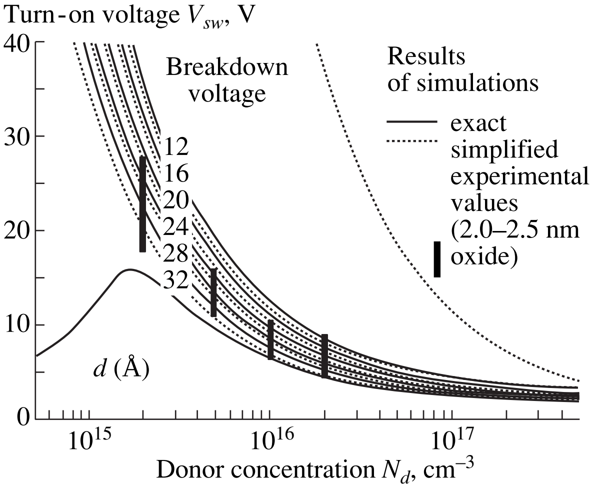

Fig. 3. Calculated turn-on voltages V_{sw} vs. donor concentration N_d: solid lines correspond to systematic calculation, dots represent the results obtained using the empirical model with an adjustable parameter $U_{th} = 2$ V. Orientation (100). The figure is supplemented with experimental data.

RESULTS OF CALCULATION

For calculations, we used the previously developed model that accounts for only the ground level of holes in the inversion layer [7, 8].

Figure 2 shows the calculated dependences of voltage drop across a tunnel MOS-structure on the oxide voltage U for the entire U range of practical interest. In addition, we present the dependences of $N_s/(N_s + N_d w)$ and $\gamma/(\gamma + P)$ on U, which quantitatively characterize the role of minority carriers and that of the two ionization processes, respectively. Similar results are obtained for the entire range of variation in the parameters N_d (10^{14}–10^{18} cm^{-3}) and d (1.2–3.0 nm).

First, we consider the portion of the curve before switching. With increasing reverse bias V applied to the structure, the voltage U at the insulator grows both due to the increasing charge of the depletion region, $N_d w$, and, no less importantly, to the increasing charge of the inversion layer N_s. The latter can be effected, to some extent, by the rise in thermal current because of SCR widening, but much more important is the role played by holes produced by impact and Auger ionization. If the thermal current j_{th} can be neglected completely, then the situation $N_s \ll N_d w$ changes to $N_s \gg N_d w$ with increasing V in a rather narrow range of the biases V. A voltage of about 1 V at the tunnel-thin oxide, necessary for the activation of the Auger process ($P > 0$), cannot be produced only by the charge in the SCR even at the instant of its breakdown. Therefore, with increasing V, holes are initially generated only by impact ionization ($M = 1 + \gamma$), and the influence of the Auger process becomes noticeable only with a further increase in V.

The peak in the $V(U)$ curve in Fig. 2 corresponds to the switching situation. It should be noted, first, that the charge of holes is responsible (for any N_d values) for more than 90% of U in the vicinity of the switching point, and, second, that both the impact and Auger ionization play a substantial role in this region. On the whole, the behavior of $\gamma/(\gamma + P)$ allows a clear interpretation. For low U, there is no Auger ionization at all. When the switching point is approached, P increases rapidly and its contribution to the multiplication factor M becomes absolutely dominant immediately after the peak (V_{sw}) is passed. After switching, V as a function of U decreases sharply, because the number of Auger holes becomes so large that they must be injected into the semiconductor bulk. This is the so-called “on” state described in our previous publication [6]. In this state, $\gamma = 0$ and the current j_{diff} flows.

As follows from the above discussion, impact ionization is the main factor that, to some extent, determines the V_{sw} value independently of Auger ionization (see Fig. 3). Impact ionization is responsible for the initial rise in U, thereby making Auger ionization possible. In its turn, the Auger process maintains the “on” state and enables the very existence of an S-shaped I–V characteristic (Fig. 4).

Figure 3 shows the turn-on voltages V_{sw} for MOS structures with different doping levels and insulator thicknesses in the range from 1.2 to 3.2 nm. The turn-on voltage limits the operating range of a tunnel MOS-emitter transistor [1, 6]. As can be seen from Fig. 3, V_{sw} is in all cases considerably lower than the SCR breakdown voltage. It was found that, at the instant of structure switching ($V = V_{sw}$), the voltage at

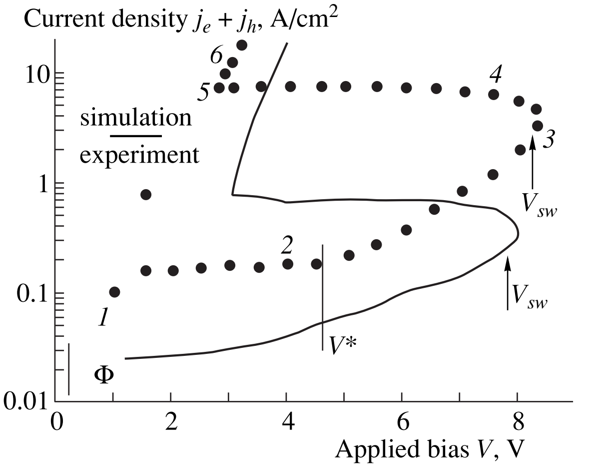

Fig. 4. *I–V* characteristic of a tunnel MOS structure. *n*-Si(100), $N_d = 10^{16}$ cm^{-3}, $d = 2.5$ nm. The solid line corresponds to calculation, dots represent typical experimental data. A pronounced *S*-shape feature is observed; its span is mainly determined by impact ionization, and its existence is due to Auger ionization.

the oxide is about 1.5–2.0 V and changes slightly with N_d and d; in this case, $M - 1 \sim 10^{-2}$–10^{-3}.

The dependence of V_{sw} on the doping level is of the form that might be expected. With increasing N_d, the turn-on voltage decreases, which must lead to the disappearance of *S*-shaped behavior. This is primarily due to an increase in γ for the same V because of the increasing field strength in the SCR. Also, the increasing contribution of the depletion-layer charge to the oxide voltage U plays some role. It should, however, be noted that, under the conditions close to switching, the key role is still played, even for heavy doping ($N_d = 10^{17}$ cm^{-3}), by the inversion layer maintained by the generated holes.

A decrease in the turn-on voltage V_{sw} with increasing insulator thickness d seems to be somewhat paradoxical, but it is explained by the fact that, with increasing d, the injection coefficient of structure j_e/j_h increases noticeably, thereby reducing the demand for generated holes. Beginning with about $d = 3.0$ nm, the thermal current j_{th} becomes an important additional factor diminishing the *S*-shape span.

EMPIRICAL MODEL

For practical purposes, the mathematical aspect of the problem of determining V_{sw} can be substantially simplified. Function $P(E_{\text{eff}})$ increases very rapidly with increasing effective energy determined primarily by the voltage U at the insulator. Therefore, it can be assumed artificially that Auger ionization exhibits strictly threshold behavior, so that $P(E_{\text{eff}}) = 0$ as long as voltage U is less than a certain value U_{th}, which is independent of the oxide thickness. Furthermore, the depletion layer charge qN_dw can be neglected near the switching point as compared to that of the inversion layer, qN_s. In this case, the problem of finding V_{sw} is reduced to simple determination of the bias V_{sw} for which the number of holes generated by impact ionization is sufficient to produce the oxide voltage U_{th}.

In fact, it is necessary to find V for which the condition $j_e(U_{\text{th}})/j_h(U_{\text{th}}) = \gamma$ is satisfied. The expressions for the currents are given above. E_0 is found as in [8]. Without introducing a large error, we can assume that the ratio of the tunneling probabilities $\theta_e(U)/\theta_h(U)$ is independent of U and equals $\exp(\hbar^{-1}(2m_l/\chi_m)^{1/2}E_gd)$ and also calculate the SCR width as $w = (2\varepsilon_0\varepsilon_s/qN_d(V - U_{\text{th}}))^{1/2}$. Substituting all the parameters, we obtain

$$U_{\text{th}} = 15.2(1 - U_{\text{th}}/6.34)^{3/5} m_z^{1/5} d^{-1/5} \exp(0.1d)\gamma^{3/5},$$

$$\gamma = 0.81(V_{sw} - U_{\text{th}}) \qquad (6)$$

$$\times \exp(-1.81 \times 10^9 N_d^{-1/2}(V_{sw} - U_{\text{th}})^{-1/2}),$$

where d is expressed in Å and N_d is expressed in cm^{-3}. Hence, V_{sw} is easily found. In Fig. 3, the results obtained by this method for $U_{\text{th}} = 2.0$ V (with U_{th} as an adjustable parameter) are compared with the systematic solution. The agreement is satisfactory, except for the case of $d = 3.2$ nm, where the role of thermal current is fairly significant. The accuracy ensured by the empirical model is nearly the same for the (100) and (111) orientations.

EXPERIMENTAL RESULTS

Al–SiO$_2$–Si tunnel MOS diodes were grown on *n*-type (100) and (111) silicon with donor concentration N_d of 2×10^{15}, 5×10^{15}, 1×10^{16}, 2×10^{16}, 2×10^{17}, and 10^{18} cm^{-3}. The insulator layer thickness was in the range of 2.0–2.5 nm. The SiO$_2$ layer was produced by low-temperature oxidation in dry oxygen, which is a conventional method for thin films.

Figure 4 shows a typical *I–V* characteristic for a sample grown on a substrate with $N_d = 10^{16}$ cm^{-3}. In complete agreement with the above analysis, several portions can be distinguished in the curve:

1–2 ($\Phi < V < V^*$). Injection of electrons occurs for U slowly increasing in the range of fractions of a volt due to the SCR charge and the charge of thermally generated holes. In the initial part of this range, the current rises relatively rapidly because of the lowering of the silicon conduction-band edge E_{c0} at the Si–SiO$_2$ interface to below the Fermi level of the metal E_{Fm} (resulting in disappearance of the low barrier $\sim(\chi_m - \chi_e)$ for electrons).

2–3 ($V^* < V < V_{sw}$). The voltage U at the insulator and the tunnel current grow considerably more rapidly due to impact ionization of silicon, which is caused by injected electrons in the SCR. Also, a contribution from

Auger ionization becomes pronounced as point *3* is approached.

3–4 ($V \sim V_{sw}$). This is the region of structure switching. This portion of the *I–V* curve varies from sample to sample because of the complex combinations of the parameters controlling the process.

4–5. Here, we have an abrupt decrease in V under insignificant increase in U due to the Auger ionization. The Auger process takes over the role of principal hole supplier, its quantum yield growing very rapidly with voltage.

5–6 ($U \sim V$). This is the "on" state (the transistor is in the saturated state [6]) characterized by such an intense generation of holes that not only is their amount sufficient to maintain the insulator voltage, but, in addition, excess holes appear and diffuse into the bulk of silicon.

Similar *S*-shaped *I–V* characteristics were observed in this and other studies [4] for lightly and moderately doped ($N_d < 10^{17}$ cm^{-3}) substrates. Our systematic study showed that the *S*-shape span (i.e., the V_{sw} value) increases with decreasing N_d (Fig. 3). At the same time, tunnel MOS-diodes based on heavily doped silicon demonstrate superlinear *I–V* characteristics without bistability, which is in complete agreement with the theoretical analysis.

We did not perform any systematic study of the influence of the oxide thickness. Nevertheless, there is some evidence indicating that reduction of the oxide thickness must lead to an increase (rather than a decrease) in V_{sw}. It was observed that many structures demonstrate, after being overloaded, qualitatively the same *I–V* characteristics, but with switching occurring at higher voltages. The reason is that oxide degradation can be considered roughly as a decrease in the injection factor of the structure, or (even more roughly) as the factor becoming effectively thinner.

SOME PRACTICAL FEATURES OF SWITCHING

(a) *Thermal current.* In our calculations, we adopted the thermal generation rate $G = 10^{22}$ s^{-1} m^{-3}, which corresponds to thermal currents j_{th} close to the actual leakage current in *p–n* junctions [12] (e.g., ~10^{-8} A/cm^2 for a SCR width of ~0.1 μm). On the basis of these assumptions, it was found that j_{th} is insignificant in the balance of currents in a tunnel structure with $d <$ 3.0 nm. We cannot exclude the possibility of more intense thermal generation that would become a substantial factor even for smaller oxide thicknesses.

(b) *Substrate resistance.* The series resistance of the silicon substrate, ρ_{sub}, can change the switching parameters in a trivial manner. In the case of a low doping level (N_d), a thin oxide (small d), and a thick substrate (d_{sub}), the substrate resistance can even make impossible the observation of bistability that would manifest itself in the coordinates j vs. $(V - j\rho_{\text{sub}}d_{\text{sub}})$.

(c) *Oxide inhomogeneity.* Generally speaking, the effective ($d_{\text{eff}} = d - \sigma^2(2m_I\chi_m)^{1/2}/\hbar$ (where σ is the standard deviation of thickness) oxide thickness, rather than the nominal thickness d, should have appeared in all the above. Since σ is, as a rule, small (0.1–0.2 nm) [3] and the dependence of V_{sw} on d is not very strong, this has no significant consequences in the ideal case. However, if σ for some reason exceeds its typical values, the observed values of V_{sw} may increase somewhat. It is not improbable that this could lead to some deviation of experimental data from the results of simulations for $N_d = 10^{16}$ cm^{-3} (Fig. 4).

(d) *S-shaped I–V characteristics without the Auger process.* In some cases, we observed an additional S shape with small span (< 1–2 V) immediately before the sample switching (near V_{sw}). We suppose that a distinct feature of carrier transport in such samples may be the existence of regions in which injection factor j_e/j_h increases with voltage U. In these regions, SCR narrowing must occur with increasing current, thus making the quantum yield γ of impact ionization lower. This fact may lead to the appearance of a minor *S*-shaped in *I–V* characteristics in the high-voltage region (i.e., for voltages where impact ionization is substantial), even without an Auger process.

CONCLUSION

Auger ionization and impact ionization are basic physical processes responsible for the formation of reverse *I–V* characteristics of Al–SiO$_2$–*n*-Si structures with a 1.2–3.2-nm-thick SiO$_2$ layer. The relative roles of Auger ionization by injected hot electrons and impact ionization in the SCR were analyzed quantitatively for different modes of the structures' operation. The turn-on voltages V_{sw} were determined experimentally and theoretically for a tunnel MOS structure and were found to be significantly lower than the breakdown voltages. V_{sw} decreases with increasing oxide thickness and an increasing doping level of the substrate.

ACKNOWLEDGMENTS

This work was supported by the State Scientific Technical Program "Nanostructures in Physics" and the Russian Foundation for Basic Research (project no. 99-02-18079-a). M.I. Vexler wishes to thank Alexander von Humboldt-Stiftung for support of the initial stage of this work. The authors thank V.F. Komarova for assistance in sample fabrication.

REFERENCES

1. K. M. Chu and D. L. Pulfrey, IEEE Trans. Electron Devices **ED-35**, 188 (1988).

2. T. Yoshimoto and K. Suzuki, Jpn. J. Appl. Phys. **32** (12), L180 (1993).
3. H. S. Momose, S. Nakamura, T. Ohguro, *et al.*, IEEE Trans. Electron Devices **ED-45**, 691 (1996).
4. S. K. Lai, P. V. Dressendorfer, T. P. Ma, and R. C. Barker, Appl. Phys. Lett. **38**, 41 (1981).
5. I. V. Grekhov, E. V. Ostroumova, A. A. Rogachev, and A. F. Shulekin, Pis'ma Zh. Tekh. Fiz. **17** (13), 44 (1991) [Sov. Tech. Phys. Lett. **17**, 476 (1991)].
6. I. V. Grekhov, A. F. Shulekin, and M. I. Vexler, Solid-State Electron. **38**, 1533 (1995).
7. E. V. Ostroumova and A. A. Rogachev, Fiz. Tekh. Poluprovodn. (St. Petersburg) **28**, 1411 (1994) [Semiconductors **28**, 793 (1994)].
8. A. F. Shulekin, M. I. Vexler, and H. Zimmermann, Semicond. Sci. Technol. **14** (5), 470 (1999).
9. Y. Wang and K. F. Brennan, J. Appl. Phys. **75** (1), 313 (1994).
10. W. E. Drummond and J. L. Moll, J. Appl. Phys. **42**, 5556 (1971).
11. T. Ando, A. Fowler, and F. Stern, Rev. Mod. Phys. **54** (2), 437 (1982).
12. S. Sze, *Physics of Semiconductor Devices* (Wiley, New York, 1981; Mir, Moscow, 1984).

Translated by D. Mashovets

Semiconductors, Vol. 34, No. 7, 2000, pp. 781–785. Translated from Fizika i Tekhnika Poluprovodnikov, Vol. 34, No. 7, 2000, pp. 809–813.

Photosensitivity of Structures Based on ZnSe Single Crystals

G. A. Il'chuk, V. Yu. Rud'***, Yu. V. Rud'*, R. N. Bekimbetov*,**
V. I. Ivanov-Omskiĭ*, and N. A. Ukrainets*

** Ioffe Physicotechnical Institute, Russian Academy of Sciences, Politekhnicheskaya ul. 26, St. Petersburg, 194021 Russia*
*** Lviv State Polytechnical University, Lviv, 79013 Ukraine*
**** St. Petersburg State Technical University, ul. Politekhnicheskaya 29, St. Petersburg, 195251 Russia*

Submitted January 12, 2000; accepted for publication January 13, 2000

Abstract—Heat treatment in vacuum and air was used to produce photosensitive structures based on ZnSe single crystals. Spectral dependences of relative quantum efficiency of photoconversion in these structures under exposure to natural and linearly polarized light were studied. The polarization photosensitivity of ZnSe-based structures was detected and studied in relation to their manufacturing conditions and photodetection configuration. Photopleochroism in these structures was shown to arise at oblique incidence of polarized light. The heat treatment of ZnSe in atmospheric air was demonstrated to reduce photopleochroism, which is related to interference phenomena in the formed layers. It was concluded that ZnSe can be employed in polarimetric short-wavelength photodetectors. This study represents a new approach to diagnostics of interaction processes at the ZnSe surface. *© 2000 MAIK "Nauka/Interperiodica".*

INTRODUCTION

Zinc selenide (ZnSe) is among the most promising wide-gap II–VI compounds and is widely used in developing short-wavelength semiconductor electronic devices and data-displaying systems [1–8]. The photosensitivity of various structures based on ZnSe single crystals has been studied only in unpolarized light, although this compound has both a wurtzite and a cubic modification [1, 7, 9]. Moreover, ZnSe is one of the typical materials of phases of variable composition; therefore, its properties "keep track" of thermodynamic equilibrium parameters, which requires precise control of the material existence conditions during growth. In this paper, we consider the first data on photosensitivity in natural and linearly polarized light for several structures produced by ZnSe heat treatment under various conditions.

EXPERIMENTAL

To produce photosensitive structures, we used *n*-ZnSe single crystals grown from a melt with a composition close to the compound stoichiometry. Single crystals had a sphalerite structure with a lattice parameter corresponding to the reported value [9]. Their resistivity and electron concentration are $\rho \approx 10^{10}\ \Omega$ cm and $n \approx 10^8$ cm^{-3}, respectively, at a temperature of $T = 300$ K. Crystals are uniformly bright yellow in white light.

To produce photosensitive structures, *n*-type single-crystal platelets cleaved over the crystallographic plane (100) with average sizes of $5 \times 4 \times 2$ mm^3 were subjected to heat treatment at $T_t \approx 500°$C in dry air. As a result, reproducibly colored *p*-type layers were formed; their color is controlled by the heat treatment time t_t. As t_t increased to 200 min, the layer color changed from lilac to dark red. The layer thickness did not exceed 1 μm.

Similar heat treatments of *n*-ZnSe crystals placed into a vacuum ampoule cause no changes in the initial crystal coloration up to the longest t_t, although the conduction type is converted ($n \longrightarrow p$) in the subsurface region. Therefore, the color change in the ZnSe subsurface region during heat treatment in air seems to be related to the formed interference oxide layers, whereas the *n*-ZnSe conduction type reversal in vacuum reflects only stoichiometry deviations changed due to preferential diffusive emergence of zinc atoms, and, hence, the origination of acceptor centers V_{Zn}. Removing the conversion layer by cleaving or mechanical polishing of all substrate sides, except for one, we produced two types of structures representing a contact of a layer $d_l \leq 1$ μm thick with a substrate $d_s \leq 0.5$–1 mm thick. These structures contained a *p*-layer representing ZnSe (type *A*) or an oxide layer (type *B*). For the sake of comparison to initial crystals, Cu/*n*-ZnSe Schottky barriers were also produced by thermal sputtering of copper onto the *n*-ZnSe cleavage surface in vacuum.

EXPERIMENTAL DATA AND DISCUSSION

The photovoltaic effect was detected in all the studied structures. Photosensitivity spectra were studied using linearly polarized light in relation to the structure production conditions. The basic results of these studies can be summarized as follows.

The typical spectral dependence of the relative quantum efficiency $\eta(\hbar\omega)$ of photoconversion of a sur-

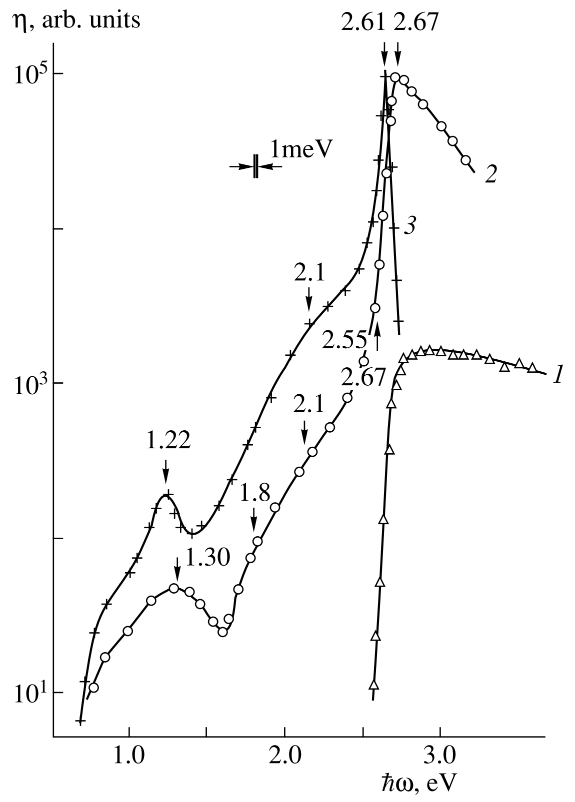

Fig. 1. Spectral dependences of the relative quantum efficiency η of photoconversion of (*1*) the Cu/*n*-ZnSe Schottky barrier and (*2*, *3*) *p*–*n* *A*-type structures based on ZnSe and obtained by ZnSe heat treatment in vacuum for time $t_t \approx$ 120 min. The samples were illuminated from the side of (*1*) the barrier contact, (*2*) the *p*-layer, and (*3*) the substrate.

face–barrier structure is shown in Fig. 1 (curve *1*). Upon illumination from the barrier contact side, the photosensitivity spectra exhibit broadband properties. The long-wavelength exponential edge of photosensitivity has a steep slope, $S = \delta(\ln\eta)/\delta(\hbar\omega) \approx 42$ eV^{-1} and corresponds to direct optical transitions in ZnSe, while the knee at $\hbar\omega = 2.67$ eV coincides with the ZnSe band gap E_g [1, 9]. The absence of a pronounced short-wavelength drop of η deep in the ZnSe bandgap absorption points to a fairly high quality of energy barriers produced by vacuum thermal sputtering of copper onto the *n*-ZnSe cleavage surface. The voltage photosensitivity S_u of Cu/*n*-ZnSe structures was typically 0.1 V/W at $T = 300$ K in the region of $\hbar\omega > E_g$. If the Cu/*n*-ZnSe structures are illuminated from the substrate side, photosensitivity spectra as a rule become highly selective, since the short-wavelength boundary of $\eta(\hbar\omega)$ is controlled by strong absorption in ZnSe near E_g.

In the case of A-type structures produced by heat treatment of the crystals grown in vacuum, the photosensitivity is observed in a wider spectral range than for Schottky barriers (see Fig. 1, curve *2*). The maximum voltage photosensitivity is found to be higher under illumination from the *p*-layer side and may be as high as about 1 V/W (higher than in the case of the Schottky barriers). The photosensitivity exponential growth sets in at $\hbar\omega > 2.55$ eV. Its slope *S* is about 26 eV^{-1}, which is somewhat lower than for Schottky barriers. This fact can reflect smearing of the bandgap absorption edge by an electric field of charged defects generated in the *p*-layer. The photosensitivity peak position $\hbar\omega_m$ = 2.67 eV corresponds to the ZnSe band gap [1, 9], while the short-wavelength slope of η can be related to the effect of optical absorption of the *p*-layer adjacent to the homojunction active region. The photosensitivity-spectrum FWHM $\delta_{1/2} \approx 290$ meV is mainly controlled by the *p*-layer thickness, and, hence, by the heat-treatment parameters. When these structures are illuminated from the substrate side (Fig. 1, curve 3), $\hbar\omega_m$ further shifts to longer wavelengths due to a significant increase in the thickness of the ZnSe layer adjacent to the structure active region; thus, the steep short-wavelength boundary of η arises in the vicinity of E_g.

The photosensitivity of *A*-type structures increases in the long-wavelength region $\hbar\omega < E_g$ (see Fig. 1, curves *2*, *3*) as compared to that of Schottky diodes made of as-grown ZnSe crystals. This circumstance points to an increase in the defect concentration and the emergence of new types of native defects in the surface layer. Spectra of *A*-type structures are also characterized by an appreciable photosensitivity increase that sets in at approximately $\hbar\omega \approx 0.7$ eV; furthermore, at least three regions of photosensitivity increase can be distinguished: for energies $\hbar\omega \approx$ 1.2–1.3, 1.8, and 2.1 eV. These features indicate that defect levels spaced away from one of the empty bands by 0.6–0.7, 1.4–1.5, and 2 eV emerge in the layer. Since long-wavelength photosensitivity increases with heat treatment, it is reasonable to believe that the above defects are caused by vacancies formed in the zinc sublattice, as well as by their interaction with defects of other types existing in the initial material.

B-type structures produced by heat treatment of ZnSe crystals in air exhibit the highest photosensitivity among those manufactured by various methods using the same initial material. The maximum voltage photosensitivity can be as high as 10^2 V/W in the best *B*-type structures produced at treatment times $t_t \approx$ 15–30 min, temperature $T = 300$ K, and illumination from the layer side. This value significantly exceeds the corresponding parameters of Schottky barriers and *A*-type structures.

The photovoltaic effect in *B*-type structures illuminated from the layer side, as well as in *A*-type structures, spans a wide spectral range from 0.7 to 3.3 eV (see Fig. 2), and the spectral contour of η corresponding to samples with $t_t < 30$ min resembles the contour typical of ZnSe heat treatment in vacuum (Fig. 1). As is evident from Fig. 2, the contribution of long-wavelength photosensitivity grows with t_t so that the broad long-wavelength component ($\delta_{1/2} \approx 650$ meV) is dominant in the spectrum beginning as early as at $t_t > 150$ min. As for

B-type structures, the spectral positions of features appearing in the long-wavelength region (indicated by arrows in Fig. 2) are close to those observed in the η spectra of *A*-type structures (Fig. 1). Thus, we may consider the energy levels arising in conversion layers on ZnSe heat treatment in vacuum and in air to be almost identical. Therefore, we may assume that natural doping of ZnSe at studied heat treatment temperatures is controlled mainly by changes in stoichiometry deviations in the ZnSe subsurface layer. At the same time, the short-wavelength threshold near 2 eV appearing in photosensitivity spectra of B-type structures suggests that oxide layers with a band gap narrower than in ZnSe are formed at the surface due to the interactions of ZnSe with air, primarily with oxygen.

If *B*-type structures are illuminated from the side of thin layers (see Fig. 2), the photosensitivity in the range of ZnSe near-edge absorption is dominant. As t_t increases, the edge-band peak position is somewhat less than E_g of ZnSe and shifts to longer wavelengths, whereas the spectra themselves become narrower band ($\delta_{1/2} \approx$ 60–70 meV) compared to spectra of *A*-type structures. These features of *B*-type structures are caused by the enhanced effect of absorption in the *p*-layer adjacent to the active region.

When linearly polarized light is incident along the normal to the photoreceiving surface, the photosensitivity of Schottky barriers, as well as of *A*- and *B*-type structures, is virtually independent of the spatial orientation of the electric field vector **E** of light wave relative to crystallographic axes in the substrate crystal. This case corresponds to isotropic photoactive absorption in ZnSe substrates with the sphalerite structure. Therefore, no natural photopleochroism is observed in ZnSe-based structures [10].

Only "induced photopleochroism" is detected in all structures produced from *n*-ZnSe; i.e., the angle of incidence of linearly polarized light onto the surface becomes distinct from 0° [11]. Typical experimental dependences of the short-circuit photocurrent $i^{\parallel}$ and $i^{\perp}$ (superscripts $\parallel$ and $\perp$ correspond to parallel and perpendicular orientations of **E** relative to the incidence plane of light) on the angle of incidence of light θ onto the photoreceiving surface are plotted in Fig. 3. Angular dependences of photocurrents for Schottky barriers and *A*-type structures conform to the Fresnel relationships [12] in the entire photosensitivity range. Actually, if **E** is parallel to the incidence plane (IP) of light, the photocurrent initially increases, passes through a maximum, and then begins to decrease (curve *1*), whereas, for the polarization $\mathbf{E} \perp$ IP, the photocurrent steadily decreases as θ increases (curve *3*). The photocurrent growth by a factor of about 1.3 corresponds to reflection loss elimination for a light wave for the polarization $\mathbf{E} \parallel$ IP in the vicinity of the pseudo-Brewster angle. Similar angular dependencies $i^{\parallel}(\theta)$ and $i^{\perp}(\theta)$ are observed in the case of *B*-type structures, but only if they are illuminated from the side of the substrate surface unaffected by heat treatment. When the surface of films produced by ZnSe heat treatment in air is used as a detecting plane in *B*-type structures, angular dependences $i^{\perp}(\theta)$ (see Fig. 3, curve *4*) become similar to the case of $\mathbf{E} \parallel$ IP (Fig. 3, curves *1*, *2*).

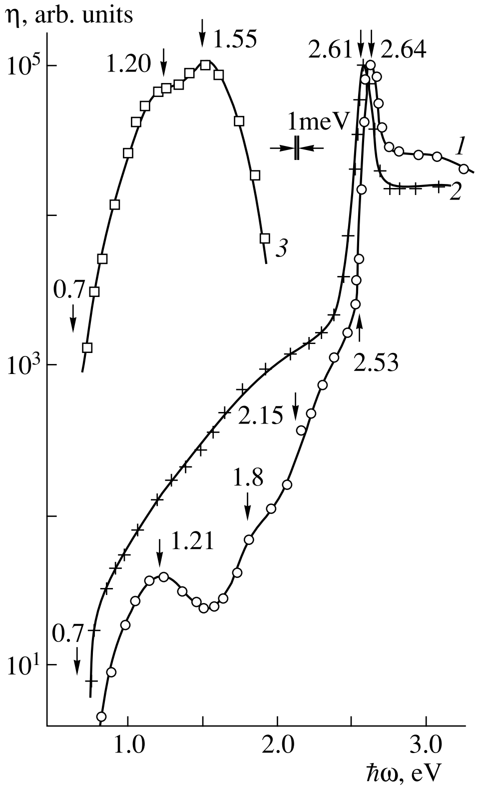

Fig. 2. Spectral dependences of the relative quantum efficiency η of photoconversion of *p*–*n* *B*-type structures based on ZnSe and produced by *n*-ZnSe heat treatment in dry air for t_t = (*1*) 10, (*2*) 25, and (*3*) 150 min. The samples were illuminated from the *p*-layer side.

As follows from Fig. 3 (curves *5*–*8*), the coefficient of induced photopleochroism in all produced structures obeys the law

$$P_I \sim \theta^2.$$

It is important to emphasize that the photopleochroism at $\theta = \theta°$ is absent in all structures produced on the basis of ZnSe crystals and that all the angular dependences $P_I(\theta)$ emerge from zero. This allows us to classify the photopleochroism observed at $\theta \neq \theta°$ as an induced photopleochroism [11].

The angular dependences of induced photopleochroism of Schottky barriers and *A*-type structures illuminated from the side of layer and substrate, as well as *B*-type structures illuminated only from the substrate side, are very similar. The refractive index *n* estimated from these dependences corresponds to the known value for ZnSe [9]. When passing to illumination of *B*-type structures by linearly polarized light from the side of layers formed due to the ZnSe–air interaction,

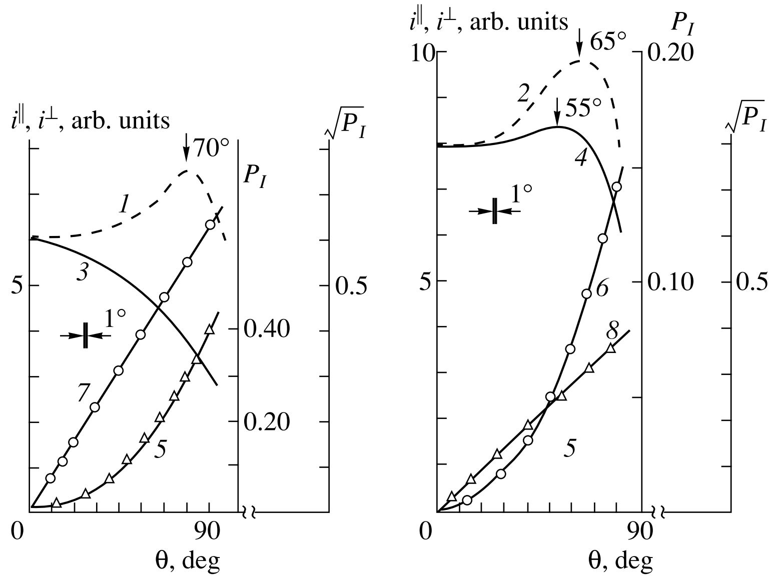

Fig. 3. Dependences of the short-circuit photocurrents (*1*, *2*) $i^{\parallel}$ and (*3*, *4*) $i^{\perp}$ and the induced photopleochroism coefficient (*5*, *6*) P_I and (*7*, *8*) $\sqrt{P_I}$ of the structure produced by *n*-ZnSe heat treatment in dry air for t_t = 10 min, illuminated (*1*, *3*, *5*, and *7*) from the substrate side at $\hbar\omega \approx 2.60$ eV and (*2*, *4*, *6*, and *8*) from the *p*-layer side at $\hbar\omega \approx 2.64$ eV.

along with the angular dependence $i^{\perp}(\theta)$ anomaly, an abrupt decrease is observed in the induced photopleochroism coefficient P_I from 40 to 12–15% for $\theta \approx 75°$ in various structures with *p*-layers, depending on heat treatment time. With regard to [13–16], the detected P_I decrease due to the ZnSe–air interactions can be related to interference phenomena in formed layers and their antireflective properties.

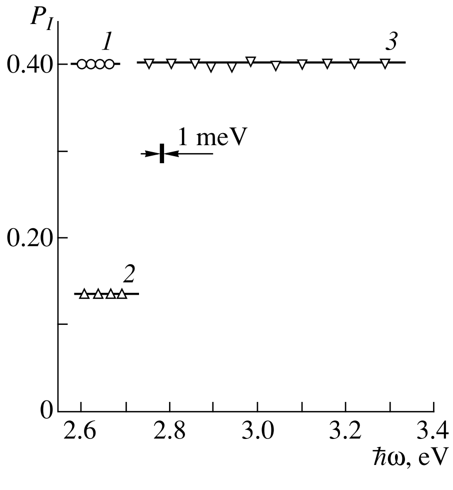

Fig. 4. Spectral dependences of the induced photopleochroism coefficient P_I for (*1*, *2*) structures manufactured by *n*-ZnSe heat treatment in dry air for t_t = 10 min and (*3*) the Cu/*n*-ZnSe surface-barrier structure, illuminated from the side of (*1*) the *p*-layer, (*2*) the ZnSe substrate, and (*3*) the barrier contact; θ = 75°.

Spectral dependences of the induced photopleochroism coefficient for typical ZnSe-based structures are compared in Fig. 4. It is evident that, as the light penetrates the active region of structures from the side of ZnSe, the photopleochroism coefficient is about 40% and is constant in the photosensitivity range of the structures (Fig. 4, curves *1* and *3*). These data are consistent with an analysis carried out with the interference phenomena disregarded [11]. As the light is incident on the active region from the side of the layer formed at the ZnSe surface due to the interaction with air, the photopleochroism coefficient decreases in the range of high photosensitivity, which, according to [13–16], can be caused by antireflective properties of such layers.

As a whole, the data obtained indicate that ZnSe single crystals can be used for the development of shortwavelength photodetectors insensitive to photon energies $\hbar\omega < 2.55$ eV or highly selective (*A*- and *B*-type structures). Such detectors allow a fast transition from a polarization-insensitive to a polarimetric photodetection mode with continuous control of the photopleochroism coefficient by varying the angle of incidence of linearly polarized light. Also noteworthy is a new opportunity to control the ZnSe surface modification, which is caused by interaction with an ambient medium, by polarization spectroscopy of photoactive absorption.

REFERENCES

1. M. Aveu and J. S. Prener, *Physics and Chemistry of II–VI Compounds* (North-Holland, Amsterdam, 1967).

2. *The Physics of II-VI Compounds*, Ed. by A. N. Georgobiani and M. K. Sheĭnkman (Nauka, Moscow, 1986).
3. L. A. Kolodziejski, R. G. Gunshor, N. Otsuka, *et al.*, Appl. Phys. Lett. **48**, 1482 (1986).
4. J. Misiewicz, C. Huber, and D. Heiman, Jpn. J. Appl. Phys. **32**, 372 (1993).
5. A. L. Gurskii, E. V. Lutsenko, G. P. Yablonskii, *et al.*, Cryst. Res. Technol. **31**, 705 (1996).
6. A. Burger and M. Roth, J. Cryst. Growth **70**, 386 (1984).
7. B. L. Sharma and P. K. Purohit, *Semiconductor Heterostructures* (Pergamon, 1974).
8. A. V. Simashkevich, *Heterojunctions Based on II–VI Semiconductor Compounds* (Shtiintsa, Kishinev, 1980).
9. *Physicochemical Properties of Semiconductor Materials: A Handbook* (Nauka, Moscow, 1978).
10. F. P. Kesamanly, V. Yu. Rud’, and Yu. V. Rud’, Fiz. Tekh. Poluprovodn. (St. Petersburg) **30**, 1921 (1996) [Semiconductors **30**, 1001 (1996)].
11. F. P. Kesamanly, V. Yu. Rud’, and Yu. V. Rud’, Fiz. Tekh. Poluprovodn. (St. Petersburg) **33**, 513 (1999) [Semiconductors **33**, 483 (1999)].
12. R. M. A. Azzam and N. M. Bashara, *Ellipsometry and Polarized Light* (North-Holland, Amsterdam, 1977).
13. V. Yu. Rud’ and Yu. V. Rud’, Fiz. Tekh. Poluprovodn. (St. Petersburg) **31**, 245 (1997) [Semiconductors **31**, 197 (1997)].
14. T. Wal’ter, V. Yu. Rud’, Yu. V. Rud’, and H. W. Schock, Fiz. Tekh. Poluprovodn. (St. Petersburg) **31**, 806 (1997) [Semiconductors **31**, 681 (1997)].
15. A. Berdinobatov, N. Nazarov, V. M. Sarkisova, *et al.*, Fiz. Tekh. Poluprovodn. (St. Petersburg) **32**, 714 (1998) [Semiconductors **32**, 642 (1998)].
16. V. Yu. Rud’, Yu. V. Rud’, and H. W. Schock, Solid State Phenom. **67**/**68**, 421 (1999).

Translated by A. Kazantsev

Semiconductors, Vol. 34, No. 7, 2000, pp. 786–789. Translated from Fizika i Tekhnika Poluprovodnikov, Vol. 34, No. 7, 2000, pp. 814–817.
Original Russian Text Copyright © 2000 by Berman, Belyakova, Kostina E. Kim, S. Kim.

SEMICONDUCTOR STRUCTURES, INTERFACES, AND SURFACES

Analysis of Charges and Surface States at the Interfaces of Semiconductor–Insulator–Semiconductor Structures

L. S. Berman*, E. I. Belyakova*, L. S. Kostina*, E. D. Kim, and S. C. Kim****

** Ioffe Physicotechnical Institute, Russian Academy of Sciences, ul. Politekhnicheskaya 26, St. Petersburg, 194021 Russia*

*** Korea Electrotechnology Research Institute, Republic of Korea*

Submitted January 17, 2000; accepted for publication January 18, 2000

Abstract—A method for determining the energy spectrum of charges and surface-state densities at the interfaces of semiconductor–insulator–semiconductor structures was developed; the method is based on the analysis of capacitance–voltage characteristics. The method was experimentally tested with Si–SiO$_2$–Si structures prepared by direct bonding of both mirror-polished smooth wafers and wafers with a regular mesoscopic relief pattern at the inner surface of the wafers to be bonded. The density of surface states is lower at the surfaces with a regular relief pattern than that at the surfaces without the surface relief. *© 2000 MAIK “Nauka/Interperiodica”.*

INTRODUCTION

In order to form the semiconductor–insulator–semiconductor (SIS) structures, e.g., a Si–SiO$_2$–Si structure and the like, direct bonding is used [1–4]. On the basis of these structures, both discrete metal–insulator–semiconductor (MIS) transistors and integrated circuits are developed [5–8]. In a thin semiconductor wafer, the space-charge region under the electrodes at the outer (operating) surface may extend to the entire thickness of the wafer. In this case, the surface states at the back side of the wafer impair the MIS-transistor parameters, including the threshold voltage, the charge-carrier mobility in the channel, and other parameters [8, 9]. Therefore, an analysis of surface states at the interfaces of directly bonded SIS structures is an urgent problem. In the case of MIS transistors, this problem can be solved by the charge-pumping method [10–12]. However, the interface parameters have to be known even prior to designing the corresponding devices. To this end, one can grind off and (or) etch off one of the wafers and deposit a metal on the insulator [2]; the parameters of the other interface are then measured by the methods developed in detail for the MIS structures [13, 14]. However, as a result of the above treatments, the surface can become additionally contaminated and the grinding-off can introduce additional stresses. In [15], the Si–SiO$_2$–Si structures were simulated; in particular, the low- and high-frequency capacitance–voltage (C–V) characteristics $C_{lf}(V)$ and $C_{hf}(V)$ were calculated for various structures. It was recommended [15] that the SIS-structure parameters (among them, the order of magnitude of the surface-state density) be determined by comparing the calculated characteristics $C_{hf}(V)$ and $C_{lf}(V)$ with experimental data. This method was also used in [16, 17]. However, the measurement of $C_{hf}(V)$ characteristics in the entire operating range of voltages is quite a challenge; this is due to the fact that, in the case of enhancement, the values of τ_{th} can be on the order of nanoseconds and less (here, τ_{th} is the characteristic time of thermal emission of carriers from the surface states whose levels coincide with the Fermi level in the semiconductor). This means that, in order to satisfy the condition $\omega\tau_{\text{th}} \gg 1$, frequencies on the order of several GHz and higher are required (here, $\omega = 2\pi f$ is the frequency at which the capacitance is measured).

In this paper, we suggest a new method for determining the energy spectrum of charges and surface states at both interfaces of a SIS structure. This method is based on the analysis of C–V characteristics measured at a single frequency; this makes it possible to eliminate the aforementioned difficulty and also to use digital capacitance meters and thus improve the accuracy of measurements. The method is used to determine the spectra of surface states at the interfaces of a Si–SiO$_2$–Si structure produced by direct bonding.

THEORY

The charges and surface states at the interface were analyzed by the method of steady-state C–V characteristics [13–15]. Figure 1 illustrates the energy diagram of a directly bonded n-Si–SiO$_2$–n-Si structure; the configuration of this structure is shown in the inset. The voltage at wafer 2 is defined by [15]

$$V + V_{bi} = \Psi_{s1} - \Psi_{s2} - (Q_{sc1} + Q_{ss1} + \bar{x}Q_f/d)/C_i, \quad (1)$$

where V_{bi} is the contact potential difference between wafers 1 and 2 (henceforth, the subscripts 1 and 2 correspond to wafers 1 and 2); Ψ_{s1} and Ψ_{s2} are the potentials of the surfaces of wafers 1 and 2, respectively; Q_{sc1} and Q_{ss1} are the near-surface space charge and the charge of surface states, respectively; Q_f is the fixed charge in SiO_2; $\bar{x}$ is the position of the centroid of the charge Q_f and is reckoned from x_2; d is the SiO_2 thickness; and C_i is the insulator capacitance.

We use the condition for electrical neutrality to obtain

$$Q_{sc1}+Q_{ss1}+Q_f+Q_{sc2}+Q_{ss2} = 0. \tag{2}$$

The capacitance of the structure is given by

$$C = [(C_{sc1}+C_{ss1})^{-1}+(C_{sc2}+C_{ss2})^{-1}+C_i^{-1}]^{-1}, \tag{3}$$

where $C_{sc1,\,2}$ and $C_{ss1,\,2}$ are the capacitances of the space-charge region and the surface states, respectively.

The quantities $Q_{sc1,\,2}$ and $C_{sc1,\,2}$ can be expressed in terms of the surface potentials $\Psi_{s1,\,2}$ [13, 14]. The capacitance C_{ss} of the surface states and the surface-state density N_{ss} are related by the formula [18]

$$C_{ss} = qN_{ss}\arctan(\omega\tau_{th})/\omega\tau_{th}, \tag{4}$$

where q is the elementary charge. Expression (4) is valid if the density of surface states and the capture cross section for electrons σ_n are independent of energy in the range from $-kT$ to $+kT$.

The quantity τ_{th} is defined by [13, 14]

$$\tau_{th} = (\sigma_n b_n T^2)^{-1}\exp\left(\frac{E_c-F_n-q\Psi_s}{kT}\right), \tag{5}$$

where b_n is a parameter of the semiconductor and F_n is the Fermi level in the semiconductor. We now use the concept of critical potential Ψ_{scr} for which $\omega\tau_{th} = 1$ (see also [19]). In this case,

$$\omega\tau_{th} = \exp\left[\frac{q(\Psi_{scr}-\Psi_s)}{kT}\right]. \tag{6}$$

If Ψ_s varies from Ψ_{scr} + (3–5)kT to Ψ_{scr} – (3–5)kT, the capacitance of the corresponding interface decreases from the low-frequency value of $C_{lf} = C_{sc} + qN_{ss}$ to the high-frequency value of $C_{hf} = C_{sc}$.

We now consider the situation in which surface 1 is depleted of, and surface 2 is enriched in, charge carriers. In this case, the inequality $C_{sc2} \gg C_{sc1}$ holds as a rule; therefore, we have $(C_{sc2} + C_{ss2})^{-1} \ll (C_{sc1} + C_{ss1})^{-1}$. To a first approximation, we ignore the term $(C_{sc2} + C_{ss2})^{-1}$ in formula (3). Formula (3) then becomes similar to the formula for the capacitance of a MIS structure. On the strength of this, to a first approximation, we determine the dependences $\Psi_{s1}(V)$, $Q_{ss1}(\Psi_{s1})$, and $N_{ss1}(\Psi_{s1})$ from the C–V characteristics by the same method as the one used in the case of a MIS structure [13, 14]. For the sake of convenience of the analysis, we approximate the dependence $Q_{ss1}(\Psi_{s1})$ with a polynomial of degree n (n = 3–5) as

$$\begin{aligned} Q_{ss1}(\Psi_{s1}) &= Q_{0(1)}+Q_{1(1)}\Psi_{s1} \\ &+ Q_{2(1)}\Psi_{s1}^2\dots\ Q_{n(1)}\Psi_{s1}^n. \end{aligned} \tag{7}$$

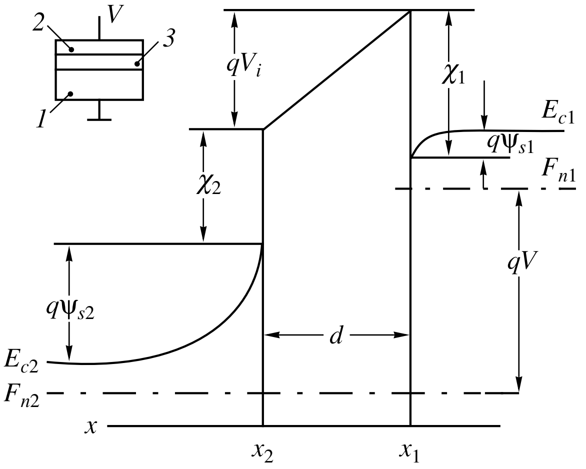

Fig. 1. The energy diagram of a Si–SiO_2–Si structure. In the inset, (*1*) is wafer 1 without a relief pattern, (*2*) is wafer 2 with a relief pattern at the inner side, and (*3*) is the silicon dioxide. A positive voltage is applied to wafer 2. V_i is the voltage drop across the insulator; χ is the electron affinity; F_n is the Fermi level; E_c is the conduction-band bottom; and x is the coordinate. Explanations of the other notations are given in the text.

Here, the subscripts (1) and (2) refer to the first and second surfaces, respectively. We then have

$$\begin{aligned} N_{ss1}(\Psi_{s1}) &= -1/q(\partial Q_{ss1}/\partial\Psi_{s1}) \\ &= -1/q(Q_{1(1)}+2Q_{2(1)}\Psi_{s1}+\dots\ nQ_{n(1)}\Psi_{s1}^{n-1}). \end{aligned} \tag{8}$$

If surface 2 is depleted of charge carriers, we similarly determine the dependences $\Psi_{s2}(V)$, $Q_{ss2}(\Psi_{s2})$, and $N_{ss2}(\Psi_{s2})$ to a first approximation; we also approximate the dependence $Q_{ss2}(\Psi_{s2})$ with a polynomial. Using the obtained results and formulas (1)–(6), we calculate to a first approximation the C–V characteristics of a SIS structure and compare it with the experimental C–V characteristics.

We then use the direct-search method [20, 21] to adjust the coefficients in the polynomials and the values of Ψ_{scr} and Q_f in order to attain the best agreement between the theoretical and experimental C–V characteristics (by visual examination and according to the smallest variance).

EXPERIMENT AND COMPARISON WITH THE THEORY

In our previous papers [22, 23], we showed that a regular relief pattern in the form of a network of mutually perpendicular grooves constitutes a sink for structural defects. In this study, the above method for the surface-state analysis was tested experimentally using the n-Si–SiO_2–n-Si structures produced by direct bonding of both the mirror-polished smooth wafers and the wafers with a regular mesoscopic relief pattern on the inner surface of one of the wafers to be bonded.

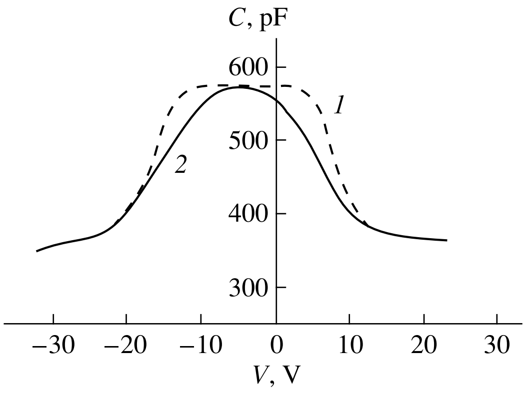

Fig. 2. The *C–V* characteristics of a SIS structure. Curve *1* corresponds to the characteristic calculated to a first approximation, and curve *2* represents the experimental data. The voltage is measured at wafer 2 (see the inset in Fig. 1).

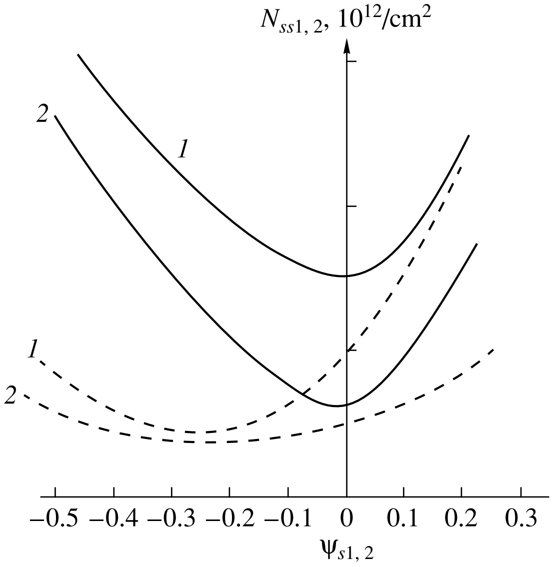

Fig. 3. Dependence of the surface-state density on the surface potential (*1*) at the surface of wafer 1 and (*2*) at the surface of wafer 2. The dashed lines correspond to a first approximation; the solid lines represent the refined values.

The samples were prepared from the Czochralski-grown *n*-Si(111) crystals ($\rho = 15\ \Omega$ cm); the thickness of the wafers was 300 μm, the thickness of the oxide layer was 0.75 μm, and the surface area of the samples was 0.12 cm^2. A regular relief pattern was formed on the surface of one of the wafers to be bonded; this pattern consisted of a network of mutually perpendicular grooves having a width of 50 μm and a depth of 0.2–0.3 μm, with the distance between the grooves being 200 μm. The details of the technology for producing the samples were reported elsewhere [22, 23].

The *C–V* characteristics (at $T \approx 293$ K) were measured and the dependences $\Psi_{s1,2}(V)$, $Q_{ss1,2}(\Psi_{s1,2})$, and $N_{ss1,2}(\Psi_{s1,2})$, and also the coefficients in the polynomials were determined using an automated facility [24]. An experimental *C–V* characteristic was inputted into a computer. The calculation of the *C–V* characteristics with formulas (1)–(6), selection of the polynomial coefficients, and comparison of the calculated and experimental *C–V* characteristics were performed with a computer.

Figure 2 shows the calculated (to the first approximation) and experimental *C–V* characteristics. The left-hand portion of the *C–V* characteristics corresponds to the depletion state of the surface of wafer 1 (without a relief pattern), whereas the right-hand portion corresponds to the depletion state of the surface of wafer 2 (with a relief pattern on the inner side). The slope of the right-hand portion of the *C–V* characteristics is larger than that of the left-hand portion. This indicates that the surface-state density is lower at the surface with the relief pattern and confirms the results reported previously [22, 23]; it was shown in [22, 23] that a regular relief pattern is an effective getter for structural defects. A shift of the *C–V* characteristics to negative voltages indicates that there is a positive surface-state charge at surface 1 and (or) a negative surface-state charge at surface 2. If the calculated and experimental *C–V* characteristics coincide, we obtain the following values of parameters: $\Psi_{scr1} = -0.15$ V, $\Psi_{scr2} = -0.15$ V, $Q_f = -0.24 \times 10^{-7}$ C/cm^2, and $\bar{x}/d = 0.5$. The density of charges at surfaces 1 and 2 for the flat-band potentials are equal to $Q_{0(1)} = 0.4 \times 10^{-8}$ C/cm^2 and $Q_{0(2)} = -0.3 \times 10^{-7}$ C/cm^2, respectively.

Figure 3 shows the dependences $N_{ss1,2}(\Psi_{ss1,2})$. In the entire range of surface potentials, the surface-state density at the surface with a relief pattern is lower than that at the surface without a relief pattern.

CONCLUSION

Thus, we developed a method for determining the energy spectrum of charges and the density of surface states at the interfaces in the semiconductor–insulator–semiconductor structures. This method was experimentally tested using the Si–SiO$_2$–Si structures prepared by direct bonding of both the mirror-polished wafers and the wafers with a regular mesoscopic relief pattern at the inner surface of one of the wafers to be bonded. The surface-state density at the surface with a regular relief pattern is lower than that at the surface without a relief pattern, because a regular relief pattern constitutes a getter for structural defects.

REFERENCES

1. K. Mitani and U. M. Gosele, J. Electron. Mater. **21**, 669 (1992).
2. W. P. Maszara, G. Goetz, A. Caviglia, and J. B. McKitterick, J. Appl. Phys. **64**, 4943 (1988).
3. S. Bengston, J. Electron. Mater. **21**, 841 (1992).
4. M. Bruel, Electron. Lett. **31**, 1201 (1995).

5. J. P. Colinge, IEEE Electron Device Lett. **EDL-7**, 244 (1986).
6. J. P. Colinge, IEEE Electron Device Lett. **EDL-8**, 410 (1987).
7. T. W. Mac Elwee, I. D. Calder, R. A. Bruce, and F. R. Shepherd, IEEE Trans. Electron Devices **ED-37**, 1444 (1990).
8. D. J. Wouters, J. P. Colinge, and H. A. Maes, IEEE Trans. Electron Devices **ED-37**, 2022 (1990).
9. B. Mazhari, S. Cristoloveanu, D. E. Joannou, and A. L. Caviglia, IEEE Trans. Electron Devices **ED-38**, 1289 (1991).
10. G. Groeseneken, H. E. Maes, N. Beltran, and R. F. Keersmaeker, IEEE Trans. Electron Devices **ED-31**, 42 (1984).
11. J. S. Brugler and G. A. Gespers, IEEE Trans. Electron Devices **ED-16**, 297 (1969).
12. J. L. Autran, F. Seigneur, C. Plossu, and B. Balland, J. Appl. Phys. **74**, 3932 (1993).
13. E. H. Nicollian and B. R. Brews, *MOS (Metal–Oxide–Semiconductor) Physics and Technology* (Wiley, New York, 1982).
14. S. Sze, *Physics of Semiconductor Devices* (Wiley, New York, 1981; Mir, Moscow, 1984), Vol. 1.
15. K. Nagai, T. Sekigava, and Y. Hayashi, Solid State Electron. **28**, 789 (1985).
16. F. T. Brady, S. S. Li, D. E. Burk, and W. A. Krull, Appl. Phys. Lett. **52**, 886 (1988).
17. K. Mitani and H. Massoud, IEICE Trans. Electron. **E-75 C**, 1421 (1992).
18. K. Lechovec, Appl. Phys. Lett. **8**, 48 (1966).
19. L. S Berman, I. V. Grekhov, I. N. Karimov, and E. V. Ostroumova, Fiz. Tekh. Poluprovodn. (St. Petersburg) **27**, 917 (1993) [Semiconductors **27**, 497 (1993)].
20. B. D. Bunday, *Basic Optimization Methods* (Edward Arnold, London, 1984; Radio i Svyaz’, Moscow, 1988).
21. D. M. Himmelblau, *Process Analysis by Statistical Methods* (Wiley, New York, 1968; Mir, Moscow, 1973).
22. L. S. Berman, I. V. Grekhov, L. S. Kostina, *et al.*, Pis’ma Zh. Tekh. Fiz. **25**, 75 (1999) [Tech. Phys. Lett. **25** (1), 32 (1999)].
23. I. V. Grekhov, T. S. Argunova, L. S. Berman, *et al.*, Pis’ma Zh. Tekh. Fiz. **22** (23), 14 (1996) [Tech. Phys. Lett. **22**, 956 (1996)].
24. L. S. Berman, M. G. Tolstobrov, and A. D. Remenyuk, Preprint No. 974 FTI (Ioffe Physicotechnical Institute, Russian Academy of Sciences, St. Petersburg, 1985).

Translated by A. Spitsyn

Semiconductors, Vol. 34, No. 7, 2000, pp. 790–793. Translated from Fizika i Tekhnika Poluprovodnikov, Vol. 34, No. 7, 2000, pp. 818–821.
Original Russian Text Copyright © 2000 by Nikolaev, V. Rud', Yu. Rud', Terukov.

SEMICONDUCTOR STRUCTURES, INTERFACES, AND SURFACES

Polarization Photosensitivity of *a*-Si:H/*c*-Si Heterojunctions

Yu. A. Nikolaev*, V. Yu. Rud', Yu. V. Rud'*, and E. I. Terukov***
** Ioffe Physicotechnical Institute, Russian Academy of Sciences, ul. Politekhnicheskaya 26,*
St. Petersburg, 194021 Russia
*** St. Petersburg State Technical University, ul. Politekhnicheskaya 29, St. Petersburg, 195251 Russia*

Submitted January 18, 2000; accepted for publication January 20, 2000

Abstract—The photosensitivity of heterojunctions formed by depositing thin amorphous films on silicon crystalline substrates is investigated. It is found that heterojunctions exhibit polarization photosensitivity, which is observed at an oblique incidence of the linearly polarized radiation on their receiving plane. The induced photopleochroism of heterojunctions increases quadratically with an increase in the angle of incidence θ and reaches 60% for θ = 80°. It is concluded that the heterojunctions obtained can be used as the broadband photodetectors of the linearly polarized radiation. © *2000 MAIK "Nauka/Interperiodica".*

The high cost of solar cells is the main obstacle to achieving the wide use of photovoltaic electrical power [1]. The development of technologies of thin film *a*-Si:H and polycrystalline silicon, as well as the fabrication of highly efficient solar cells on their basis, offer some hope for a solution to this problem [2–5]. The process of the photoconversion of the solar radiation in the amorphous silicon (*a*-Si:H)/(crystalline silicon) (*c*-Si) heterojunctions (HJs) with a maximum efficiency of up to 18% was investigated in the studies cited above. Our report is devoted to the first investigations of polarization photosensitivity of the *a*-Si:H/*c*-Si HJs. The possibility of applying them in a new field for major semiconductor material in electronics is demonstrated.

HJs were fabricated by depositing *a*-Si:H films on the polished surface of uniformly boron-doped Si(100) wafers, which had a resistivity of $\rho \cong 7.5\ \Omega$ cm at T = 300 K. The *a*-Si:H films of up to 1 μm thick were deposited on the *c*-Si substrates at 230°C using the method of RF glow discharge. The *a*-Si:H films were of *n*-type conduction with $\rho \cong 10^7\ \Omega$ cm at T = 300 K. The typical *c*-Si substrate dimensions were ~10 × 10 × 0.3 mm. The outside surface of the *a*-Si:H film was specular, and the films exhibited a good adhesion to the *c*-Si surface.

The typical steady-state current–voltage (*I*–*V*) characteristic for one of the HJs obtained is shown in Fig. 1. The *c*-Si/*a*-Si:H HJ, as follows from Fig. 1, is a typical rectifying one. The forward direction always corresponds to the positive voltage at the *c*-Si substrate. For forward bias voltages $U > 3$ V, the steady-state *I*–*V* characteristic is governed by the relationship

$$I = \frac{U - U_0}{R_0}, \qquad (1)$$

where the residual resistance $R_0 \cong (0.3–10) \times 10^6\ \Omega$ for various structures at the cutoff voltages of $U_0 \cong 2–2.8$ V. The reverse current follows the power law $I \sim U^{0.8}$. For the reverse biases $U \approx 5$ V, the reverse current in the HJs studied was on the order of $\sim 10^{-7}$ A.

The photovoltaic effect in the HJs obtained is dominant under their illumination from the *a*-Si:H wide-gap film side. The negative charge of this film is independent of the spot of incidence of the light probe on the structure surface and thus corresponds to the rectifying direction. The maximum voltage photosensitivity of the heterostructures obtained reaches ~60 V/W, while the current photosensitivity is ~5 μA/W at 300 K.

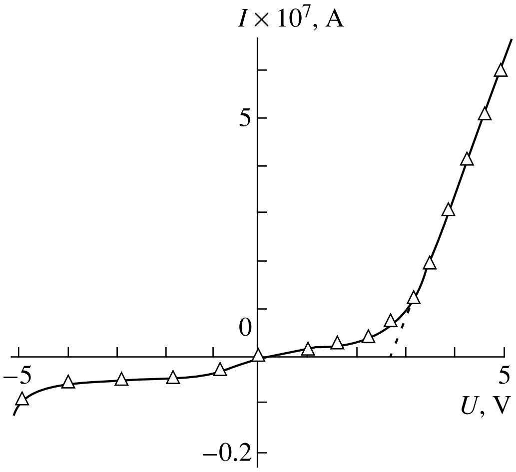

Fig. 1. Steady-state *I*–*V* characteristic of the *a*-Si:H/*c*-Si HJ at T = 300 K. Sample 2, the forward direction corresponds to the negative polarity of the external bias at the *a*-Si:H film.

The typical spectral dependences of the relative quantum efficiency of photovoltaic conversion η for one of the HJs are shown in Fig. 2. Once the HJ is illuminated from the *a*-Si:H side, the typical photosensitivity spectra are broadband. The maximum photosensitivity is realized in the photon energy range of 1.3–1.6 eV, and the full width at half-maximum of the η spectral band $\delta_{1/2} \cong 700$–720 meV. The long-wavelength edge of photosensitivity for these HJs is independent of the light-detection configuration (Fig. 2, curves *1*, *2*) and is caused by band-to-band optical transitions in *c*-Si. According to the character of band-to-band transitions in *c*-Si, the long-wavelength edge η is described by a straight line in the $(\eta h\omega)^{1/2}$–$h\omega$ coordinates. The extrapolation of this dependence to zero energy ($h\omega \longrightarrow 0$) yields a value (Fig. 3) that correlates with the band gap for *c*-Si [6].

The HJ illumination from the *c*-Si side causes the spectral band of photosensitivity to narrow (Fig. 2, curve *2*). As a result, $\delta_{1/2} \cong 160$ meV and decreases with an increase in the substrate thickness owing to the fact that the influence of optical absorption in the substrate becomes more pronounced. The cause of the short-wavelength decay of η is the same in the case of the HJ illumination from the wide-gap material side. In this case, a decrease in the HJ photosensitivity for $h\omega >$ 1.7 eV depends on optical losses in the *a*-Si:H film. In general, the broadband character of the photosensitivity of the *a*-Si:H/*c*-Si HJ under illumination from the wide-gap material side demonstrates the attainment of the window effect for incident radiation. This indicates that the *c*-Si/*a*-Si:H heteroboundary is sufficiently perfect in relation to the recombination processes is obtained.

The HJs obtained were investigated under illumination with the linearly polarized radiation along the normal to the receiving plane. It was demonstrated that no polarization sensitivity was observed for these HJs and, consequently, the natural photopleochroism was absent [7]. This circumstance is in accordance with the isotropic character of optical processes in *a*-Si:H and *c*-Si.

As soon as the angle of incidence θ of the linearly polarized radiation on the receiving plane diverges from 0°, the short-circuit photocurrent i becomes dependent on the azimuth angle φ between the vector of the electric field **E** of the light wave and the plane of incidence (PI) of the radiation according to the law

$$i_\varphi = i^p \cos^2\varphi + i^s \sin^2\varphi, \qquad (2)$$

where i^p and i^s are the photocurrents at $\mathbf{E} \parallel$ PI and $\mathbf{E} \perp$ PI, respectively. These dependences are defined by the amplitude coefficients of the transmission of the light wave with different polarizations through the air/*a*-Si:H interface according to the Fresnel relationships [8]. The typical dependences of the photocurrents i^p and i^s on the angle of incidence on the *a*-Si:H receiving plane of one of the HJs for a fixed energy of incident photons, which corresponds to the photosensitiv-

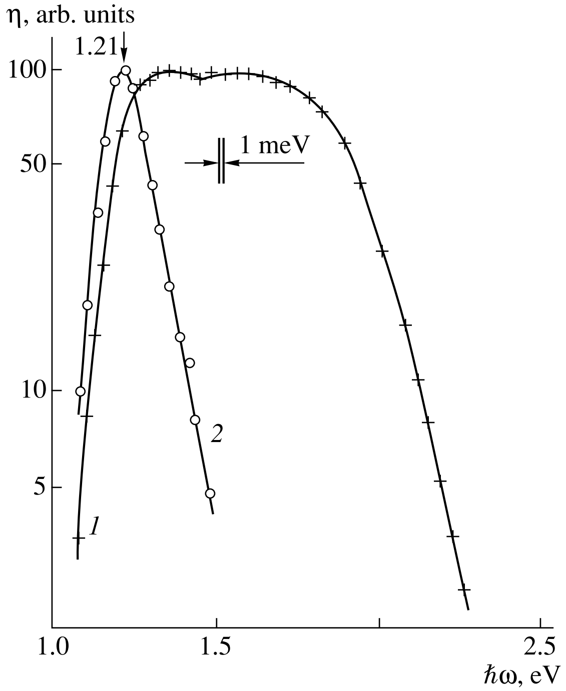

Fig. 2. Spectral dependences of the relative quantum efficiency of the photoconversion for the *a*-Si:H/*c*-Si HJ at T = 300 K. Sample 5, (*1*) illumination with the natural radiation from the *a*-Si:H film side, and (*2*) illumination from the *c*-Si substrate side.

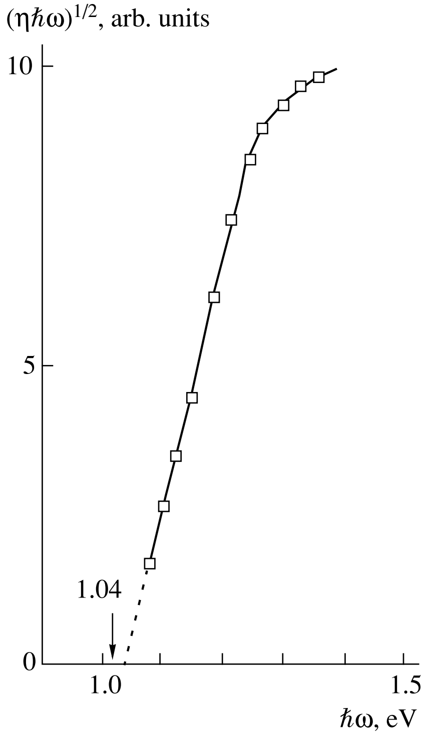

Fig. 3. Dependence $(\eta\hbar\omega)^{1/2} - \hbar\omega$ for the *a*-Si:H/*c*-Si HJ at T = 300 K, sample 5.

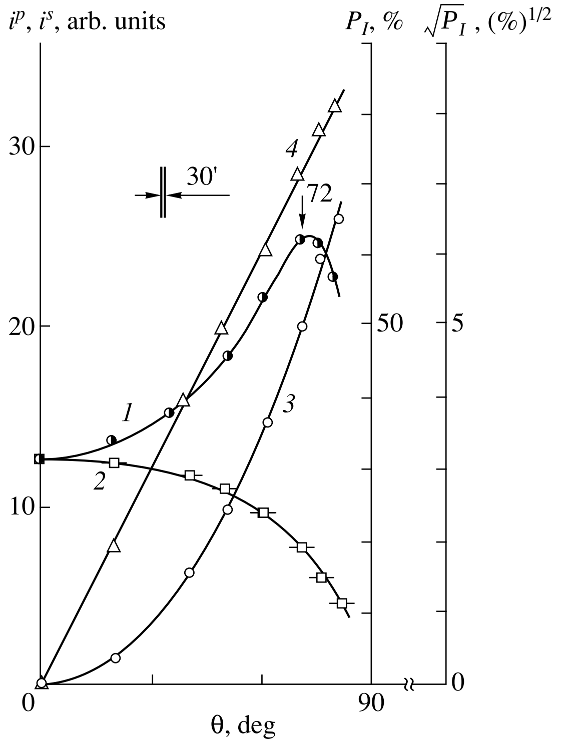

Fig. 4. Short-circuit currents ((*1*) i^p and (*2*) i^s) and the coefficient of the induced photopleochroism (*3*) $P_I = f(\theta)$ and (*4*) $\sqrt{P_I} = f(\theta)$ for the *a*-Si:H/*c*-Si HJ as a function of the angle of incidence of the linearly polarized radiation on the *a*-Si:H film side at $T = 300$ K.

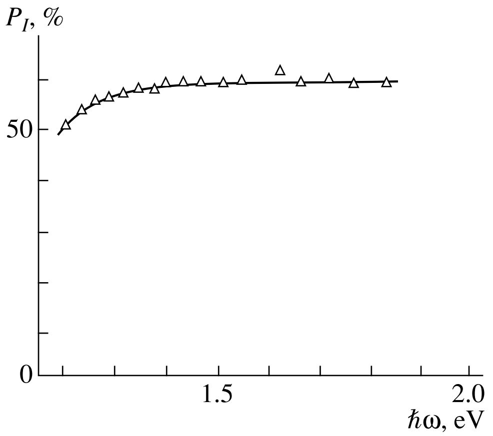

Fig. 5. Spectral dependence of the coefficient of the induced photopleochroism for the *a*-Si:H/*c*-Si HJ at $T = 300$ K. Sample 5, illumination from the *a*-Si:H film side, θ = 75°.

ity region of the HJ, are shown in Fig. 4 (curves *1*, *2*). The form of angular dependences of the photocurrents is retained over the entire region of the HJ photosensitivity. According to criteria [9], the *a*-Si:H films formed on *c*-Si can be characterized as sufficiently perfect films.

The coefficient of the induced pleochroism for the HJs investigated under illumination from the *a*-Si:H side in the entire region of their photosensitivity increases steadily with the angle of incidence according to the square law $\sqrt{P_I} \sim \theta$, which corresponds to the data reported in [9] (Fig. 4, curves *3*, *4*). It is important that the angular dependences of P_I in the entire photosensitivity range of the HJ always emerge from zero. This is typical of the systems with isotropic photosensitivity. For this reason, there is reason to believe that the polarization photosensitivity observed is related solely to anisotropy of optical processes on the air/*a*-Si:H boundary. The experimental dependences $P_I(\theta)$ (Fig. 4, curve *3*) also demonstrate that the coefficient of the induced photopleochroism can be smoothly controlled from 0 to 65% by increasing the angle of incidence of linearly polarized radiation from 0 to 80°. A similar curve $P_I(\theta)$ is observed also under the HJ illumination from the *c*-Si side. For this reason, the estimation of the refractive index from the experimental values of P_I for HJ illumination from the sides both of crystalline and of amorphous material yields equal values $n \approx 3.4$, which are in agreement with the known results [6].

The typical spectral dependence of the coefficient of the induced photopleochroism for one of the *a*-Si:H/*c*-Si HJs under illumination from the amorphous film side is presented in Fig. 5. In this case, the photosensitivity of these HJs is the highest and remains high in the energy range between the band gaps of the phases brought into contact. It can be seen from Fig. 5 that the induced photopleochroism coefficient in the region of the maximum photosensitivity of such HJs also remains high at a fixed angle of incidence and depends weakly on the wavelength. This experimental dependence $P_I(\hbar\omega)$ is close to the data for the *p*–*n* structure in *c*-Si [9]. This also indicates that the refractive indices for the *c*-Si substrates and *a*-Si:H films grown on them are almost the same.

Thus, the polarization studies of photosensitivity for the *a*-Si:H/*c*-Si HJ exposed to linearly polarized radiation were performed for the first time. The investigations demonstrated that the *a*-Si:H/*c*-Si HJs exhibit induced polarization photosensitivity and can find a new application, namely, as the wide-range photodetectors of linearly polarized radiation. The polarization photoabsorption spectroscopy can be used both for the approximate quality control of the *a*-Si:H films and for correction of their growth conditions.

ACKNOWLEDGMENTS

This work was partially supported by the International Association of Assistance for the promotion of cooperation with scientists from the New Independent States of the former Soviet Union (INTAS), grant no. 97-1910.

REFERENCES

1. *Polycrystalline Semiconductors V—Bulk Materials. Thin Films and Devices*, Ed. by J. H. Werner, H. P. Strunk, and H. W. Schock (Scitec., Uetikon-Zürich, 1999).
2. K. O. Kuda, H. Okamoto, and Y. Hamakawa, Jpn. J. Appl. Phys. **22**, L605 (1993).
3. W. Wang and K. Liao, Mater. Res. Soc. Symp. Proc. **70**, 399 (1986).
4. R. De Rosa, M. L. Grill, G. Sasikala, *et al.*, Solid State Phenom. **67**/**68**, 563 (1999).
5. R. M. Hausner, N. Jensen, R. B. Bergman, *et al.*, Solid State Phenom. **67**/**68**, 551 (1999).
6. *Physicochemical Properties of Semiconductor Materials: A Handbook* (Nauka, Moscow, 1978).
7. F. P. Kesamanly, V. Yu. Rud’, and Yu. V. Rud’, Fiz. Tekh. Poluprovodn. (St. Petersburg) **30**, 1921 (1996) [Semiconductors **30**, 1001 (1996)].
8. G. S. Landsberg, *Optics* (Fizmatgiz, Moscow, 1976).
9. F. P. Kesamanly, V. Yu. Rud’, and Yu. V. Rud’, Fiz. Tekh. Poluprovodn. (St. Petersburg) **33**, 513 (1999) [Semiconductors **33**, 483 (1999)].

Translated by N. Korovin

Semiconductors, Vol. 34, No. 7, 2000, pp. 794–798. Translated from Fizika i Tekhnika Poluprovodnikov, Vol. 34, No. 7, 2000, pp. 822–826.
Original Russian Text Copyright © 2000 by Ovsyuk, Vasil'ev, Mashukov.

SEMICONDUCTOR STRUCTURES, INTERFACES, AND SURFACES

Photosensitivity of In–SiO_2–$Cd_{0.28}Hg_{0.72}Te$ Structures with a Nontransparent Field Electrode

V. N. Ovsyuk, V. V. Vasil'ev, and Yu. P. Mashukov
Institute of Semiconductor Physics, Siberian Division, Russian Academy of Sciences,
pr. Akademika Lavrent'eva 13, Novosibirsk, 630090 Russia

Submitted January 18, 2000; accepted for publication January 27, 2000

Abstract—The photoeffect in a metal–insulator–semiconductor (MIS) structure that incorporated a $Cd_{0.28}Hg_{0.72}Te$ compound, a low-temperature pyrolitic SiO_2, and an In layer with a thickness of 500 nm and an area of 0.5×0.5 mm^2 was studied. For a MIS structure with a nontransparent field electrode, the observed photoeffect consists in variation in the capacitance and high-frequency electrical conductivity of the MIS structure; this photoeffect is caused by photocarriers that are formed outside the MIS structure and reach this structure either due to diffusion or along the surface channel. This happens if the MIS structure is in the state of inversion; in this case, an eddy electric current formed crosses the induced *p–n* junction and closes on itself at the MIS structure periphery. It is assumed that this current and the extra voltage across the *p–n* junction are related by the Shockley formula. The following parameters were evaluated: the coefficient β in the Shockley formula (β characterizes the nonideality of the *p–n* junction); the product R_0A of the resistance for zero bias by the area of the *p–n* junction; and the surface area ΔS of collection of the charge carriers. It was found that $\beta = 1.52$, $R_0A = 2.7 \times 10^5\ \Omega$ cm^2, and ΔS corresponds to a stripe that goes along the MIS-structure perimeter and has a width of 15 μm. The MIS structure studied is considered as a photodetector. *© 2000 MAIK “Nauka/Interperiodica”.*

INTRODUCTION

$Cd_xHg_{1-x}Te$ (MCT) compounds with various molar content *x* are widely used to produce photodetectors for the middle- and far-infrared (IR) regions of the spectrum [1]. The metal–insulator–semiconductor (MIS) structures based on this material are used as active components of photodetectors [2] and also as test elements in photodetector arrays [3]. In this paper, we report the results of studying the photosensitivity of MIS structures with a nontransparent electrode; the photosensitivity was observed under illumination of the periphery of the control electrode. It is shown that the results of such studies can be used to prognosticate the *p–n*-junction characteristics, which are defined by the parameters of the near-surface MCT layer, and also the coefficient of photoelectronic coupling between the neighboring photoelements in multielement detectors of IR radiation.

EXPERIMENTAL

We studied experimentally the MIS structures based on the bulk $Cd_{0.28}Hg_{0.72}Te$ material; for an insulator, we used a layer of low-temperature pyrolitic silicon dioxide (SiO_2), which was 700 Å thick and was grown at the substrate temperature of 100°C. The control electrodes with an area of 0.5×0.5 mm^2 and thickness of 5000 Å were formed by vacuum evaporation of In. We measured the capacitance *C* and the dielectric-loss angle δ of these structures either in the dark or under irradiation with light of various intensities. The capacitance–voltage (*C–V*) characteristics and the dependences $\delta(V)$ were measured at the test-signal frequency of 500 kHz and the frequency of the sawtooth voltage sweep of 5×10^{-3} Hz. The temperature of the sample during measurements was 80 K. A specially calibrated, miniature incandescent lamp, which had a tungsten filament and was rated at 6.5 V and 0.34 A, was used as a radiation source; this lamp was mounted inside a cryostat in the immediate vicinity of the sample, and a focusing system was not used. The irradiance E_e and the corresponding flux of photons incident on the sample were determined allowing for (i) the dependences of the emissivity of tungsten on the wavelength and temperature [4] and (ii) absorption of radiation by the glass envelope of the lamp. We took into account the flux of photons that fell within the spectral region of absorption in the sample ($\lambda < 6$ μm). The irradiance E_e was varied by three orders of magnitude by varying either the heating of the lamp filament or the distance between the lamp and the sample (14–50 mm). The temperature of the filament was determined from its resistance.

RESULTS

Figure 1a shows typical *C–V* characteristics. It can be seen that they are of the high-frequency type, which is characteristic of MCT of the given composition at the chosen test-signal frequency; there is no hysteresis in the used range of sweep voltages. The state of the sur-

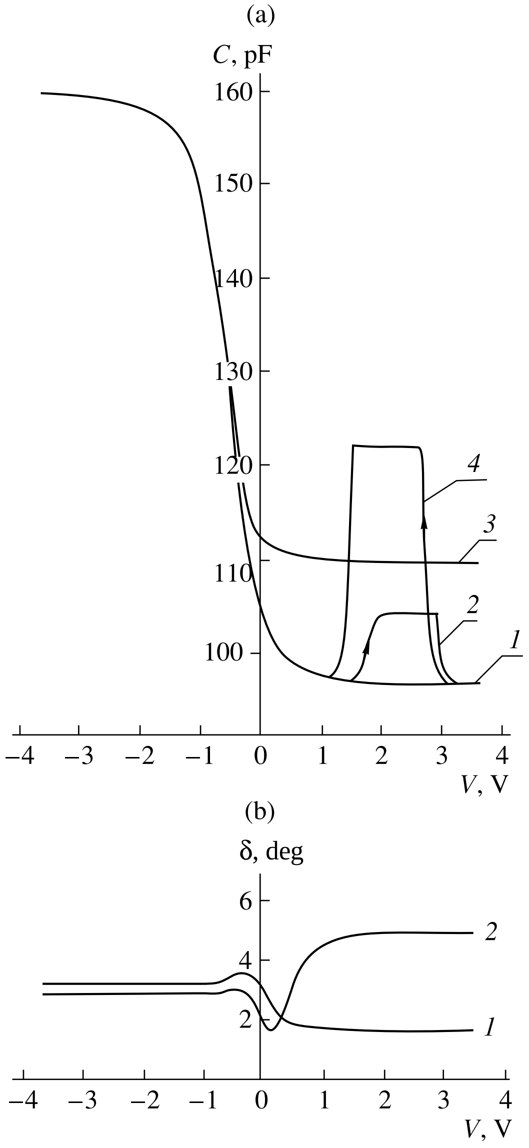

Fig. 1. (a) Capacitance–voltage (C–V) characteristics of a $Cd_{0.28}Hg_{0.72}Te$-based MIS structure with a nontransparent metal electrode; the characteristics were measured (*1*) without illumination and under illumination with a tungsten-filament incandescent lamp placed at a distance of 14 mm from the sample, with the voltage at and the current through the lamp being equal to (*2*) 0.52 V and 97 mA; (*3*) 2.48 V and 195 mA; and (*4*) 5.27 V and 296 mA. In the case of (*3*), the lamp was turned on all the time; curves (*2*) and (*4*) corresponds to the case where the lamp was turned on for a certain time. The arrows indicate the direction of measurements of the C–V characteristics. (b) The $\delta(V)$ curves measured (*1*) without illumination and (*2*) under illumination for the voltage of 2.82 V and at a current of 212 mA through the lamp placed at a distance of 14 mm from the sample. δ is the dielectric-loss angle of the MIS structure and is measured in degrees of arc.

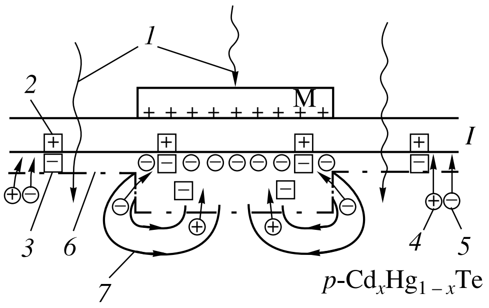

Fig. 2. Schematic diagram illustrating the origination of the photoeffect in a nontransparent MIS structure. M stands for metal and *I* stands for insulator. We also indicate (*1*) photons, (*2*) positive charges in the insulator, (*3*) acceptors, (*4*) holes, (*5*) electrons, (*6*) the boundary of the space-charge region, and (*7*) the electric-current lines.

face for zero bias corresponded to slight inversion. The illumination-dependent characteristics were typically measured under the conditions of switching on the lamp for a certain time. In this case, the transient processes distinct in Fig. 1a were defined by the time needed to heat up the filament.

Figure 1b shows the bias dependence of the quantity δ that characterizes the high-frequency electrical conductance; in the case of inversion, δ increases when the illumination is switched on.

We now consider a scheme of the processes that occur under illumination of a MIS structure that has a nontransparent field electrode and is in the state of inversion (Fig. 2). Photoelectrons diffusing in the direction of the induced *p*–*n* junction are pulled in from the periphery by the *p*–*n*-junction field and increase the concentration of mobile inversion-inducing electrons, which are located in the vicinity of the semiconductor–insulator boundary. In this case, the width of the space-charge region decreases, the height of the potential barrier is reduced, and the barrier capacitance (and, correspondingly, the structure capacitance) increases. The majority-carrier current appearing due to a decrease in the potential-barrier height compensates for the photoelectron current. Since the majority-carrier current crosses the induced *p*–*n* junction over the entire area of the MIS structure, whereas the photoelectrons arrive at the structure only from the periphery, an eddy electric current originates; this current flows from the bulk to the surface in the middle part of the MIS structure and flows in the opposite direction at the periphery. The magnitude of this current is equal to that of the photoelectron current.

There is no spatial separation of the electron and hole fluxes that cross the *p*–*n* junction in conventional *p*–*n*-junction photodetectors operating in the photovoltage mode or in the MIS photodetectors with a transparent field electrode in the case of illumination uniform over the entire area; as a result, an eddy electric current is not observed.

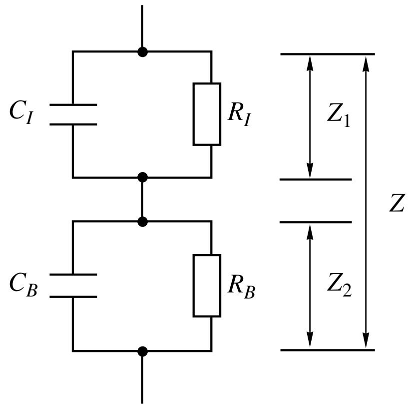

Fig. 3. Equivalent circuit of a MIS structure.

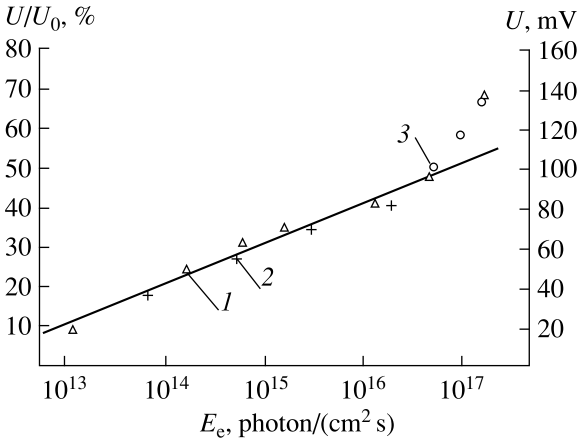

Fig. 4. The additional voltage across the barrier as a function of illuminance of the sample. Different experimental points correspond to the distances between the lamp and the sample of (*1*) 14, (*2*) 17, and (*3*) 38 mm. The theoretical dependence (shown by the solid line) was calculated on the basis of the Shockley equation (1).

CALCULATION PROCEDURE AND DISCUSSION OF THE RESULTS

Since the current inducing the voltage drop flows over the inversion layer, the potential of this layer and, along with it, the potential-barrier height depend on the longitudinal coordinate. However, in the case under consideration, this dependence may be disregarded, because the resistance of the eddy-current spreading over the inversion layer is much lower than that of the barrier. The same conclusion can be drawn on the basis of the concept reported in [5]; in fact, the longitudinal-diffusion length for the excess carrier in the inversion layer is found to be much larger than the MIS-structure size, and, thus, the longitudinal variation of potential in the inversion layer is insignificant.

Thus, the current through the barrier flows with uniform density and may be calculated using the conventional Shockley formula

$$I = I_s\left(e^{\frac{qU}{\beta kT}} - 1\right), \tag{1}$$

where q is the elementary charge, U is the external voltage applied to the barrier, I_s is the saturation current, kT is the electron thermal energy, and β is the parameter that characterizes the nonideality of a p–n junction.

The voltage U can be determined using the following relation between the capacitance of the p–n junction (the barrier) C_B and the barrier height:

$$C_B = \sqrt{\frac{qN_A\varepsilon\varepsilon_0}{2U_B}}. \tag{2}$$

Here, N_A is the acceptor concentration and U_B is the barrier height expressed in volts.

Taking into account that

$$U_B = U_0 - U, \tag{3}$$

where U_0 is the initial or dark barrier height, we can obtain the following expression:

$$\frac{U}{U_0} = 1 - \left(\frac{C_0}{C_B}\right)^2. \tag{4}$$

Here, C_0 is the dark barrier capacitance and C_B is the corresponding capacitance under illumination.

In order to separate the barrier parameters from the MIS-structure parameters, we used the simplest generalized equivalent circuit of a MIS structure (Fig. 3). Calculations were performed using the relations

$$Z_2 = Z - Z_1, \tag{5}$$

$$\frac{1}{\omega C_B} = \frac{|Z_2|^2}{\operatorname{Im} Z_2}, \tag{6}$$

$$R_B = \frac{|Z_2|^2}{\operatorname{Re} Z_2}, \tag{7}$$

where $\operatorname{Re} Z_2$ and $\operatorname{Im} Z_2$ are the real and imaginary parts of the complex barrier impedance Z_2, respectively.

Determining in such a manner the value of U, we can plot the dependence of U on $\log E_e$ (Fig. 4). The quantity U is expressed either in % of U_0 or in mV. In the latter case, it was assumed that $U_0 = \frac{\Delta W}{q} = 200$ mV, where ΔW is the band gap of the semiconductor material.

It can be seen that the dependence under consideration features an extended linear portion, which is consistent with expression (1) in which the quantity I is proportional to the illuminance. The slope of this linear portion allows us to determine the parameter β, which is found to be equal to 1.52.

Knowledge of the value of β makes it possible to assess the intensity of generation–recombination processes within the *p–n* junction. Apparently, we are dealing with the case intermediate between (i) $\beta = 1$ (the mobile charge carriers surmount an abrupt barrier with the height ΔW) and (ii) $\beta = 2$ (the barrier of the type present in a *p–i–n* structure (the majority carriers, both electrons and holes, surmount the barrier with the height of $\Delta W/2$ before arriving at the *i*-region where their recombination occurs)).

As the illuminance increases, the barrier capacitance increases and the barrier conductance increases as well (R_B decreases), as indicated by an increase in δ of the MIS structure. We now determine the value of R_B for the illuminance corresponding to the data in Fig. 1b ($E_e = 5.75 \times 10^{16}$ cm^{-2} s^{-1}). We determine the parameters of the insulator $C_1 = 160$ pF and $\delta_1 = 3.2°$ from the left-hand portions of the $C(V)$ and $\delta(V)$ curves that correspond to the enhancement mode of the MIS structure. Then, using the values of C and δ for the MIS structure in the inversion mode ($C = 111$ pF and $\delta = 4.9°$) and formulas (5)–(7) and (4), we obtain $R_B = 6 \times 10^3\ \Omega$ and $U = 103$ mV. If we use the dark values $C = 97$ pF and $\delta = 1.7°$ and apply the same method, we find that $R_B = \infty$. This means that there are no mechanisms introducing appreciable dielectric losses in the barrier at the test frequency of 500 kHz and, in addition, the initial dark barrier resistance R_0 is so large that its shunting effect on C_B is negligibly small.

Thus, the obtained value of R_B represents the barrier resistance under the forward bias of 103 mV. Using the barrier-resistance dependence on the bias

$$R_B = R_0 e^{-\frac{qU}{\beta kT}}, \tag{8}$$

which follows from (1) under the condition that $\exp(qU/\beta kT) \gg 1$, we can determine the values of R_0 and R_0A (A is the area of the *p–n* junction); the quantity R_0A is an important characteristic of the *p–n* junction. As a result, we have $R_0 = 1.1 \times 10^8\ \Omega$ and $R_0A = 2.7 \times 10^5\ \Omega$ cm^2. The latter value is among the highest ever obtained for conventional *p–n* junctions based on MCT of the corresponding composition [6].

Both R_0A and the value of β obtained above characterize the properties of the near-surface region of the MCT sample; in turn, these properties are defined to a large extent by chemical treatment of the surface and subsequent operation of depositing the insulator.

The data obtained make it possible to estimate the area ΔS, from which the photocarriers are collected, or the effective diffusion length of the photocarriers. First of all, combining (1) and (8), we derive the expression for the photocurrent in the form of

$$I = \frac{\beta kT}{qR_B}. \tag{9}$$

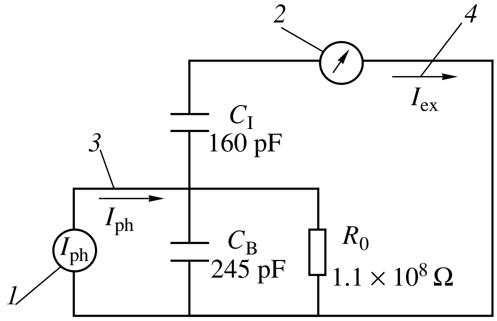

Fig. 5. Equivalent circuit of a MIS photodetector: (*1*) the photocurrent generator, (*2*) the current meter, (*3*) photocurrent of the photocurrent generator, and (*4*) the photocurrent in the external circuit.

On the other hand, if the quantum yield is assumed to be equal to unity, the photocurrent obtained from the area ΔS is given by

$$I = qE_e(1-\rho)\Delta S, \tag{10}$$

where the multiplier $1 - \rho$ accounts for the losses by reflection. Using the above values of R_B, β, and E_e and assuming that $\rho = 0.35$, we use (9) and (10) to obtain $\Delta S = 3 \times 10^{-4}$ cm^2. This corresponds to a stripe that is arranged along the perimeter of the MIS structure and has a width of $\Delta l = 15$ µm. This value of Δl is smaller than the bulk-diffusion length for electrons (50 µm), which can be attributed to a restriction imposed on the diffusion length by the surface recombination of photoelectrons.

The obtained value of Δl confirms the conclusion, which follows from the *C–V* measurements, that the region outside the MIS structure is in the state of depletion, rather than in the states of enrichment or inversion. In the case of enrichment, Δl would be close to the diffusion length L_D, whereas, in the case of inversion, Δl could have large values that were in multifold excess of the value of L_D; the latter effect is caused by the fact that the photocarriers could be pulled from large distances to the entire inversion-state surface and then drained into the MIS-structure potential well along the surface channel.

For illuminance higher than 5×10^{16} cm^{-2} s^{-1}, a steeper increase in the voltage across the *p–n* junction with increasing $\log E_e$ is observed (Fig. 4). This effect can be caused by a decrease in the bulk-recombination rate for high injection levels [7].

It makes sense to evaluate the parameters of the given MIS structure as a photodetector. We compare its parameters with those of a photodetector based on a conventional *p–n* junction. Since the resistance R_0 of the induced *p–n* junction in our case is fairly large, we can consider its operation in the mode of the current generator. The equivalent circuit then takes the form shown in Fig. 5.

We express the current I_{ex} measured in the external circuit in terms of I_{ph}; as a result, we have

$$I_{\mathrm{ex}} = I_{\mathrm{ph}}\frac{j2\pi f C_I R_0}{1 + j2\pi f R_0(C_I + C_B)} \approx I_{\mathrm{ph}}\frac{C_I}{C_I + C_B}, \qquad (11)$$

where f is the modulation frequency of light. The approximate equality is valid at frequencies above a certain limiting frequency f_b, which is defined by the time constant $R_0(C_I + C_B)$ and is equal to 4 Hz. The ratio of photosignals coming from the two photodetectors that we compare is given by $\frac{\Delta S}{A + \Delta S}\frac{C_I}{C_I + C_B}$. For a sufficiently small area of the junction and for a small insulator thickness, this ratio is close to unity. We may expect that, due to a simpler production technology and better parameters of the induced *p–n* junction compared to the conventional *p–n* junction, a photodetector based on the MIS structure would be found to be quite competitive.

We estimated the photosensitivity B (expressed in A/W) for the radiation wavelength of 5 μm and the normalized detectivity D^* for the MIS structure under consideration as a photodetector; we used the Nyquist formula for the noise current of the current generator

$$I_n = \sqrt{\frac{4kT\Delta f R}{|Z|^2}}, \qquad (12)$$

where Z is the complex impedance of the photodetector and R is its real component. As a result, we obtained $B = 0.12$ A/W and $D^* = 2.3 \times 10^{12}$ cm Hz$^{1/2}$/W. The area of the field electrode was assumed to be equal to the photodetector area.

CONCLUSION

Illumination of a MIS structure that has a nontransparent control electrode and is in the state of inversion makes it possible to (i) determine the parameters of the induced *p–n* junction such as the product of the resistance under zero bias by the area R_0A and the nonideality factor β of the *p–n* junction (these quantities characterize the suitability of the semiconductor material for producing the multielement photodetectors based on this material) and (ii) evaluate the longitudinal diffusion length for the minority charge carriers, which allows one to assess the coefficient of photoelectronic coupling between neighboring photoelements.

ACKNOWLEDGMENTS

We thank A.F. Kravchenko and D.G. Esaev for their interest in this study and a number of valuable comments.

REFERENCES

1. A. Rogalski and J. Piotrovski, Prog. Quantum Electron. **12**, 87 (1988).
2. R. A. Charman, S. R. Bollero, A. Simmons, *et al.*, IEEE Trans. Electron Devices **ED-27**, 134 (1980).
3. V. V. Vasilyev, D. G. Esaev, A. G. Klimenko, *et al.*, Proc. SPIE **3061**, 956 (1997).
4. *Physical Quantities: A Reference Book*, Ed. by I. S. Grigor’ev and E. Z. Meĭlikhov (Énergoizdat, Moscow, 1991), p. 192.
5. V. N. Ovsyuk, *Electronic Processes in Semiconductors with Space-Charge Regions* (Nauka, Novosibirsk, 1984).
6. I. M. Baker, M. D. Jenner, J. Parsons, *et al.*, in *Proceedings of the International Conference on Advanced Infrared Detectors and Systems, London, 1983*, p. 12.
7. S. M. Ryvkin, *Photoelectric Effects in Semiconductors* (Fizmatgiz, Moscow, 1963; Consultants Bureau, New York, 1964).

Translated by A. Spitsyn

Semiconductors, Vol. 34, No. 7, 2000, pp. 799–802. Translated from Fizika i Tekhnika Poluprovodnikov, Vol. 34, No. 7, 2000, pp. 827–830.
Original Russian Text Copyright © 2000 by Galkin, Goroshko, Konchenko, Zakharova, Krivoshchapov.

SEMICONDUCTOR STRUCTURES, INTERFACES, AND SURFACES

The Hall Effect in Fe Submonolayer Systems on *n*- and *p*-type Si(111)

N. G. Galkin, D. L. Goroshko*, A. V. Konchenko**, E. S. Zakharova*, and S. Ts. Krivoshchapov***

** Institute for Automation and Control Processes, Far East Division, Russian Academy of Sciences,*
ul. Radio 5, Vladivostok, 664041 Russia
*** Far East State Technical University, Vladivostok, 690069 Russia*
e-mail: galkin@iacp.vl.ru

Submitted December 7, 1999; accepted for publication February 7, 2000

Abstract—The *in situ* Hall effect measurements at room temperature showed that formation of the atomically clean Si(111) 7 × 7 surface as a result of high-temperature annealing (T = 1250°C, t = 120–180 s) of *n*-Si reverses the majority carrier sign at the surface, and a hole-enriched layer is formed at the *p*-Si surface. The different dynamics of Hall and resistivity voltage variations within the first monolayer of iron adsorbed onto substrates with a *p*–*n* junction or with a hole-enriched layer is not related to conduction over the adsorbed layer. Conduction in the Fe layer of thickness exceeding three monolayers is caused in both cases by the transport of electrons with densities 2×10^{13}–2×10^{14} cm^{-2} and mobilities 65–90 cm^2/(V s). *© 2000 MAIK “Nauka/Interperiodica”.*

The transport properties of two-dimensional materials on monocrystalline semiconductor substrates in an ultrahigh vacuum represent a topical problem in the physics of semiconductors. At the same time, the *in situ* Hall effect measurements [1, 2] in an ultrahigh vacuum are not currently a conventional technique for studying the transport properties of ultrathin films and adsorbed layers on silicon substrates. This is related to technical problems in achieving fairly high magnetic fields in a vacuum chamber, as well as to the fact that the measurements are time-consuming. Low (liquid-helium) temperatures are conventionally chosen when measuring the electrical conductivity [3] and mobility [1, 2] *in situ* to freeze out the carriers in silicon substrates and to solve the problem of shunting ultrathin films by a substrate. When measuring the conductivity at room temperature, another method is widely used, allowing one to neglect the substrate shunting action. This method consists in using silicon with a resistivity above 500 Ω cm [4]. However, as far as we know, only one team [5–7] attempted to measure the Hall and resistivity voltage on atomically clean silicon with an initial resistivity of 5–20 Ω cm at room temperature and during the adsorption of Ag, Au, and In atoms. Unfortunately, these data were not interpreted in terms of the majority carrier mobility, which was explained by the nonperpendicularity of the magnetic field lines of force to a sample and a wide scatter of experimental data.

We have built and put into operation [8] an ultrahigh-vacuum setup with a built-in Hall attachment with a pressed six-point probe that was powered by ac, operated at a bipolar pulsed magnetic field, and was controlled by a computer. This probe allows one to measure a voltage proportional to the Hall voltage (U_H) and the resistivity voltage (U_ρ) on an atomically clean silicon surface and after adsorption of metals at various temperatures with an error of measurements less than 1.5%. This allows for accurate measurements of the Hall parameter variations during layer-by-layer metal deposition onto silicon in submonolayer and monolayer thickness ranges within a so-called “dead” layer, that is, when the adsorbed layer is not conducting. In this case, the conductivity can vary in the space-charge region of the silicon substrate. Furthermore, the recharging of surface states formed as a result of the interaction between metal atoms and the silicon lattice can contribute to the conductivity [5]. Such variations can be detected and taken into account only by Hall measurements in an ultrahigh vacuum. However, comparative Hall measurements *in situ* on silicon substrates with different conduction types before and after formation of an atomically clean surface have not been carried out previously. The results of Hall measurements *in situ* for submonolayer iron coatings at the Si(111) 7 × 7 surface are also lacking, although the initial growth stages of iron and its silicides on silicon attract much attention [9–11] from fundamental and applied standpoints.

This work is aimed at studying the Hall parameter variations in *n*- and *p*-Si substrates when forming the atomically clean Si(111) 7 × 7 surface in ultrahigh vacuum, as well as at studying the conduction in samples in the case of adsorption of submonolayer and monolayer Fe coatings at Si(111) 7 × 7 at room temperature.

An ultrahigh-vacuum chamber with an operating pressure of 5×10^{-10} Torr is equipped with a low-energy

Table

Substrate state	Majority carriers	ρ_{eff}, Ω cm	μ_{eff}, $\mathrm{cm}^2/(\mathrm{V\ s})$	n_{eff}, cm^{-3}	σ_s, S	R_{H}^{s}, $\mathrm{cm}^2\ \mathrm{C}^{-1}$	μ_s, $\mathrm{cm}^2/(\mathrm{V\ s})$	n_s, cm^{-2}
n-Si(111) (certificate)	Electrons	4.5	1450	1×10^{15}	–	–	–	–
n-Si(111) with oxide	Electrons	5.3	1420	8.2×10^{14}	–	–	–	–
n-Si(111) 7 × 7	Holes	26.3	90	2.6×10^{15}	–	–	–	–
$d_{\mathrm{Fe}} = 0.1$ nm	Electrons	–	–	–	1.3×10^{-3}	-2.2×10^{5}	293	2.9×10^{13}
$d_{\mathrm{Fe}} = 0.2$ nm	Electrons	–	–	–	1.9×10^{-3}	-6.3×10^{4}	117	9.9×10^{13}
$d_{\mathrm{Fe}} = 0.3$ nm	Electrons	–	–	–	2.3×10^{-3}	-2.8×10^{4}	65	2.2×10^{14}
p-Si(111) (certificate)	Holes	10	550	8×10^{14}	–	–	–	–
p-Si(111) 7 × 7	Holes	5.4	330	3.9×10^{15}	–	–	–	–
$d_{\mathrm{Fe}} = 0.25$ nm	Electrons	–	–	–	3.4×10^{-4}	-5.2×10^{5}	167	1.25×10^{13}
$d_{\mathrm{Fe}} = 0.3$ nm	Electrons	–	–	–	3.8×10^{-4}	-2.4×10^{5}	90	2.6×10^{13}

electron diffraction (LEED) analyzer, an evaporation unit with three sources (Cr, Fe, and Si) and with a shield cooled by liquid nitrogen, a Hall attachment with a computerized measuring system [8], a sample holder with direct and indirect heating systems, and a quartz thickness gage. We used *n*- and *p*-type Si(111) substrates ($17 \times 5.8 \times 3$ mm^3) with $\rho = 4.5$ and 10 Ω cm, respectively. The samples were chemically cleaned before placing them into the vacuum chamber. Surface oxide and residual carbon contaminations were removed by high-temperature annealing at a temperature of 1250°C for 120–180 s. The sample temperature within 350—1250°C was determined from conductivity measurements and by an optical pyrometer. The Fe deposition rate was $(6–8) \times 10^{-4}$ nm/s.

Hall measurements *in situ* were first carried out at the *n*-type Si(111) surface coated with native oxide. Ranges of sample currents and magnetic fields, for which observed dependences of the Hall voltage were linear, were determined. The measured Hall voltage was negative, which confirms the fact that majority carriers are electrons with parameters close to those in the substrate certificate (see table). After forming the Si(111) 7 × 7 atomically clean surface, the Hall voltage sign reversed, its amplitude decreased, and the resistivity increased drastically (see table). This points to the formation of a *p*–*n* junction in the substrate subsurface region. Electrons in the *n*-layer compensate for the contribution of *p*-layer holes to the Hall voltage, which reduces the net Hall voltage amplitude [12]. As is known, high-temperature annealing forms the *p*-layer on either side of an *n*-type uniformly doped sample [13]. Hall measurements carried out on one side of such a substrate do not allow the determination of *p*-layer parameters. Therefore, to simplify calculations, we introduced the effective parameters n_{eff}, μ_{eff}, and σ_{eff} of the silicon substrate, calculated from measured data on the assumption of uniform doping. The calculated Hall parameters of the effective substrate showed a drastic mobility decrease for majority carriers from 1420 to 90 cm^2/(V s) and their type change (see table). When depositing a metal or semiconductor layer with a certain conductivity onto such a substrate, the conventional two-layer model [2] can be used to calculate the deposited layer Hall parameters as

$$U_{\mathrm{Htot}} = I_0 B_z K_R \times (\sigma_1^2 R_{\mathrm{H1}} d_1 - \sigma_2^2 R_{\mathrm{H2}} d_2)/(\sigma_1 d_1 + \sigma_2 d_2), \qquad (1)$$

$$\sigma_{\mathrm{tot}} = (\sigma_1 d_1 + \sigma_2 d_2)/(d_1 + d_2), \qquad (2)$$

where I_0, B_z, and K_R are the sample current, magnetic induction, and shape factor, respectively. The electrical conductivity σ_1, Hall coefficient R_{H1}, and thickness d_1 characterize the Fe layer, whereas the values σ_2, R_{H2}, and d_2 correspond to the substrate with effective parameters.

We failed to carry out accurate measurements for the *p*-type Si(111) substrate with native oxide due to the fact that the pressed contacts were rectifying. However, the contacts became nonrectifying in the entire current range (5–40 μA) after high-temperature annealing and formation of the Si(111) 7 × 7 atomically clean surface. Calculated Hall parameters of the substrate slightly differed from the certificate data (see table), since the hole concentration increased in the silicon subsurface region [13]. Hence, the calculated Hall parameters can also be considered as effective for the *p*-Si substrate.

Figure 1 displays the dependences of the Hall (U_{H}) and resistivity (U_ρ) voltages on the thickness of the Fe layer formed at room temperature at the Si(111) 7 × 7 surface with an initial *n*-type substrate. Iron was deposited by portions of 0.005, 0.01, and 0.025 nm, depending on the deposited layer thickness. The measured Hall voltage sign changes from positive to negative in the submonolayer range below 0.025 nm (see Fig. 1). The Hall voltage magnitude is largest for $d_{\mathrm{Fe}} = 0.1$ nm and then rapidly decreases as the Fe-layer thickness

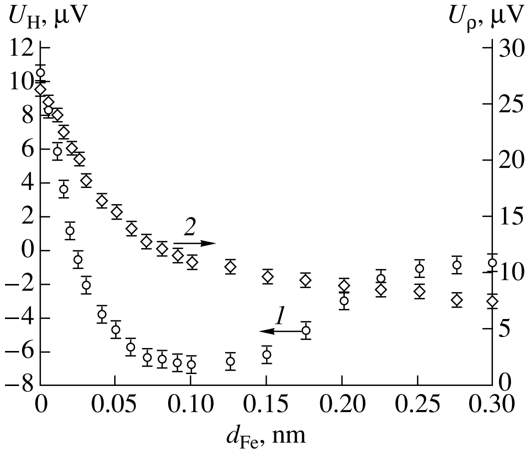

Fig. 1. Dependences of the Hall U_H (*1*) and resistivity U_ρ (*2*) voltages on the thickness d_{Fe} of the Fe layer deposited on the Si(111) 7 × 7 surface with an initial *n*-type substrate. The current through the sample was 30 µA and the magnetic induction was 0.016 T.

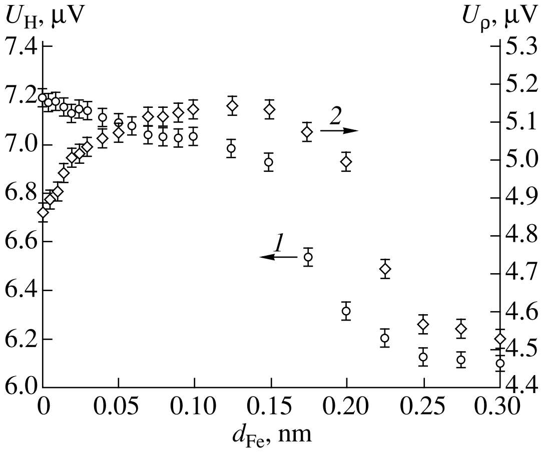

Fig. 2. Dependences of the Hall U_H (*1*) and resistivity U_ρ (*2*) voltages on the thickness d_{Fe} of the Fe layer deposited on the Si(111) 7 × 7 surface with an initial *p*-type substrate. The current through the sample was 30 µA and the magnetic induction was 0.016 T.

increases. The resistivity voltage initially decreases sharply (up to the thickness of $d_{Fe} = 0.05$ nm). Then the curve slope decreases at 0.1 nm and from this point on U_H remains virtually unchanged. According to the ion-scattering spectroscopy and scanning tunnel microscopy [10], Fe atoms diffuse under the first Si(111) substrate monolayer even at room temperature, pushing Si atoms to the surface. This disorders the Si(111) 7 × 7 surface superstructure. In our experiments, superreflections 7 × 7 disappeared at a Fe-layer thickness of 0.025 nm, while basic reflections 1 × 1 were retained to a thickness of 0.3 nm. According to the ultraviolet photoelectron spectroscopy data [10], metallic conduction was observed only after depositing more than three Fe monolayers (one monolayer corresponds to 0.083 nm) onto Si(111) 7 × 7. Hence, a sharp resistivity-voltage decrease in the submonolayer thickness range (0.01–0.06 nm, see Fig. 1) cannot be explained by conduction over the adsorbed Fe layer. As is known, Fe atoms in the Si lattice produce deep donor states in the Si forbidden band [14] with energies $E_v + 0.40$ eV and $E_c - 0.53$ eV. The Hall effect sign reversal and the measured conductivity increase in the submonolayer thickness range of the adsorbed Fe layers (see Fig. 1) can be reasonably explained only by donor surface states [5] formed and then charged due to interstitial iron atoms in the silicon lattice [10]. This should lead to pinning of the Fermi level by these atoms. In this case, as the Fe layer thickness increases, the silicon subsurface region is enriched in electrons that compensate rapidly for the contribution of the *p*-Si layer formed by high-temperature annealing to the Hall effect. As one Fe monolayer is deposited, electron accumulation due to charge exchange of surface states seems to cease. The adsorbed layer parameters calculated within the two-layer model are listed in the table. It is evident that, as the Fe-layer thickness grows from 0.1 to 0.3 nm, the density of majority carriers (electrons) increases from 2.9×10^{13} to 2.2×10^{14} cm^{-2}. However, their mobility drops from 293 to 65 cm^2/(V s), which abruptly reduces the contribution of electrons to the measured Hall voltage (Fig. 1). Hence, the conduction over the adsorbed Fe layer sets in at Fe coatings thicker than three monolayers and is maintained by electrons.

Figure 2 shows dependences of the Hall (U_H) and resistivity (U_ρ) voltages for Fe atom adsorption at room temperature at the Si(111) 7 × 7 surface with the *p*-type initial substrate. Iron was also deposited in variable steps of 0.005, 0.01, and 0.025 nm, depending on the deposited layer thickness. The observed pattern does not correlate at all with the Fe atom behavior on the initial *n*-Si substrate (see Fig. 1). The voltage U_ρ mainly varies for thicknesses of up to 0.15 nm, while the value U_H exhibits merely a slight tendency to decrease (see Fig. 2). There exists a resistivity-voltage maximum corresponding to a substrate resistivity growth approximately by 6% when the Fe-layer thickness is in the submonolayer range. The U_ρ growth was earlier observed only during gold and cesium deposition onto ordered Si(111) 5 × 2-Au and Si(111) $\sqrt{3} \times \sqrt{3}$-Au [5–7] superstructures but was not detected during gold, silver, and indium deposition onto Si(111) 7 × 7 [5]. The U_ρ maximum (Fig. 2) seems to be also related to the effect of pinning the Fermi level by donor surface states on the space-charge region conductivity. In this case, electrons from donor surface states merely partially compensate for the high concentration of holes from acceptor levels in the *p*-type substrate subsurface region; as a result, the measured layer resistivity increases. A further Fe-layer growth to 0.2 nm (thicker than two monolayers) and more leads to a rather sharp decrease in the

Hall and resistivity voltages (Fig. 2). The resistivity becomes lower than that of the sample with an atomically clean surface. The conduction over the adsorbed layer, as in the case of the *n*-type substrate, sets in at an Fe-layer thickness exceeding three monolayers. According to the calculated data (see table), the Fe-layer conduction is also maintained by electrons with a density of 2.5×10^{13} cm^{-2} and mobility of 90 cm^2/(V s). The simplified model of the effective substrate for conducting Fe layers adsorbed on *n*- and *p*-Si substrates yields almost the same basic Hall parameters. This indicates that the model is sufficiently correct and is applicable to calculations of transport properties of other metal layers adsorbed on atomically clean silicon surfaces from *in situ* Hall measurements at room temperature.

The above study of the Hall effect when forming the atomically clean Si(111) 7×7 surface shows that high-temperature annealing even at 1250°C produces a *p*–*n* junction built in the *n*-Si surface and reverses the Hall voltage sign, while the *p*-Si surface layer becomes enriched in holes. The study of Fe atom adsorption at substrates with a *p*–*n* junction and with the hole-enriched layer is indicative of the formation of donor surface states, whose recharging leads to different dynamics of changes in the Hall and resistivity voltages within the first monolayer. The Fe-layer conduction at thicknesses exceeding three monolayers is caused in both cases by the transport of electrons with densities of 2×10^{13}–2×10^{14} cm^{-2} and mobilities of 65–90 cm^2/(V s).

ACKNOWLEDGMENTS

We are grateful to V.G. Lifshits for his fruitful participation in discussions.

This work was supported by the Russian Foundation for Basic Research (project no. 99-02-16833), the Federal Program “Atomic Surface Structures (project no. 2.12.99), and the Program “Basic Research in Electronics and Radio Engineering” (project no. 98-3.1.11) of the Ministry of General and Professional Education.

REFERENCES

1. S. Neun, J. Bange, R. Schad, and M. Henzler, J. Phys.: Condens. Matter. **5**, 2913 (1993).
2. F. Jentzsch, H. Froitzheim, and R. Theile, J. Appl. Phys. **66**, 5901 (1989).
3. V. A. Gasparov and K. R. Nikolaev, Phys. Low-Dimens. Semicond. Struct. **1/2**, 53 (1996).
4. M. Henzler, C. Adamski, and K. Rönner, J. Vac. Sci. Technol. A **5**, 2127 (1987).
5. S. Hasegawa and S. Ino, Int. J. Mod. Phys. B **7**, 3817 (1993).
6. S. Hasegawa, X. Tong, C.-S. Jiang, *et al.*, Surf. Sci. **386**, 322 (1997).
7. X. Tong, C.-S. Jiang, and S. Hasegawa, Phys. Rev. B **57**, 9015 (1998).
8. N. G. Galkin, V. A. Ivanov, A. V. Konchenko, and D. L. Goroshko, Prib. Tekh. Éksp., No. 2, 154 (1999).
9. E. G. Michel, Appl. Surf. Sci. **117/118**, 294 (1995).
10. J. Álvarez, A. L. Vásquez de Parga, J. J. Hinarejos, *et al.*, Phys. Rev. B **47**, 16048 (1993).
11. K. L. Whiteaker, I. K. Robinson, C. Benson, *et al.*, Phys. Rev. B **51**, 9715 (1995).
12. V. L. Kon’kov, Zavod. Lab. **32**, 451 (1966).
13. M. Liehr, M. Renier, R. A. Wachnik, and G. S. Scilla, J. Appl. Phys. **61**, 4619 (1987).
14. V. V. Emtsev and T. V. Mashovets, in *Impurities and Point Defects in Semiconductors* (Radio i Svyaz’, Moscow, 1981), Chap. 2, p. 101.

Translated by A. Kazantsev

Semiconductors, Vol. 34, No. 7, 2000, pp. 803–806. Translated from Fizika i Tekhnika Poluprovodnikov, Vol. 34, No. 7, 2000, pp. 831–834.
Original Russian Text Copyright © 2000 by Sankin, Lepneva.

LOW-DIMENSIONAL SYSTEMS

Negative Differential Conductance and the Bloch Oscillations in the Natural Superlattice of 8*H* Silicon Carbide Polytype

V. I. Sankin and A. A. Lepneva

Ioffe Physicotechnical Institute, Russian Academy of Sciences, Politekhnicheskaya ul. 26,
St. Petersburg, 194021 Russia

Submitted January 13, 2000; accepted for publication January 14, 2000

Abstract—Special features of electron transport in the strong electric fields in a hexagonal 8*H*–SiC polytype were studied; these features are caused by the natural superlattice in the crystal structure and are related to the periodic potential of minibands in the electron spectrum. It is shown that in this polytype, as in the case of 6*H*– and 4*H*–SiC polytypes studied previously, negative differential conductance is observed. This conductance is defined by the Bloch oscillation effect. © *2000 MAIK "Nauka/Interperiodica".*

INTRODUCTION

It is well known that silicon carbide (SiC) is of interest, first of all, due to physical and chemical properties such as hardness, chemical resistance in aggressive media, preservation of semiconductor characteristics at high temperatures up to 1000°C, high thermal conductivity, high breakdown fields, and many others. However, most interest is aroused by the existence of SiC polytype crystals with large and very large sizes of the unit cell or so-called superstructures. In almost all polytypes, in addition to the basic periodicity determined by the lattice constant, it is possible to distinguish an additional periodicity with the period equal to several or several tens of the lattice constants. This superperiodicity is referred to as a natural superlattice (SL). In addition to the question of the nature of superstructures, the problem of the influence of superperiodicity on the electronic properties of crystals arouses particular interest. This problem, of course, is fundamental, but at the same time the results of such studies have great practical importance, because, without any doubt, SiC crystals have a practical application.

Attention was drawn to systems with crystalline superperiodicity in the middle of the 1960s after a publication by Keldysh [1] in which he proposed to use a sonic wave for the creation of superperiodicity in a crystal. This should cause splitting of the continuous and wide band into a series of narrow bands or minibands. A strong electric field F applied to such a system creates conditions for the electron Bragg reflection [2], and, as a result, negative differential conductance (NDC) occurs. In [3], the possibility of NDC appearing in the artificial SL related to the localization induced by the electric field was demonstrated. The threshold field F_t at which NDC appears is defined by the Esaki–Tsu criterion

$$eF_t d > \hbar/\tau . \quad (1)$$

The criterion for the Bloch oscillations is expressed as

$$eF_t d > 2\pi\hbar/\tau . \quad (2)$$

Here, $\hbar$ and τ are Planck's constant and the electron relaxation time, respectively; and d is the SL period. It follows from (1) and (2) that NDC related to these effects appears if the oscillation frequencies $eF_t d/\hbar$ or $eF_t d/2\pi\hbar$ exceed the electron scattering rate.

In the effects described in [3], the Stark energy eFd is still so low that quasi-continuum of the first miniband is conserved; i.e., many Stark levels can be present in this band.

We may state that the above idea stimulated the creation of artificial SLs based on the sequence of heterostructures, which until now have been the main object of numerous investigations. However, the main objective of these efforts was and still is the detection of NDC, which, unfortunately, has not been fully accomplished till now. The same problem is central in studying the transport properties of the natural SLs in SiC polytypes in strong electric fields. We will discuss here Bragg's reflection, the Bloch oscillations, and other phenomena which are generally related to the Wannier–Stark localization. Results of these studies along with the fundamental problems concerning the Wannier–Stark localization would allow us to clarify the aspects of influence of the natural SL on the electronic properties of SiC, namely, to find the causal relation between the periodical potential and the miniband formations. The electron transport study of the strong electric fields in SL of silicon carbide polytypes originated from investigation of the 6*H*–SiC polytype. It was shown

[4–10] that, in the electron transport measurements, a number of effects related to the Wannier–Stark localization were observed. In fact, for the first time, NDC was observed in the current–voltage characteristics (*I*–*V*) in static mode for a critical field higher than 100 kV/cm. The performed analysis suggested that this effect was a result of the Bloch oscillations in the natural SL of the 6*H*–SiC polytype. For much stronger electric fields, when the Stark energy was comparable with the width of the first miniband in the natural SL of this polytype, such effects as the Stark-phonon resonances (500–1400 kV/cm), complete localization of the first miniband (~1600 kV/cm), interminiband resonance tunneling (1950 kV/cm), and other effects related to the Wannier–Stark localization were observed. This made it possible to estimate the most important parameters of the miniband electronic spectrum of 6*H*–SiC (the width of the first miniband E_1 = 256 meV, the energy gap between the first and second minibands $E_{1,2}$ = 180–190 meV). These parameters are basic for estimations of similar parameters in the other polytypes if experimental data are not available or it is impossible to obtain them in principle. Among the last ones is the 4*H*–SiC polytype in which the NDC effects related to the Bloch oscillations and the Stark-phonon resonances were observed, but the effects, in which critical fields exceed characteristic breakdown fields, were not detectable due to the large value of the first miniband width and the energy gap between minibands [11–13]. Study of polytypes of the hexagonal series allows one to analyze correlations between the parameters of the natural SL and such important quantities as the miniband electron spectrum parameters and critical field values for different effects related to the Wannier–Stark localization. Such a comparison yields valuable data for development of the Wannier–Stark localization theory and often provides most convincing arguments for an explanation of the experimental data. This also allows one to choose the optimal polytype for further applied development. In this paper, the results of the Wannier–Stark localization studies of hexagonal polytype 8*H*–SiC are reported.

EXPERIMENTAL

Triode bipolar structures N^+–π–N^+ were grown for the experimental studies. Similar structures were used in previous investigations of 4*H*–SiC and 6*H*–SiC polytypes [4]. The central π-region doped unconventionally with the deep acceptor scandium impurity provides the basic functions of the structure. Due to the inertia of the recharge processes, in which scandium atoms and an extremely low concentration of free holes are involved, a pulsed field of a microsecond duration is practically not screened over distances of several tens of micrometers. It turns out to be sufficient for creation of the uniform electric field in a π-region of several μm in size. Due to the selection of scandium as the doping impurity, the triode structure can operate at room temperature. In general, this structure provides (i) uniformity of the electric field in the operating π-region; (ii) a solely electron current in the operating region; (iii) parallelism of the electric field with the axis of the natural SL; (iv) conditions for the drift current flow; and (v) control of the operating current irrespective of the field in the operating region. We should take into account that all these functions are provided if the triode structure operates in a pulsed mode. We could use a convenient range of microsecond pulses, which is determined by the electron parameters of scandium in the energy spectrum. We emphasize that the most important problem in creating a N^+–π–N^+ structure is formation of the epitaxial π-layer with a structure identical to the substrate polytype. Doping with scandium during the epitaxial growth mostly stimulates the 4*H*–SiC polytype growth. For different polytypes, we should search for new epitaxial growth conditions which can provide the reproducible growth conditions. They are determined to a great extent by variation of the epitaxial growth temperature rather than by other factors. In this way, we succeeded in suppressing the mechanism of preferential 4*H*–SiC growth and ensured the reproducible growth of several polytypes, such as 6*H*–, 8*H*–, 21*R*–, and 15*R*–SiC.

EXPERIMENTAL DATA AND DISCUSSION

The *I*–*V* characteristics of the triode structure based on 8*H*–SiC are shown in Fig. 1. A steady increase in the current *I* ceases at the electric field $F \approx 110$ kV/cm; for higher fields, we observe a decrease in the current over a wide range of the electric fields and, therefore, the NDC effect.

In Fig. 2, *N*-shaped *I*–*V* characteristics for 4*H*–, 6*H*–, and 8*H*–SiC polytypes are shown. Threshold fields corresponding to the current decrease onset, i.e., to the appearance of NDC, are equal for different samples to $F_t \approx 1.1 \times 10^5$ V/cm for 8*H*–SiC, 1.5×10^5 V/cm for 6*H*–SiC, and 2.9×10^5 V/cm for 4*H*–SiC. The value of F_t was obtained with about 10% error related, first of all, to the error in determining the width of the base layer. Such variation of the threshold fields for 4*H*–, 6*H*–, and 8*H*–SiC series correlates with variation of the natural SL period in these polytypes: 5, 7.5, and 10 Å. According to the Wannier–Stark localization criteria (1) and (2), the critical field is inversely proportional to the period of the natural SL for a constant value of the relaxation time. It can be seen from Fig. 2 that *I*–*V* characteristics are similar; however, the threshold fields are significantly different. We note that Fig. 2 shows the *I*–*V* characteristics of the structures with distinct *N*-shaped features. In some samples, a decrease in current was no more than 20%; in addition, in many cases, uncontrolled current leakage and microplasma breakdown prevented the observation of this effect. In 30% of the samples, *I*–*V* characteristics were monotonic up to the breakdown fields [11] even if leakage was absent.

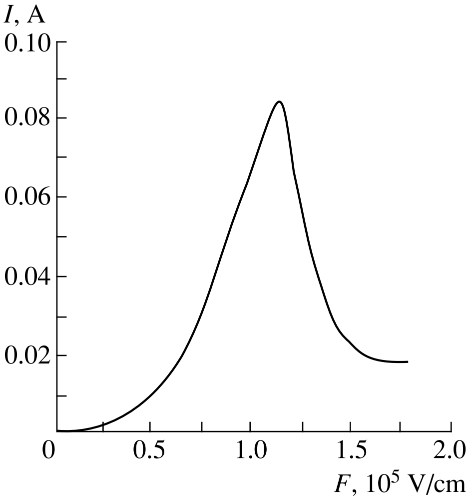

Fig. 1. *I–V* characteristic of a three-electrode structure based on the natural SL of the 8*H*–SiC polytype.

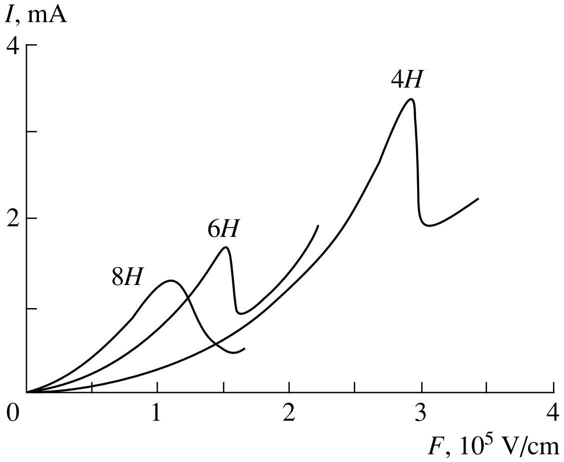

Fig. 2. *I–V* characteristic of three-electrode structures based on the natural SL in 4*H*–, 6*H*–, and 8*H*–SiC polytypes.

For numerical estimations according to (1) and (2), it is necessary to know the relaxation time τ, which we can estimate from the relation $\tau = m^*\mu/e$. In this case, the effective mass m^* and mobility μ should be determined at strong electric fields close to the threshold ones. For these estimations, the experimental data on the electron drift velocity in the saturation region v_s were used for a field directed parallel to the natural SL axis [14]. The drift velocity saturated for the electric fields F_s of 135, 140, and 155 kV/cm; values of the drift velocity v_s were equal to 1.0×10^6, 2.0×10^6, and 3.3×10^6 cm/s for 8*H*–, 6*H*–, and 4*H*–SiC, respectively. μ and m^* were determined from the following formulas:

$$\mu = v_s/F_s, \tag{3}$$

$$m^* = 8E_p/3\pi v_s^2, \tag{4}$$

where $E_p = 106$ meV is the averaged energy of the optical phonon [15]. In this case, the relaxation time was equal to $\tau = 1.6 \times 10^{-13}$, 3×10^{-13}, and 5.9×10^{-13} s for 4*H*–, 6*H*–, and 8*H*–SiC, respectively. From (1), the threshold fields are equal to 80, 27, and 10.6 kV/cm for 4*H*–, 6*H*–, and 8*H*–SiC, respectively, which are much lower than the experimental values 290, 150, and 110 kV/cm. The threshold fields estimated from criterion (2) are 500, 170, and 65 kV/cm, which are much closer to the experimental data. Considering that error in the v_s determination is 30%, we may state that the agreement is rather good. Thus, the observed effects correlate with the Bloch oscillation conditions rather than with the Esaki–Tsu effects. According to [3], the electron drift velocity in the miniband is expressed as

$$v_d = A(F/B)\{1/[1 + (F/B)^2]\}, \tag{5}$$

where $A = dE_1/2\hbar$ and $B = \hbar/ed\tau$. For 6*H*–SiC, the width of the first miniband is $E_1 = 256$ meV. The relaxation time $\tau = 5 \times 10^{-13}$ s calculated from (5) is consistent with the values mentioned above.

Apparently, the NDC observed in our experiment may also be explained by another reason. It is well known that the *N*-shaped *I–V* characteristics are also observed in the case of recombination instability when carriers are captured by the repulsive centers [16]. However, the electron transit time through the base layer $t \approx 10^{-10}$ s is much smaller than the recombination time, which makes this process highly improbable. In addition, we can state with assurance that, in the case of any other mechanisms (including the mechanism of the recombination instability), the threshold fields for the polytypes 4*H*–, 6*H*–, and 8*H*–SiC would be practically the same. Thus, interpretation of the observed effects in the context of the Wannier–Stark localization theory seems to be justified. Parameters characterizing these effects satisfy criteria for the Wannier–Stark localization, and the difference in the threshold fields for the three polytypes correlates with the difference in the SL parameters. An increase in the current to the right from the threshold-field point in the *I–V* characteristic may be explained by an increase in the injection as the field increases and, also, by the transverse heating of electrons. In addition, not all electrons involved in the current flow are subjected to the Wannier–Stark quantization. In the investigated structures, current can flow in directions which are not parallel to the natural SL axis. We emphasize that we consider the NDC observed in the above polytypes under the Bloch oscillation conditions as the first phase of the process of the Wannier–Stark localization.

ACKNOWLEDGMENTS

This work was supported in part by the Russian Foundation for Basic Research (project no. 97-02-

18295) and the Interindustry Scientific and Technical Program “Physics of Solid-State Nonostructures” (project no. 97-1038)

REFERENCES

1. L. V. Keldysh, Fiz. Tverd. Tela (Leningrad) **4**, 2265 (1962) [Sov. Phys. Solid State **4**, 1658 (1962)].
2. G. N. Wannier, Phys. Rev. **11**, 432 (1960).
3. L. Esaky and R. Tsu, IBM J. Res. Dev. **14**, 61 (1970).
4. V. I. Sankin and A. V. Naumov, Pis’ma Zh. Tekh. Fiz. **16** (7), 91 (1990) [Sov. Tech. Phys. Lett. **16**, 281 (1990)].
5. V. I. Sankin and A. V. Naumov, Springer Proc. Phys. **43**, 221 (1991).
6. V. I. Sankin and A. V. Naumov, Superlattices Microstruct. **10**, 353 (1991).
7. V. I. Sankin and I. A. Stolichnov, Pis’ma Zh. Éksp. Teor. Fiz. **59**, 703 (1994) [JETP Lett. **59**, 744 (1994)].
8. V. I. Sankin and I. A. Stolichnov, in *Proceedings of the International Symposium “Nanostructures: Physics and Technology,” St. Petersburg, 1994*, p. 87.
9. V. I. Sankin, Superlattices Microstruct. **18** (4), 309 (1996).
10. V. I. Sankin and I. A. Stolichnov, Pis’ma Zh. Éksp. Teor. Fiz. **64**, 105 (1996) [JETP Lett. **64**, 114 (1996)].
11. V. I. Sankin, A. V. Naumov, and I. A. Stolichnov, Pis’ma Zh. Tekh. Fiz. **17** (23), 38 (1991) [Sov. Tech. Phys. Lett. **17**, 838 (1991)].
12. V. I. Sankin, Inst. Phys. Conf. Ser. **142**, 2401 (1996).
13. V. I. Sankin, I. A. Stolichnov, and A. A. Mal’tsev, Pis’ma Zh. Tekh. Fiz. **22** (24), 29 (1996) [Tech. Phys. Lett. **22**, 881 (1996)].
14. V. I. Sankin and A. A. Lepneva, Fiz. Tekh. Poluprovodn. (St. Petersburg) **33**, 586 (1999) [Semiconductors **33**, 547 (1999)].
15. V. I. Sankin, Fiz. Tverd. Tela (Leningrad) **17**, 1820 (1975) [Sov. Phys. Solid State **17**, 1191 (1975)].
16. A. F. Volkov and Sh. M. Kogan, Usp. Fiz. Nauk **96**, 633 (1968) [Sov. Phys. Usp. **11**, 881 (1968)].

Translated by I. Kucherenko

Semiconductors, Vol. 34, No. 7, 2000, pp. 807–809. Translated from Fizika i Tekhnika Poluprovodnikov, Vol. 34, No. 7, 2000, pp. 835–837.
Original Russian Text Copyright © 2000 by Glazov, Kryuchkov.

Plasma Oscillations in Two-Dimensional Semiconductor Superstructures

S. Yu. Glazov and S. V. Kryuchkov

Volgograd State Pedagogical University, Volgograd, 400013 Russia

Submitted November 12, 1999; accepted for publication January 24, 2000

Abstract—The possibility of plasma oscillations occurring in a two-dimensional electron gas with a superstructure was studied taking into account the Umklapp processes. In the case of high temperatures ($\Delta \ll T$, where Δ is the width of the conduction miniband and T is temperature expressed in energy units), the dispersion relation $\omega(k)$ was obtained. It is shown that, for small values of k (k_x, $k_y \ll \pi/d$), the plasmon spectrum features the characteristic dispersion $\omega^2 \sim k$, which corresponds to a two-dimensional electron gas without a superstructure. For arbitrary values of k, the spectrum is periodic with a period of $2\pi/d$. Numerical estimation of the characteristic frequency of the plasma oscillations for the two-dimensional superstructures currently under experimental investigation yields 10^{13} s^{-1}. *© 2000 MAIK “Nauka/Interperiodica”.*

Interest in two-dimensional (2D) electron structures has significantly grown in recent years, not only because of the diverse and effective applications of these structures in microelectronics but also due to the discovery of a radically new fundamental phenomenon in this field, namely, the quantum Hall effect [1].

Recently, new objects involving a 2D electron gas in a system with periodic potential have made their appearance in semiconductor physics. It was reported [2] that such a 2D superlattice was formed using the electron-beam lithography and reactive ion etching; emission related to microwave photoconductivity in a magnetic field was observed. The Shubnikov–de Haas oscillations of 2D electrons in a 2D periodic potential with a period of $d = 0.24$ μm were studied [3]. A method was suggested [4] for producing GaAlAs/GaAs-based 2D electron systems whose energy has been described to a good accuracy in the context of the tight-binding approximation. Optical properties of such a structure were also studied theoretically. The possibility of propagation of the solitary electromagnetic waves in 2D superstructures was demonstrated [5].

The effect of additional periodic potential (superstructure) in such objects can be taken into account by defining the energy spectrum of charge carriers to the tight-binding approximation as

$$\varepsilon(\mathbf{p}) = \Delta - \frac{\Delta}{2}[\cos(p_x d) + \cos(p_y d)], \qquad (1)$$

where Δ is the width of the conduction miniband, d is the superstructure period, and p_x and p_y are the quasi-momentum components in the superstructure plane (henceforth, it is assumed that $\hbar = 1$).

On the other hand, it is known that the plasma waves in a 2D electron gas have a number of specific features compared with those in a 3D electron gas. Thus, for example, the spectrum of 2D plasmons is zero-gap and exhibits the characteristic dispersion $\omega^2 \sim k$ [6, 7]. In addition, it was shown [8] that, in the vicinity of the plasma resonance of a 2D electron gas in a thin semiconductor film, the reflectivity decreased drastically and the dispersion law for 2D plasmons changed radically. In connection with this, it is of interest to study the possibility of origination of the plasma oscillations with the spectrum given by (1) in 2D superstructures and to determine the dispersion law for these oscillations.

Let us consider a 2D electron gas in a system with periodic potential. Restricting ourselves to the single-miniband approximation, we define the electron wave function in the miniband as

$$\Psi_P(x, y) = \frac{1}{\sqrt{N_x}}\frac{1}{\sqrt{N_y}}\sum_{n=1}^{N_x}\sum_{m=1}^{N_y}\exp(inp_x d + imp_y d) \times \varphi(x - nd)\varphi(y - md), \qquad (2)$$

where φ is the wave function of the state corresponding to the allowed miniband under consideration in one of the potential wells that form the superstructure, and N_x and N_y are the number of such wells along the x-axis and y-axis, respectively.

To the approximation of a self-consistent field, the Hamiltonian of interacting electrons with allowance

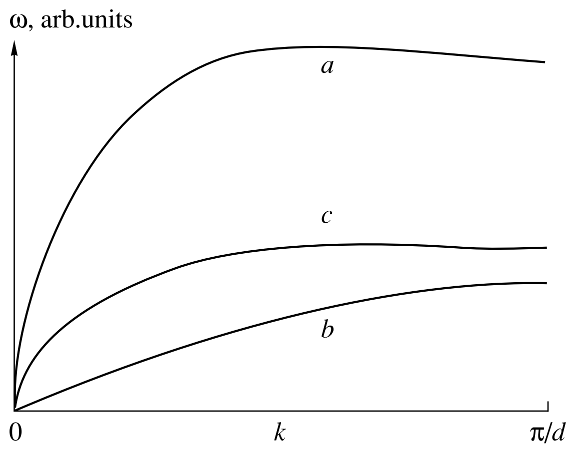

The dependence $\omega(k)$ in arbitrary units for (*a*) $k_x = k_y$ for $z \ll 1$, (*b*) $k_x = k_y$ for $z \approx 1$, and (*c*) $k_y = 0$.

made for the Umklapp processes can be written as

$$\begin{aligned} H = {} & \sum_{\mathbf{p}} \varepsilon_{\mathbf{p}} a^+_{\mathbf{p}} a_{\mathbf{p}} + e\frac{1}{\sqrt{N_x N_y}} \\ & \times \sum_{\mathbf{p},\,\mathbf{k}}\sum_{n,\,m} U(\mathbf{k}, t) M(k_x) M(k_y) a^+_{\mathbf{p}-\mathbf{k}+\mathbf{g}} a_{\mathbf{p}}, \end{aligned} \tag{3}$$

where $a^+_{\mathbf{p}}$ and $a_{\mathbf{p}}$ are the creation and annihilation operators for an electron with the momentum $\mathbf{p}$; $\mathbf{g} = (n2\pi/d, m2\pi/d)$;

$$\begin{aligned} M(k_x) &= \int_0^{N_x d} \varphi^*(x)\varphi(x)\exp(-ik_x x)dx, \\ M(k_y) &= \int_0^{N_y d} \varphi^*(y)\varphi(y)\exp(-ik_y y)dy, \end{aligned} \tag{4}$$

and $U(\mathbf{k}, t)$ is the self-consistent potential defined by

$$U(\mathbf{k}, t) = \frac{2\pi e}{\chi k}\sum_{\mathbf{p}}\sum_{n,\,m}\langle a^+_{\mathbf{p}+\mathbf{k}+\mathbf{g}} a_{\mathbf{p}}\rangle M(-k_x)M(-k_y). \tag{5}$$

Here, χ is the permittivity of the crystal lattice and the broken brackets signify the averaging over the density matrix that corresponds to the Hamiltonian defined by (3).

In the random-phase approximation, the equation of motion for the mean values $\langle a^+_{\mathbf{p}+\mathbf{k}+\mathbf{g}} a_{\mathbf{p}}\rangle$ is given by

$$\begin{aligned} & \left\{\frac{\partial}{\partial t} + i[\varepsilon(\mathbf{p}+\mathbf{k}) - \varepsilon(\mathbf{p})]\right\}\langle a^+_{\mathbf{p}+\mathbf{k}+\mathbf{g}} a_{\mathbf{p}}\rangle \\ & = -ieU(\mathbf{k}, t)(n_{\mathbf{p}+\mathbf{k}+\mathbf{g}} - n_{\mathbf{p}}), \end{aligned} \tag{6}$$

where $n_{\mathbf{p}} = \langle a^+_{\mathbf{p}} a_{\mathbf{p}}\rangle$ are the occupation numbers for electron levels in a 2D electron gas. Substituting a solution to (6) into (5) and performing certain transformations, we obtain the following expression for the Fourier component of $U(\mathbf{k}, t)$:

$$\begin{aligned} \tilde{U}(\mathbf{k}, \omega) = {} & \frac{2\pi e^2}{\chi k}\sum_{p}\sum_{n,\,m} M^*(k_x)M^*(k_y)M([\mathbf{k}+\mathbf{g}]_x) \\ & \times M([\mathbf{k}+\mathbf{g}]_y)\Pi(\mathbf{k}, \omega)\tilde{U}(\mathbf{k}+\mathbf{g}, \omega). \end{aligned} \tag{7}$$

Here,

$$\Pi(\mathbf{k}, \omega) = \sum_{\mathbf{p}} \frac{n_{\mathbf{p}+\mathbf{k}} - n_{\mathbf{p}}}{\varepsilon(\mathbf{p}+\mathbf{k}) - \varepsilon(\mathbf{p}) - \omega} \tag{8}$$

is the operator of polarization. We use (7) to derive the equation that defines the dispersion relation $\omega(\mathbf{k})$ as

$$\frac{2\pi e^2}{\chi}\Pi(\mathbf{k}, \omega)S(\mathbf{k}) = 1, \tag{9}$$

where

$$S(\mathbf{k}) = \sum_{n,\,m}\frac{|M([\mathbf{k}+\mathbf{g}]_x)|^2 |M([\mathbf{k}+\mathbf{g}]_y)|^2}{\sqrt{(k_x+g_x)^2 + (k_y+g_y)^2}}. \tag{10}$$

We now consider a nondegenerate electron gas, in which case

$$n(\mathbf{p}) \approx \exp(-\varepsilon(p_x, p_y)/T), \tag{11}$$

where T is temperature expressed in energy units. Calculation of the polarization operator is simplified appreciably for high temperatures, such that $2\Delta \ll T$. In this case, we obtain

$$\begin{aligned} & \Pi(\mathbf{k}, \omega) \\ & = -\frac{N_0}{T}\left[1 - \frac{2}{\pi}\frac{\omega K(z)}{\sqrt{\omega^2 - \Delta^2\left(\sin\frac{k_x d}{2} - \sin\frac{k_y d}{2}\right)^2}}\right], \end{aligned} \tag{12}$$

where N_0 is the surface density of the electron gas and $K(z)$ is the complete elliptic integral of the first kind, with z given by

$$z = 2\Delta\left[\frac{\sin\frac{k_x d}{2}\sin\frac{k_y d}{2}}{\omega^2 - \Delta^2\left(\sin\frac{k_x d}{2} - \sin\frac{k_y d}{2}\right)^2}\right]^{1/2}. \tag{13}$$

It follows from (8)–(10) that the frequency of plasma oscillations depends on the wave vector periodically with a period of $2\pi/d$. Therefore, we may restrict ourselves to consideration of the oscillation spectrum within the first Brillouin zone; i.e.,

$$-\pi/d < k_x < \pi/d, \quad -\pi/d < k_y < \pi/d. \tag{14}$$

In order to calculate the multiplier $S(\mathbf{k})$, we should know the specific shape of potential wells that form the superstructure. We consider the case where $\varphi(x) = \text{const}$ for $0 \le x \le d$ and $\varphi(x) = 0$ for $x < 0$ and $x > d$. In this case, expression (10) takes the form

$$S(\mathbf{k}) = \sum_{n,m} \frac{4[1-\cos(k_x d)][1-\cos(k_y d)]}{(k_x+g_x)^2(k_y+g_y)^2\sqrt{(k_x+g_x)^2+(k_y+g_y)^2}}. \tag{15}$$

For arbitrary values of $\mathbf{k}$, the sum in (15) cannot be expressed in terms of tabulated functions. However, for small values of k (k_x, $k_y \ll \pi/d$), the quantity $S(\mathbf{k})$ varies proportionally to $1/|\mathbf{k}|$. Furthermore, it follows from (8) and (9) that the spectrum of plasmons exhibits the characteristic dispersion $\omega^2 \sim k$, which corresponds to a 2D electron gas without a superstructure.

We now turn our attention to consideration of several special cases.

1. $k_x = k_y = k$.

(i) For $z \ll 1$, we have

$$K(z) \approx \frac{\pi}{2}\left(1+\frac{z^2}{4}\right), \tag{16}$$

and the dispersion law for the plasma oscillations is defined as

$$\omega^2 = \frac{2\pi e^2}{\chi}\frac{N_0\Delta^2}{T}S(k)\sin^2\frac{kd}{2}. \tag{17}$$

The figure illustrates (curve *a*) the dependence $\omega(k)$ obtained by numerically analyzing formulas (15)–(17). For $kd/2 \ll 1$, we have the dispersion law $\omega^2 \sim k$.

(ii) for $z \approx 1$, we have

$$K(z) \approx \ln\frac{4}{\sqrt{1-z^2}}; \tag{18}$$

in this case, we obtain the following dependence:

$$\omega = 2\Delta\left|\sin\frac{kd}{2}\right| \times\left[1-16\exp\left(-2-\frac{\chi T}{\pi e^2 N_0}\frac{1}{S(k)}\right)\right]^{-1/2}. \tag{19}$$

The figure shows (curve *b*) the plot of the dependence $\omega(k)$ defined by relationship (19). For $kd/2 \ll 1$, we obtain the dispersion law in the form of $\omega \sim k$.

2. $k_y = 0$. In this case,

$$\omega = \Delta\left|\sin\frac{k_x d}{2}\right|\frac{f(k_x)}{\sqrt{f(k_x)^2-1}}, \tag{20}$$

where

$$f(k_x) = 1+\frac{\chi T}{2\pi e^2 N_0}\frac{1}{S(k_x)}.$$

For $k_x \ll \dfrac{2\pi e^2 N_0}{\chi T}$, we have

$$\omega^2 = \frac{\pi e^2\Delta^2 N_0}{\chi T}\sin^2\frac{k_x d}{2}S(k_x). \tag{21}$$

The dispersion relation defined by (21) is illustrated in the figure (curve *c*). For $k_x d/2 \ll 1$, we have the dispersion law $\omega^2 \sim k_x$.

We now give numerical evaluations. For the concentration $N_0 = 10^{11}$ cm^{-2}, for $d = 10^{-5}$ cm, $\Delta = 10^{-2}$ eV (the values of the parameters N_0 and d were taken from [3] and the value of Δ was adopted from [4]), for $T \approx 100$ K, and for $k \approx 10^4$ cm^{-1}, we find that the plasma-oscillation frequency is on the order of $\omega \approx 10^{13}$ s^{-1}.

REFERENCES

1. K. Klitzing, G. Dorda, and M. Pepper, Phys. Rev. Lett. **45** (5), 494 (1980).
2. A. A. Bykov, G. M. Gusev, Z. D. Kven, *et al.*, Pis'ma Zh. Éksp. Teor. Fiz. **53**, 407 (1991) [JETP Lett. **53**, 427 (1991)].
3. G. M. Gusev, Z. D. Kven, V. B. Besman, *et al.*, Fiz. Tekh. Poluprovodn. (St. Petersburg) **26**, 539 (1992) [Sov. Phys. Semicond. **26**, 304 (1992)].
4. D. Ferry, L. Akers, and E. Greeneich, *Ultra Large Scale Integrated Microelectronics* (Prentice-Hall, Englewood Cliffs, 1988; Mir, Moscow. 1991).
5. S. V. Kryuchkov and A. I. Shapovalov, Fiz. Tverd. Tela (St. Petersburg) **39**, 1470 (1997) [Phys. Solid State **39**, 1305 (1997)].
6. F. Stern, Phys. Rev. Lett. **18** (14), 546 (1967).
7. T. Ando, A. B. Fowler, and F. Stern, Rev. Mod. Phys. **54**, 437 (1982).
8. N. N. Zinov'ev, D. I. Kovalev, I. D. Yaroshetskiĭ, and A. Yu. Blank, Pis'ma Zh. Éksp. Teor. Fiz. **53**, 147 (1991) [JETP Lett. **53**, 154 (1991)].

Translated by A. Spitsyn

Semiconductors, Vol. 34, No. 7, 2000, pp. 810–814. Translated from Fizika i Tekhnika Poluprovodnikov, Vol. 34, No. 7, 2000, pp. 838–843.

LOW-DIMENSIONAL SYSTEMS

Study of Multilayer Structures with InAs Nanoobjects in a Silicon Matrix

V. N. Petrov*, N. K. Polyakov*, V. A. Egorov*, G. E. Cirlin*, N. D. Zakharov, P. Werner**, V. M. Ustinov***, D. V. Denisov***, N. N. Ledentsov***, and Zh. I. Alferov*****

** Institute for Analytical Instrumentation, Russian Academy of Sciences, St. Petersburg, 198103 Russia*

e-mail: cirlin@beam.ioffe.rssi.ru

*** Max-Planck Institute of Microstructure Physics, Halle/Saale, Germany*

**** Ioffe Physicotechnical Institute, Russian Academy of Sciences, Politekhnicheskaya ul. 26,*
St. Petersburg, 194021 Russia

Submitted January 24, 2000; accepted for publication January 25, 2000

Abstract—MBE-grown multilayer structures with InAs quantum dots embedded in a crystalline silicon matrix were studied by high resolution transmission electron microscopy. The properties of the grown structures depend critically on the substrate temperature, growth cycle sequence, and layer thicknesses. It is shown that the silicon matrix can "accommodate" only a limited volume of InAs in the form of coherent clusters about 3 nm in size. With an increasing amount of deposited InAs, large dislocated InAs clusters are formed during Si overgrowth, accumulating excess InAs. © *2000 MAIK "Nauka/Interperiodica".*

INTRODUCTION

Efforts to combine the silicon and III–V semiconductor technologies have long been made with the aim of producing a new generation of microelectronic devices. However, most attention has been given to thick III–V layers on silicon. Recently, by analogy with III–V heteroepitaxial systems, the idea arose to directly use MBE to produce coherent nanometer-scale InAs islands (quantum dots, QDs) incorporated into a silicon matrix [1]; in this case, the effect of the spontaneous formation of nanoobjects during the initial stages of heteroepitaxial growth is beneficial. We used MBE to grow InAs QDs directly on the silicon surface and studied them by reflection high-energy electron diffraction (RHEED) and scanning tunneling microscopy (STM) [2]. Optical studies of InAs QDs embedded in a silicon matrix and overgrown with a silicon layer revealed a broad (~100 meV) line at about 1300 nm in the photoluminescence (PL) spectrum at 10 K [3, 4]. Nevertheless, the applied methods failed to produce data on the geometry and coherence parameters of the InAs QDs incorporated into the silicon matrix. A model of the QD self-organization process involving the formation of multilayer structures with vertically correlated QDs (VCQD) was proposed in [5], and experimental evidence of the "efficient" self-organization of $Si_{0.25}Ge_{0.75}$ on the Si surface was presented. With VCQD structures, in particular, the parameters of laser structures based on InAs QDs have been significantly improved [6].

The aim of this work was to use transmission electron microscopy (TEM) to study multilayer structures with MBE-grown InAs QD layers incorporated into a crystalline silicon matrix.

EXPERIMENTAL METHODS

The structures studied were grown in a Riber-Supra MBE setup (ISA Riber, France). Standard effusion cells were used to produce In and As fluxes; silicon was deposited using an electron-beam evaporator. To obtain an atomically-clean structurally-ordered surface, Si substrates were subjected to pregrowth chemical treatment and two-stage vacuum thermal annealing, described in detail elsewhere [7]. For substrates, we used *n*-type KÉF-4.5 (100) silicon wafers (*n*–Si:P, ρ = 4.5 Ω cm) mechanically attached to indium-free molybdenum substrate holders. The sample holder was continuously rotated during growth. After removing the oxide layer from the substrate surface, a silicon buffer layer was grown at substrate temperature T_s = 630–640°C prior to depositing InAs. During the thermal annealing and growth, the surface structure was monitored with a system of detection and computer processing of RHEED patterns, including a video camera, TV monitor, videorecorder, and a computer videointerface [8]. Figure 1 demonstrates the sequence of layers and the technological growth parameters (substrate temperature, number of layers, and their thickness) for the samples studied. The growth rates were

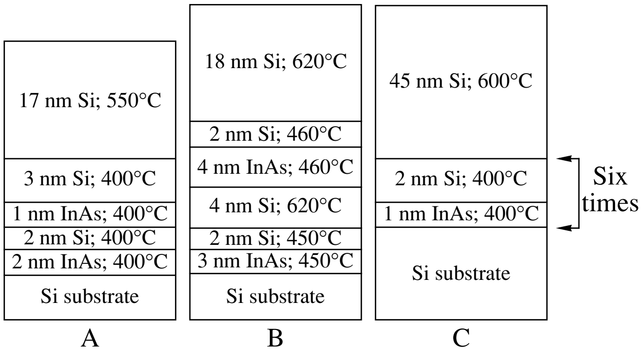

Fig. 1. Sequence of layers in the samples and technological parameters of growth processes.

0.03 and 0.02 nm s^{-1} for InAs and Si, respectively. The limits of T_s variation were chosen on the basis of previous results [2], indicating that at T_s above 450°C a structure is formed with dislocated clusters up to 400 nm in size instead of a spatially uniform array of nanometer-scale islands [2]. The lower limit of the temperature range was chosen based on the fact that the cap Si layer grown at low T_s has very poor crystal perfection, making it impossible to fabricate device structures. According to previous data, in this T_s range, InAs QDs grow on the silicon surface by the Volmer–Weber mechanism [4].

The crystal structure quality and layer composition were studied by TEM with varied resolution using a JEOL JEM-4000EX setup and by X-ray electron-probe analysis on a Philips CM20T electron microscope with a Voyager I attachment (a Ge detector). Computer simulation and electronic processing of TEM images were performed using a MacTempas software package [9].

RESULTS AND DISCUSSION

Figure 2 shows cross-sectional (a) and plan-view (b) low-resolution TEM images of some fragments of sample A. InAs-island inclusions are seen on the bottom of surface depressions (16 nm) formed upon the subsequent silicon overgrowth. TEM images of the surface of these islands show “square moiré” patterns. The insert in Fig. 2b presents the corresponding transmission

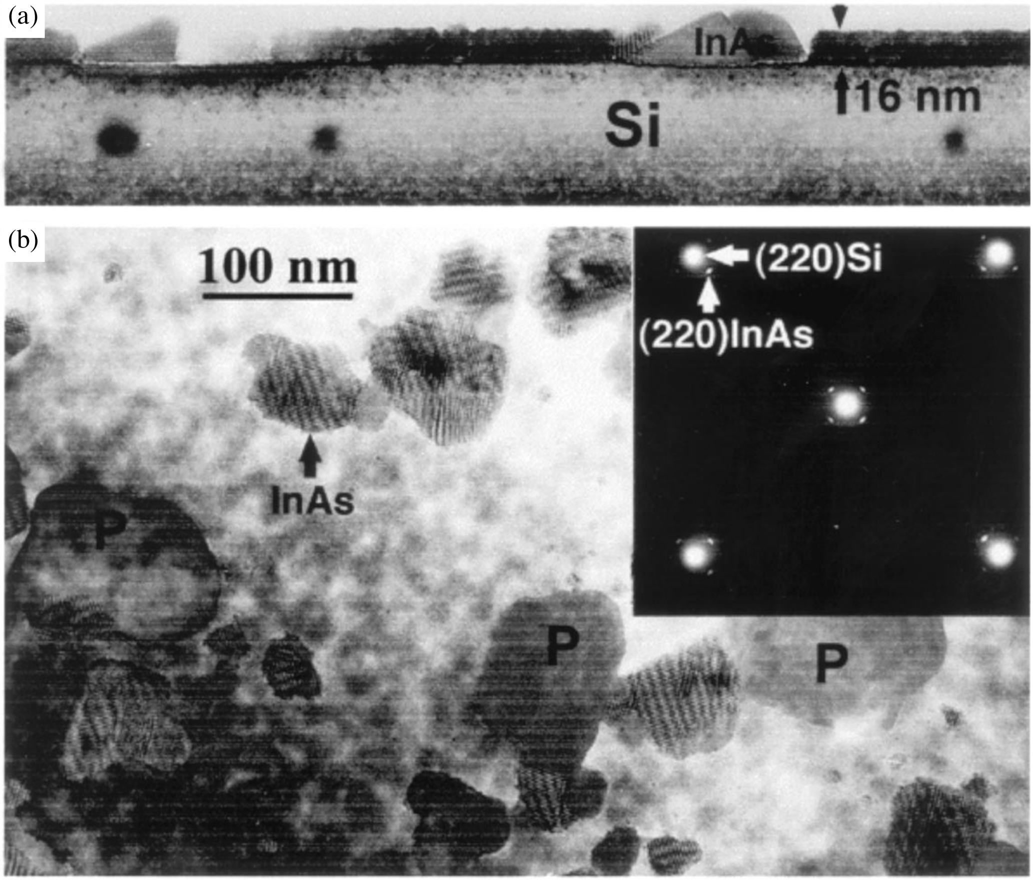

Fig. 2. (a) Cross-sectional and (b) plan-view TEM images of sample A. Extra reflections from InAs islands are marked by arrows in the insert.

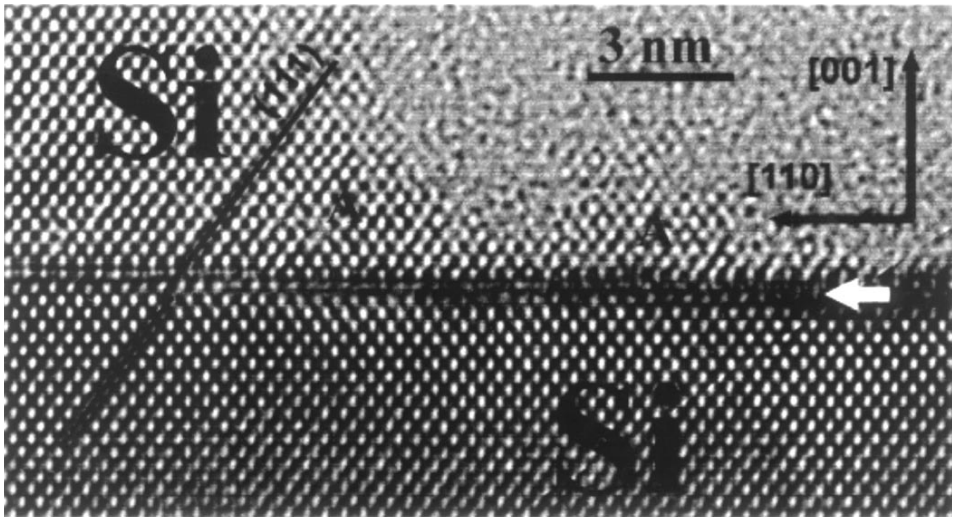

Fig. 3. Cross-sectional TEM image of the interface between the Si matrix and silicon islands (A) formed at the bottom of a shallow depression.

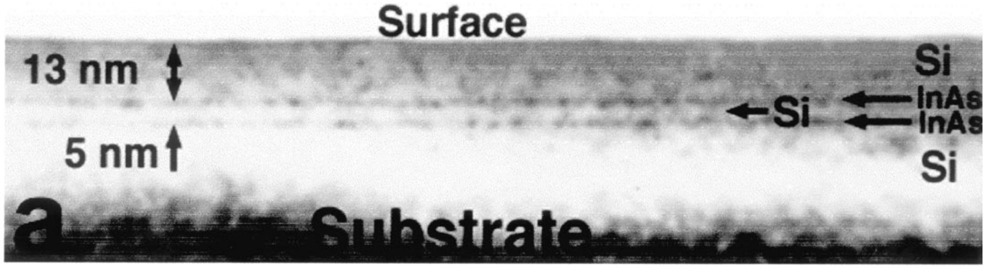

Fig. 4. Cross-sectional TEM image of sample B. Two InAs layers are marked.

electron microdiffraction patterns, with clearly defined reflections from both the silicon matrix and InAs clusters. Digital processing of the interreflection distances (in reciprocal space) shows a ~10% mismatch between InAs and Si crystal lattices, which is consistent with the well-known value of ~11%. X-ray microprobe-analysis spectra of InAs clusters, taken in the transmission mode, also exhibited clearly defined additional In and As peaks. The fact that these islands commonly occupy shallow depressions shows that, during silicon overgrowth, Si does not grow in the immediate vicinity of InAs islands. A possible reason for this is that a wetting layer is formed around an island, leading to surface passivation. Figure 3 shows a cross-sectional HRTEM image of a fragment of such a surface structure formed at the bottom of a shallow depression. A conclusion can be made on the basis of this image that the atomic structure of the surface layer differs from the bulk structure and that of {111} atomic planes of small silicon islands (A, Fig. 3) formed on it. In addition, the surface layer is shifted by $a/4[110]$ with respect to the corresponding atomic planes of the silicon matrix.

Figure 4 presents a low-resolution cross-sectional TEM image of sample B. The arrows mark two layers of InAs inclusions in the silicon matrix. The thickness (5 nm) of the silicon spacer between InAs layers is somewhat smaller than that expected from the amount of deposited silicon (6 nm, Fig. 1). The effective thickness of InAs inclusions is also less than the expected 4 nm, indicating that only a minor part of the deposited InAs was incorporated into nanoobjects after overgrowth with silicon. In our opinion, the most probable reason for this is that the substrate temperature increases upon InAs deposition and during the growth of an ultrathin (2 nm) silicon cap layer. This stage is important for maintaining the high quality of a structure, since the excess InAs effectively evaporates at 620°C, preventing the formation of large InAs islands appearing in the case of sample A.

We note also that the total area occupied by depressions (Fig. 2b) in sample B is nearly half that in sample A. On the other hand, these depressions are nearly empty in sample B, whereas they contain relaxed InAs islands in sample A. Thus, the elevated temperature during sil-

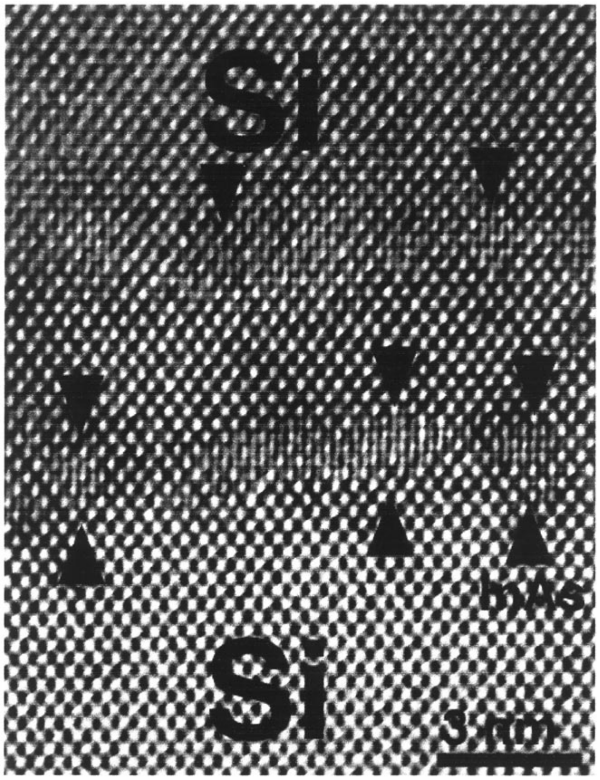

Fig. 5. Cross-sectional HRTEM image of sample B. InAs clusters are marked by arrows.

icon overgrowth is substantial for reevaporation of the excess InAs.

To analyze the lattice structure and dimensions of InAs clusters embedded in the silicon matrix, cross-sectional HRTEM images of samples were obtained. Figure 5 shows such an image for sample B. Formations about 3 nm in diameter spaced by 0.5–1 nm in the lateral direction are marked by arrows. Moreover, no distinct vertical correlation between cluster positions is observed.

Numerical simulation of the formation of small InAs clusters in the silicon matrix yielded simulated TEM images. Figure 6a shows a crystallographic model of InAs clusters used for calculations. This model deals with the situation where silicon atoms are replaced by interconnected In and As atoms in the process of epitaxial growth of InAs on the silicon surface, with the matrix symmetry lowered. The growth processes were simulated for conditions close to experimental for different thicknesses of InAs embedded in the silicon matrix. The results of simulation are presented in Fig. 6c. As expected, the correlation is rather poor for small thicknesses (~1.2 nm), whereas for thicker crystals (about 4 nm) the simulated TEM image shows good agreement with the experiment (Fig. 5). The specifity of the observed contrast is due to a great difference of atomic scattering amplitudes for In, As, and Si.

Figure 7 presents a cross-sectional TEM image of sample C. The arrows mark six well distinguishable layers of coherent InAs clusters. As in the case of sample A grown at the same temperature (400°C), no reduction of distances between the QD layers is observed. The distinctive feature of this structure is that a high density of structural defects of two types, which start to form predominantly after the fourth InAs layer, is observed in the upper part of the multilayer structure. One of the possible reasons for the presence of a high defect density is that intermediate silicon layers are grown under an elevated background arsenic pressure, leading to the incorporation of As atoms into the silicon structure. The first results obtained in studying the influence of the background arsenic pressure on the properties of autoepitaxial silicon layers can be found elsewhere [7].

All attempts to obtain spectra of excited PL for VCQD structures have failed. This is presumably due to the presence of a high defect density in the crystal structure of silicon spacers between QD layers. Another possible reason for the absence of PL lines is the necessity for a more accurate adjustment of all growth parameters (substrate temperature and thickness of InAs and Si spacer layers) evidently exerting a

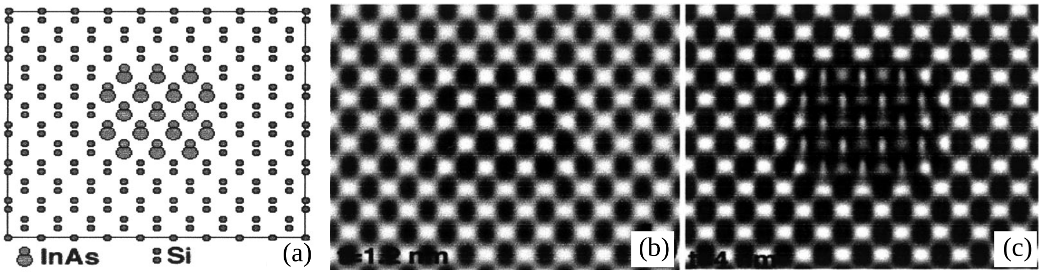

Fig. 6. (a) Atomic model for InAs clusters in the Si matrix and two simulated HRTEM images for sample thicknesses of (b) 1.2 and (c) 4 nm.

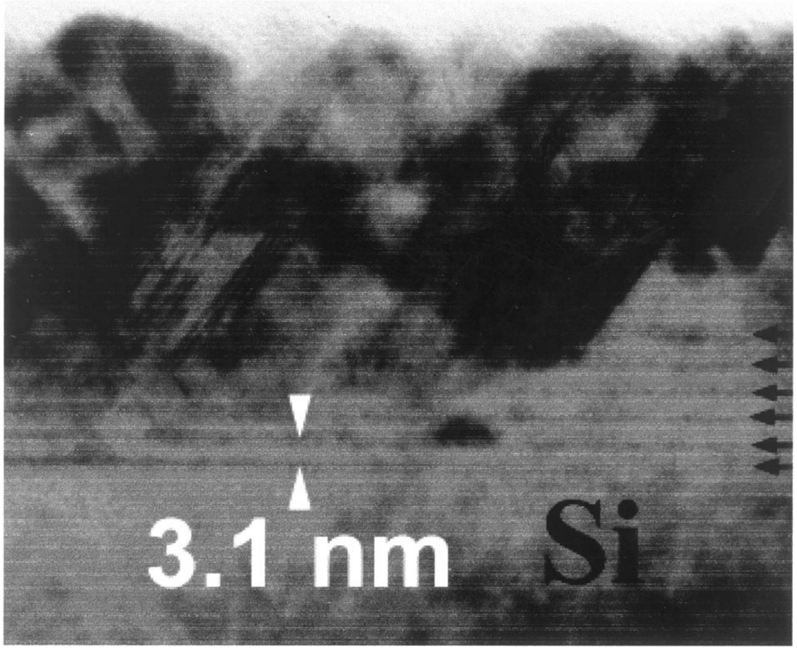

Fig. 7. Cross-sectional TEM image of sample C. Six layers containing coherent InAs clusters are marked by arrows.

pronounced effect on the properties of VCQD structures by analogy with (InGaAs)/GaAs systems [10].

CONCLUSION

Thus, our experiment shows that layers with coherent InAs inclusions can be fabricated in a single-crystal silicon matrix. The quality of the fabricated structures depends strongly on the substrate temperature, growth sequence, and sample geometry. It is also shown that the silicon matrix can accommodate only a limited amount of InAs in the form of coherent clusters. Increasing the amount of the deposited InAs leads to the formation of large dislocated InAs clusters, accumulating the excess InAs in silicon overgrowth. Taking into account previous STM results [3], we conclude that, to obtain high-quality structures with multiple InAs inclusions in a silicon matrix, the average thickness of the deposited InAs, the thickness of the Si spacer between the InAs insertions, and the substrate temperature during InAs deposition and silicon overgrowth are to be optimized.

ACKNOWLEDGMENTS

The authors are grateful to Yu.B. Samsonenko for participation in the growth experiments and to I.P. Soshnikov for valuable consultations.

The work was supported by INTAS (grant no. 96-0242), the Russian Foundation for Basic Research (project nos. 98-02-18317 and 99-02-16799), scientific programs “Promising Technologies and Devices for Microelectronics and Nanoelectronics” (project no. 02.04.5.1.40.É.46) and “Physics of Solid-State Nanostructures” (project no. 98-2029).

REFERENCES

1. N. N. Ledentsov, in *Proceedings of the 23rd International Conference on Physics of Semiconductors, Berlin, 1996*, Ed. by M. Scheffer and R. Zimmermann (World Scientific, Singapore, 1996), Vol. 1, p. 19.
2. G. É. Tsyrlin, V. N. Petrov, V. G. Dubrovskiĭ, *et al.*, Pis’ma Zh. Tekh. Fiz. **24** (8), 10 (1998) [Tech. Phys. Lett. **24**, 290 (1998)].
3. G. E. Cirlin, V. G. Dubrovskii, V. N. Petrov, *et al.*, Semicond. Sci. Technol. **13**, 1262 (1998).
4. G. É. Tsyrlin, V. N. Petrov, V. G. Dubrovskiĭ, *et al.*, Fiz. Tekh. Poluprovodn. (St. Petersburg) **33**, 1066 (1999) [Semiconductors **33**, 972 (1999)].
5. J. Tersoff, C. Teichert, and M. G. Lagally, Phys. Rev. Lett. **76**, 1675 (1996).
6. N. N. Ledentsov, V. A. Shchukin, M. Grundmann, *et al.*, Phys. Rev. B **54**, 8743 (1996).
7. G. É. Tsyrlin, V. N. Petrov, N. K. Polyakov, *et al.*, Fiz. Tekh. Poluprovodn. (St. Petersburg) **33**, 1158 (1999) [Semiconductors **33**, 1054 (1999)].
8. G. M. Gur’yanov, V. N. Demidov, N. P. Korneeva, *et al.*, Zh. Tekh. Fiz. **67** (8), 111 (1997) [Tech. Phys. **42**, 956 (1997)].
9. R. Kilaas, in *Proceedings of the 45th Annual EMSA Meeting, 1987*, Ed. by G. W. Bailey (San-Francisco Press, San Francisco, 1987), p. 66.
10. G. É. Tsyrlin, V. N. Petrov, S. A. Masalov, and A. O. Golubok, Fiz. Tekh. Poluprovodn. (St. Petersburg) **33**, 733 (1999) [Semiconductors **33**, 677 (1999)].

Translated by D. Mashovets

Semiconductors, Vol. 34, No. 7, 2000, pp. 815–816. Translated from Fizika i Tekhnika Poluprovodnikov, Vol. 34, No. 7, 2000, pp. 844–845.
Original Russian Text Copyright © 2000 by Sinyavskiĭ, Sokovnich.

LOW-DIMENSIONAL SYSTEMS

Impurity Absorption of Light in Confined Systems Subjected to a Longitudinal Magnetic Field

É. P. Sinyavskiĭ and S. M. Sokovnich
Institute of Applied Physics, Academy of Sciences of Moldova, Chisinau, 2028-MD Moldova

Submitted August 16, 1999; accepted for publication, January 27, 2000

Abstract—The multiphonon-assisted impurity absorption of light is analyzed theoretically. The bound state is described in terms of the zero-radius potential model. The obtained frequency dependence of the light absorption coefficient and the full widths at half maximum (FWHMs) of the absorption lines are compared with experimental data. © *2000 MAIK “Nauka/Interperiodica”.*

The magnetooptical absorption due to an electron transition from a shallow donor ($D^{(-)}$ center) to the Landau levels in systems with GaAs–$Ga_{0.75}Al_{0.25}$As multiple quantum wells (QWs) was studied experimentally by Huant *et al.* [1]. The frequency dependence of the light absorption coefficient was oscillatory with the peaks' full width at half-maximum (FWHM) $\Delta = 4.8$ meV. Experimental studies showed that the quantity $K(\Omega)$ attained its maximum for the transition of a bound electron to the first Landau level and decreased with increasing Landau level number. Fujito *et al.* calculated the light absorption coefficient, describing the localized state of an electron at the $D^{(-)}$ center in terms of Gaussian variation functions [2]. To explain the observed values of $K(\Omega)$ quantitatively, they assumed that the shape of the absorption lines was described by a Lorentzian function with FWHM $\Delta = 4.8$ meV. However, if the magnetic field is parallel to the size-quantization axis (longitudinal magnetic field), the electron energy spectrum is completely quantized, i.e., consists of a series of discrete levels

$$E_c = \hbar\omega_c(N+1/2) + \varepsilon_0\nu^2,$$

where $\varepsilon_0 = \pi^2\hbar^2/2m_cd^2$ is the size-quantization energy step, d is the rectangular QW width, and ω_c is the cyclotron frequency for an electron with effective mass m_c. Hence, the absorption line broadening can only be associated with electron inelastic scattering by phonons (electron transitions between Landau levels with absorption or emission of an acoustic phonon). However, in this case, the FWHM of absorption lines is $\Delta \sim 10^{-3}$ meV for typical GaAs–AlGaAs QW parameters, which is much lower than the experimental value [1].

In this study, $K(\Omega)$ is calculated using the model of multiphonon optical processes [3, 4]. As shown by experimental studies [5], the binding energy of $D^{(-)}$ centers in bulk semiconductors is low ($E_i \approx 0.5$ meV) and increases with increasing magnetic field H. Such behavior can be well described in terms of the zero-radius potential model [6]. As follows from experimental data [1], E_i in confined systems increases with increasing H: $E_i \approx 1$ meV in the zero field and $E_i \approx 7$ meV for $H = 20$ T. Theoretical calculations of E_i with the use of variation wave functions [2] or in terms of the zero-radius potential model [7] are in qualitative agreement with experimental data [1]. In narrow QWs ($d <$ 100 Å), ε_0 may significantly exceed E_i (for $d = 100$ Å, $\varepsilon_0 \approx 51$ meV for a typical quasi-2D GaAs–AlGaAs system). Hence, $E_i/\varepsilon_0 \ll 1$ for $D^{(-)}$ centers and the multiphonon light absorption may be very efficient.

The final expression, obtained for $K(\Omega)$ with the use of the wave functions $\Psi_S(\mathbf{r})$ in the zero-radius potential model [7] and a quasi-classical description of crystal lattice vibrations [8], has the form

$$K(\Omega) = K_0\sum_N\left\{\frac{(N+1)}{(\hbar\Omega+\hbar\omega_c)^2} + \frac{N}{(\hbar\Omega-\hbar\omega_c)^2}\right\} \times \exp\left\{-\frac{[E_i+\hbar\omega_c(N+1/2)+\varepsilon_0-\hbar\Omega]^2}{2\alpha\hbar^2}\right\}. \quad (1)$$

Here,

$$K_0 = \frac{8e^2n_DE_i^2\omega_c}{n_0\Omega m_cc}\sqrt{\frac{2}{\pi\alpha}},$$

$$\alpha = \sum_{\mathbf{q}}\frac{1}{\hbar^2}|C_q|^2|M_S(\mathbf{q})|^2(2N_q+1), \quad (2)$$

$$M_S(\mathbf{q}) = \int|\Psi_S(\mathbf{r})|^2\exp[i(\mathbf{qr})]d\mathbf{r},$$

$$N_q = [\exp(\hbar\omega_q/k_0T)-1],$$

where n_D is the shallow-donor concentration, C_q is the electron–phonon coupling constant, N_q is the equilibrium distribution of phonons with energy $\hbar\omega_q$ and wave vector $\mathbf{q}$, and n_0 is the refractive index of the confined

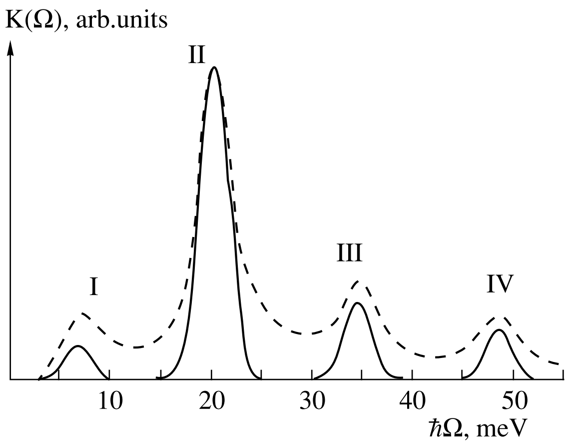

Frequency dependence of the light absorption coefficient. Peaks I, II, III, and IV correspond to the transitions of localized electrons to the zeroth, first, etc., Landau levels, respectively. The frequency dependence of the absorption coefficient obtained in [2] is shown by dashed line.

system. When deriving (1), we assumed that $E_i/\varepsilon_0 \ll 1$ ($E_i < \hbar\omega_c$) and that electron transitions occur from the bound state to Landau levels of the first ($\nu = 1$) size-quantization state. As evident from (1), the frequency dependence of the light absorption coefficient is described by a series of Gaussian peaks spaced by $\hbar\omega_c = 12$ meV. In accordance with (1), the FWHM Δ of these absorption lines is given by

$$\Delta = 2\sqrt{2\ln 2\hbar^2\alpha}. \tag{3}$$

For shallow donor states, the binding energy in a quantizing magnetic field is mainly governed by $\hbar\omega_c/2$, the shift of the conduction-band bottom. If we restrict our consideration to narrow rectangular QWs with $\hbar\omega_c \ll \varepsilon_0$, then the impurity binding energy mainly depends on the size-quantization energy. Therefore, the influence of the magnetic field on the wave function of the localized state may be neglected. In this approximation, the wave function of an impurity-bound state can be written as a product of the wave function of 1D motion in a rectangular QW by the wave function of a bound state in the zero-radius potential for 2D systems [9]:

$$\Psi_S^{(0)} = \sqrt{\frac{2\pi}{d^2}}\sin\left(\frac{\pi z}{d}\right)K_0\left[\frac{\pi\rho}{d}\right], \tag{4}$$

where $K_0(x)$ is the zero-order Macdonald function and $\rho^2 = x^2 + y^2$.

In the case of electron interaction with acoustic phonons at $N_q \approx \hbar wq/k_0T > 1$, the FWHM of the absorption line is calculated directly, taking into account (4), to yield

$$\Delta = 2\sqrt{\frac{6\pi\ln 2}{\rho_0 w^2 d^3}k_0 T E_1^2}\ [\text{eV}], \tag{5}$$

where w is the velocity of sound, ρ_0 is the mass density of the system, and E_1 is the electron deformation-potential constant. For typical parameters of GaAs–AlGaAs QWs, $\rho_0 = 5.4$ g/cm^3, $w = 3 \times 10^5$ cm/s, $E_1 = 10$ eV for $T = 10$ K, and $d = 50$ Å and $\Delta \approx 3.4$ meV.

The figure shows the frequency dependence of the light absorption coefficient (in relative units) governed by electron transitions from donor-bound states to Landau levels (solid line). It is this oscillatory frequency dependence of the light absorption coefficient that was observed in systems with GaAs–$Al_{0.25}Ga_{0.75}As$ multiple QWs [1]. The dashed line shows the frequency dependence $K(\Omega)$ presented in [2], consistent with experimental data [1]. As evident from the figure, the light absorption in electron transition from the donor-bound state to the first Landau level ($N = 1$) is the most efficient. The experimental FWHM $\Delta = 4.8$ meV differs somewhat from that calculated by (5). This is due to the existence of inhomogeneous broadening typical of the optical properties of systems with multiple QWs.

Hence, the proposed multiphonon mechanism of absorption-line broadening in a longitudinal magnetic field is important for single QWs and may be essential (along with the inhomogeneous broadening) for multilayered structures.

REFERENCES

1. S. Huant, S. P. Najda, and B. Etienne, Phys. Rev. Lett. **65**, 1486 (1990).
2. M. Fujito, A. Natori, and H. Yasunada, Phys. Rev. B **51**, 4637 (1995).
3. Yu. E. Perlin, Usp. Fiz. Nauk **80**, 553 (1963) [Sov. Phys. Usp. **6**, 542 (1963)].
4. V. A. Kovarskiĭ, *Multiquantum Transitions* (Shtiintsa, Kishinev, 1974).
5. M. Toniguchi and S.-I. Narito, J. Phys. Soc. Jpn. **47**, 1503 (1979).
6. E. P. Sinyavskii and E. Yu. Safronov, Phys. Status Solidi B **160**, 357 (1990).
7. E. P. Sinyavskii, S. M. Sokovnich, and E. I. Pasechnik, Phys. Status Solidi B **209**, 55 (1998).
8. Yu. E. Perlin and B. S. Tsukerblat, *The Effects of Electron–Phonon Interaction in Optical Spectra of Paramagnetic Impurity Ions* (Shtiintsa, Kishinev, 1976).
9. É. P. Sinyavskiĭ, Izv. Akad. Nauk Resp. Mold., Ser. Fiz. Tekh., No. 1, 12 (1992).

Translated by S. Goupalov

Semiconductors, Vol. 34, No. 7, 2000, pp. 817–824. Translated from Fizika i Tekhnika Poluprovodnikov, Vol. 34, No. 7, 2000, pp. 846–856.
Original Russian Text Copyright © 2000 by Bagraev, Buravlev, Ivanov, Klyachkin, Malyarenko, Rykov, Shelykh.

LOW-DIMENSIONAL SYSTEMS

Charge Carrier Interference in One-Dimensional Semiconductor Rings

N. T. Bagraev*, A. D. Buravlev*, V. K. Ivanov, L. E. Klyachkin*,**
A. M. Malyarenko*, S. A. Rykov, and I. A. Shelykh****

** Ioffe Physicotechnical Institute, Russian Academy of Sciences, ul. Politekhnicheskaya 26, St. Petersburg, 194021 Russia*
*** St. Petersburg State Technical University, ul. Politekhnicheskaya 29, St. Petersburg, 194251 Russia*

Submitted February 7, 2000; accepted for publication February 7, 2000

Abstract—Interference of the ballistic charge carriers in one-dimensional (1D) rings formed by two quantum wires in the self-ordered silicon quantum wells was investigated for the first time. The charge carrier transmission coefficient, which is dependent on the carrier energy, is calculated as a function of the length and modulation depth of the parallel quantum wires. The wires can be linked to the two-dimensional reservoirs either by the common source–drain system or by the quantum point contacts. It is predicted that the conductance of a 1D ring in the first case is four times higher than in the second due to the carrier interference. The calculated dependences manifest themselves in the conductance oscillations observed in the 1D silicon rings upon varying the source–drain voltage or the external magnetic field. The results obtained made it possible to design an Aharonov–Bohm interferometer based on a 1D silicon ring in the weak localization mode; its characteristics are demonstrated in the studies of the phase coherence in the tunneling of single charge carriers through the quantum point contact. *© 2000 MAIK "Nauka/Interperiodica".*

1. INTRODUCTION

It is known that the basic parameter commonly used to characterize the charge carrier transport in semiconductor structures is the conductivity, which is primarily determined by the inelastic scattering processes. This statement is valid if the typical dimensions of semiconductor devices under study are larger than the inelastic scattering mean free path; however, the statement should be corrected to take into account the effects related to the wave properties of electrons when the devices based on quantum wires and quantum dots (QDs) are considered [1, 2]. In such structures with one or more one-dimensional (1D) channels whose length is smaller than the mean free path, the charge carrier transport proceeds without Joule losses, since inelastic scattering is suppressed [1–4]. Thus, the ballistic properties can be exhibited by the carriers under 1D transport conditions.

To the first approximation, conductance of a ballistic quantum wire depends only on the transmission coefficient T and does not contain any information about the phase of the tunneling charge carriers [1, 2]:

$$G = G_0 T. \tag{1}$$

Here,

$$G_0 = g_s g_v \frac{e^2}{h} N, \tag{2}$$

where g_s and g_v are the spin and valley degeneracy factors, respectively, and N is the number of occupied quantum confinement subbands, which corresponds to the number of the highest occupied 1D subband in the quantum wire and can be varied by the gate voltage V_g that controls the number of carriers in the wire [5]. The $G(V_g)$ curve has a pronounced steplike shape, because the wire conductance changes abruptly each time the Fermi level crosses the bottom of a quantum-confinement subband. It is worth noting that the use of a split gate [5] to record the quantized conductance $G(V_g)$, observed as a series of 1D conductance plateaus separated by steps of height $g_s g_v e^2/h$, is the main technique employed to identify the ballistic quantum wires [6, 7].

Since the wave-function phase changes upon tunneling of the charge carrier through a low-dimensional structure, one has to measure the phase of the transmission and reflection coefficients to obtain the data on the coherence of electron and hole transport. Currently, studies of the negative magnetoresistance in the weak localization mode [8] and of the conductance fluctuations under the single-electron transport conditions [3] are mainly used to obtain information on the coherent component of the electron transport. However, the phase of the charge carrier transmission coefficient in 1D or zero-dimensional structures cannot be accurately measured with these techniques; measurement became possible only with the development of the nanotechnology for creating 1D Aharonov–Bohm (AB) rings in the metallic [9] and semiconductor [10, 11] two-dimensional (2D) systems, which are the most illustrative examples of a mesoscopic conducting structure. An interferometer based on such a ring was used to demonstrate the phase coherence of the single-electron trans-

1063-7826/00/3407-0817$20.00 © 2000 MAIK "Nauka/Interperiodica"

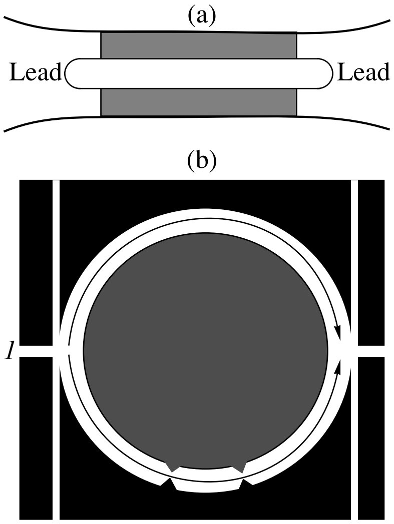

Fig. 1. One-dimensional ring composed of two parallel-connected quantum wires linked to the 2D reservoirs (a) by a common source–drain system and (b) by quantum point contacts *1* and *2*.

port through a QD embedded in one of its arms [10, 11]. Success of this experiment requires that the structure design with the interferometer ring (composed of two 1D wires) be linked to the 2D reservoir by two quantum point contacts. In only this case, the number of charge carriers present in the ring at a given instant is limited to just a single carrier, which makes it possible to control the phase shifts of the AB oscillations originating from the carrier transport through the quasi-bound states in a QD.

The use of 1D rings linked to the 2D reservoirs by a common source–drain system, in turn, creates broad possibilities of studying the quantum interference in the case where a charge carrier is present in both interferometer arms simultaneously. With this interferometer design, one can expect to observe the effects related to the doubling of the quantum conductance steps; the demonstration of these effects was one of the goals of this study.

Another important goal is the study of the coherent transport through QDs embedded in a 1D ring in the weak localization mode. In this case, important information can be obtained by measuring the transmission coefficient phase as a function of the strength of external magnetic field (normal to the ring plane) and in relation to the charge carrier energy. To tackle this problem, we used an AB interferometer based on a silicon 1D ring in the weak localization mode with a quantum point contact embedded in one of its arms, which enabled us to record the phase shift acquired by the charge carrier upon tunneling through the quantum confinement levels.

First, we consider the energy and field dependences of the coefficient of transmission through the system of parallel quantum wires linked to the 2D reservoir either by a common source–drain system or by quantum point contacts; thus, the features in quantized conductance related to the quantum interference will be revealed. Next, we present experimental data on the quantized conductance investigations carried out using the aforementioned interferometer designs implemented on the basis of 1D rings formed within self-organized silicon quantum wells. The results obtained indicate that interference in the parallel wires affects the height of the quantum steps in the conductance and that the phase coherence is maintained in the single-electron tunneling through the quantum point contact and in the processes resulting in negative magnetoresistance in 1D rings under weak localization conditions.

2. BALLISTIC CARRIER INTERFERENCE IN 1D RINGS COMPOSED OF TWO QUANTUM WIRES LINKED TO THE 2D RESERVOIR BY A COMMON SOURCE–DRAIN SYSTEM

We consider a system composed of two quantum wires connected in parallel (Fig. 1a). In general, the wires should not be identical. In the classical case, the conductance of this system is given by the sum of the wire conductances:

$$G = G_1 + G_2. \tag{3}$$

However, this is not true in the quantum case related to the wave properties of the electron, which results in the interference between the waves propagating through different arms of the 1D ring. The phase shift between these waves depends on the external longitudinal electric and transverse magnetic fields; the system conductance can be changed by varying the field strength.

Let the probability amplitude for the transmission of an electron with the wave number $k \propto E$ through the upper arm be equal to t_1, and that through the lower arm be equal to t_2.The squares T_1 and T_2 of the absolute values of the amplitudes are proportional to the conductances of the corresponding arms G_1 and G_2. Let us designate the phases of the probabilities t_1 and t_2 as ϕ_1 and ϕ_2. The total amplitude of the transmitted-electron wave function equals

$$t = t_1 + t_2 = \sqrt{T_1}e^{i\phi_1} + \sqrt{T_2}e^{i\phi_2}, \tag{4}$$

and the transmitted flux density equals

$$\begin{aligned} T = tt^* &= (\sqrt{T_1}e^{i\phi_1} + \sqrt{T_2}e^{i\phi_2}) \\ &\times (\sqrt{T_1}e^{-i\phi_1} + \sqrt{T_2}e^{-i\phi_2}) \\ &= T_1 + T_2 + 2\sqrt{T_1T_2}\cos(\phi_1 - \phi_2). \end{aligned} \tag{5}$$

Taking into account the quantum interference and formula (1), we obtain the following expression for the conductance of two parallel-connected wires:

$$G = G_1 + G_2 + 2\sqrt{G_1G_2}\cos(\phi_1 - \phi_2). \tag{6}$$

This formula differs from (3) in the presence of the interference term $2\sqrt{G_1G_2}\cos(\phi_1 - \phi_2)$. In the classical case, when the arms are macroscopic objects, this term has to be averaged and, as a result, vanishes. However, if the arms are ballistic quantum wires, this term must be taken into account; its inclusion has immediate impact on the conductance and its dependence upon the external factors and the parameters of the arms of the 1D ring. If the two quantum wires are identical, the phase shift is zero and the total conductance of the two parallel-connected wires is four times the conductance of an individual wire. This is in contrast to the classical case, where the total conductance is twice the conductance of an individual wire.

We now consider the various possible reasons for the appearance of the phase shift $\phi_1 - \phi_2$.

First, it may result from the application of magnetic field B threading the ring:

$$\Phi = \iint\limits_{\Sigma}\mathbf{B}d\mathbf{S} = \oint\limits_{\mathfrak{P}}\mathbf{A}d\mathbf{l}, \tag{7}$$

where Σ and $\mathfrak{P}$ are the ring area and the perimeter of the ring, respectively. The probability amplitude for transition of a free particle from the source point to the drain point is related to the vector potential A appearing in the ring plane by

$$Q = \exp\left[i\mathbf{k}(\mathbf{r}_{\text{out}} - \mathbf{r}_{\text{in}}) - \frac{ie}{\hbar c}\int\limits_{\text{in}}^{\text{out}}\mathbf{A}d\mathbf{r}\right], \tag{8}$$

where the integral is taken along the particle trajectory. If the parameters of the source and drain points are identical, the difference between the trajectories in the two arms of the ring results in the phase shift between the two transmission probability amplitudes, although the amplitude absolute values are equal. For example, in the ring formed by parallel-connected identical smooth wires (Fig. 1a) with no internal potential barriers stimulating elastic scattering of the charge carriers, the phase shift acquired upon traveling along the two arms equals

$$\begin{aligned}\phi_2 - \phi_1 &= \frac{e}{\hbar c}\left(\int\limits_1\mathbf{A}d\mathbf{r} - \int\limits_2\mathbf{A}d\mathbf{r}\right) \\ &= \frac{e}{\hbar c}\oint\limits_{\mathfrak{P}}\mathbf{A}d\mathbf{r} = \frac{e}{\hbar c}\iint\limits_{\Sigma}\mathbf{B}d\mathbf{S} = \frac{eBS}{\hbar c},\end{aligned} \tag{9}$$

which leads to the following expression describing the conductance dependence on external magnetic field:

$$G = 2G_1\left[1 + \cos\left(\frac{eBS}{\hbar c}\right)\right]. \tag{10}$$

Thus, the conductance of a 1D ring oscillates with varying magnetic field; this behavior is closely related to the well-known Aharonov–Bohm oscillations [9].

One important specific case should be noted: if $B = 0$, the ring conductance is four times greater than the conductance of an individual wire; in the classical case, the conductance increases by only two times.

The phase shift $\phi_1 - \phi_2$ may also result from the difference in the lengths of the parallel-connected wires composing the ring:

$$\phi_2 - \phi_1 = k\Delta l = \gamma U_{\text{ds}}\Delta l, \tag{11}$$

where γ is the coefficient of proportionality between the longitudinal voltage U_{ds} and the carrier wave vector $k \propto U_{\text{ds}}$. In this case, the conductance depends on the source–drain voltage:

$$G = 2G_1[1 + \cos(\gamma U_{\text{ds}}\Delta l)]. \tag{12}$$

In addition, the phase shift $\phi_1 - \phi_2$ may appear if potential barriers are present in one (or both) of the arms: the phase of the transmitted wave shifts upon tunneling through the barrier, because the transmission amplitude is a complex quantity. The dephasing depends primarily on the wave vector of the carrier incident on the barrier system. Since $k \propto U_{\text{ds}}$, the conductance of an individual modulated quantum wire equals

$$G_1 = g_s g_v\frac{e^2}{h}NT(U_{\text{ds}}), \tag{13}$$

where $T(U_{\text{ds}})$ is the transmission coefficient for the charge carriers, which oscillates as a function of the source–drain voltage [12]. Correspondingly, the conductance of a system composed of a smooth wire connected in parallel to a modulated wire is given by

$$G = g_s g_v\frac{e^2}{h}N(1 + T + 2\sqrt{T}\cos\Delta\phi), \tag{14}$$

where $\Delta\phi$ is the wave phase shift resulting from the passage of a carrier through the system.

To calculate the energy dependence of the charge-carrier transmission coefficient $T(U_{\text{ds}})$ in a modulated quantum wire, we proposed the δ-barrier model [12]. It is assumed in this model that the actual shape $V(x)$ of a potential barrier can be replaced by a δ-function, so that the scattering potential in the wire is represented by

$$U(x) = \alpha\sum_{j=1}^{n}\delta(x - Lj), \tag{15}$$

where n is the number of the barriers, L is the distance between them, and α stands for the barrier strength defined as

$$\alpha = \int\limits_{-\infty}^{+\infty}V(x)dx. \tag{16}$$

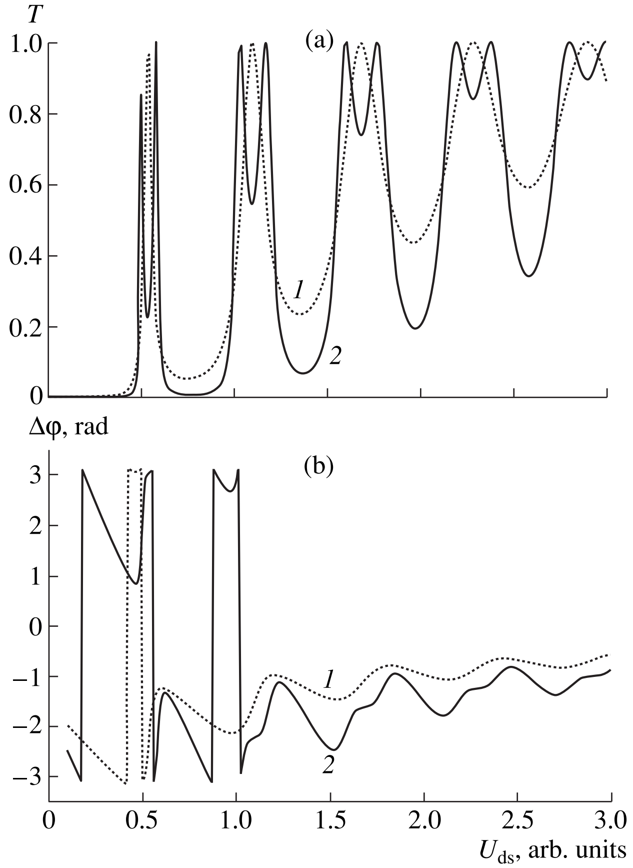

Fig. 2. Quantum-interference-related oscillations of (a) the transmission coefficient $T(U_{ds})$ and (b) the phase shift $\Delta\phi(U_{ds})$ with variation of the source–drain voltage applied to a quantum wire modulated by δ-like barriers. Calculation was performed in the context of the δ-barrier model; no potential drop along the wire was assumed. The conductance $G = (4e^2/h)T(E)$ corresponds to the occupation of the 1D subbands in an *n*-type Si(100) wire ($g_s = 2$, $g_v = 2$), as well as to the Fermi level position corresponding to the occupation of the 1D subbands in a *p*-type silicon wire. The barrier strength $\alpha = 1$ and the distance between the barriers $L = 5$ (in atomic units); the number of barriers *n* equals (*1*) 2 and (*2*) 3.

In the context of this model, the dependences of the transmission coefficient *T* and the phase shift $\Delta\phi$ on $k \propto U_{ds}$ were obtained analytically and numerically. The calculated curves are plotted in Fig. 2 for the case of a quantum wire modulated by two or three barriers. One can see that the $T(U_{ds})$ curve has the shape of damped oscillations. The phase varies between $-\pi$ and π and tends to zero with increasing $k \propto U_{ds}$.

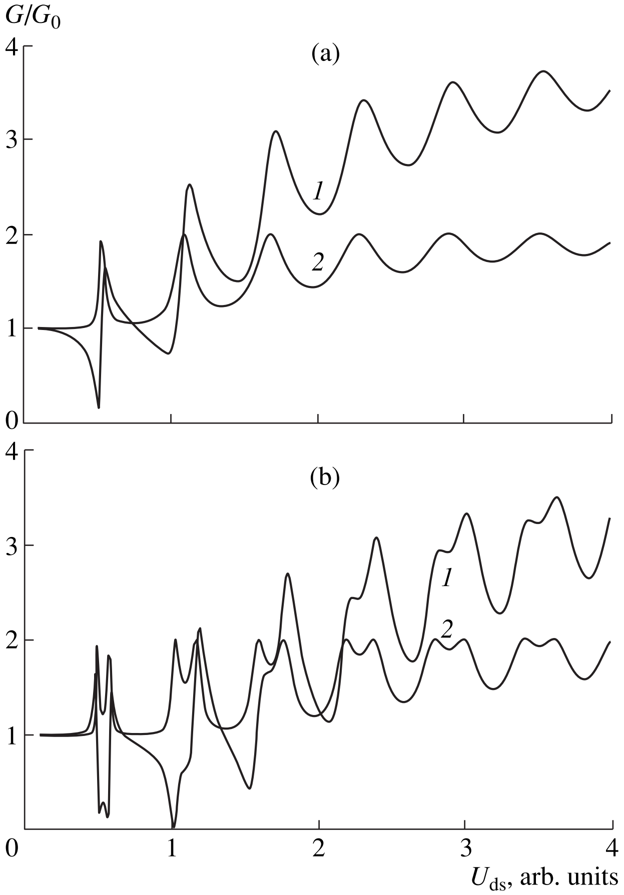

Fig. 3. Oscillations of the conductance in relation to the source–drain voltage applied to the 1D ring connected to the 2D reservoirs by a common source–drain system (Fig. 1a); one of the ring arms is modulated by δ-barriers. The barrier parameters are $\alpha = 1$ and $L = 5$, and the number of barriers *n* equals (a) 2 and (b) 3. The calculation was performed (*1*) with and (*2*) without considering the interference effects.

Using the dependences shown in Fig. 2, we employ equation (14) to calculate the conductance of a 1D ring composed of two parallel-connected wires linked to the 2D reservoir by a common source–drain system. In Fig. 3, we present the $G(U_{ds})$ dependences of such a system with one of its arms modulated by two or three barriers. One can see that inclusion of the interference term significantly affects the shape of the $G(U_{ds})$ curve. At high fields, the total conductance exceeds the sum of the individual arm conductances by ~2 times. Conversely, at low source–drain voltages, the interference results in the suppression of the conductance down to zero, which is very clearly seen in Fig. 3.

If the longitudinal electric and normal magnetic fields are simultaneously applied to the ring (with one of the arms modulated by barriers), the conductance is given by

$$G = G_0\left[1 + T + 2\sqrt{T}\cos\left(\Delta\phi + \frac{eBS}{\hbar c}\right)\right], \qquad (17)$$

where $\Delta\phi$ is the phase shift acquired by the carrier traveling through the barrier system under the applied source–drain voltage, and $eBS/\hbar c$ is the phase shift resulting from the Aharonov–Bohm effect. In Fig. 4, we plot the corresponding dependences $G = G(U_{ds})$ calculated for the different magnitudes of the external magnetic field assuming that one of the ring arms is modulated by three δ-barriers. Obviously, the magnetic field considerably affects the source–drain voltage dependence of the conductance; in particular, the asymptotic value approached by G with increasing U_{ds} is strongly influenced.

Experimental studies of the effects of quantum interference in the conductance of a 1D ring linked to 2D reservoirs by a common source–drain system were carried out on the mesoscopic nanostructures formed in the self-ordered silicon quantum wells.

Single quantum wells of this kind are spontaneously formed in the unltrashallow diffusion p^+-profiles at the Si(100) surface [12, 13]. Such impurity profiles were formed by the nonequilibrium boron diffusion under the precise control of the fluxes of intrinsic interstitials and vacancies generated by the Si–$\mathrm{SiO_2}$ interface. These defects stimulate the dopant diffusion by the *kick-out* and vacancy-dissociation mechanisms, respectively [14]. Varying the parameters of the surface oxide layer, the concentration of the chlorine-containing component in the gas phase, and the diffusion temperature, one can attain a balance between these competing mechanisms. The sharp reduction of the diffusion rate under balance conditions enables us to obtain ultrashallow p^+-profiles at the (100) surface of n-type silicon ($N(P) = 2 \times 10^{14}$ cm^{-3}) by the short-term boron diffusion from the gas phase at 900°C. The front and back surfaces of the substrate were thermally oxidized prior to the dopant diffusion, which was performed through the photolithographically defined window in the oxide mask. The depth of the ultrasharp diffusion profile and the boron concentration in it, measured by the secondary-ion mass-spectrometry, equal 7 nm and 10^{21} cm^{-3}, respectively.

The grown ultrashallow diffusion p^+-profiles were studied by cyclotron resonance (CR) and quantized conductance methods. The CR angle dependences were recorded at 3.8 K by the X-band 9.1–9.5 GHz ESR spectrometer [13, 15]. The quenching and shift of the CR peaks exhibit 180° symmetry with respect to the magnetic field rotation in the {100} plane, normal to the p^+–n junction plane. This indicates that there is a single self-ordered longitudinal quantum well (LQW) between the heavily doped 2D impurity barriers within the ultrashallow diffusion p^+-profile.

The ESR and thermoelectric-power studies demonstrated that such 2D barriers with ultrahigh boron concentration possess pyroelectric properties due to the presence of the reconstructed $\mathrm{B^+}$–$\mathrm{B^-}$ impurity dipoles that have trigonal symmetry [13]. As electrostatic ordering within the pyroelectric barriers takes place, the reconstructed boron dipoles provide for the transverse confinement of the charge carrier motion in the LQW plane; thus, smooth and modulated quantum wires are formed (see also [12, 13]). A quantum wire of such type appears when the external electric field $U_{\mathrm{DS}} = U_g + U_{\mathrm{ds}}$ is applied along the LQW. On the one hand, application of this field results in the transverse confinement caused by the impurity dipole ordering (due to the U_g component); on the other hand, the field initiates the transport of the individual charge carriers (due to the U_{ds} component). In this study, we used this object to investigate interference effects in the quantized conductance of a 1D ring formed in the plane of a self-ordered QW.

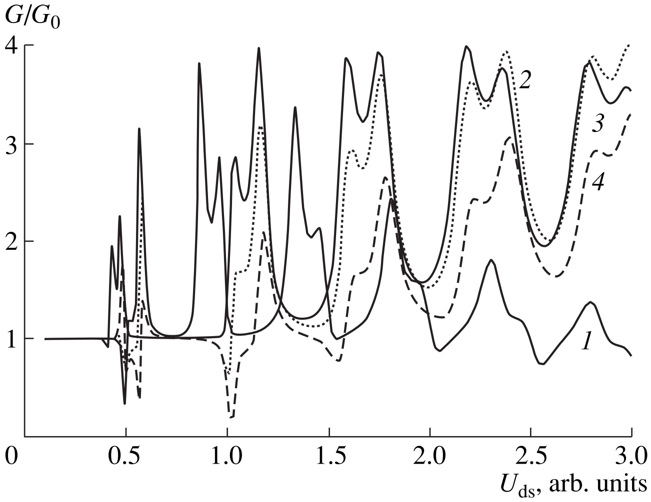

Fig. 4. Quantum-interference-related oscillations of the conductance in relation to the source–drain voltage applied to the 1D ring under external magnetic field. One of the ring arms is modulated by δ-like barriers ($\alpha = 1$ and $L = 5$, $n = 3$) and is connected to the 2D reservoirs by a common source–drain system (Fig. 1a). The phase shift $\Delta\phi$ is proportional to the magnetic flux Φ through the ring ($\Delta\phi = e\Phi/\hbar c = eBS/\hbar c$) and equals (*1*) π, (*2*) π/4, (*3*) π/2, and (*4*) 0.

A 1D ring composed of two electrostatically ordered quantum wires was formed around a microdefect, whose STM image is shown in Fig. 5a. Such microdefects, whose size and distribution depend on the conditions of the preliminary oxidation and subsequent selective etching, occur due to the injection of the controlled flux of self-interstitials and thread through the entire depth of the ultrashallow diffusion profile. A 1D ring is formed electrostatically at the intersection of the microdefect and the quantum well. The problem of reproducible fabrication of point contacts connecting the 1D ring to the 2D reservoir of the quantum well is rather complicated. However, controllably varying the surface deformation potential at the preliminary oxidation stage, one can obtain the necessary concentration of microdefects composed of self-interstitials in the vicinity of the 1D ring; in this way, 1D rings either with the common source–drain system (Fig. 5a) or with the two quantum point contacts (Fig. 5b) can be formed.

The width of the dynamic quantum wires formed around the microdefect between the two pyroelectric barriers increases as the electrostatic ordering of the

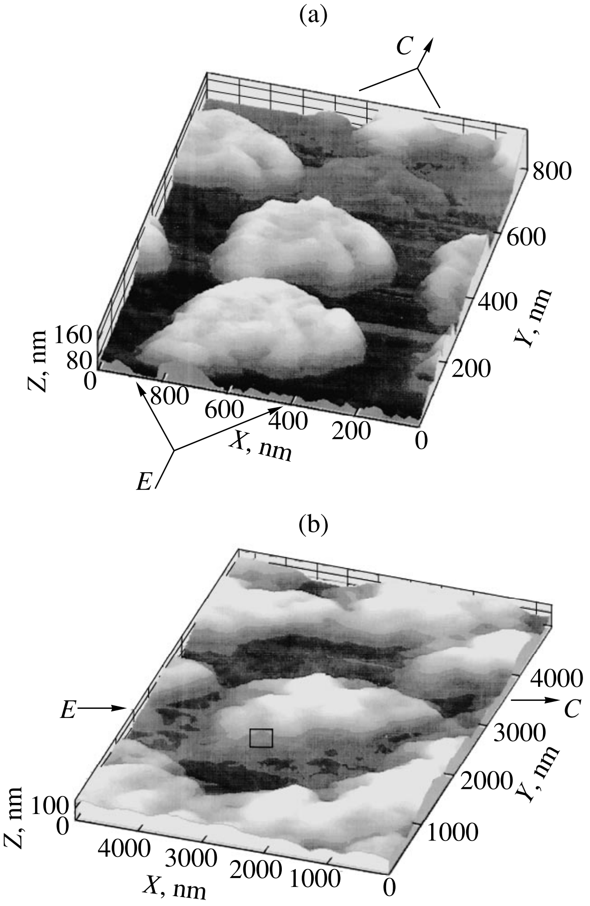

Fig. 5. Three-dimensional STM image of the microdefects threading through the self-ordered quantum well within an ultrashallow diffusion p^+-profile in Si(100) single crystal. A 1D ring is formed in the quantum well plane around such a defect; the ring may be connected to the 2D reservoirs (a) by a common source–drain system and (b) by quantum point contacts. Letters *E* and *C* denote the positions of the source and the drain in Fig. 5a and of the emitter and collector in Fig. 5b. The rectangle in Fig. 5b indicates the position of the additional point contact in one of the arms.

impurity dipoles takes place, whereas their modulation is determined by the number of unreconstructed dipoles that can be regarded as δ-like barriers. We note that the number of unreconstructed dipoles can be controlled by varying the concentration of the chlorine-containing compounds, which are responsible for the uniformity of the dopant distribution within the 2D pyroelectric barriers.

The quantized conductance that appears due to the 1D transport of the individual holes in the quantum wires composing the 1D ring (Fig. 5a) was observed at 77 K upon application of external electric field U_{DS} (Fig. 6). The cross section of the dynamic quantum wires under consideration is determined by the width of the LQW and of the electrostatically induced transverse channel; both are close to the distance between the dipoles, ~2 nm, which is in turn related to the boron concentration in the pyroelectric barriers. These parameters, along with the 2D hole density (2.5×10^{13} m^{-2}) and the effective 1D channel length (see Fig. 5a), which is smaller than the inelastic scattering mean free path, govern the contribution provided by light and heavy holes to the quantized conductance and reflected in the step height.

The observed doubling of the quantum step height (Fig. 6) compared to the value obtained for an individual quantum wire [12] is directly related to the influence of the quantum interference on the conductance of a 1D ring with a common source–drain system, which was discussed above (Fig. 3). It should be mentioned that interference effects evident in the light- and heavy-hole transport apparently result from the shift of the transmission coefficient phase due to the presence of narrow potential barriers in one of the arms of the 1D ring. This is evidenced by the observation of oscillations superimposed on the quantized conductance plateau (Fig. 6).

Although the estimate of the energy separation between the 1D subbands based on the area of the quantum wire cross section (2×2 nm^2) gives a value much in excess of the temperature broadening at 77 K, the quantized conductance decays with the increase in the number of the highest occupied subband (see Fig. 6). We suppose that the observed quenching of the quantized conductance is caused by the nonlinear noise fluctuations that develop when eU_{ds} becomes comparable to the energy gap between the 1D subbands [16].

3. BALLISTIC CARRIER INTERFERENCE IN 1D RINGS COMPOSED OF TWO QUANTUM WIRES LINKED TO THE 2D RESERVOIR BY QUANTUM POINT CONTACTS

In the case considered above, both wires composing the 1D ring originate directly from the carrier reservoirs. However, the wires can be connected to the reservoirs through the quantum point contact (Figs. 1b, 5b). Conductance of such a system cannot exceed the conductance of an individual point contact (see (2)). Upon passing such a contact, the charge carrier enters either of the two arms with equal probability. The conductance dependence on external electric and magnetic fields is then given by the following expression:

$$\begin{aligned} G &= \frac{j_{\text{tr}}}{U_{\text{ds}}} \propto g_s g_v \frac{e^2}{h} N(1/2 + 1/2t)^2 \\ &= \frac{1}{4} g_s g_v \frac{e^2}{h} N(1 + T + 2\sqrt{T}\cos\Theta), \end{aligned} \tag{18}$$

where Θ is the total phase shift caused both by the effect of the source–drain voltage and the Aharonov–Bohm effect (see Fig. 7).

Studies of the temperature dependence of the conductance [17] revealed that it obeyed the well-known logarithmic law [8]. This indicates that the weak local-

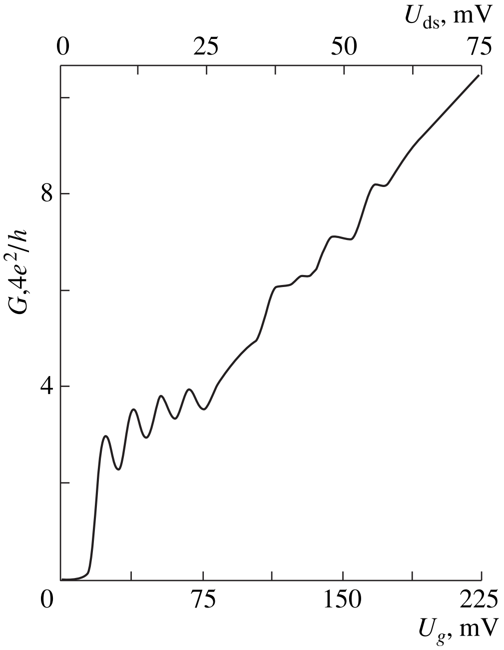

Fig. 6. Quantized conductance $G(U_g)$ as a function of U_{ds} at T = 77 K; this conductance is due to the light- and heavy-hole transport through the 1D ring composed of a smooth and a modulated quantum wire. The ring is formed in a self-ordered quantum well within an ultrashallow diffusion p^+-profile in Si(100) single crystal and is connected to the 2D reservoirs by a common source–drain system (see Fig. 1a).

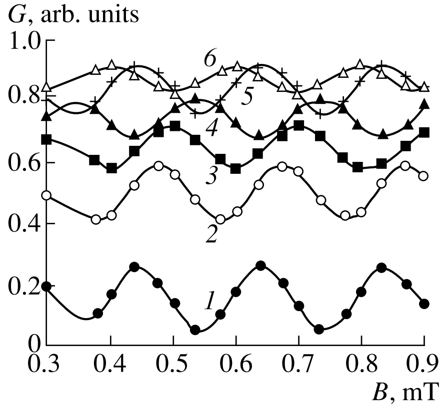

Fig. 7. Aharonov–Bohm oscillations in the conductance of a 1D ring (formed in a self-ordered silicon quantum well) with an additional quantum point contact in one of its arms. The ring is connected to the 2D reservoirs by the two other quantum point contacts (see Fig. 1b). U_g = (*1*) 7.5, (*2*) 15, (*3*) 22.5, (*4*) 30, (*5*) 37.5, and (*6*) 45 mV.

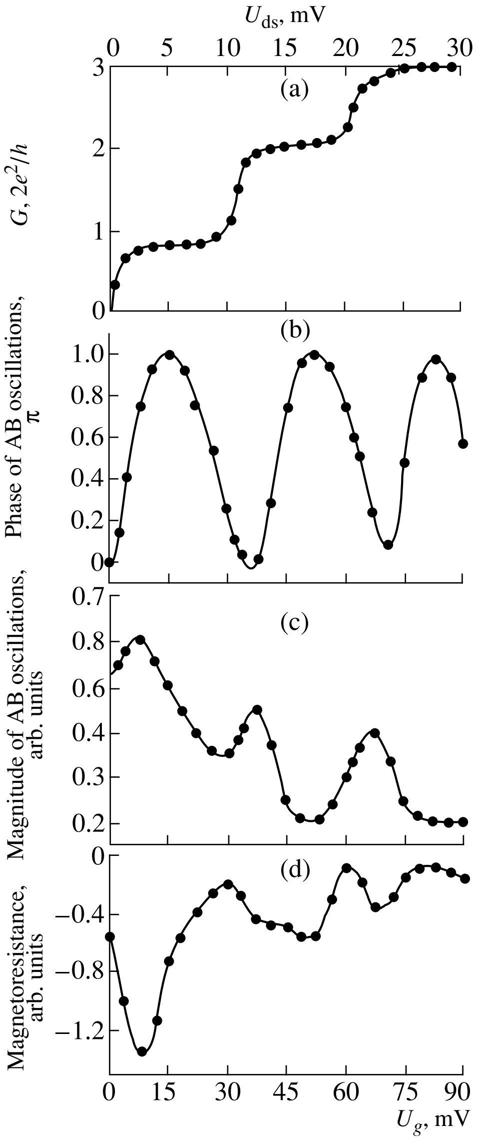

Fig. 8. (a) Quantized conductance, (b) phase shift and (c) amplitude of the Aharonov–Bohm oscillations, and (d) negative magnetoresistance in relation to U_g in a 1D ring with an additional quantum point contact in one of its arms. The ring is formed within a self-ordered silicon quantum well and is connected to the 2D reservoirs by two quantum point contacts. The field strength B = 0.055 mT. The 1D ring is formed within a self-ordered quantum well and is separated from 2D reservoirs by two quantum point contacts.

ization mode is realized in a system of heavy holes in the obtained 1D ring (Fig. 5b), which is also confirmed by the observation of negative magnetoresistance [17].

It should be emphasized that unreconstructed impurity dipoles in the pyroelectric barriers, which introduce modulation into one or both arms of the 1D ring as described above, may also serve as additional quantum point contacts (Fig. 5b). In experiments designed to measure the phase of the charge carrier transmission coefficient, the role of these quantum point contacts is similar to the role of quantum dots [10, 11]: they serve to control the current in the 1D ring. However, if an additional quantum point contact is introduced, the $G(U_g)$ dependence determined by the carrier tunneling through the quantum confinement levels is observed; on the other hand, if a quantum dot is present, one measures the periodicity of the Coulomb oscillations as a function of the gate voltage ($\Delta U_g = e/2C$, where C is the quantum dot capacitance).

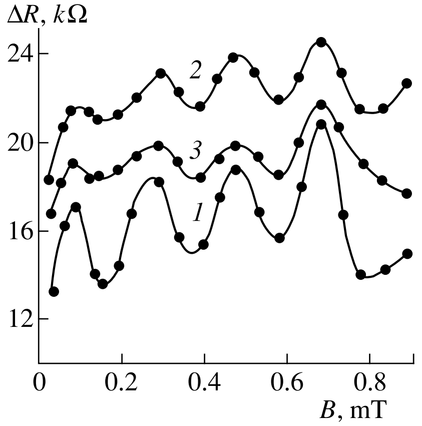

Fig. 9. Aharonov–Bohm oscillations in a 1D ring formed in a self-ordered silicon quantum well. The ring has an additional quantum point contact in one of its arms and is connected to the 2D reservoirs by the other two quantum point contacts (see Fig. 1b). U_{ds} = (*1*) 45, (*2*) 72.5, and (*3*) 87.5 mV.

Therefore, in this study, the current of heavy holes transmitted through the 1D ring, initially in the weak localization mode, was recorded as a quantum staircase of a quantum point contact conductance (Fig. 8a). The height of the quantum steps corresponds to the main contribution of heavy holes to the quantized conductance; their 2D density in the quantum well under study was 0.8×10^{13} m^{-2}. To reveal the coherent component of the charge carrier transport, the conductance quantum staircase was studied at different magnetic fields oriented perpendicularly to the plane of the 1D ring (Fig. 5b). The typical Aharonov–Bohm oscillations were observed (Fig. 7), with their amplitude and phase depending on the gate voltage U_g, which was determined as a component of the total applied voltage U_{DS} using the above-described procedure (see Figs. 8b, 8c). The phase of the transmission coefficient oscillates between 0 and π when charge carriers tunnel through the quantum confinement levels. The observed correlation of the behavior of the conductance quantum staircase (Fig. 8a) with the negative magnetoresistance (Fig. 8d) clearly demonstrates the coherence of the single-particle transport and of the weak localization processes. Reduction of the coherent component contribution to the transport of individual carriers upon an increase in the source–drain voltage (Figs. 8b–8d) that accompanies the characteristic erosion of the quantum staircase is, apparently, related to the induced transitions between the quantum-confinement levels [16] and to the enhancement of the multiparticle effects [11]. However, for the appropriate parameters of the 1D ring, the applied source–drain voltage might also induce the Aharonov–Bohm effect [9], which manifests itself, e.g., in the additional periodicity in the conductance variation both with U_{ds} and with the external magnetic field (see Fig. 9).

4. CONCLUSION

Thus, the quantum interference of light and heavy holes in 1D rings formed in the self-ordered silicon quantum wells was studied. Energy dependences of the magnitude and phase of the coefficient of transmission through the parallel-connected quantum wires linked to the 2D reservoirs either by a common source–drain system or by quantum point contacts are calculated; the dependences predict conductance enhancement caused by the coherence of individual carrier transport. It is demonstrated that, in the former case, the conductance of a 1D ring is four times higher than in the latter case, which is related to the charge carrier interference. The relationships obtained enabled us to explain the characteristics of the conductance oscillations in relation to the source–drain voltage and the external magnetic field observed in measurements of the quantized conductance of 1D silicon rings. These results create the possibility of designing an Aharonov–Bohm interferometer based on a 1D silicon ring in the weak localization mode; the coherence of the individual charge carrier transport under negative magnetoresistance conditions was demonstrated using this device.

REFERENCES

1. R. Landauer, IBM J. Res. Dev. **1**, 233 (1957).
2. M. Büttiker, Phys. Rev. Lett. **57**, 1761 (1986).
3. T. J. Thornton, Rep. Prog. Phys. **58**, 311 (1995).
4. U. Merrav and E. B. Foxman, Semicond. Sci. Technol. **10**, 255 (1996).
5. T. J. Thornton, M. Pepper, H. Ahmed, *et al.*, Phys. Rev. Lett. **56**, 1198 (1986).
6. D. A. Wharam, T. J. Thornton, R. Newbury, *et al.*, J. Phys. C **21**, L209 (1988).
7. B. J. van Wees, H. van Houten, C. W. J. Beenakker, *et al.*, Phys. Rev. Lett. **60**, 848 (1988).
8. G. Bergmann, Phys. Rep. **107**, 1 (1984).
9. S. Washburn and R. A. Webb, Adv. Phys. **35**, 375 (1986).
10. A. Yacoby, M. Heiblum, D. Mahalu, and H. Shtrikman, Phys. Rev. Lett. **74**, 4047 (1995).
11. R. Schuster, E. Bucks, M. Heiblum, *et al.*, Nature (London) **385**, 417 (1997).
12. N. T. Bagraev, V. Gel'khoff, V. K. Ivanov, *et al.*, Fiz. Tekh. Poluprovodn. (St. Petersburg) **34**, 477 (2000) [Semiconductors **34**, 462 (2000)].
13. N. T. Bagraev, L. E. Klyachkin, A. M. Malyarenko, and W. Gehlhoff, Superlattices Microstruct. **23**, 1333 (1998).
14. N. T. Bagraev, W. Gehlhoff, L. E. Klyachkin, *et al.*, Defect Diffus. Forum **143–147**, 1003 (1997).
15. W. Gehlhoff, N. T. Bagraev, and L. E. Klyachkin, Mater. Sci. Forum **196–201**, 467 (1995).
16. L. P. Kouwenhoven, B. J. van Wees, C. J. P. M. Harmans, *et al.*, Phys. Rev. B **39**, 8040 (1989).
17. N. T. Bagraev, W. Gehlhoff, L. E. Klyachkin, *et al.*, Mater. Sci. Forum **258–263**, 1683 (1997).

Translated by M. Skorikov

Semiconductors, Vol. 34, No. 7, 2000, pp. 825–828. Translated from Fizika i Tekhnika Poluprovodnikov, Vol. 34, No. 7, 2000, pp. 857–860.
Original Russian Text Copyright © 2000 by Kaliteevskaya, Seĭsyan.

AMORPHOUS, VITREOUS, AND POROUS SEMICONDUCTORS

Simulation of Photochemical Transformations and Photodarkening in Photoresist Films Exposed to Pulsed Vacuum-Ultraviolet Radiation

N. A. Kaliteevskaya and R. P. Seĭsyan

Ioffe Physicotechnical Institute, Russian Academy of Sciences,
ul. Politekhnicheskaya 26, St. Petersburg, 194021 Russia

Submitted January 13, 2000; accepted for publication January 14, 2000

Abstract—A theoretical description of photochemical transformations occurring in the films of chalcogenide vitreous semiconductors (in particular, AsSe) is proposed. Results obtained in studying the photodarkening of thin films of chalcogenide vitreous semiconductors exposed to pulsed radiation of an ArF excimer laser (193 nm) are analyzed. The photochemical transformation is characterized by optical sensitivity on the order of 3 cm^3 kJ^{-1} and a threshold light intensity of ~17 kJ cm^{-2} s^{-1}. *© 2000 MAIK “Nauka/Interperiodica”.*

Recently, much attention has been given to various properties of chalcogenide vitreous semiconductors, such as AsSe, As_2Se_3, AsTe, etc. [1–13]. This interest is due both to the possibility of technological application of these semiconductors (e.g., fabrication of sensors to detect heavy metal ions in liquids [5] or membranes for chemical thin-film transducers [14]) and to the interesting physicochemical properties of chalcogenide vitreous semiconductors, primarily their ability to undergo various photoinduced transformations. The appearance and reorientation of a photoinduced dichroism [3, 4, 10] is such an effect.

The occurrence of photoinduced transformations allows chalcogenide vitreous semiconductors to be considered as a promising photoresist for microelectronic technology. In particular, it has been shown that AsSe and As_2Se_3 can be used as both positive and negative photoresists [7].

Many experimental studies have been concerned with photoinduced changes in properties under the effect of visible light [6, 10, 11]. However, transformations occurring in chalcogenide vitreous semiconductors exposed to short-wavelength radiation of an ArF excimer laser (λ_0 = 193 nm, so-called vacuum ultraviolet, VUV range) exhibit a number of important features [12]. This is, in the first place, the very low (on the order of several mJ cm^{-2} units) dose that is necessary for optical properties to be changed noticeably. Changes in optical properties are accompanied by photostimulated changes in the etching rate, which permits these chalcogenide vitreous semiconductors to be used as high-sensitivity inorganic photoresists. In particular, it was shown [12] that, in a single-pulse mode at a pulse duration of 20 ns, the threshold exposure dose H is 8 mJ cm^{-2} for a 200-nm-thick film, which is a fairly low value for both inorganic and organic resists. This allows *in situ* exposure without arresting the substrate motion. Another important feature is the high photochromic sensitivity $\partial\alpha/\partial H$ (where α is the absorption coefficient and H is the exposure dose) that can attain a value as high as ~10^6 cm J^{-1} in the VUV spectral range in irradiation with 193-nm light. We note the following experimental fact: the reaction rate is strongly affected by the spectrum of the radiation, which points to the nonthermal origin of the phenomenon.

An important property of the photolithographic processes studied is the sharp contrast of the image, For example, a high-quality image of a periodic (200-nm period) structure was obtained on an As_2Se_3 film by a contact print under 193 nm irradiation [13]. The high quality of image transfer suggests an enhancement of the image contrast.

It should also be noted that creating new highly sensitive resists for short- and ultrashort-wavelength electromagnetic radiation is a topical problem. Conventional photoresists based on polymethyl methacrylate have low sensitivity in the VUV spectral range [15].

The aim of this study was to construct a theoretical model describing photochemical transformations in the films of inorganic photoresists, AsSe in particular, exposed to VUV radiation of an excimer laser.

A detailed experimental study of photochemical transformations in a 200-nm-thick AsSe film [12] demonstrated the following. Under irradiation with 2- and 4-mJ cm^{-2} pulses, the material of the film transforms to a new state upon exposure to $H \approx 100$ mJ cm^{-2} and further irradiation does not change the physicochemical properties of the film. In addition, it was found that the higher the pulse energy, the lower the dose required for complete exposure of a film; as already noted, complete photochemical transformation of a film is attained in a single-pulse mode at a pulse energy of 8 mJ cm^{-2}.

Photochemical transformations in a positive photoresist can be described by Dill's equations [16]. A positive photoresist generally consists of a resin and a photosensitive inhibitor that has low solubility and prevents the resin from dissolving during development. The inhibitor decomposes under the effect of light so that the irradiated regions can dissolve. Denoting the concentration of the inhibitor, the light absorption coefficient, and light intensity at a given point of the layer with the coordinate z at an instant of time t by $M(z, t)$, $\alpha(z, t)$, and $I(z, t)$, respectively, we obtain the equations

$$\alpha(z, t) = AM(z, t) + B, \tag{1a}$$

$$\frac{\partial I(z, t)}{\partial z} = -\alpha(z, t)I(z, t), \tag{1b}$$

$$\frac{\partial M(z, t)}{\partial t} = -CM(z, t)I(z, t). \tag{1c}$$

Here, A and B are constants and C is the optical sensitivity. It should be noted that, in Dill's model, the optical sensitivity is independent of light intensity. Consequently, the dose necessary for film exposure is also independent of the incident light intensity.

In the case of chalcogenide vitreous semiconductors, the light intensity strongly affects the necessary exposure. To adequately describe photoinduced transformations in chalcogenide semiconductors, the system of equations (1a)–(1c) should be modified.

We assume that the material of the film is transformed under the action of light from the initial state I into a final state II having different physical (e.g., the absorption coefficient) and chemical (e.g., solubility in a certain solvent) properties. Let us denote the absorption coefficients of materials I and II at the wavelength of the excimer laser radiation (inducing photochemical transformations) by α_1 and α_2, respectively. During irradiation, the material of the film will be a mixture of materials I and II. Let us denote the relative concentrations of materials I and II by ρ_1 and ρ_2, respectively, so that $\rho_1 + \rho_2 = 1$. It seems reasonable to assume that the absorption coefficient of the irradiated material is expressed by the formula

$$\alpha = \alpha_1\rho_1 + \alpha_2\rho_2 = \alpha_2 + (\alpha_1 - \alpha_2)\rho_1. \tag{2a}$$

The absorption in the layer is described by the Bouguer–Lambert–Beer law, so that

$$\frac{\partial I(z, t)}{\partial z} = -\alpha(z, t)I(z, t). \tag{2b}$$

Changes in the concentration of the starting material under the effect of light is described by the formula of the type

$$\frac{\partial \rho_1(z, t)}{\partial t} = -f\rho_1(z, t), \tag{2c}$$

where f stands for the rate of the photoinduced transformation. It seems reasonable to assume that f is proportional to the energy flux absorbed at a given point of the layer: $f \sim C\alpha(z, t)I(z, t)$, where the sensitivity C has a dimension of [volume][energy]$^{-1}$. Physically, the constant C is equivalent to the volume of the material that can be converted from state I to state II on absorbing the unit energy.

In addition, it is necessary to introduce a dimensionless intensity-dependent multiplier $F[I(z, t)]$ that accounts for the fact that the dose necessary for material exposure depends on the incident light intensity.

Thus, the photochemical transformation of the film is described by the system of differential equations

$$\begin{cases} \alpha(z, t) = \alpha_2 + (\alpha_1 - \alpha_2)\rho_1(z, t) & \text{(3a)} \\ \dfrac{\partial I}{\partial z} = -\alpha(z, t)I(z, t), & \text{(3b)} \\ \dfrac{\partial \rho}{\partial t} = -C\alpha(z, t)I(z, t)F(I)\rho_1 & \text{(3c)} \end{cases}$$

with the initial condition $\rho_1|_{t=0} = 1$ and the boundary condition $I(t)|_{z=0} = I_0(t)$, where $I_0(t)$ is the incident light intensity.

The most efficient way to monitor photoinduced changes in the course of irradiation is to analyze the photodarkening with a probing light beam of wavelength λ_p, different from the excimer-laser emission wavelength, passing through the layer. Denoting the light absorption coefficients for materials I and II at the probing light wavelength by β_1 and β_2 and assuming, similarly to (2a), that the absorption coefficient of the material during irradiation is described by the formula

$$\beta = \beta_1\rho_1 + \beta_2\rho_2, \tag{4}$$

we obtain the light transmission coefficient T at the probing wavelength, assuming that substrate is transparent, to be

$$T(t) = \exp\left\{-\int_0^d [\beta_2 + (\beta_1 - \beta_2)\rho_1(z, t)]dz\right\}, \tag{5}$$

where d is the photoresist layer thickness.

The dependence on intensity ($F(I)$ multiplier) can be either determined by developing a detailed microscopic theory of the photoinduced transformation or determined phenomenologically, by analyzing photodarkening curves, from which it follows that the function $F(I)$ must possess the following properties. First, photoinduced transformations are negligible at low incident light intensities and $F(I)$ tends to zero. Second, it is

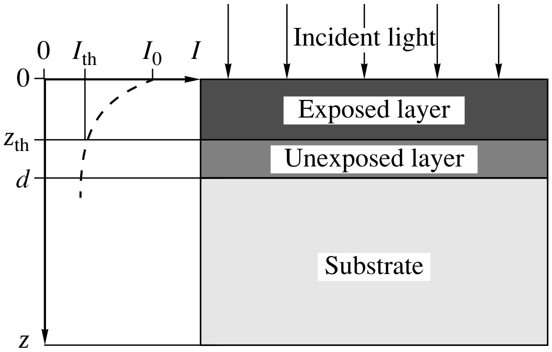

Fig. 1. Schematic representation of a structure under study: photoresist layer deposited onto a substrate. Also shown is the light intensity profile I in the resist bulk. The threshold thickness z_{th} corresponding to the threshold intensity I_{th} denotes the boundary between the exposed and unexposed regions.

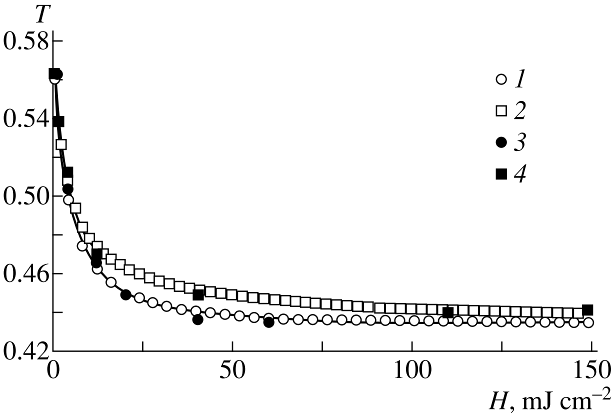

Fig. 2. Photodarkening curves: transmission coefficient at probing light wavelength λ_p = 630 nm vs. exposure dose in the pulsed mode. Curves *1* and *2* correspond to experimental data at pulse energies of 2 and 4 mJ, respectively; *3* and *4* represent data of [14].

known that quite a number of photochemical processes show a threshold behavior: photoinduced transformation sets in at a light intensity higher than some threshold value I_{th}. Third, the transformation rate cannot grow infinitely; i.e., the $F(I)$ value is limited.

Even though the exact form of the function $F(I)$ is unknown, we approximate it by the expression

$$F(I) = \frac{1}{2}\left\{1 + \tanh\left(\frac{I - I_{th}}{\delta}\right)\right\}, \tag{6}$$

which satisfies all the three criteria listed above. The parameter δ having dimension of energy characterizes the spread of the threshold intensity. In the case where the spread δ is small, only a photoresist layer of thickness z_{th} defined by

$$z_{th} = -\frac{1}{\alpha_1}\ln\left(\frac{I_{th}}{I_0}\right) \tag{7}$$

is exposed, as shown in Fig. 1.

Figure 2 shows experimental [14] and calculated photodarkening curves for 200-nm-thick AsSe films exposed to pulsed excimer laser radiation. In simulation, the following parameters ensuring the best fit of the calculated curves to the experimental results were used. These are the sensitivity $C = 3 \times 10^{-3}$ cm^3 J^{-1}, threshold intensity $I_{th} = 1.7 \times 10^4$ J cm^{-2} s^{-1}, and threshold spread $\delta = 8.5 \times 10^3$ J cm^{-2} s^{-1}. The absorption coefficients of the film found experimentally before and after irradiation [14] are given in the table. It should be noted that the results of simulation are affected not only by the energy and duration of a pulse but also by its shape: the intensity of light corresponding to "tails" on its leading and trailing edges is lower than the threshold. The minor discrepancy between the calculated and experimental dependences in Fig. 2 can be accounted for by the fact that the actual time dependence of the intensity in the excimer laser pulse differs from the Gaussian shape used in simulation.

The parameters C, I_{th}, and δ can be determined from the slope $K = \partial T/\partial H$ of the photodarkening curve $T(H)$ in the initial stage of irradiation. Assuming that the incident pulse is rectangular, we have

$$K = \frac{\partial T}{\partial H} = \frac{1}{I_0}\frac{\partial T}{\partial t}, \tag{8}$$

where I_0 is the pulse intensity. Substituting transmission coefficient (5) into (8), we obtain

$$K = \frac{1}{I_0}\frac{\partial}{\partial t}\left\{\exp\left(-\int_0^d [\beta_2 + (\beta_1 - \beta_2)\rho_1]dz\right)\right\}, \tag{9}$$

or

$$K = \frac{1}{I_0}\exp\left\{-\int_0^d [\beta_2 + (\beta_1 - \beta_2)\rho_1]dz\right\} \times \int_0^d (\beta_2 - \beta_1)\frac{\partial\rho_1}{\partial t}dz. \tag{10}$$

Taking into account equation (3c), we transform (10) into

$$K = \frac{1}{I_0}\exp\left\{-\int_0^d [\beta_2 + (\beta_1 - \beta_2)\rho_1]dz\right\} \times \int_0^d (\beta_1 - \beta_2)C\alpha(z)I(z)F[I(z)]\rho_1 dz. \tag{11}$$

Simulation of photochemical transformations and photodarkening of photoresist films under the effect of pulsed VUV radiation

Wavelength, nm	Absorption coefficient before irradiation, cm^{-1}	Absorption coefficient after irradiation, cm^{-1}	Notes
630	$\beta_1 = 2.9 \times 10^4$	$\beta_2 = 4.1 \times 10^4$	Probing light wavelength
193	$\alpha_1 = 1.0 \times 10^5$	$\alpha_2 = 1.2 \times 10^5$	Excimer laser wavelength

In the initial stage of exposure, at the instant of time $t = 0$, the film is composed of a type-I material and, consequently, $\rho_1 = 1$, $\alpha = \alpha_1$, and $\beta = \beta_1$. The light intensity profile within the film has the form $I(z) = I_0\exp(-\alpha_1 z)$, which allows (11) to be rewritten as

$$K = (\beta_1 - \beta_2)C\exp\left(-\int_0^d \beta_1 dz\right) \times \int_0^d \alpha_1 \exp(-\alpha_1 z) F[I_0 \exp(-\alpha_1 z)]dz. \tag{12}$$

The expression $\exp(-\int_0^d \beta_1\, dz)$ is simply the light transmission coefficient T_{β_1} at the initial instant of time. Taking into account expression (6), we have, finally,

$$K = T_{\beta_1}(\beta_2 - \beta_1)C\Bigg\{1 - \exp(-\alpha_1 d) + \int_0^d \exp(-\alpha_1 z)\tanh\left[\frac{I_0\exp(-\alpha_1 z) - I_{\text{th}}}{\delta}\right]dz\Bigg\}. \tag{13}$$

The sensitivity C can be tentatively evaluated considering the fact that the absorption coefficient α is on the order of 10^5 cm^{-1} and the photoresist layer thickness is typically several hundred micrometers, and using the approximate relation [13]; thus, we have

$$K \approx T_{\beta_1}(\beta_2 - \beta_1)C. \tag{14}$$

To conclude, we summarize the basic results of this study.

A model is proposed for describing theoretically the photoinduced transformations in chalcogenide vitreous semiconductors. The model explains the departure from the interchangeability law for the exposure time and light intensity and the enhancement of the image transfer contrast observed experimentally in AsSe-based photoresists. The simulation of experiments with photodarkening of AsSe films suggests that the proposed model describes quite adequately photoinduced transformations in chalcogenide vitreous semiconductors.

REFERENCES

1. V. Mastelaro, S. Benazeth, and H. Dexpert, J. Phys. IV **2** (c2), 195 (1992).
2. C. J. Benmore and P. S. Salmon, Phys. Rev. Lett. **73** (2), 264 (1994).
3. V. Lyubin, M. Klebanov, V. Tikhomirov, and G. Adriaenssens, J. Non-Cryst. Solids **200**, 719 (1996).
4. G. J. Adriaenssens, V. K. Tikhomirov, and S. R. Elliott, J. Non-Cryst. Solids **230**, 688 (1998).
5. M. Brun, H. Klewe-Nebenius, G. Pfennig, *et al.*, Surf. Coat. Technol. **97** (1–3), 707 (1997).
6. V. Palyok, A. Mishak, I. Szabo, *et al.*, Appl. Phys. A **68** (4), 489 (1999).
7. V. M. Lubin, A. M. Sedykh, N. N. Smirnova, and V. P. Shilo, Sov. Microelectron. **18** (6), 303 (1989).
8. S. V. Mamedov, M. D. Mikhailov, V. G. Pogoreva, and O. A. Yakovuk, Inorg. Mater. **23** (11), 1592 (1987).
9. A. V. Razin, Inorg. Mater. **17** (2), 162 (1981).
10. V. Lyubin and M. Klebanov, Phys. Rev. B **53**, 11924 (1996).
11. A. A. Kikineshi, V. I. Mikla, D. G. Semak, and M. M. Shiplyak, Ukr. Fiz. Zh. **28** (5), 786 (1983).
12. E. G. Barash, A. Yu. Kabin, V. M. Lyubin, and R. P. Seĭsyan, Zh. Tekh. Fiz. **62** (3), 106 (1992) [Sov. Phys. Tech. Phys. **37**, 292 (1992)].
13. L. G. Gladysheva, N. A. Kaliteevskaya, R. P. Seĭsyan, and D.V. Smirnov, Pis'ma Zh. Tekh. Fiz. **22** (15), 91 (1996) [Tech. Phys. Lett. **22**, 640 (1996)].
14. A. V. Legin, E. A. Bychkov, and Y. G. Vlasov, Sens. Actuators B **15** (1–3), 184 (1993).
15. E. A. Chandross, E. Reichmanis, C. W. Wilkins, *et al.*, Solid State Technol. **24**, 81 (1981).
16. F. H. Dill, W. P. Hornberger, and P. S. Hauge, IEEE Trans. Electron Devices **ED-22** (7), 445 (1975).

Translated by M. Tagirdzhanov

Semiconductors, Vol. 34, No. 7, 2000, pp. 829–834. Translated from Fizika i Tekhnika Poluprovodnikov, Vol. 34, No. 7, 2000, pp. 861–867.

The Influence of Erbium on Electrical and Photoelectric Properties of Amorphous Silicon Produced by Radio-Frequency Silane Decomposition

E. I. Terukov*, M. M. Kazanin*, O. I. Kon'kov*, V. Kh. Kudoyarova*,
K. V. Kougiya, Yu. A. Nikulin**, and A. G. Kazanskiĭ*****

** Ioffe Physicotechnical Institute, Russian Academy of Sciences, ul. Politekhnicheskaya 26, St. Petersburg, 194021 Russia*
*** St. Petersburg State Pediatric Medical Academy, St. Petersburg, 194100 Russia*
**** Moscow State University, Vorob'evy gory, Moscow, 119899 Russia*

Submitted December 29, 1999; accepted for publication January 18, 2000

Abstract—Thermal evaporation of tris(2,2,6,6-tetramethyl–2,5-heptadionato) Er(III) inside the plasma gap was used to introduce erbium into amorphous hydrogenated silicon (*a*-Si:H) obtained by radio-frequency silane decomposition. The samples obtained had a pronounced layered structure due to exhaustion of the erbium source. The layer nearest to the substrate was enriched with erbium, oxygen, and carbon; gave rise to luminescence with a wavelength of 1.535 μm characteristic of $^4I_{13/2} \longrightarrow {}^4I_{15/2}$ intra-atomic transitions of erbium; and contained a large number of defects. The top layer contained much fewer defects, was close to undoped *a*-Si:H in the photoelectric characteristics, and was responsible for photoconductivity in the samples obtained. The experimental data are analyzed in the context of the models for doping of *a*-Si:H with Er with the resulting emergence of *n*-type conduction and formation of heterojunction as the film grows. *© 2000 MAIK "Nauka/Interperiodica".*

1. INTRODUCTION

The most significant drawback of silicon-based technology is the absence of efficient light-emitting devices; therefore, technological experiments with introduction of luminescent impurities (such as erbium) into the base material are of considerable interest [1, 2]. Luminescence of erbium is observed at a wavelength of 1.54 μm (i.e., in the range of the highest transparency of quartz optical fibers) due to partial removal of the prohibition of intra-atomic $^4I_{13/2} \longrightarrow {}^4I_{15/2}$ 4*f* transitions; this removal is caused by the influence of the nearest neighbors.

Erbium is introduced into amorphous silicon by the methods of dc silane decomposition in a magnetic field (the so-called MASD technology) [3], sequential deposition [4], ion implantation [5], or cosputtering [6]. As is known, the samples obtained by the above methods have mediocre photoelectric properties; therefore, it is of interest to attempt to introduce erbium into amorphous silicon using the conventional technology of radio-frequency (RF) silane decomposition, which is accomplished by adding metal-organic compounds into the plasma gap [7, 8].

In this paper, we discuss the photoelectric properties of the material obtained and the effect of the erbium introduced.

2. EXPERIMENTAL

The samples to be studied were obtained in a conventional installation for *a*-Si:H synthesis by RF silane decomposition. However, this installation was equipped with an additional component, i.e., a thermal vaporizer; on the latter component, a charge of tris(2,2,6,6-tetramethyl–2,5-heptadionato) Er(III) metal-organic compound was placed. The time sequence of the technological operations is illustrated in Fig. 1. Following the preliminary pumping and degassing of the chamber, the substrate was heated to the operating temperature for the *a*-Si:H film deposition. After the required temperature was attained, a silane–argon mixture was fed into the chamber at the point in time $t = t_1$ and the desired rate of gas flux was set. Simultaneously, the heating of the thermal vaporizer of metal-organic compound was started; the operating temperature of the vaporizer was attained in $t_3 \approx$ 15 min. The RF power needed for initiating the discharge was fed at the point in time t_2 ($t_2 - t_1 \approx 7$ min). The sequence of shutoffs at the point in time t_4 was as follows: first, the thermal vaporizer and RF power were switched off and the silane flux was shut off; the substrate heater was then switched off (at the point in time t_5). The deposition time is assumed to be equal to the time during which the RF power was switched on.

In this study, we compare the properties of five groups of samples: a group of undoped *a*-Si:H samples 0.6 μm thick and four groups of *a*-Si:H samples doped

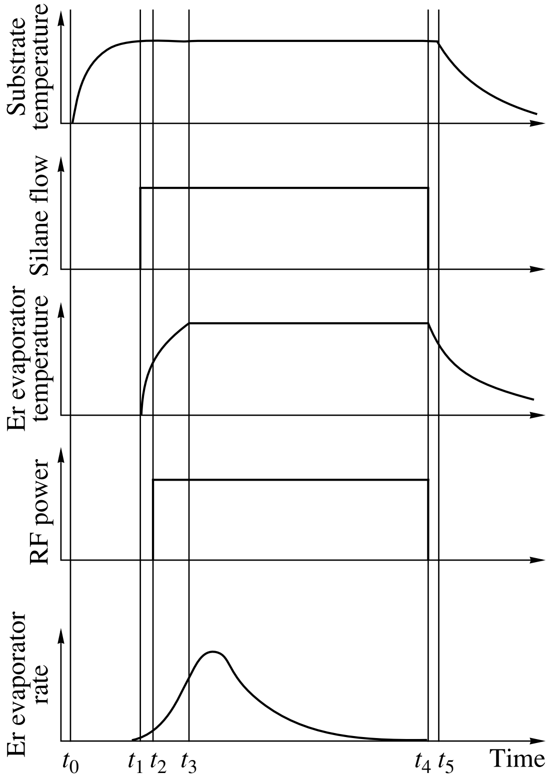

Fig. 1. Time sequence of technological operations. The significance of the points in time $t_0 - t_5$ is explained in the text.

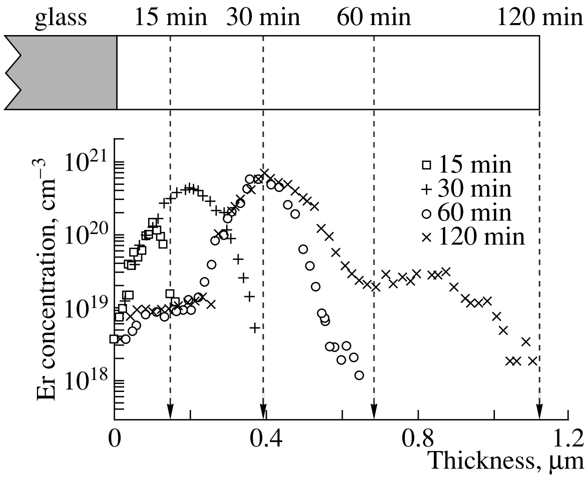

Fig. 2. Concentration profiles for Er in *a*-Si:H films in relation to the deposition times. The profiles were measured by Rutherford backscattering. The zero thickness on the left corresponds to the coordinate of the substrate.

with Er and deposited for 15, 30, 60, and 120 min (henceforth, for the sake of brevity, we refer to the Er-doped samples as 15m, 30m, 60m, and 120m, respectively). For the substrate material, we used either quartz (for electrical measurements and optical measurements in the visible range of the spectrum) or a KDB silicon (Si:B) (in the case of optical measurements in the infrared region of the spectrum). In order to measure the electrical and photoelectric characteristics, the Al or Cr contacts in coplanar configuration were deposited on the surface of the sample using thermal evaporation. The photoluminescence (PL) spectra were measured at room temperature and were excited with an argon laser (488 nm); the PL was detected with a cooled Ge detector. The depth distribution of Er in the film was measured by the methods of Rutherford backscattering (RBS) and secondary-ion mass spectrometry (SIMS).

3. RESULTS AND DISCUSSION

The RBS data are shown in Fig. 2. It follows from these data that the Er depth distribution in the film is nonuniform and the peak of the distribution shifts from the substrate to larger depths as the film grows. The SIMS data (Fig. 3) confirm the nonuniformity of Er distribution and show that the H, C, and O distributions are also nonuniform, with the peaks in the C and H distributions coinciding closely with that in the Er distribution.

Evolution of PL spectra as the film grows is illustrated in Figs. 4 and 5a. As can be seen from Fig. 4, a broad PL band with a peak at ~1.44 μm and a half-width of ~0.19 μm is observed in undoped material. This PL band is conventionally related to recombination at dangling bonds [9]. Doping with Er results in the emergence of a second, much narrower band that is peaked at 1.535 μm and is typical of $^4I_{13/2} \longrightarrow {}^4I_{15/2}$ transitions. As the film grows, the intensity of the bands varies differently (see Fig. 5a). The intensity of the narrow Er-related band changes only slightly as the film thickness increases. The intensity of the defect-related broad band associated with dangling bonds depends only slightly on the film thickness in the films grown for 30 min and less; a further increase in the intensity is directly proportional to the thickness of the growing film. Thus, the PL data indicate that the growing films have a pronounced layered structure. The lower layer is enriched in Er, is located near the substrate, and is responsible for PL band peaked at 1.535 μm. The upper layer grows at the surface of the first layer and has a lower Er concentration and an almost uniform depth distribution of defects of the type of dangling bonds that are responsible for the PL band peaked at 1.44 μm.

The assumption that the samples are two-layered is supported by the data on the optical-absorption coefficient measured by the method of constant photoconductivity. As can be seen from Fig. 6, the optical absorption edge of samples 60m and 120m is similar to that of undoped material. At the same time, films 15m and 30m have a much larger absorption coefficient for photon energies below 1.5 eV. The results of deconvolution of absorption spectra are shown in Fig. 5b; these results make it possible to determine the characteristic energy of the valence-band exponential tail and the concentration of dangling bonds. As can be seen, thicker samples deposited for 60 and 120 min exhibit the same parameters as in the case of undoped material. At the same time, both the concentration of dangling bonds and the slope of the exponential Urbach tail are much larger. These facts can be easily interpreted if we take into account the above-suggested model of a layered structure of the samples. In fact, both the dangling bonds and the states in the valence-band tail act as effective recombination centers. Therefore, photosensitivity of the first layer that grows for the first 30 min is much lower than that of the subsequent layers; it is the latter that would define all photoelectric properties of the samples.

Degradation of *a*-Si:H under the effect of intense illumination (the Staebler–Wronski effect) is also defined to a large extent by the duration of the film deposition. Figure 7 shows the time dependences of dark (equilibrium) conductivity of the samples exposed to illumination with white light with the intensity of 60 mW/cm^2 for a certain time. As can be seen from Fig. 7, all the samples show a tendency for a decrease in dark conductivity, which is typical of the Staebler–Wronski effect. However, the extent of degradation in undoped material and in thin (enriched in Er) samples does not exceed an order of magnitude, whereas this degradation amounts to four orders of magnitude in thick (two-layered) samples, with the dark conductivity in the thinner 60m sample degrading much faster than that in the thicker 120m sample.

In contrast to the above-listed characteristics, the temperature dependences of dark conductivity vary smoothly as the film grows (see Fig. 5c, where the dependence of the activation energy of electrical conductivity on the film thickness is shown). It follows from Fig. 5c that, as the film grows, the activation energy decreases steadily from 0.80 (15-min deposition) to 0.44 eV (120-min deposition). In the undoped samples, the activation energy was equal to ~0.80 eV. It should be mentioned that the above data correspond to temperatures above 300 K and may be associated with conduction over delocalized states. At lower temperatures, temperature regions with lower activation energies were observed for samples 30m, 60m, and 120m; these regions can be related to conduction over localized states, which is beyond the scope of this paper.

As previously demonstrated, the analysis of experimental data on PL and the optical-absorption edge suggests a two-layer model of the material; according to this model, the first (lower) layer formed in the initial several minutes of deposition is characterized by an increased Er concentration, has a defect density much larger than that in undoped *a*-Si:H, and is responsible for the PL band peaked at 1.535 μm; at the same time, the characteristics of the upper layer grown during the longer deposition are close to those of undoped material and this layer is responsible for photoconductivity due to its higher photosensitivity.

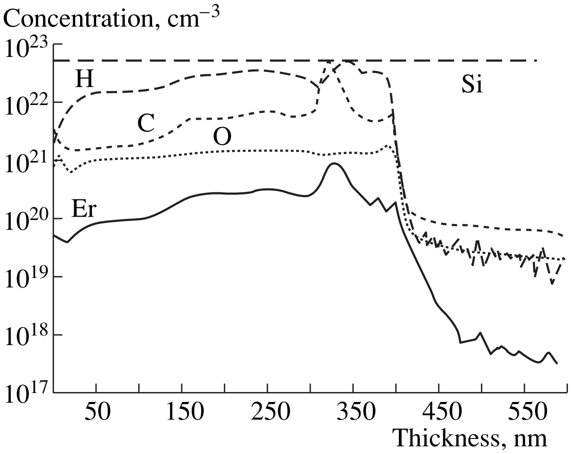

Fig. 3. Depth distribution of concentrations of constituents in the film grown for 60 min and doped with erbium. The data were obtained by SIMS. The substrate is on the left.

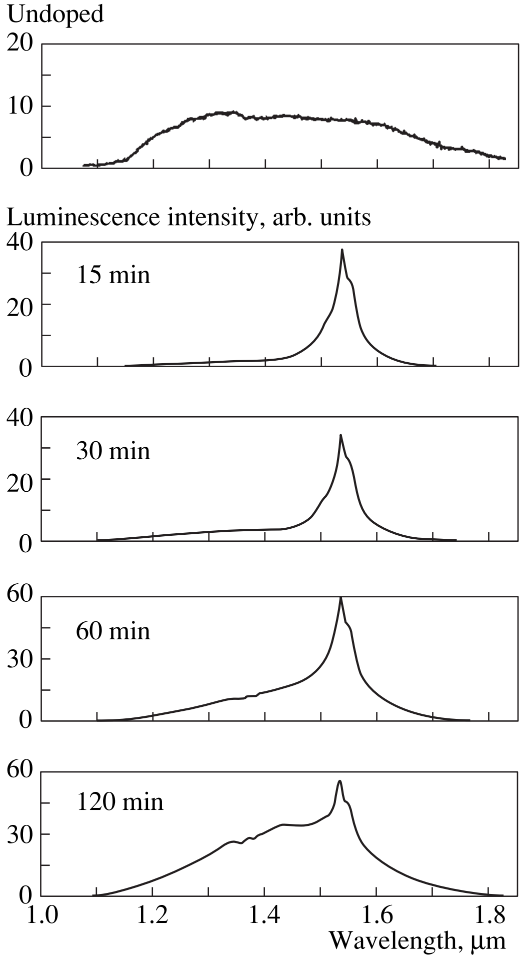

Fig. 4. Evolution of photoluminescence spectra with the film-deposition time. All spectra are normalized in order to facilitate the comparison.

In the context of the layered-film model, one may suggest two possible interpretations of the data on the smooth variation of the activation energy of electrical

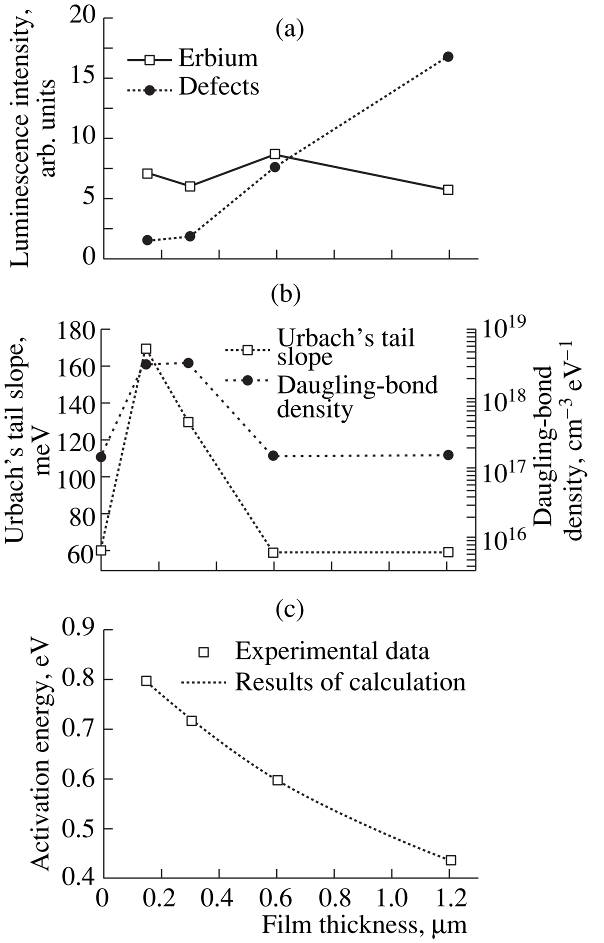

Fig. 5. The film-thickness dependences of (a) the intensity of photoluminescence associated with the presence of erbium (Er) and dangling bonds (Defects), (b) Urbach's tail slope and the dangling-bond density, and (c) the activation energy for dark conductivity measured at a temperature above 300 K (the dotted line represents the results of calculations as explained in the text).

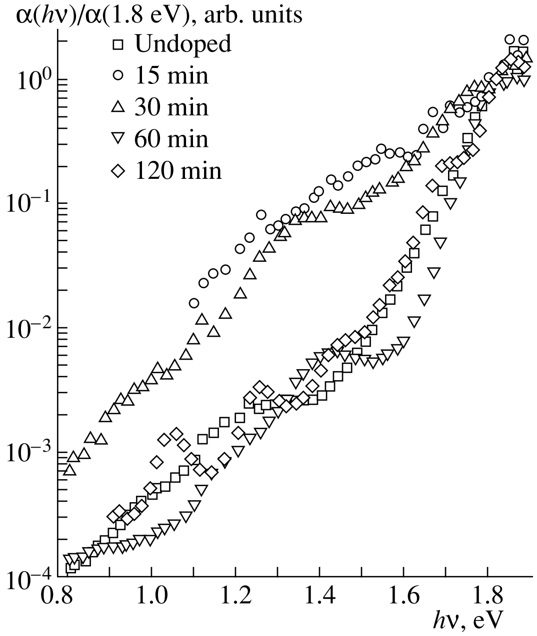

Fig. 6. The optical-absorption spectra measured by the method of constant photocurrent for the films of undoped and Er-doped *a*-Si:H films.

conductivity and the magnitude of the Staebler–Wronski effect as the film grows. The first interpretation is based on the assumption that doping with erbium induces *n*-type conduction in *a*-Si:H. This assumption contradicts the data obtained for single-crystal silicon [10]; however, it is supported by the results of the measurements of thermoelectric power (the data were kindly supplied to us by Dr. J.P. Kleider of the Laboratoire de Genie Electrique de Paris). In this case, an increase in Er concentration (evident for samples 15m, 30m, and 60m in Fig. 2) would result in a decrease in the activation energy and an increase in the magnitude of the Staebler–Wronski effect in the layer with the highest Er concentration, which is well known for P-doped materials [11]. However, an appreciable distinction between samples 60m and 120m, in which the peak Er concentrations are the same, remains unclear. This induces us either to assume that an additional 1-h-long "annealing" during the growth of the film transforms a fraction of Er atoms into another, electrically active form, or to advance an alternative hypothesis, which consists in the following.

The second possible explanation is based on the concept of the formation of a peculiar "heterojunction." In fact, we have to bear in mind that, according to the SIMS data, evaporation of the Er-containing metal-organic compound results in incorporation not only of Er but of other elements as well (including O and C) into the growing film. Thus, an amorphous alloy with complicated composition [to a first approximation, *a*-Si:(C, O, H)], rather than just *a*-Si:H, is formed on the substrate during the initial several minutes of deposition. Eventually, as a result of prolonged deposition, a heterojunction (amorphous alloy) / *a*-Si:H is formed. In what follows, we will attempt to construct a possible energy-band diagram of this heterojunction; to this end, data on the optical band gap of the amorphous alloy are required. These data are not available, but it is reasonable to assume that the forbidden band of the amorphous alloy is close to that of *a*-Si:H, because, on the one hand, introduction of O and C causes the band gap to increase, whereas, on the other hand, an increase in the number of defects and in the general degree of disorder in the material results in a decrease of the band gap. If it is given that the work function of *a*-Si:H is less than that of the amorphous alloy, the heterojunction formation would occur approximately in the manner illustrated in Fig. 8. Figure 8a shows the energy band diagram of undoped *a*-Si:H, and Fig. 8b shows that of the amorphous alloy formed in the initial 15 min of growth. Under these assumptions, the energy band diagram of the film grown for 60 min would presumably appear as shown in Fig. 8d. Figure 8c illustrates the formation of a transition layer during the time lapse between 15 and 30 min of deposition.

The energy band diagram shown in Fig. 8 makes it possible to interpret the experimental data obtained. In fact, the requirement that the Fermi level position remains the same throughout the entire film would obviously lead to a flow of electrons from the material with a smaller work function (*a*-Si:H) to the material with a larger work function; it is this effect that causes a gradual decrease in the activation energy for electrical conductivity as the film of undoped *a*-Si:H grows. This reasoning can be supported by calculations. If we assume that the heterojunction is fairly abrupt and the density of localized states near the Fermi level is almost independent of energy, then, in order to estimate the variation in the activation energy for electrical conductivity, we should make equal the positive and negative charges that arise as a result of the flow of electrons in the vicinity of the Fermi level; thus, we have

$$\begin{aligned}&(\Delta E_{15} - \Delta E(d))d_{15}N_{15}\\ &= (\Delta E(d) + \Delta\Psi - \Delta E_u)d_u N_u,\end{aligned} \tag{1}$$

where $\Delta E(d)$ is the activation energy for electrical conductivity in the film with a thickness of d, $\Delta\Psi$ is the difference between the work functions, ΔE_{15} is the activation energy for electrical conductivity in the film grown for initial 15 min, d_{15} is its thickness, N_{15} is the corresponding density of localized states at the Fermi level, ΔE_u is the activation energy for electrical conductivity in an undoped *a*-Si:H layer, d_u is its thickness, and N_u is the corresponding density of localized states at the Fermi level.

The results of calculations based on formula (1) are shown in Fig. 5c by the dotted line and are to be compared with experimental data. For the adjustable parameters, we used the ratio of the localized-state densities at the Fermi level (N_{15}/N_u) and the difference between the work functions ($\Delta\Psi$). The best agreement between the results of calculations and experimental data is obtained for $N_{15}/N_u \approx 7$, which is quite consistent with an estimate based on the ratio of the absorption coefficients at $h\nu = 0.8$ eV. The optimal value of $\Delta\Psi$ is found to be equal to 0.7 eV; this value is to be further verified and discussed.

The heterojunction model makes it also possible to resolve easily an apparent paradox related to the Staebler–Wronski effect; this paradox consists in the fact that the extent of degradation of dark conductivity in undoped *a*-Si:H and in the layer enriched in Er does not exceed an order of magnitude, whereas, in thick films (60m and 120m), it amounts to almost four orders of magnitude (Fig. 7). It is obvious that, in materials with the energy band diagram shown in Fig. 8d, generation of nonequilibrium charge carriers under the effect of illumination is accompanied by their active trapping by charged localized states in the vicinity of the Fermi level. Recharging of localized states causes the demarcation line separating the filled and empty states to shift into the depth of the forbidden band; as a result, the activation energy increases and the magnitude of the dark conductivity decreases. The only restriction imposed on the value of the shift consists in the require-

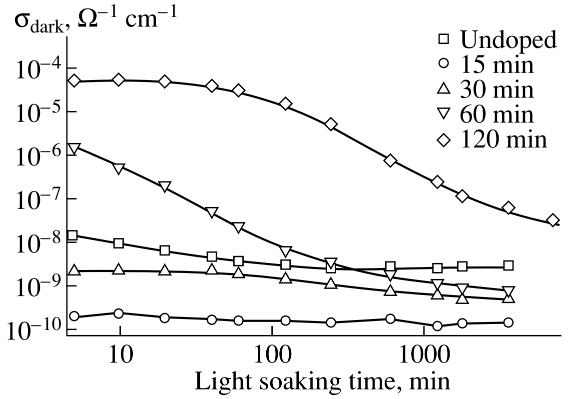

Fig. 7. Degradation of dark (equilibrium) conductivity under the effect of intense illumination.

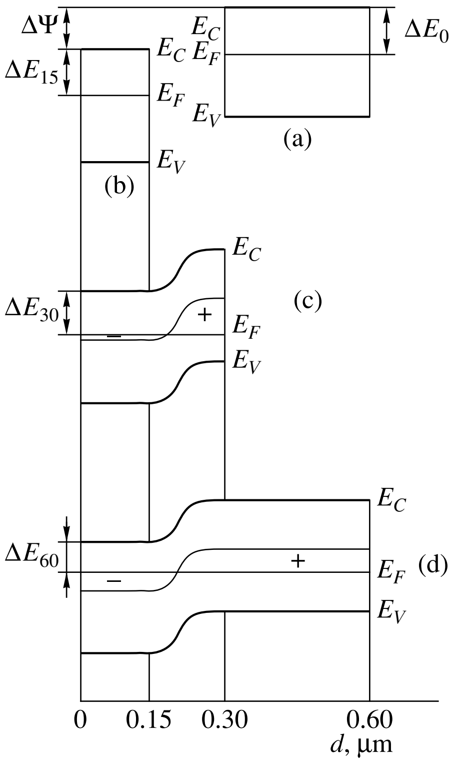

Fig. 8. A model of formation of a heterojunction during the growth of *a*-Si:H film doped with Er. (a) The energy-band diagram for undoped *a*-Si:H (ΔE_0 is the corresponding activation energy for electrical conductivity); (b) the energy-band diagram for sample 15m (ΔE_{15} is the corresponding activation energy); and (c) and (d) illustrate the heterojunction formation and the activation energy for thicker samples.

ment that this shift cannot exceed the difference between the activation energies ($\Delta E_{15} - \Delta E_{120}$) ≈ 0.35 eV. This is more than sufficient, because the shift of the level at room temperature should be merely ≈0.23 eV in order to ensure an increase in electrical conductivity by ≈4 orders of magnitude. In the context of the suggested model of recharging of localized states, the cause of the difference between the degradation rates in samples 60m and 120m becomes clear. Actually, if the generation and trapping rates are equal, there is a higher concentration of charged localized states in sample 120m; as a result, these states are recharged (owing to the capture of nonequilibrium carriers) with a relatively lower rate than in the case of sample 60m.

4. CONCLUSION

Thermal evaporation of tris(2,2,6,6-tetramethyl–2,5-heptadionato) Er(III) within the plasma gap was used to introduce erbium into amorphous hydrogenated silicon obtained by RF decomposition of silane. The obtained samples featured a pronounced layered structure due to exhaustion of the erbium source. The layer nearest to the substrate was enriched in erbium, oxygen, and carbon; was responsible for the luminescence band peaked at a wavelength of 1.535 μm characteristic of ${}^4I_{13/2} \longrightarrow {}^4I_{15/2}$ intra-atomic transitions in erbium; and contained a large number of defects. The top layer contained much fewer defects, was similar to undoped *a*-Si:H in photoelectric characteristics, and was responsible for photoconductivity of the samples. The obtained data were analyzed in the context of the models of doping *a*-Si:H with erbium that resulted in the emergence of *n*-type conduction and formation of a heterojunction as the film grew.

ACKNOWLEDGMENTS

This work was supported by INTAS (grant no. 97-1910) and COPERNICUS (grant no. 977048-SIER).

REFERENCES

1. G. S. Pomrenke, P. B. Klein, and D. W. Langer, Mater. Res. Soc. Symp. Proc. **301** (1993).
2. C. Coffa, A. Polman, and R. N. Shwartz, Mater. Res. Soc. Symp. Proc. **422** (1996).
3. M. S. Bressler, O. B. Gusev, V. Kh. Kudoyarova, *et al.*, Appl. Phys. Lett. **67**, 3599 (1995).
4. T. Oestereich, C. Swiatowski, and I. Broser, Appl. Phys. Lett. **56**, 446 (1990).
5. J. H. Shin, R. Serna, G. N. van den Hoven, *et al.*, Appl. Phys. Lett. **68**, 997 (1996).
6. A. R. Zanatta, L. A. O. Nunes, and L. R. Tessler, Appl. Phys. Lett. **70**, 511 (1997).
7. V. B. Voronkov, V. G. Golubev, A. V. Medvedev, *et al.*, Phys. Solid State **40**, 1301 (1998).
8. E. I. Terukov, O. I. Kon'kov, V. Kh. Kudoyarova, *et al.*, Fiz. Tekh. Poluprovodn. (St. Petersburg) **32**, 8 (1998) [Semiconductors **32**, 884 (1998)].
9. R. A. Street, in *Hydrogenated Amorphous Silicon*, Ed. by R. W. Cahn, E. A. Davis, and I. M. Ward (Cambridge Univ. Press, Cambridge, 1991), p. 293.
10. S. Libertino, S. Coffa, G. Franzo, and F. Priolo, J. Appl. Phys. **78**, 3867 (1995).
11. S. Hasegawa, J. Kasajima, and T. Shimiru, Philos. Mag. B **43**, 149 (1981).

Translated by A. Spitsyn

Semiconductors, Vol. 34, No. 7, 2000, pp. 835–843. Translated from Fizika i Tekhnika Poluprovodnikov, Vol. 34, No. 7, 2000, pp. 868–876.
Original Russian Text Copyright © 2000 by Kyuregyan.

PHYSICS OF SEMICONDUCTOR DEVICES

Fringing Field of High-Voltage Planar *p–i–n* Diodes with a Nonuniformly Doped Guard Ring

A. S. Kyuregyan
All-Russia Power Institute, ul. Krasnokazarmennaya 12, Moscow, 111250 Russia

Submitted October 15, 1999; accepted for publication January 18, 2000

Abstract—An exact analytical solution to the problem of the electric-field distribution in a plane capacitor with infinitely long interelectrode space, thin electrodes, and a nonuniform surface charge at the boundary of an insulator that fills the capacitor was derived. Such a capacitor represents an adequate model of a *p–i–n* diode with shallow planar junctions, a stopper ring, and a lightly doped guard ring. It is shown that a guard ring with the surface charge density Q_s varying over the semiconductor–free space interface makes it basically possible to reduce the largest value of the fringing field to the bulk value E_0. To this end, it is necessary that (i) the width of the guard ring is at least three times as large as the depletion region thickness d and (ii) the quantity Q_s is equal to $-E_0\varepsilon_0(\varepsilon + 1/2)$ in the internal region of the guard ring and increases gradually to $E_0\varepsilon_0(\varepsilon + 3/2)$ (if there is a stopper ring) or to zero (if there is no stopper ring) in a band that has a width no less than d and is located at the outer boundary of the guard ring. The results of calculations can be also used to optimize the doping profile in the diodes fabricated using silicon-on-insulator technology. *© 2000 MAIK “Nauka/Interperiodica”.*

1. INTRODUCTION

The problem of minimizing the fringing electric field of shallow high-voltage planar *p–n* junctions has become especially urgent in the last 10–15 years owing to the fact that these junctions form the basis of all known types of the most promising high-power devices (such as MOSFETSs, IGBTs, SITs, MCTs, etc.) [1]. In most cases, this problem has been solved by introducing several (typically, from two to seven) separating rings at the periphery of the device. Such a periphery configuration was first suggested more than 30 years ago [2] and incorporates not only indubitable technological merits but also at least two basic drawbacks.[1] First, due to heavy doping of the rings, the field strength E increases drastically in the vicinity of the surface exposure of these rings compared with the mean level and exceeds the largest value E_0 in the central (planar) region of the device by at least 10–20% (see, e.g., [3]). Second, the presence of a large number of separating rings sharply reduces the active area of the device for a given chip size, especially in the case of high-voltage devices of not-too-high power. The most promising alternative solution, suggested almost simultaneously by a number of researchers in the mid-1980s [4–10], consists in the replacement of heavily doped separating rings, which are isolated from the main junction and from each other, with a single lightly doped guard ring that is in contact with the main junction (Fig. 1a). Numerical calculations of the two-dimensional (2D) distribution of the field in such structures showed [3–12] that the efficiency of a guard ring depends appreciably on its depth, width, and the impurity concentration. However, as is often the case, the conduction of even an extensive set of diverse and unrelated numerical calculations has not made it possible to formulate the general quantitative requirements for optimal parameters of the rings or to prove conclusively their efficiency in protecting a large class of devices. These problems can be solved only by using an analytical theory, which has not been developed thus far. It is clear that such a 2D theory can only be developed for the simplest model. For example, if we ignore the fact that the diode base is doped and regard the thickness of all diffusion layers and the protective insulator as infinitely small, the problem is then reduced to calculation of the field strength in a plane capacitor with an infinitely long gap filled with an insulator.[2] Such a capacitor is shown schematically in Fig. 1b. In this case, the charge of doping impurities in the guard ring degenerates into the surface charge at the semiconductor–free space interface. The third electrode of the capacitor simulates the stopper ring formed in certain cases to separate the depletion region from the crystal edge. The suggested model of the device is not only the simplest, but it can also be used in the situation where the capacitor has infinitely thin (i.e., sharp) electrodes, in which case it is much more difficult to minimize the fringing field than in any actual device with diffusion layers of finite thickness. However, if the problem can be solved for the extreme model mentioned above, it can even

---

[1] In implementing this configuration, there is no need for any additional operation compared with the case of a simple planar junction; it is sufficient to simply change the relevant photomask.

[2] The gap may be considered as rectilinear if the minimal radius of curvature of the main junction is much larger than the base thickness.

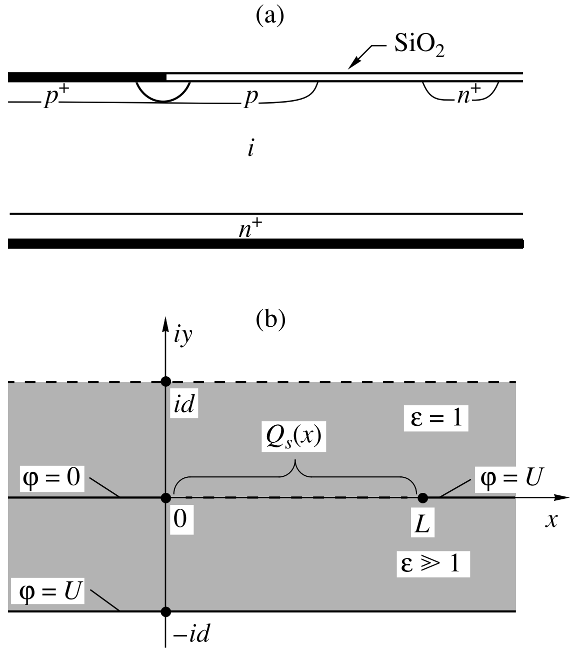

Fig. 1. (a) Schematic representation of cross section of the peripheral region of a planar p^+–i–n^+ structure with a lightly doped guard ring and (b) a model in the complex plane $z = x + iy$; this model was used in calculation of the fringing field.

more readily solved for actual devices. This is exactly the objective of this study.

2. GENERAL SOLUTION TO THE FRINGING-FIELD PROBLEM

It is most convenient to calculate the potential $\varphi(x, y)$ and the field $E(x, y)$ for the suggested 2D model using the well-known methods in the theory of the complex-variable functions [13]. Let $\varphi_1(x, y)$ be the function that is harmonically conjugate to $\varphi(x, y)$. In this case, $\mathbf{E}(z) = -d(\varphi + i\varphi_1)/dt$ is a function that is analytical in the upper half-plane (i.e., above the capacitor) and within the band $-d < y < 0$ (inside the capacitor) of the complex plane $z = x + iy$ (see Fig. 1b). Since the electrodes of the capacitor are equipotential, we have

$$\operatorname{Re}\mathbf{E}(z) = 0 \quad \text{for} \quad z = x < 0, \quad z = x > L, \text{ and } z = x - id. \tag{1}$$

At the semiconductor–insulator interface, the typical conditions for the normal $E_n(x)$ and tangential $E_t(x)$ fields must be satisfied; therefore, for $0 < x < L$, we should have

$$\operatorname{Re}\mathbf{E}(x + i0) = \operatorname{Re}\mathbf{E}(x - i0) = E_t(x), \tag{2}$$

$$\operatorname{Im}\mathbf{E}(x + i0) = \frac{Q_x(x)}{\varepsilon_0} + \varepsilon \operatorname{Im}\mathbf{E}(x - i0). \tag{3}$$

Here, ε is the relative permittivity of the semiconductor; ε_0 is the permittivity of free space; and $Q_s(x) \equiv Q_0 f_q(x)$ is the surface-charge density, where $Q_0 = Q_s(0)$ and $f_q(x)$ is a dimensionless function. Solutions to the boundary value problems for the internal and external regions of the capacitor with the boundary conditions given by (1) are expressed in terms of the tangential field $E_t(x)$ using the corresponding Schwarz integrals for the band and half-plane [13]. Joining these solution and taking into account conditions (2) and (3), we can readily obtain a singular integral equation for $E_t(x)$. Unfortunately, regularization of this equation by the known method [14] leads to a Fredholm equation of the second kind with a bounded kernel; generally, this equation cannot be solved analytically and is extremely difficult to analyze qualitatively. Therefore, we use a method that makes it possible to simplify the problem in the case under consideration. Namely, we will seek a solution assuming that the distribution of potential $\varphi(x, d)$ along the straight line $y = d$ is known. In this case, for the boundary condition that is applied to the band $0 < y < d$ in the upper half-plane in Fig. 1b and complements condition (1), the following equality can be used:

$$\operatorname{Re}\mathbf{E}(x + id) = -E_0 f_e(x) \equiv -\frac{d\varphi(x, d)}{dx}. \tag{4}$$

Here, $E_0 = U/d$; U is the anode and the stopper ring potential with reference to the cathode; and the function $f_e(\xi)$ is bell-shaped, has the limiting values of $f_e(\pm\infty) = 0$, and is normalized as[3]

$$\int_{-\infty}^{\infty} f_e(x)dx = d. \tag{5}$$

In this case, the Schwarz integral becomes

$$\mathbf{E}(z) = -\frac{i}{2d}\left[\int_0^L E_t(x')\coth\left(\frac{\pi}{2}\frac{x'-z}{d}\right)dx' + E_0\int_{-\infty}^{\infty} f_e(x')\tanh\left(\frac{\pi}{2}\frac{x'-z}{d}\right)dx' - 2dc_0\right], \tag{6}$$

for the band $0 < y < d$ and

$$\mathbf{E}(z) = -\frac{i}{2d}\left[\int_0^L E_t(x')\coth\left(\frac{\pi}{2}\frac{x'-z}{d}\right)dx' - 2dc_1\right], \tag{6a}$$

for the band $-d < y < 0$.

---

[3] These basic properties of the function $f_e(\xi)$ follow from the obvious fact that $\varphi(x, d)$ varies steadily from 0 for $x \longrightarrow -\infty$ to U for $x \longrightarrow \infty$.

The constants of integration c_0 and c_1 are to be determined from the obvious additional conditions

$$\int_{-d}^{0} \operatorname{Im}\mathbf{E}(-\infty + iy)dy = U, \qquad \int_{0}^{d} \operatorname{Im}\mathbf{E}(-\infty + iy)dy = 0. \tag{7}$$

Substituting (6) and (6a) in (7), changing the order of integration, and taking into account the equality

$$\int_0^L E_t(x)dx = -U, \tag{8}$$

we can show that $c_0 = 0$ and $c_1 = U/2d$. Calculating the boundary values of $\operatorname{Im}\mathbf{E}(x \pm i0)$ in the interval $0 < x < L$ with the use of (6), (6a), and the Sokhotskiĭ–Plemel' formula [13, 14], substituting these values into (3), and performing elementary transformations, we obtain the formula for the normal field

$$E_n(x) = \frac{1}{\varepsilon + 1}\left[\frac{Q_0}{\varepsilon_0} f_q(\xi) - E_0\Phi(\xi)\right] \tag{9}$$

and the equation for the tangential field

$$\frac{1}{\pi}\int_1^a E_t[x(\xi')]\frac{d\xi'}{\xi' - \xi} = E_n[x(\xi)], \tag{10}$$

where $\Phi(\xi) = \frac{1}{\pi}\int_0^\infty f_e[x(\xi')]\frac{d\xi'}{\xi' + \xi}$ and the notation $\xi = \xi(x) = \exp\left(\pi\frac{x}{d}\right)$ and $a = \xi(L)$ is used. As is known [14], the bounded solution to equation (10) has the form

$$E_t[x(\xi)] = -\frac{\sqrt{(\xi - 1)(a - \xi)}}{\pi} \times \int_1^a \frac{E_n[x(\xi')]}{\sqrt{(\xi' - 1)(a - \xi')}}\frac{d\xi'}{\xi' - \xi} \tag{11}$$

and exists only if

$$\int_1^a \frac{E_n[x(\xi)]d\xi}{\sqrt{(\xi - 1)(a - \xi)}} = 0. \tag{12}$$

In addition, equality (8) should hold; substituting this equality into expression (11) for $E_t(\xi)$, we obtain the additional condition

$$\frac{\sqrt{a}}{\pi}\int_1^a \frac{E_n[x(\xi)]}{\sqrt{(\xi - 1)(a - \xi)}}\frac{d\xi}{\xi} = -E_0. \tag{13}$$

Finally, substituting (9) into (11)–(13) and changing the order of integration, we have, correspondingly,

$$E_t(x) = \frac{E_0}{\varepsilon + 1}\sqrt{\frac{(\xi - 1)(a - \xi)}{a}} \times \left[\frac{\varepsilon + F_e^1(0)}{F_q^1(0)}F_q^1(\xi) - F_e^1(\xi)\right], \tag{14}$$

$$F_e^0 F_q^1(0) = -F_q^0[\varepsilon + F_e^1(0)], \tag{15}$$

$$\frac{Q_0}{\varepsilon_0} = -E_0\frac{\varepsilon + F_e^1(0)}{F_q^1(0)}, \tag{16}$$

where

$$F_q^n(\xi) = \frac{1}{\pi}\int_1^a \left(\frac{\sqrt{a}}{(\xi' - \xi)}\right)^n \frac{f_q[x(\xi')]d\xi'}{\sqrt{(\xi' - 1)(a - \xi')}}, \tag{17}$$

$$F_e^n(\xi) = \frac{1}{\pi}\int_0^\infty \left(\frac{\sqrt{a}}{\xi' + \xi}\right)^n \frac{f_e[x(\xi')]d\xi'}{\sqrt{(\xi + 1)(a + \xi')}}. \tag{18}$$

Formulas describing the distribution of the surface field in a *p–i–n* structure without a stopper ring can be most readily derived by performing the passage to the limit $a \longrightarrow \infty$ in (14) and (17). Taking also into account that the functions $f_q(\xi)$ and $f_e(\xi)$ tend to zero with increasing ξ, we obtain

$$E_t(x) = E_0\frac{\sqrt{\xi - 1}}{\varepsilon + 1}\left[\frac{\varepsilon + F_e^1(0)}{F_q^1(0)}F_q^1(\xi) - F_e^1(\xi)\right], \tag{14a}$$

$$F_q^1(\xi) = \frac{1}{\pi}\int_1^\infty \frac{f_q[x(\xi')]}{\sqrt{\xi' - 1}}\frac{d\xi'}{\xi' - \xi}, \tag{17a}$$

$$F_e^1(\xi) = \frac{1}{\pi}\int_0^\infty \frac{f_e[x(\xi')]}{\sqrt{\xi + 1}}\frac{d\xi'}{\xi' + \xi}. \tag{18a}$$

Furthermore, it follows from (17) and (18) that $\lim_{a \to \infty} F_q^0 = \lim_{a \to \infty} F_e^0 = 0$; therefore, condition (15) for the existence of a bounded solution $E_t(x)$ in a *p–i–n* structure without a stopper ring is satisfied automatically for any distribution of the charge $Q_s(x)$ that meets condition (16).

Strictly speaking, the performed transformations did not bring us any closer to the solution of the problem, because the right-hand sides of formulas (9) and (14)–(16) involve an unknown function $f_e(x)$. Basically, this function can be eliminated by expressing it in terms of the tangential field $E_t(x)$ using the Poisson integral (see Appendix). However, in that case, we obtain the integral Fredholm equation for $E_t(x)$ rather than expression (14); this equation again cannot be solved analytically, although it is now not singular. Nevertheless, the regularization method used above has an important advantage in the case under consideration compared with the known method [14]. Namely, all the terms in (9) and (14)–(16) that do not contain $f_e(x)$ incorporate (and those that contain $f_e(x)$ do not incorporate) the large multiplier ε; in addition, the inequalities $\Phi(\xi) < 1$, $F_e^0 < 1$, and $F_e^1(\xi) < F_e^1(0) < 1$ hold. Therefore, substitution of any bell-shaped function with correct limiting values and normalization (5) for $f_e(x)$ introduces an error in any case no larger than $1/\varepsilon$. In other words, the conditions at the outer boundary $y = d$ affect only slightly the distribution of potential and the surface field inside the semiconductor due to the fact that the effects external with respect to the semiconductor are screened owing to the pronounced polarizability of the crystal. Henceforth, we will use the simplest approximation defined as

$$f_e(x) = \begin{cases} \dfrac{\pi}{2\ln\Lambda} & \text{for} \quad \Lambda^{-1} < \xi < \Lambda, \\ 0 \quad \text{for} \quad \xi < \Lambda^{-1} & \text{and} \quad \xi > \Lambda, \end{cases} \tag{19}$$

assuming that $\Lambda \gg a$ in the presence of the stopper ring and $1 \ll \Lambda \ll a$ in the absence of this ring. Evaluation of the relevant integrals yields (in the limit of $\Lambda \longrightarrow \infty$) the following simple expressions:

$$F_e^1(\xi) = 0 \quad \text{for} \quad 1 < \xi < a, \tag{20}$$

$$F_e^1(0) = \Phi(\xi) = 1/2, \tag{21}$$

$$F_e^0 = \begin{cases} 1/2 \text{ for finite } a \text{ (there is a stopper ring)}, \\ 0 \quad \text{for } a \gg \Lambda \text{ (there is no stopper ring)}. \end{cases} \tag{22}$$

This approximation corresponds to the use of the boundary condition $\varphi(x, d) = U/2$ and, as shown in Appendix, introduces an error no larger than $1/2\varepsilon$. All the results of the next section are correct to the same accuracy.

3. MINIMIZATION OF THE FRINGING FIELD

Further calculations can be performed only after the form of function $f_q(x)$ is specified. In this case, we should bear in mind the main objective in forming the guard ring, which consists in minimizing the field strength at the interface

$$E_s(x) = \sqrt{E_n^2(x) + E_t^2(x)}, \tag{23}$$

which is necessary to ensure the highest breakdown voltage of the device.

It was found that, in the presence of a stopper ring, this objective can be accomplished, if we use, in particular, a function

$$f_q(x) = \frac{1 - \gamma\left(\dfrac{\xi - 1}{a - \xi}\right)^m}{1 + \left(\dfrac{\xi - 1}{a - \xi}\right)^m} \tag{24}$$

with the parameters m and γ related to each other by equation (15). The plots of function (24) are shown in Fig. 2a for several values of the parameters. If m is an integer, the integrals in (18) are evaluated by a conventional method using the theory of residues [13]; thus, we have

$$F_q^0 = \frac{1 - \gamma}{2}, \tag{25}$$

$$F_q^1(0) = 1 - (\gamma + 1)\left[\frac{1}{(-a)^m + 1} + \Psi_m(a, 0)\right], \tag{26}$$

$$F_q^1(\xi) = -(\gamma + 1)\sqrt{\frac{a}{a - \xi}}\Psi_m(a - \xi; \xi), \tag{27}$$

$$\text{for } 1 < \xi < a,$$

where

$$\Psi_m(x, y) = \frac{x + y - 1}{m}\sqrt{\frac{x}{2}}$$

$$\times \sum_{k=1}^{m} \frac{\sqrt{1 - \cos\theta_k}}{x^2 - 2x(y - 1)\cos\theta_k + (y - 1)^2},$$

$$\theta_k = \pi\frac{2k - 1}{m}.$$

Substituting (22) and (23) into (15) and solving the resulting equation for γ, we obtain

$$\gamma = \frac{\dfrac{\varepsilon + F_e^1(0)}{2F_e^0} + 1 - \dfrac{1}{1 + (-a)^m} - \Psi_m(a, 0)}{\dfrac{\varepsilon + F_e^1(0)}{2F_e^0} + \dfrac{1}{1 + (-a)^m} + \Psi_m(a, 0)}. \tag{28}$$

The dependences $E_s(x)$, $E_t(x)$, and $E_n(x)$ plotted using the above formulas for certain values of the parameters are shown in Fig. 3. As can be seen, the normal field $E_n(x)$ is highest at the ends of the interval $0 < x < L$ where the tangential field $E_t = 0$. As the distance from the interval ends increases, $E_n(x)$ decreases, whereas $E_t(x)$ increases. For $m = 1$, a unique situation arises: variations in the quantities $E_n(x)$ and $E_t(x)$ compensate each other exactly, so that the field strength at

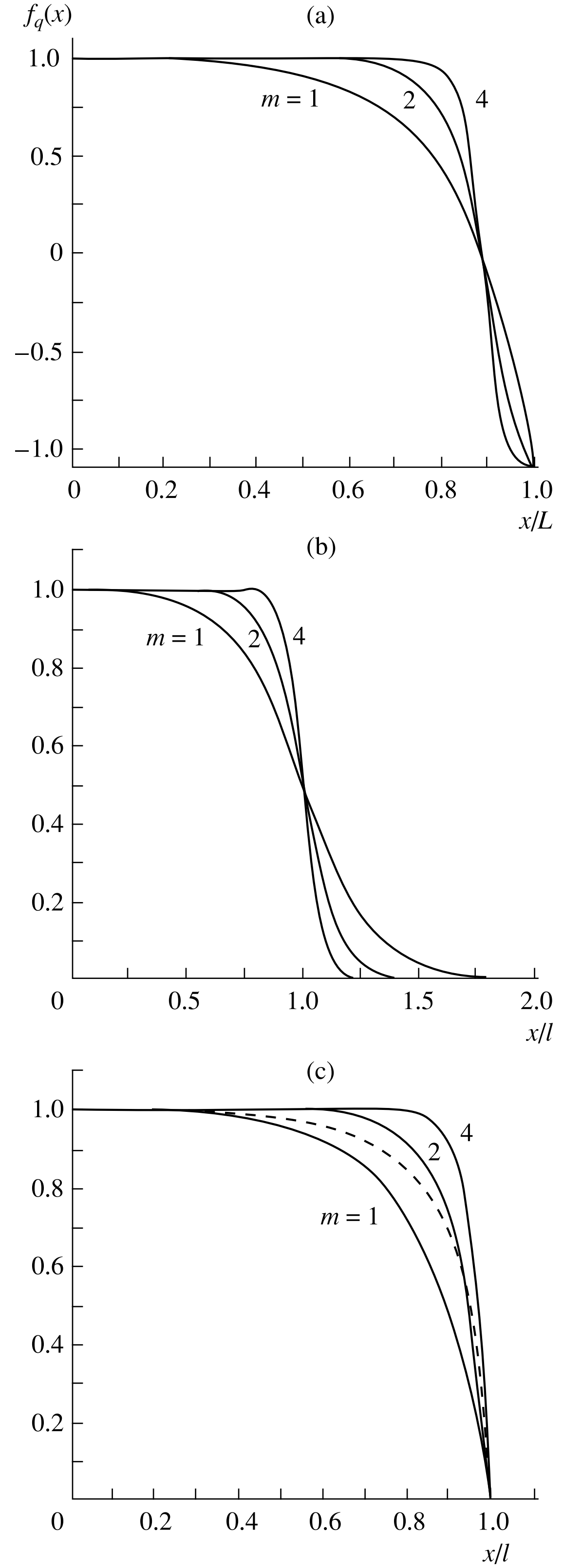

Fig. 2. Distributions of the surface charge density used in calculations of the fringing field in planar p^+–i–n^+ structures (a) with and (b, c) without a stopper ring.

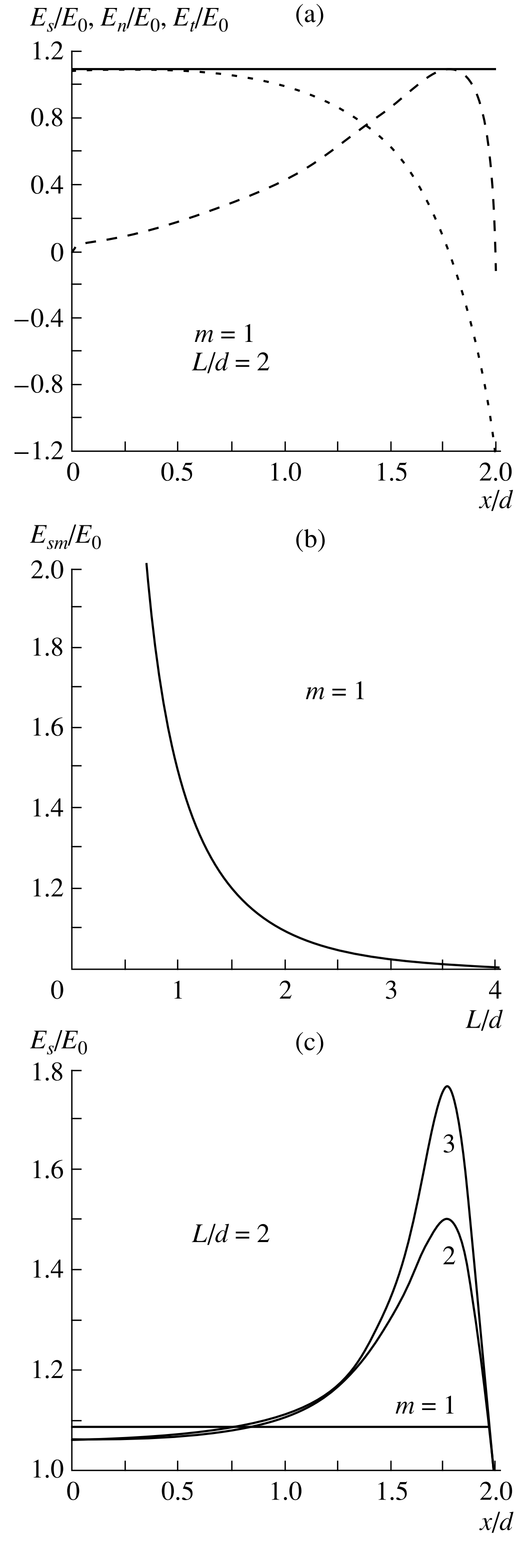

Fig. 3. The results of calculations of fringing fields in planar p^+–i–n^+ structures with stopper rings. (a) The functions $E_n(x)$ (dotted line), $E_t(x)$ (dashed line), and $E_s(x)$ (solid line) in relation to the dimensionless coordinate for $m = 1$ and $L/d = 2$; (b) the dependence of the ratio E_{sm}/E_0 on the value of L/d for $m = 1$; and (c) the dependence of the ratio $E_s(x)/E_0$ on the dimensionless coordinate for $L/d = 2$ and several values of the parameter m.

the interface $E_s(n)$ is independent of the coordinate and equals

$$E_s(x) = E_0 \coth\frac{\pi L}{4d}. \tag{29}$$

In this special case, the distribution of the surface charge $Q_s(x)$ is of the form

$$Q_s(x) = Q_0\left[1 - (1+\gamma)\frac{\xi(x) - 1}{a - 1}\right], \tag{30}$$

and the parameters Q_0 and γ are given by

$$Q_0 = -E_0\varepsilon_0(\varepsilon + 1)\coth\frac{\pi L}{4d}, \tag{31}$$

$$\gamma = \frac{2(\varepsilon+1) + \tanh\frac{\pi L}{4d}}{2(\varepsilon+1) - \tanh\frac{\pi L}{4d}}. \tag{32}$$

Fringing field (29) is much larger than the bulk value E_0 for small L/d and is almost identical to E_0 for $L/d > 3$.

If $m \geq 2$, the "surface" *p–n* junction is more "abrupt" and the field $E_t(x)$ increases more rapidly than $E_n(x)$ decreases as the distance from the ends of the interval $0 < x < L$ increases. For arbitrary m, the maximum of $E_t(x)$ is located at the point

$$x = x_0 \equiv \frac{d}{\pi}\ln\frac{a+1}{2},$$

and the position of the surface *p–n* junction is at the point

$$x = x_s \equiv \frac{d}{\pi}\ln\frac{a + \gamma^{1/m}}{1 + \gamma^{1/m}},$$

where $|E_n(x_s)| = \frac{1}{2}\frac{E_0}{\varepsilon + 1} \ll |E_t(x_0)|$. Since $(\gamma - 1) \approx 1/\varepsilon \ll 1$, we have $x_0 \approx x_s$; therefore,

$$E_{sm} = \max E_s(x) \approx |E_t(x_0)|$$
$$= \frac{E_0}{\varepsilon+1}\frac{2\varepsilon+1}{2F_q^1(0)}\frac{1+\gamma}{2}\sum_{i=1}^{m}(m\sin\theta_k/2)^{-1}. \tag{33}$$

The sum in the right-hand side of (33) can be approximated rather accurately with the function $1 + 0.62\ln m$; it is the latter that largely defines the dependence of E_{sm} on the degree of abruptness of the surface *p–n* junction. It can be easily verified that, even for $m = 2$, the largest magnitude of the fringing field exceeds E_0 by a factor of 1.5 even if $L/d > 3$.

It is clear that not only an increase in the parameter m but also the use of any surface-charge distribution $Q_s(x)$ different from (30) would cause the field $E_s(x)$ to become nonuniform; consequently, this field would exceed the value given by formula (29). Thus, we found a solution to the above-formulated problem: for a given distance between the main electrode and the stopper ring, the fringing field is smallest if the surface-charge distribution $Q_s(x)$ is described by formula (30).

If there is no stopper ring, the fringing field may be minimized by using, for example, the following approximation:

$$f_q(x) = \frac{1}{1 + \left(\frac{\xi - 1}{\lambda - 1}\right)^m}. \tag{34}$$

Here, $\lambda = \xi(l)$, where l is the width of the band in which most of the surface charge is concentrated (see Fig. 2b). In this case, for integer m, substitution of (34) into (18) yields

$$F_q^1(0) = 1 - \frac{1}{(1-\lambda)^m + 1} - \Psi_m(\lambda - 1; 0), \tag{35}$$

$$F_q^1(\xi) = -\Psi_m(\lambda - 1; \xi), \quad \text{for} \quad 1 < \xi. \tag{36}$$

The results of calculating the fringing field using these formulas are shown in Fig. 4. As can be seen, the normal field $E_n(x)$ is almost constant for $0 < x < l - d$, decreases by a factor of about 2 for $x = l$, and then rapidly tends to the value of $\frac{1}{2}\frac{E_0}{\varepsilon+1}$.[4] Conversely, the tangential field $|E_t(x)|$ has the largest magnitude for $x = l$, with the value of $|E_t(l)|$ being also defined by formula (33) for $\gamma = 0$. As in the case where the stopper ring is present, an increase in $|E_t(x)|$ with increasing x is more rapid than a decrease in $|E_n(x)|$ if $m \geq 2$. However, under these conditions, the absolute maximum of $E_s(x)$ exceeds $E_s(0)$ merely by several percent for $m = 2$. Therefore, the surface-charge distribution given by (34) may be used without significantly increasing the value of $\max E_s(x)$ for $m \leq 2$.

In order to gain insight into the extent of influence of details of the surface-charge distribution on the fringing field, we performed calculations for two other cases. Using the functions given by

$$f_q(x) = \begin{cases} 1 - \left(\frac{\xi - 1}{\lambda - 1}\right)^m & \text{for} \quad x < l, \\ 0 \quad \text{for} \quad x \geq l \end{cases} \tag{37}$$

we have

$$F_q^1(0) = \frac{2}{\pi}\left\{\left[1 - \frac{1}{(1-\lambda)^m}\right]\arctan\sqrt{\lambda - 1} + \frac{1}{\sqrt{\lambda - 1}}\sum_{k=1}^{m}\frac{(-1)^k(\lambda-1)^{1-k}}{2m + 1 - 2k}\right\}. \tag{38}$$

---

[4] This result is a consequence of the fact that we used approximation (19) for $f_e(\xi)$. Actually, of course, we should have $E_n(\infty) = 0$.

If we use the distribution defined as

$$f_q(x) = \begin{cases} \sqrt{\dfrac{\lambda-\xi}{\lambda-1}} & \text{for} \quad x < l, \\ 0 \quad \text{for} & x \ge l \end{cases} \tag{39}$$

with the root singularity for $x \longrightarrow l$, we obtain

$$F_q^1(0) = \sqrt{\tanh\frac{\pi l}{4d}}. \tag{40}$$

In both cases, all the results of numerical calculations qualitatively completely coincide with the results shown in Fig. 4. In particular, in all cases, $E_{sm} = E_n(0)$ if $f_q(x)$ varies from 1 to $-\gamma$ (in the presence of stopper ring) or from 1 to 0 (without a stopper ring) in a band with a width on the order of d at the outer boundary of the guard ring. Qualitatively, the distinctions are insignificant. For example, if $\sqrt{a} \gg 1$, the important parameter $F_q^1(0)$ can be in all cases expressed as $F_q^1(0) = 1 - \eta\exp\left(-\dfrac{\pi L}{2d}\right)$ and the constant η alone varies in the range from $2/\pi$ to 2, depending on the features of the $Q_s(x)$ distribution.

4. DISCUSSION OF THE RESULTS

The main results reported above can be formulated in the following way. First, the highest strength of the fringing field E_{sm} is invariably larger than the bulk value E_0. Second, the proper choice of the surface-charge distribution $Q_s(x)$ makes it possible to reduce the difference $E_{sm} - E_0$ to any given value. With this aim in view, the following two conditions should be satisfied:

(i) The surface-charge density $Q_s(x)$ should vary gradually from the smallest value Q_0 to the largest value (equal to $-\gamma Q_0$ and zero in the presence and in the absence of the stopper ring, respectively) within the band that has a width no smaller than the thickness d of the ith layer and is located at the outer boundary of the guard ring. If this condition is satisfied, E_{sm} is equal to the field $E_n(0)$ normal to the surface at the inner boundary of the guard ring.

(ii) The width of the guard ring should exceed d by several times. If this condition is satisfied, the largest fringing field (to an accuracy on the order of $a^{-1/2}$) may be expressed as

$$E_{sm} = E_n(0) \approx E_0\left[1 + \delta - \frac{\Phi(1)}{\varepsilon+1}\eta\exp\left(-\frac{\pi L}{2d}\right)\right] \times \left[1 - \eta\exp\left(-\frac{\pi L}{2d}\right)\right]^{-1}, \tag{41}$$

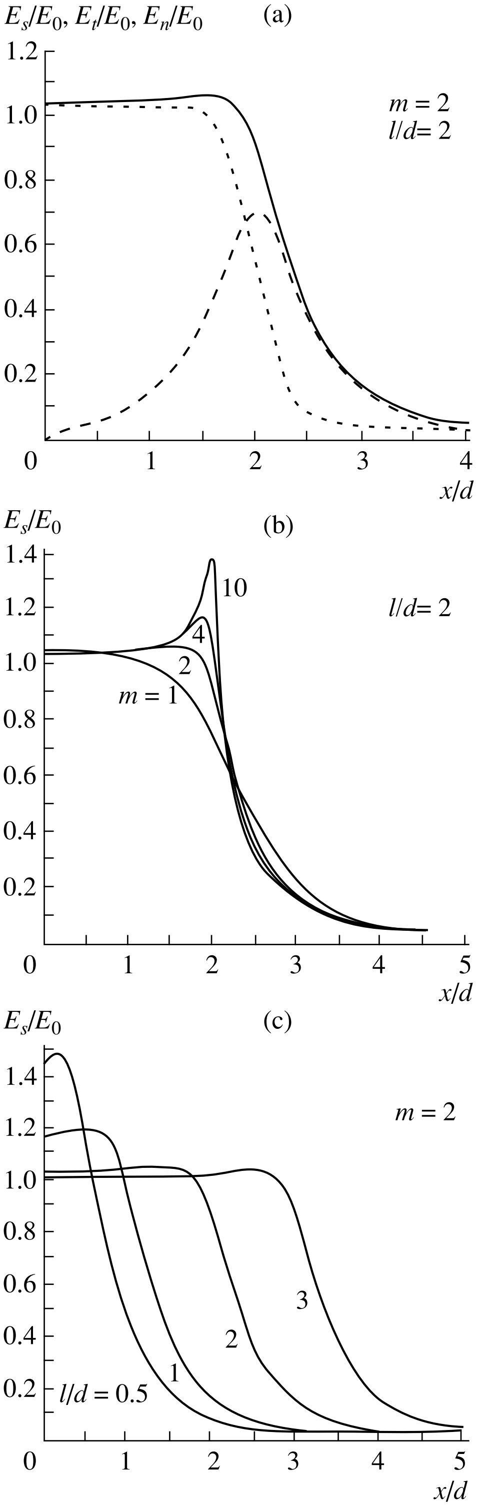

Fig. 4. The results of calculations of fringing fields in planar p^+–i–n^+ structures without a stopper ring. (a) The functions $E_n(x)$ (dotted line), $E_t(x)$ (dashed line), and $E_s(x)$ in relation to the dimensionless coordinate for $m = 2$ and $l/d = 2$; (b) the dependences of the ratio $E_s(x)/E_0$ on the dimensionless coordinate for $l/d = 2$ and several values of the parameter m; and (c) the dependences of the ratio $E_s(x)/E_0$ on the dimensionless coordinate for $m = 2$ and several values of the quantity l/d.

where $\delta = [F_e^1(0) + \Phi(1) - 1]/(\varepsilon + 1)$. Even for $L \geq 3d$, the exponential in (41) becomes negligibly small and $E_{sm} = E_0(1 + \delta)$.

If the function $f_e(x)$ is approximated by (19), we have $\delta = 0$. A more accurate estimate of the value of δ can be obtained using (14) and (A.1) (see Appendix); then we have

$$\delta = \frac{d}{\pi}\frac{1}{U(\varepsilon + 1)}\int_{-\infty}^{\infty} dx \int_0^L dx' \frac{\sqrt{a(\xi + 1)} - \sqrt{a + \xi}}{(\xi + 1)\sqrt{a + \xi}} \times \frac{E_t(x')}{(x - x')^2 + d^2}. \tag{42}$$

For large $\sqrt{a}$, the integrand in (18) exhibits sharp maximums at the points $x \approx \frac{\ln 3}{\pi} d$ and $x' \approx L - d$; therefore, the multiplier $[(x - x')^2 - d^2]^{-1}$ that depends only slightly on x and x' may be factored outside the integral sign for the above values of the arguments. As a result, we have the estimate

$$\delta \approx \frac{2\ln 2}{(\varepsilon + 1)\pi^2}\frac{d^2}{(L - 1.35d)^2 + d^2} < 0.01\frac{d^2}{L^2}. \tag{43}$$

As can be seen from (43), we may actually assume that, for $L \geq 3d$, $\delta = 0$ and $E_{sm} = E_0$ to an accuracy acceptable for practical purposes.

It should be emphasized that, for a capacitor with a given surface-charge distribution $Q_s(x)$, all the above-obtained results are valid only for a single value of the voltage

$$U = U_q \equiv -d\frac{Q_0}{\varepsilon_0}\frac{F_q^1(0)}{\varepsilon + F_e^1(0)} \approx -d\frac{2Q_0}{\varepsilon_0(2\varepsilon + 1)}, \tag{44}$$

defined by formula (16). For any other values of U, equation (11) does not have a bounded solution; i.e., the tangential component of the fringing field tends to infinity at the electrode boundaries. However, this divergence is a result of the fact that we used the capacitor model with infinitely thin metallic electrodes of constant width. In an actual *p–i–n* junction for $U \neq U_q$, the situation is radically different. Namely, if $U > U_q$, the tangential field increases drastically near the boundary of the guard ring, albeit remaining finite. The quantity E_{sm} strongly depends on the impurity distribution in the p^+-layer and the stopper ring (like in conventional planar junctions [1]) and cannot be calculated in the context of the model under consideration. In fact, there is no need for such a calculation as long as U_q is equal to the bulk breakdown voltage U_B, which cannot be exceeded by the bias U. However, if $U < U_q$, the guard-ring regions adjacent to the electrodes become progressively filled with charge carriers until complete neutralization is attained. As a result, the electrodes "expand," whereas the effective width of the ring depleted of the charge carriers decreases to the value that ensures the fulfillment of condition (16) for the existence of a bounded solution to equation (11). In this case, the ratio E_{sm}/E_0 increases, but the fringing field E_{sm} decreases compared to what was observed for $U = U_q$.

Thus, when calculating the quantity Q_0 for an "optimal" guard ring using formula (16), we should use the value of the bulk breakdown-field strength $E_0 = E_B$; in particular, for $L \geq 3d$, we have $Q_0 \approx -E_B\varepsilon_0(\varepsilon + 1/2)$. In other words, a merging of the depleted zone of the optimal guard ring with heavily doped p^+- and n^+- regions should occur for $U = U_B$. The fulfillment of this (third) condition in addition to conditions I and II above should ensure the highest possible surface-breakdown voltage of the device; this voltage can be as close to the bulk value U_B as is wished.

The results reported above can be used to optimize the design of another type of device, namely, high-voltage diodes fabricated on the basis of silicon-on-insulator (SOI) technology. The typical ratio of thicknesses of the insulator d_i and silicon d_s films can be as large as 10 or more; therefore, the approximation of infinitely thin electrodes used by us can be applied in this case as well. The charge of ionized impurities in the semiconductor film plays the role of the surface charge. The only distinction consists in the fact that the interelectrode space of the capacitor is filled with an insulator with a permittivity equal to four (in the case of SiO_2) rather than with a semiconductor depleted of free charge carriers and having a much larger permittivity. Therefore, the error introduced by using an incorrect approximation for $f_e(x)$ can be as large as 10%. However, the fact that the field in SOI diodes can be minimized by using the profile given by (30)–(32) is beyond question. This result is believed to be especially important, because the linear distribution of impurities over the surface has thus far been regarded as optimal [15, 16].

In conclusion, we note that the methods for forming an arbitrary profile of the dopant over the surface using high-resolution lithography are rather well developed [5, 17]; these methods require only that the dose of the ion implantation be accurate to within a few percent.

APPENDIX

An exact relationship between the tangential field at the interface $E_t(x)$ and the function $f_e(x)$ can be derived using the Poisson integral for the half-plane $y > 0$ [13]; thus, we have

$$f_e(x) = \frac{d}{E_0}\frac{1}{\pi}\int_0^L \frac{E_t(x')}{(x' - x)^2 + d^2}dx'. \tag{A.1}$$

For any dependence $E_t(x)$ (including the correct one), the function $f_e(x)$ exhibits a maximum located within the interval $0 < y < L$ and the asymptotic behavior

$f_e(x) \propto x^{-2}$ for large $|x|$. Unfortunately, analytical evaluation of the integrals $\Phi(\xi)$ and $F_e^1(\xi)$ for any function $f_e(x)$ that features the above asymptotic behavior is impossible. Therefore, in order to estimate the error related to the use of an "incorrect" approximation for $f_e(x)$, we compare two extreme limiting cases. One of them was already considered in Sections 2 and 3 of this paper: the function $f_e(x)$ described by formula (19) diminishes in the range of the values of interest of x much slower than x^{-2}. In the second case, we use the function

$$f_e(x) = \pi\frac{a-1}{\ln a}\frac{\xi}{(a+\xi)(\xi+1)}, \qquad (A.2)$$

which features a maximum for $x = L/2$ and the asymptotic behavior $f_e \propto \exp(-\pi|x|/d)$. For this function, we have

$$\Phi(\xi) = \frac{1}{\ln a}\left(\frac{a\ln a/\xi}{a-\xi} - \frac{\ln\xi}{\xi-1}\right), \qquad (A.3)$$

$$F_e^0 = F_e^1(0) = \frac{2}{\ln a}\frac{\sqrt{a}-1}{\sqrt{a}+1} = \frac{2d}{\pi L}\tanh\frac{\pi L}{4d}, \qquad (A.4)$$

$$F_e^1(\xi) = \frac{2\sqrt{a}}{\ln a}\frac{a-1}{(\xi-1)(a-\xi)}\left[\frac{\xi}{\sqrt{(\xi-1)(a-\xi)}}\right. \qquad (A.5)$$
$$\left.\times\arctan\frac{\sqrt{(\xi-1)(a-\xi)}}{\xi+\sqrt{a}} - \frac{\xi+\sqrt{a}}{(\sqrt{a}+1)^2}\right].$$

Obviously, the exact solution should be found in between these two extreme cases; therefore, an error introduced into the results of calculations based on either approximation (19) or (A.2) does not exceed the difference between these approximations. The numerical calculations that we performed for a wide range of values of the parameters of interest showed that the difference is largest when calculating the quantity Q_0 using formula (16) for large values of a. It can be easily verified that, in the limit of $a \gg 1$, we have

$$\frac{\Delta Q_0}{Q_0} \le \frac{1}{2\varepsilon}\left(1 - \frac{2d}{\pi L}\right). \qquad (A.6)$$

In particular, in the case of Si, we have $\frac{\Delta Q_0}{Q_0} \le 0.035$ for $L = 3d$. In practice, such an error is of no importance, because the actually attainable accuracy in a reproduction of the dopant concentration is typically much lower than 3.5%.

ACKNOWLEDGMENTS

This study was supported by the Russian Foundation for Basic Research, project no. 98-02-17424.

REFERENCES

1. B. J. Baliga, *Modern Power Devices* (World Sci., Singapore, 1987), p. 132.
2. V. C. Kao and E. D. Wolley, Proc. IEEE **55**, 1409 (1967).
3. H. Yilmaz, IEEE Trans. Electron Devices **ED-38**, 1666 (1991).
4. K. Hwang and D. H. Navon, IEEE Trans. Electron Devices **ED-31**, 1126 (1984).
5. R. Stengl and U. Gosele, Tech. Dig. Int. Electron Devices Meet. 154 (1985).
6. S. Ahmad and J. Akhtar, IEEE Electron Device Lett. **EDL-6**, 465 (1985).
7. R. Stengl *et al.*, IEEE Trans. Electron Devices **ED-33**, 46 (1986).
8. V. Boisson, M. Le Helley, and J.-P. Chante, IEEE Trans. Electron Devices **ED-33**, 80 (1986).
9. S. Georgescu, T. Dunca, D. Sdrulla, and I. Gupta, Solid-State Electron. **29**, 1035 (1986).
10. V. K. A. Temple and W. Tanrapourn, IEEE Trans. Electron Devices **ED-33**, 1601 (1986).
11. J. Akhtar and S. Ahmad, Solid-State Electron. **33**, 1459 (1990).
12. P. Austing, J. L. Sanches, and R. Berriane, Solid-State Electron. **39**, 593 (1996).
13. M. A. Lavrent'ev and B. V. Shabat, *The Theory of the Functions of Complex Variables: Methods* (Nauka, Moscow, 1987).
14. N. I. Muskhelishvili, *Singular Integral Equations* (Nauka, Moscow, 1968; Wolters-Noordhoff, Groningen, 1972), p. 511.
15. S. Merchant *et al.*, in *Proceedings of the 3rd International Symposium on Power Semiconductor Devices and IC's*, 1991, p. 31.
16. S. Merchant, IEEE Trans. Electron Devices **ED-46**, 1264 (1999).
17. S. Merchant, IEEE Trans. Electron Devices **ED-42**, 1264 (1995).

Translated by A. Spitsyn

Semiconductors, Vol. 34, No. 7, 2000, pp. 844–847. Translated from Fizika i Tekhnika Poluprovodnikov, Vol. 34, No. 7, 2000, pp. 877–880.
Original Russian Text Copyright © 2000 by Vasil'ev, Esaev, Kravchenko, Osadchiĭ, Suslyakov.

PHYSICS OF SEMICONDUCTOR DEVICES

Study of the Effect of Graded Gap Epilayers on the Performance of $Cd_xHg_{1-x}Te$ Photodiodes

V. V. Vasil'ev, D. G. Esaev, A. F. Kravchenko, V. M. Osadchiĭ, and A. O. Suslyakov
Institute of Semiconductor Physics, Siberian Division, Russian Academy of Sciences,
pr. Akademika Lavrent'eva 13, Novosibirsk, 630090 Russia

Submitted January 10, 2000; accepted for publication January 24, 2000

Abstract—The characteristics of the photodiodes based on $Cd_xHg_{1-x}Te$ solid solutions with graded gap layers were calculated in the context of a one-dimensional diffusion–drift model. The parameters of the photodiodes were shown to be improved when the *p*–*n* junction was located in the near-surface graded gap region rather than in the central homogeneous section of the structure. The photodiodes with the *n*-type layer adjacent to the substrate were found to offer an advantage over the diodes with the *p*-layer close to the substrate in the case of illumination from the substrate side. © *2000 MAIK “Nauka/Interperiodica”.*

The surface recombination in $Cd_xHg_{1-x}Te$ photodiodes and photoresistors can be suppressed using the graded gap epilayers grown at the outer boundaries. The band gap of these layers increases towards the outer boundaries [1, 2]. There are theoretical [3] and experimental [4] data indicating that the photosensitivity of diodes changes if the *p*–*n* junction is brought into the graded gap region. It is apparent that the photodiode resistance also changes in this case. In this paper, the influence of the position of the *p*–*n* junction with respect to the graded gap layers on the photodiode characteristics was consistently studied by a numerical technique.

The detectivity D^* is the main characteristic of a photodiode. It is expressed as $D^* = R_\lambda\sqrt{A\Delta f}/\sqrt{I_n^2}$, where A is the photodiode area, Δf is the frequency band, I_n is the noise current, $R_\lambda = \eta q\lambda/hc$ is the sensitivity (expressed in A/W) at the wavelength λ, η is the quantum efficiency, q is the elementary charge, h is Planck's constant, and c is the speed of light. The device performance is also characterized by the product of the differential resistance at zero bias by the photodiode area, i.e., $R_0A = A\left(\frac{dI}{dV}\right)^{-1}_{V=0}$. For the sake of brevity, R_0A will be hereinafter referred to simply as the photodiode resistance. This parameter is of importance for conjugation with the readout device, and the larger its value the better.

In this paper, the calculations of the photodiode characteristics at the temperature $T = 77$ K are performed within the context of a one-dimensional diffusion–drift model including the Poisson equation and equations of continuity for electrons and holes, which take into account carrier recombination and photogeneration and the built-in field. The latter arises because of the dependence of the band structure parameters on the coordinate [5]. Similarly to [6], allowances are made for the Auger, Shockley–Read, and radiative recombination mechanisms. The material parameters are taken from [6]. The light absorption is taken into account according to [7]. The initial differential equation system is approximated by the finite difference scheme and solved numerically. The distributions of the electric-field potential and of the carrier density are the output parameters of this system. The currents are determined from these parameters. The values of R_λ and R_0A are calculated from the foregoing expressions, the quantum efficiency is defined as $\eta = I_p/q\Phi$, where Φ is the photon flux density and I_p is the photocurrent at zero bias across a photodiode. The detectivity D^* is calculated with consideration for thermal noise only, $I_n^2 = \frac{4k_0T}{R_0}\Delta f$, where k_0 is the Boltzmann constant.

The photodiodes with nearly realistic [1] profiles of the cadmium content across the structure are considered. These profiles for the cadmium content in the homogeneous region x^b_{Cd} equal to 0.22 and 0.3 are shown in Fig. 1. The position of the *p*–*n* junction is varied from the middle of the photodiode ($z = 5$ μm) to its surface (at the right in Fig. 1). The doping levels correspond to the actual conditions [1]. Namely, the layer adjacent to the buffer (at the left in Fig. 1) is characterized by the *p*-type conductivity and a doping level of 10^{16} cm^{-3}, while the near-surface *n*-type layer has a doping level of 10^{17} cm^{-3}. We shall designate this structure as the “*n*-on-*p*” type one. The *p*–*n* junction is assumed to be abrupt, which is a good approximation for that formed by ion implantation. The band diagram of the photodiode structure with the *p*–*n* junction located in the middle of the homogeneous region with

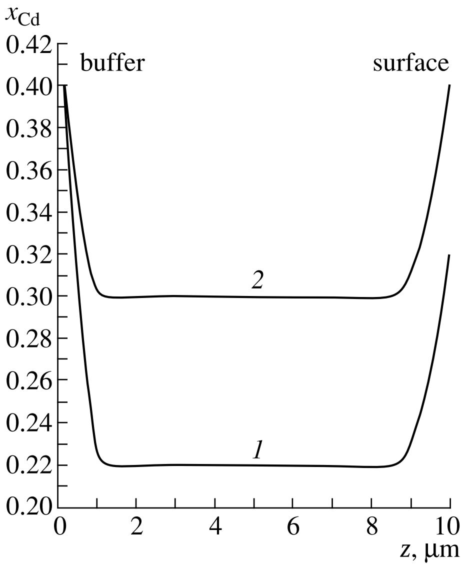

Fig. 1. Profiles of the cadmium content in the simulated structures for x^b_{Cd} = 0.22 (*1*) and x^b_{Cd} = 0.3 (*2*).

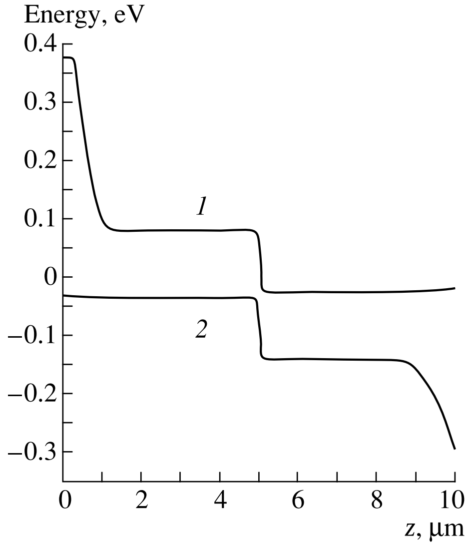

Fig. 2. Profiles of the (*1*) conduction- and (*2*) valence-band edges in the "*n*-on-*p*" photodiode with the *p*–*n* junction located in the middle of the structure. The data for x^b_{Cd} = 0.22 and zero bias are shown. The energy is reckoned from the Fermi level.

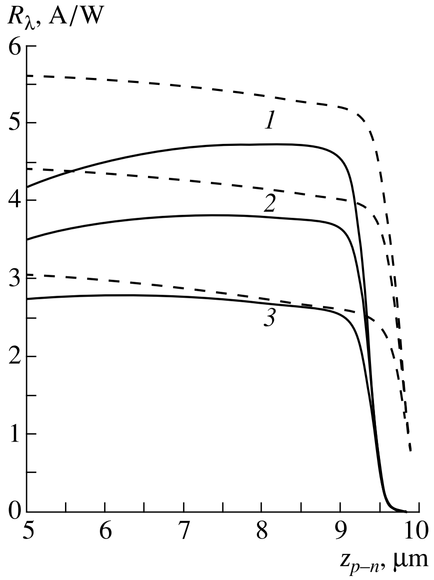

Fig. 3. Dependences of the current sensitivity of the photodiode R_λ on the position of the *p*–*n* junction in the cases of (*1*) x^b_{Cd} = 0.22 and λ = 8 µm; (*2*) x^b_{Cd} = 0.25 and λ = 6 µm; and (*3*) x^b_{Cd} = 0.3 and λ = 4 µm. The data for the photodiodes of the "*n*-on-*p*" (solid lines) and "*p*-on-*n*" (dashed lines) types are presented.

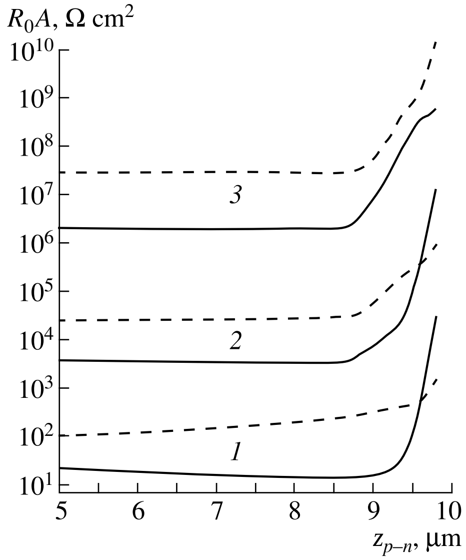

Fig. 4. Dependences of the differential resistance of the photodiode R_0A on the position of the *p*–*n* junction in the cases of (*1*) x^b_{Cd} = 0.22; (*2*) x^b_{Cd} = 0.25; and (*3*) x^b_{Cd} = 0.3. The data for the photodiodes of the "*n*-on-*p*" (solid lines) and "*p*-on-*n*" (dashed lines) types are presented.

x^b_{Cd} = 0.22 at zero applied voltage is shown in Fig. 2. The structure is illuminated from the substrate side.

The results of calculation of R_λ and R_0A dependences on the position of the *p*–*n* junction for different values of x^b_{Cd} are shown in Figs. 3 and 4 by solid lines. The maximum values of R_λ are presented for the position of the *p*–*n* junction in the middle of the photodiode. These values depend on the wavelength and vary

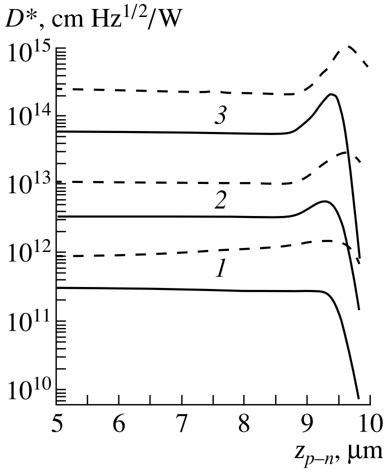

Fig. 5. Dependences of the photodiode detectivity D^* on the position of the p–n junction for $x^b_{\rm Cd}$ = (*1*) 0.22, (*2*) 0.25, and (*3*) 0.3. The data for the photodiodes of the "*n*-on-*p*" (solid lines) and "*p*-on-*n*" (dashed lines) types are presented.

slightly with the shift of the p–n junction. It is evident from Fig. 3 that, regardless of the cadmium content, the drastic drop of the sensitivity R_λ is observed at the same depth of the p–n junction occurrence, i.e., at a distance of approximately 1μm from the surface. The sensitivity falls and the differential resistance R_0A increases with an increase in $x^b_{\rm Cd}$ in the homogeneous section regardless of the position of the p–n junction. The weak variation of the sensitivity R_λ with the shift of the p–n junction in the homogeneous section of the structure is presumably associated with the fact that the diffusion lengths of electrons (≈35 μm) and holes (≈12 μm) are comparable to the photodiode thickness. Because of this, the distribution of photogenerated nonequilibrium carriers over the structure thickness is defined by the photogeneration function rather than by the diffusion.

The increase in R_0A with $x^b_{\rm Cd}$ when the p–n junction is formed in the homogeneous section of the photodiode is obviously related to the increase in the resistance of the quasi-neutral region. The much smaller decrease in the sensitivity with an increase in $x^b_{\rm Cd}$ when the p–n junction is located in the homogeneous region is due to the decrease in the wavelength alone at which R_λ is calculated. The reason for this is that in the vicinity of the sensitivity maximum the quantum efficiency η is close to unity in the relatively wide wavelength range.

When the p–n junction is shifted towards the structure surface in the graded gap region, the parameter R_0A increases steeply. In this case, the rise in the differential resistance occurs somewhat earlier than the drop in the sensitivity. The drastic increase in R_0A with the shift of the p–n junction towards the surface is quite reasonably explained by the increase in the energy gap. The fall in the sensitivity in the graded gap region near the surface is caused by the increase in the barrier height for carriers. This height is defined by both the composition and doping profiles [3, 4].

The variations in R_0A and R_λ discussed are responsible for the maximum in the dependence of detectivity D^* on the coordinate of the p–n junction when the latter is located at a depth of 0.7–0.8 μm from the surface (see Fig. 5). This maximum becomes more pronounced in the graded-gap region against the background of the general increase in the detectivity D^* with $x^b_{\rm Cd}$, and its height is approximately 3.5 times greater than D^* for the p–n junction located in the homogeneous section of the structure and $x^b_{\rm Cd}$ = 0.3. It is notable that a pronounced increase in R_0A is observed with the shift of the p–n junction to the graded-gap region while the decrease in D^* is relatively small. Thus, for $x^b_{\rm Cd}$ = 0.22 and the location of the p–n junction at a depth of 0.4 μm from the surface, R_0A increases 30-fold when compared to the case of the p–n junction in the middle of the structure, whereas D^* decreases by a factor of 5.5. This effect is even more pronounced with the increase in the cadmium content. For example, in the structure with $x^b_{\rm Cd}$ = 0.25 and the location of the p–n junction at a depth of 0.4 μm from the surface R_0A increases 110-fold when compared to the case of the p–n junction in the middle of the structure while D^* decreases only by a factor of 2.5.

Similar characteristics were calculated for the photodiode having a layer with the n-type conductivity and a doping level of 10^{15} cm^{-3} close to the substrate and the p-type layer with a doping level of 10^{16} cm^{-3} at the structure surface (dashed lines in Figs. 3–5). Until now, such photodiodes have not been implemented. Similar dependences are characteristic of these photodiode structures ("*p*-on-*n*") as of those of the "*n*-on-*p*" type but with some specific features. In contrast to the latter structure, the variation of the parameter R_0A with the shift of the p–n junction towards the surface in the graded gap region is substantially smaller for the "*p*-on-*n*" structures. In addition, for these structures at $x^b_{\rm Cd}$ = 0.22, the slow increase in R_0A begins even in the region of the homogeneous layer of the photodiode. For all values of $x^b_{\rm Cd}$, the current sensitivity of the "*p*-on-*n*" structures decreases steadily with the shift of the p–n junction towards the surface and decreases dramatically in the graded gap region as in the case of "*n*-on-*p*" structures. Lastly, the detectivity of the "*p*-on-*n*" photodiode with $x^b_{\rm Cd}$ = 0.22 increases steadily with the shift of the p–n junction towards the surface and attains a distinct maximum in the graded gap region. The decrease in D^* beyond its maximum is much smaller for the “*p*-on-*n*” structures than for the structures of the “*n*-on-*p*” type. It should be emphasized that the value of D^* in “*p*-on-*n*” structures exceeds noticeably that of “*n*-on-*p*” structures.

Thus, the numerical calculations performed demonstrate the possibility of improving the characteristics of the photodiodes based on $Cd_xHg_{1-x}Te$ graded-gap solid solutions when the p–n junction is formed in the graded gap region. The photodiode with a *p*-type layer on the *n*-layer offers few advantages over the diode with an *n*-layer on the *p*-layer.

REFERENCES

1. V. N. Ovsyuk, A. O. Suslyakov, T. I. Zakharyash, *et al.*, Proc. SPIE **2746**, 277 (1996).
2. V. M. Osadchiĭ, A. O. Suslyakov, V. V. Vasil’ev, and V. A. Dvoretskiĭ, Fiz. Tekh. Poluprovodn. (St. Petersburg) **33**, 293 (1999) [Semiconductors **33**, 297 (1999)].
3. K. Kosai and W.A. Radford, J. Vac. Sci. Technol. A **8**, 1254 (1990).
4. P. R. Bratt, J. Vac. Sci. Technol. A **1**, 1687 (1983).
5. K. M. van Vliet and A. H. Marshak, Solid State Electron. **23**, 49 (1980).
6. A. Rogalski and J. Piotrowski, Prog. Quantum Electron. **12**, 87 (1988).
7. W. W. Anderson, Infrared Phys. **20**, 363 (1980).

Translated by Yu. Aleshchenko

Semiconductors, Vol. 34, No. 7, 2000, pp. 848–852. Translated from Fizika i Tekhnika Poluprovodnikov, Vol. 34, No. 7, 2000, pp. 881–885.
Original Russian Text Copyright © 2000 by Aĭdaraliev, Beyer, Zotova, Karandashev, Matveev, Remennyĭ, Stus’, Talalakin.

PHYSICS OF SEMICONDUCTOR DEVICES

InGaAsSb(Gd)/InAsSbP Double Heterostructure Lasers (λ = 3.0–3.3 μm) for Diode Laser Spectroscopy

M. Aĭdaraliev*, T. Beyer, N. V. Zotova*, S. A. Karandashev*, B. A. Matveev*,**
M. A. Remennyĭ*, N. M. Stus’*, and G. N. Talalakin*
** Ioffe Physicotechnical Institute, Russian Academy of Sciences, Politekhnicheskaya ul. 26, St. Petersburg, 194021 Russia*
e-mail: bmat@iropt3.ioffe.rssi.ru
*** Fraunhofer Institute of Physical Measurement Techniques, 79110 Freiburg, Germany*

Submitted January 27, 2000; accepted for publication January 27, 2000

Abstract—Data on threshold currents, the differential quantum efficiency, the emission spectrum, current tuning, and radiation power of mesastripe InGaAsSb(Gd)/InAsSbP double heterostructure lasers with λ = 3.0–3.3 μm and a cavity length of 70–150 μm in a temperature range of 50–107 K are reported. In the experiments, the threshold currents $I_{\rm th} < 10$ mA, a total output power of 0.5 mW/facet, and a single-mode power of 0.43 mW at 77 K in the cw regime were obtained. Lasers operated in the single-mode regime at currents $I \le 6I_{\rm th}$, the spectral purity was as high as 650 : 1, the tuning rate was 210 cm^{-1}/A, and the tuning range was 10 cm^{-1} wide. An example of methane detection at 3028.75 cm^{-1} is presented. *© 2000 MAIK “Nauka/Interperiodica”.*

1. INTRODUCTION

The wavelength range λ = 3–4 μm contains the strongest absorption bands of methane (CH_4), formaldehyde (H_2CO), and other hydrocarbons, whose intensities exceed by one or two orders of magnitude the intensities of overtones in the IR region where it is common to detect gases. Because of this, the application of tunable lasers in the range of λ = 3.0–3.3 μm considerably expands the potentialities of high-resolution diode-laser spectroscopy and gas analysis. In recent years, diode lasers on the basis of double heterostructures (DHs) and solid solutions of III–V compounds, specifically, solid solutions on the basis of indium arsenide, have been intensively studied [1–4]. However, studies of single-mode lasers are few in number. Mesastripe lasers on the basis of such structures had threshold currents $I_{\rm th} \approx 100$ mA at the temperature T = 77 K [5] and worked in the quasi-single-mode regime at currents up to $2I_{\rm th}$ [6], which does not meet the requirements of the majority of practical problems.

As shown in [7], one can realize type I or II heterojunctions (HJs) depending on the composition of the active region and confining layers of InGaAsSb/InAsSbP DHs (λ = 3.0–3.6 μm). The HJ type determines the difference in radiative recombination mechanisms and temperature dependences of the energy and the type of radiation polarization. It was also shown [8] that the intraband absorption by holes accompanied by their change to the spin-orbitally split-off band represents the dominant mechanism of internal loss, which leads to a number of specific features, including laser mode tuning to the short-wavelength region [9].

In this paper, which continues our investigations [7–9], we study spectral characteristics of InGaAsSb/InAsSbP DH lasers (λ = 3.0–3.3 μm), with an InGaAsSb active region grown from a melt with an optimum gadolinium content, and present an example of the use of lasers based on InGaAsSb(Gd) in gas analysis.

2. EXPERIMENTAL

DHs were grown by liquid-phase epitaxy and consisted of an undoped n-InAs (111)A substrate [with an electron concentration $n = (1\text{–}2) \times 10^{16}$ cm^{-3}] and three epilayers. They represented a wide-gap n-$\mathrm{InAs}_{1-x-y}\mathrm{Sb}_x\mathrm{P}_y$ ($0.05 \le x \le 0.09$, $0.09 \le y \le 0.18$) confining layer, an n-$\mathrm{In}_{1-v}\mathrm{Ga}_v\mathrm{As}_{1-w}\mathrm{Sb}_w$ ($v \le 0.07$, $w \le 0.07$) active region, and a wide-gap p–(Zn)–$\mathrm{InAs}_{1-x-y}\mathrm{Sb}_x\mathrm{P}_y$ ($0.05 \le x \le 0.09$, $0.09 \le y \le 0.18$) emitter. The active region was grown from the melt with a gadolinium concentration $X_{\rm Gd}$ = 0.004–0.005 at. %, which is known [10] to give the lowest concentration of residual impurities ($n = 5 \times 10^{15}$ cm^{-3}) in the n-$\mathrm{In}_{1-v}\mathrm{Ga}_v\mathrm{As}_{1-w}\mathrm{Sb}_w$ solid solution and the maximum carrier mobility. Like in [10, 11], we observed an increase in the photoluminescence (PL) intensity by a factor of up to ten in comparison with the layers grown without the use of Gd. The improvement of layer parameters and the decrease in the threshold currents [6] because of the use of Gd as a dopant are caused by the gettering action of rare-earth elements, namely, the interaction of Gd with foreign impurities found in the melt (first of all, Si, C, and O) and the formation of poorly soluble compounds. This results in a

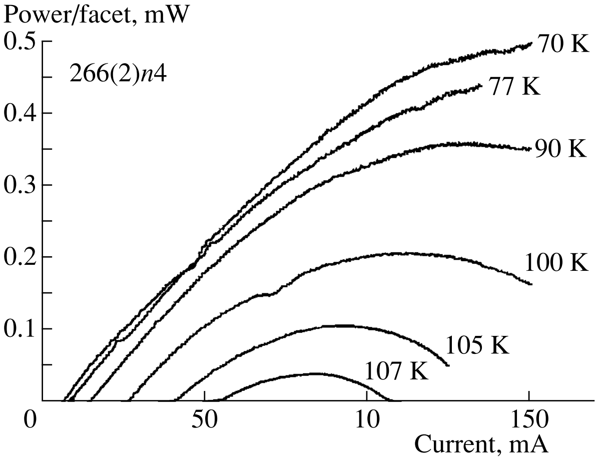

Fig. 1. Dependences of the output laser power on the pump current for a cw laser with $L = 140$ μm and $\lambda = 3.2$ μm at $T = 100$ K.

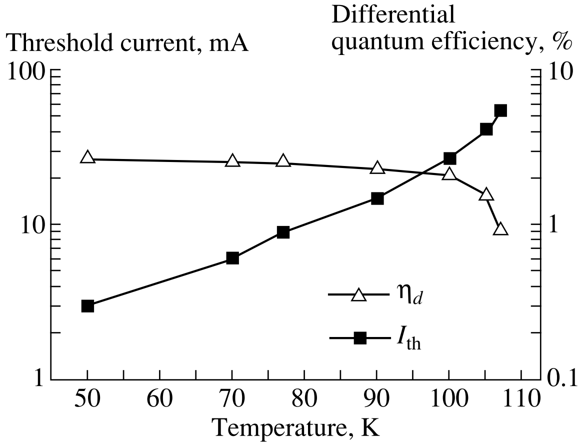

Fig. 2. Temperature dependences of the threshold current and the differential quantum efficiency for the laser with radiation wavelength $\lambda = 3.2$ μm and $L = 140$ μm.

decrease in the defect (nonradiative center) concentration and a decrease in the free-carrier concentration in the crystallizing solid phase. The latter fact also leads to an increase in the quantum yield because of a decrease in the Auger recombination rate.

The wide-gap layers were 3–5 μm thick, the active region was 1 μm thick, and the substrate, which was initially 350 μm thick, was thinned down to ~100 μm. The lasers had a mesastripe configuration, with a stripe width $w = 20$ μm and cavity length $L = 70$–150 μm. The structures were split into chips of area (70–150) × (150–300) μm^2, and their *p*-layer was soldered to a copper heat sink.

We measured PL at $T = 77$ K in the pulsed mode by using synchronous detection. PL was excited by an LPI-14 GaAs diode laser (with $\lambda = 0.8$ μm, power $P \sim 50$ W, pulse duration $\tau = 5$ μs, and repetition rate $f = 500$ Hz) whose radiation was directed onto a wide-gap *p*-InAsSbP emitter. The signal was recorded in the reflection configuration. PL was analyzed by an IKS-21 spectrometer.

Electroluminescence was measured in the cw regime at temperatures $T = 30$–110 K with a resolution of ≤0.75 cm^{-1}. The emission power was determined using a calibrated pyroelectric detector. In these measurements, emission was collected in a solid angle of π/6 sr. When measuring the transmission spectra, we transmitted radiation through a gas cell with an optical path length of 10 cm, which was filled with a methane–nitrogen mixture, with a methane content of 1%. The measurements were made at pressures of 1000 (atmospheric pressure), 200, 150, 100, 50, 20, and 10 hPa. The current tuning rate in the region of the linear pump current increase was measured with a Fabry–Perot (Ge) etalon. In these measurements, the laser was pumped by sawtooth current pulses ($\tau = 150$ μs, $f = 500$ Hz).

3. RESULTS AND DISCUSSION

3.1. Threshold Current, Differential Quantum Efficiency, and Output Power

Figures 1 and 2 present dependences of the output power on the pump current, and the temperature dependences of the threshold current and the differential quantum efficiency of the laser with $\lambda = 3.2$ μm and cavity length $L = 140$ μm. The maximum total power measured in the cw regime in a solid angle of π/6 sr was 0.5 mW/facet; the maximum power in a single spectral mode was 0.42 mW. The power increased up to currents exceeding $30I_{th}$. The total power from both facets (1 mW) exceeded the values obtained in similar lasers, but containing nonoptimal Gd concentration, by a factor of two [10].

The threshold current at 77 K in the cw regime was $I_{th} = 9$ mA (the current density was 320 A/cm^2), which is lower by a factor of 1.5 than the values obtained for a laser with the same cavity length in [8] and is lower, as far as we know, than the threshold currents previously obtained in the DH lasers emitting in this spectral region. The approximation of the experimental dependence of the threshold current density shows that, for lasers with a cavity length of ~1 mm, it is reasonable to expect values of ~50 A/cm^2, which is comparable to the best data for quantum well lasers [12].

The temperature dependence of the threshold current, in the case of its approximation by the function $\exp(T/T_0)$, is characterized by $T_0 \approx 20$ K, and this value is typical of the Auger processes. The differential quantum efficiency η_d at 77 K exceeded 2% (10 mW/A). A decrease in η_d in the temperature region $T < 105$ K was associated with a decrease in the internal quantum yield because of an increase in the Auger recombination rate. At $T > 105$ K, the intraband absorption led to a sharp decrease in η_d and quenching of the lasing [8].

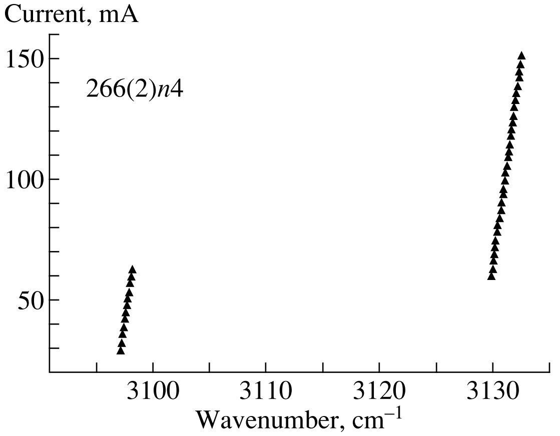

Fig. 3. Mode characteristics of the laser at T = 100 K.

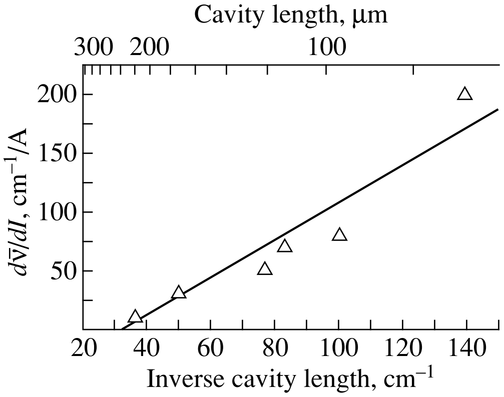

Fig. 4. Dependence of the current tuning rate on the cavity length.

3.2. Emission Spectra and Current Tuning

In most cases, lasers with small cavity lengths L = 70–150 μm operated in the single-mode regime at currents $I \le 6I_{th}$. At currents $I = (3–6)I_{th}$, the spectral purity was 100 or even better, i.e., the ratio of intensities of the dominant mode and the strongest subsidiary one was no less than 100 : 1, and this value was determined by the detection system noise. Figure 3 presents the mode composition of laser radiation at T = 100 K. At a current of 150 mA, the spectral purity was 650 : 1. A high stability of single-mode lasing may be caused by nonlinearities in the spectral hole burning or in the modulation of the inverse population because of the beating of fields corresponding to the dominant mode and a subsidiary one [13]. These effects cause gain suppression at frequencies differing from the radiation frequency by several mode spacings and account for the situation presented in Fig. 3, where lasing at I > 50 mA was observed at a frequency differing from the initial one by three mode spacings.

Current tuning of a laser mode was caused by an increase in the charge carrier concentration above the lasing threshold, which causes a decrease in the refractive index of the active region and mode shift to shorter wavelengths [9]. This process is associated with absorption in the valence band, which leads to an increase in the internal loss beyond the lasing threshold and an increase in the carrier concentration required to fulfill the threshold condition. The advantages of this mechanism are its fast response and a high current tuning rate, which exceeds the rate calculated for the tuning caused by Joule heating by an order of magnitude [9].

For simplicity, we may assume that current tuning is caused by a change in the refractive index $\bar{n}$ that is associated only with an increase in the carrier concentration N beyond the lasing threshold. In the approximation of intraband absorption linearly depending on the carrier concentration, in which case $\alpha_i = \alpha_0 + k_0N$, where α_i is internal loss, α_0 is the loss in the active region in the absence of injection, k_0 is the interband absorption coefficient, and N is the injected-carrier concentration, the derivative of the refractive index with respect to the current density (or the carrier concentration) is constant ($d\bar{n}/dj$ = const). Under these assumptions, the current tuning rate is inversely proportional to the cavity length because $d\lambda/dI \sim d\bar{n}/dI = (1/Lw)(d\bar{n}/dj)$, where w is the stripe width. One can see that the experimental data (Fig. 4) are consistent with the assumptions made above.

A decrease in the cavity length leads to an increase in the outcoupling loss and internal loss caused by intraband absorption [8]. Because of this, we previously studied lasers with a cavity length up to 600 μm, although lasers with a short cavity are attractive owing to the single-mode lasing and low threshold currents. An increase in the internal quantum yield obtained in this study in the case of optimal doping with Gd led to a decrease in the threshold current, an increase in the radiation power, and the feasibility of obtaining lasing in cavities as short as 70–140 μm. In a laser with a cavity 70 μm long, we obtained the highest current tuning rate $d\bar{\nu}/dI$ = 210 cm^{-1}/A and the widest single-mode tuning range, which was as wide as ~10 cm^{-1} (ΔI = 40 mA). These values exceed the parameters of conventional PbSrSe DH lasers [14], which have at T = 95 K the threshold current I_{th} = 510 mA, the single-mode tuning range ~5 cm^{-1} (ΔI = 60 mA), and $d\bar{\nu}/dI$ = 80 cm^{-1}/A.

3.3. Measurement of Emission Spectra of Methane

Figure 5 presents oscillograms of a sawtooth pump current pulse of a single-mode laser with L = 120 μm and $d\bar{\nu}/dI$ = 70 cm^{-1}/A (the left-hand scale) and signals of a photodetector measuring the radiation transmitted through a Fabry–Perot etalon and a gas cell filled with a 1% CH_4–N_2 mixture at atmospheric pressure (the right-hand scale). The measurements were carried out at the laser temperature $T = 98$ K, when the strongest minimum of the signal, which corresponds to methane absorption, was obtained. The corresponding transmission spectra for 1% mixtures of CH_4 with N_2 at pressures of 10, 50, and 150 hPa are presented in Fig. 6. The spectra are symmetric, have a sine shape, and a decrease in the line width is consistent with a decrease in the methane vapor pressure. Figure 6 also presents the transmission line of the 1%-CH_4–N_2 mixture at a pressure of 10 hPa at $\bar{\nu} = 3028.8$ cm^{-1} and a series of transmission lines in the range $\bar{\nu} = 2950$–3150 cm^{-1} ($\lambda \approx 3.4$–3.15 μm) corresponding to the HITRAN database (for the optical path length of 10 cm). One can see that the distance between absorption lines is comparable to the current tuning range obtained for lasers with a short cavity. We make no conclusions from the comparison of profiles of the lines measured in our experiments with the HITRAN data, because we used a pulse generator with a rather high noise level, which is known to cause laser line broadening. However, we note a high resolution obtained in our experiments.

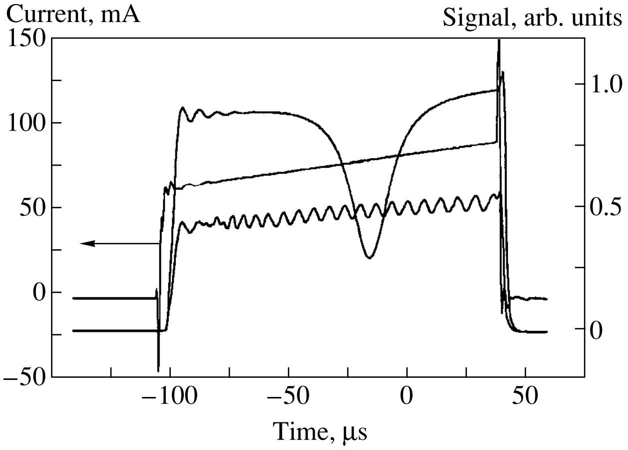

Fig. 5. Oscillograms of the pump current (left-hand scale) and output signals from the photodetector detecting radiation transmitted through the Fabry–Perot etalon and the gas cell filled with the 1%-CH_4–N_2 mixture at atmospheric pressure (right-hand scale).

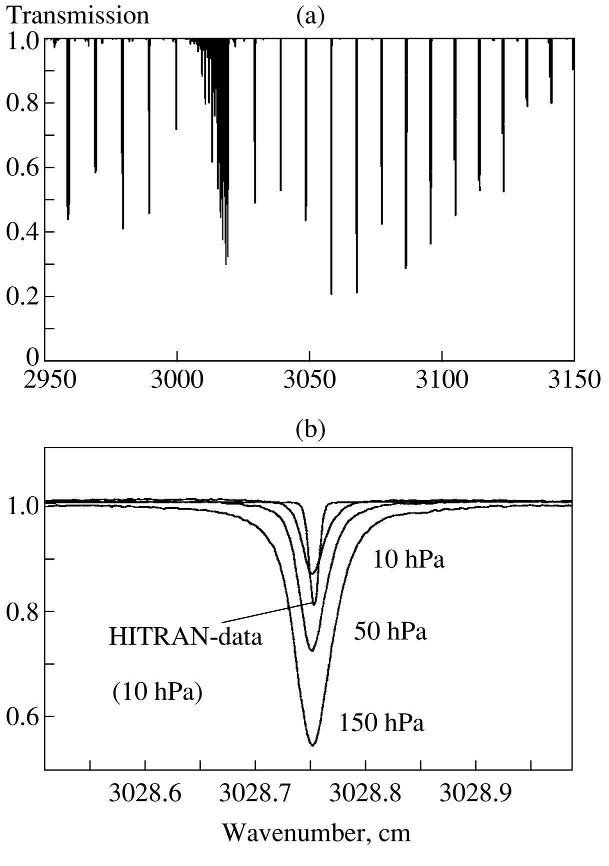

Fig. 6. (a) Transmission spectra of the 1% CH_4–N_2 mixture at a pressure of 50 hPa for the 10-cm optical path length (HITRAN Database); (b) the experimental transmission spectra of 1%-CH_4–N_2 mixtures at pressures of 10, 50, and 150 hPa, and the transmission spectrum (HITRAN) at a pressure of 10 hPa.

4. CONCLUSION

Thus, solution–melt doping with gadolinium made it possible to produce single-mode mesastripe InGaAsSb/InAsSbP DH lasers ($\lambda = 3.0$–3.3 μm) with record-breaking threshold currents below 10 mA and output single-mode power in the cw regime up to 0.43 mW/facet (cw, 77 K). Lasers with a short cavity ($L < 150$ μm) provided single-mode lasing up to currents $I \le 6I_{th}$, with a spectral purity factor as high as ~650, a record-breaking current tuning rate of 210 cm^{-1}/A, and a single-mode tuning range wider than 10 cm^{-1}.

ACKNOWLEDGMENTS

This work was supported by the “Optics. Laser Physics” Program of the Russian Ministry of Science and Technology (project no. 4.14), NATO expert visit stipendium PST.EV. 975482, and the European Office of Aerospace Research and Development, Air Force Office Scientific Research, Air Force Lab. (SPC-994016 Contract no. 61775-99-WE016).

REFERENCES

1. M. Aĭdaraliev, N. V. Zotova, S. A. Karandashev, *et al.*, Semicond. Sci. Technol. **8**, 1575 (1993).
2. H. K. Choi, G. W. Turner, and Z. L. Liau, Appl. Phys. Lett. **65** (18), 2251 (1994).
3. A. Rybaltowski, Y. Xiao, D. Wu, *et al.*, Appl. Phys. Lett. **71** (17), 2430 (1997).
4. A. N. Baranov, A. N. Imenkov, V. V. Sherstnev, and Y. P. Yakovlev, Appl. Phys. Lett. **64** (19), 2480 (1994).

5. A. A. Popov, V. V. Sherstnev, and Yu. P. Yakovlev, Fiz. Tekh. Poluprovodn. (St. Petersburg) **32**, 1139 (1998) [Semiconductors **32**, 1019 (1998)].
6. N. V. Zotova, S. A. Karandashev, B. A. Matveev, *et al.*, Pis'ma Zh. Tekh. Fiz. **23** (1), 72 (1997) [Tech. Phys. Lett. **23**, 41 (1997)].
7. M. Aĭdaraliev, N. V. Zotova, S. A. Karandashev, *et al.*, Fiz. Tekh. Poluprovodn. (St. Petersburg) **33** (2), 233 (1999) [Semiconductors **33**, 200 (1999)].
8. M. Aĭdaraliev, N. V. Zotova, S. A. Karandashev, *et al.*, Fiz. Tekh. Poluprovodn. (St. Petersburg) **33** (6), 759 (1999) [Semiconductors **33**, 700 (1999)].
9. M. Aĭdaraliev, N. V. Zotova, S. A. Karandashev, *et al.*, Fiz. Tekh. Poluprovodn. (St. Petersburg) **34** (4), 124 (2000) [Semiconductors **34**, 488 (2000)].
10. N. V. Zotova, S. A. Karandashev, B. A. Matveev, *et al.*, Fiz. Tekh. Poluprovodn. (St. Petersburg) **33** (8), 1010 (1999) [Semiconductors **33**, 920 (1999)].
11. A. Krier, H. H. Gao, and V. V. Sherstnev, in *Abstracts of Third International Conference on Midinfrared Optoelectronics, Materials and Devices, MIOMD III, Aachen, 1999*, p. O 20.
12. W. W. Bewley, H. Lee, I. Vurgaftman, *et al.*, Appl. Phys. Lett. **76** (3), 256 (2000).
13. *Semiconductors and Semimetals*, Vol. 22: *Lightwave Communications Technology,* I. *Semiconductor Injection Lasers*, Ed. by W. T. Tsang (Academic, New York, 1985; Radio i Svyaz', Moscow, 1990).
14. U. P. Schiesl and H. E. Wagner, in *Proceedings of the 5th International Symposium on Gas Analysis by Tunable Diode Lasers*, VDI Berichte **1366**, 251 (1998).

Translated by A. Kirkin

Semiconductors, Vol. 34, No. 7, 2000, pp. 853–856. Translated from Fizika i Tekhnika Poluprovodnikov, Vol. 34, No. 7, 2000, pp. 886–890.
Original Russian Text Copyright © 2000 by Golikova, Kureshov, Leshko, Lyutetskiĭ, Pikhtin, Ryaboshtan, Skrynnikov, Tarasov, Alferov.

PHYSICS OF SEMICONDUCTOR DEVICES

Properties of Wide-Mesastripe InGaAsP/InP Lasers

E. G. Golikova, V. A. Kureshov, A. Yu. Leshko, A. V. Lyutetskiĭ, N. A. Pikhtin,
Yu. A. Ryaboshtan, G. A. Skrynnikov, I. S. Tarasov*, and Zh. I. Alferov

Ioffe Physicotechnical Institute, Russian Academy of Sciences, Politekhnicheskaya ul. 26, St. Petersburg, 194021 Russia

** e-mail: tarasov@hpld.ioffe.rssi.ru*

Submitted January 27, 2000; accepted for publication January 27, 2000

Abstract—Wide-mesastripe InGaAsP/InP heterostructure lasers emitting at 1.3–1.5 μm were grown by metal-organic chemical vapor deposition (MOCVD). Radiation-power–current and spectral characteristics of the lasers have been studied in pulsed and continuous wave (cw) operation in the temperature range of 10–60°C. The temperature of the active region of the diode laser is higher by 30–60°C than that of the copper heatsink upon saturation of the cw output power. The temperature dependence of the differential quantum efficiency strongly affects the cw output power. Output powers of 3 and 2.6 W are achieved in mesastripe lasers in cw operation, and 9 and 6.5 W in pulsed operation, at wavelengths of 1.3 and 1.5 μm, respectively. *© 2000 MAIK “Nauka/Interperiodica”.*

1. INTRODUCTION

Advances in power semiconductor lasers rely on the concept of reducing the internal optical loss [1]. The use of a modified liquid-phase epitaxy has allowed the successful implementation of this concept [2]. A record-breaking optical power of ~11 W in cw operation has been obtained from $\lambda = 0.98$ μm lasers [3–5]. A 5 W continuous-wave (cw) output power was attained in an InGaAsP/InP diode laser with a 200-μm-wide mesastripe contact [6]. The difference in record-breaking values is mainly associated with the energy band structure of semiconducting solid solutions in the AlGaAs/GaAs, InGaAsP/GaAs, and InGaAsP/InP systems [7].

As noted in [8, 9], the maximum optical cw power of InGaAsP/GaAs lasers strongly depends on the parameter T_1 characterizing the temperature dependence of the differential quantum efficiency [9]. The parameter T_1 is particularly important for lasers based on InGaAsP/InGaAs/InP solid solutions, demonstrating a high temperature sensitivity [10, 11].

The principal goal of this work was to study the properties of InGaAsP/InP separate-confinement diode lasers grown by metal-organic chemical vapor deposition (MOCVD) [12] in order to reveal the main factors limiting the maximum optical output power. For this purpose, the cw and pulsed radiation-power–current (*P*–*I*) characteristics, the temperature dependences of the threshold current density and differential quantum efficiency, and the emission spectra were studied in diodes with various cavity lengths.

2. EXPERIMENTAL SAMPLES

For a base laser heterostructure (HJ), we chose a separate-confinement structure with two strained quantum-well (QW) active regions [3–5, 12]. The waveguide doping level, determined by the technological capacity of the employed grower, was 10^{16} cm^{-3}. The concentration of free carriers in *p*- and *n*-type emitter layers was chosen to be 10^{17} cm^{-3}, since making this parameter still lower led to higher series resistance of the structure. To minimize the internal optical loss, the waveguide width was increased to 0.9 μm. Making the waveguide even thicker is inadvisable because of the appearance of higher order modes (Fig. 1). The internal optical losses in the emitter layers α_i^{cl} and in the active region α_i^a were calculated for such a structure as functions of the quantity $\Delta E = E_g^{cl} - E_g^w$, where E_g^{cl}, E_g^w, and E_g^a are, respectively, the band gaps of the emitter layer, waveguide, and active layer (Fig. 2). In the case of two 60-Å-wide QWs, the optical loss in the active region can be neglected (Fig. 2). The loss in the emitter layers is the lowest at $E_g^w = E_g^a$. In this case, the optical confinement factor of the waveguide is the highest. Therefore, the solid solution composition was chosen for the waveguide layer so that the depth of the QW for electrons was $4kT$. In doing so, we took into account the fact that the band offset in the InGaAsP/InP structure amounted to one-third of the total difference in the band gaps ΔE_g [7]. On this basis, the band gap of the waveguide layer was chosen to be 1.25 eV for the $\lambda =$ 1.3 μm laser structure and 1.1 eV for that emitting at

1063-7826/00/3407-0853$20.00 © 2000 MAIK “Nauka/Interperiodica”

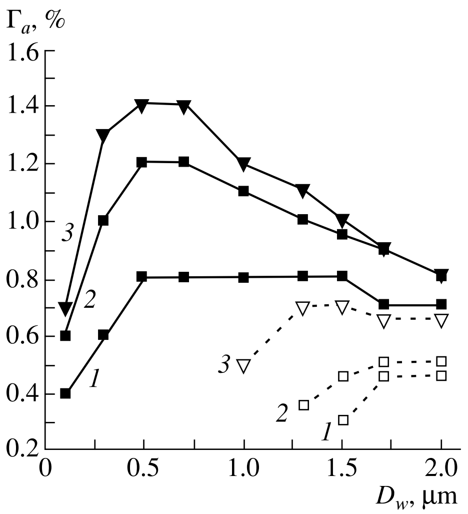

Fig. 1. Calculated dependence of the optical confinement factor of the active region (Γ_a) for zeroth-order (solid line) and second-order (dashed line) modes on the waveguide width (D_w) for a separate-confinement InGaAsP/InP laser heterostructure. Band gap of the InGaAsP solid solution constituting the waveguide E_w = (*1*) 1.25, (*2*) 1.18, and (*3*) 1.1 eV.

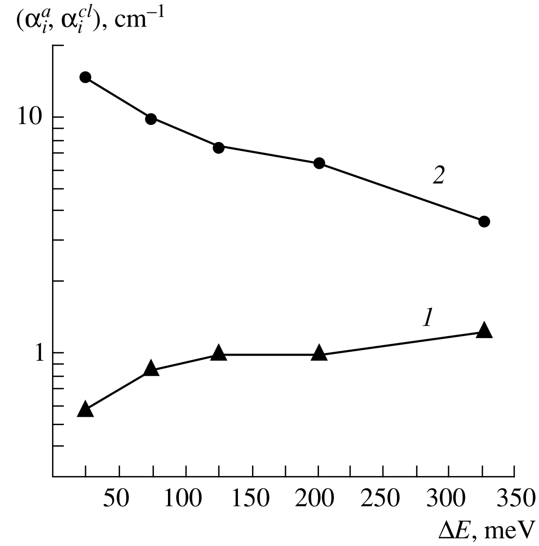

Fig. 2. Calculated dependence of the internal optical loss in (*1*) the active region, α_i^a, and (*2*) emitter layers, α_i^{cl}, on $\Delta E = E_g^{cl} - E_g^w$.

λ = 1.55 μm. Laser HJs of this kind have been grown by hybrid MOCVD [13]. Mesastripe diode lasers with 100-μm-wide contacts were fabricated from HJs by the conventional postgrowth technology [12].

3. EXPERIMENTAL RESULTS

3.1. Output-Power–Current Characteristics

Pump current pulses shorter than 100 ns are preferable in studying diode lasers under pulsed operation. This practically rules out heating of the active region of a diode laser but introduces certain complications in the measurement of the optical radiation power on the order of watts. Therefore, a pulse duration of 2 μs was chosen for pulsed experiments with diode lasers. In this case, a certain temperature rise in the active region was observed in a diode laser with cavity length L = 1.5–2 mm for pump currents $I > 10$ A (Fig. 3a). Nevertheless, an optical power P = 9 W was obtained in pulsed operation from λ = 1.3 μm diode lasers, and as high a power as P = 6.5 W, from diodes with λ = 1.5 μm (Fig. 3a).

An appreciable temperature rise in the active region is observed in cw operation, which manifests itself in a saturation of the *P–I* characteristic. This is most noticeable in short-cavity diode lasers ($L \approx 500$ μm) (Fig. 3b). Nevertheless, a 3-W optical output power was obtained from long-cavity ($L \approx 1.5$ mm) 1.3 μm diode lasers, and as high an output power as 2.5 W, in 1.5 μm diode lasers with a mesastripe contact width of 100 μm. To our knowledge, the highest cw optical power at 1.48 μm is 5 W for a mesastripe contact width of 200 μm [6].

3.2. Active-Region Overheating in the Diode Laser

The temperature of the active region of diode lasers was determined by two methods. In the first of these, *P–I* characteristics were compared and measured in cw operation at a copper heatsink temperature of 10°C and in pulsed operation at heatsink temperatures higher than 10°C. The temperatures of the active region overheating were determined at the intersection point of the *P–I* characteristics (Fig. 3b) from the difference of heatsink temperatures in cw and pulsed operation.

In the second case, pulsed and cw emission spectra were measured at a certain drive current. The active-region overheating of a laser heterostructure was determined from the difference in emission peak positions. The overheating-temperature values determined by the two techniques coincided to within ±2°C. The temperature rise in the active region of a diode laser at the highest pump currents in cw operation was in the range of 30–60°C, depending on the cavity length.

It should be noted that the specific resistance of the laser structure could be reduced in the samples under study to $\rho_s \leq 10^{-4}\ \Omega\ \mathrm{cm}^2$. The series resistance of a diode laser with a 2-mm cavity was in this case 0.05 Ω, which, to our knowledge, surpasses any of the reported values. Lowering the series resistance further to any noticeable extent requires a fundamental change in the postgrowth process. Therefore, the temperature dependence of the differential quantum efficiency becomes important for increasing the optical output power of diode lasers.

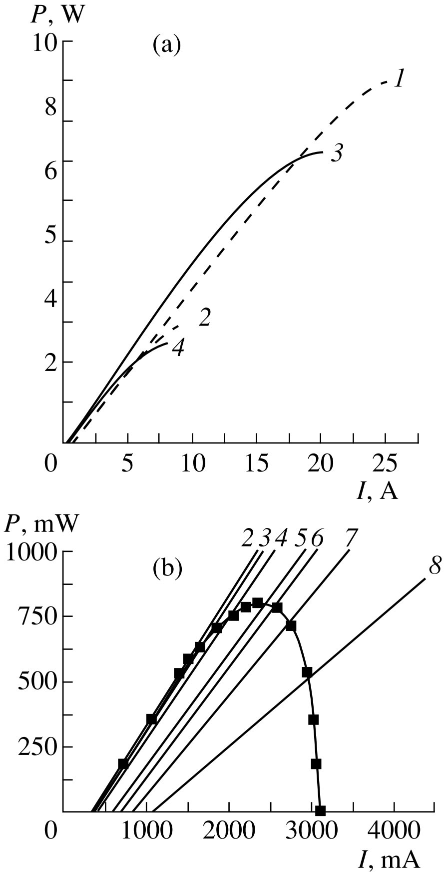

Fig. 3. *P–I* characteristics of diode lasers. (a) (*1*, *2*) Diode lasers with $\lambda = 1.3$ μm and $L = 2$ mm and (*3*, *4*) $\lambda = 1.55$ μm and $L = 1.2$ mm; curves *1* and *3* are for pulsed operation; curves *2* and *4* are for cw operation; heatsink temperature is 10°C. (b) Diode laser with $\lambda = 1.55$ μm and $L = 500$ μm; curve *1* is for cw operation, curves *2–8*, for pulsed operation; heatsink temperature is (*1*, *2*) 11, (*3*) 14, (*4*) 20, (*5*) 34, (*6*) 41, (*7*) 50, and (*8*) 56°C.

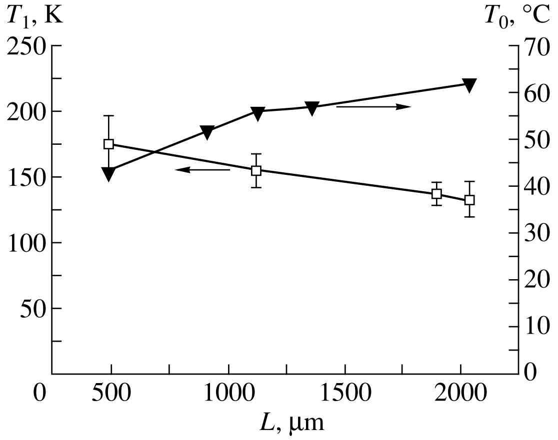

Fig. 4. Characteristic parameters T_0 and T_1 vs. diode-laser cavity length.

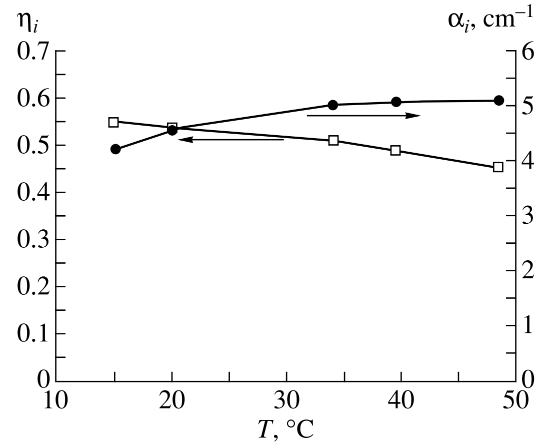

Fig. 5. Internal optical loss α_i and internal quantum efficiency η_i vs. temperature.

3.3. Temperature Dependence of the Threshold Current Density and Differential Quantum Efficiency

The temperature dependences of the threshold current density and differential quantum efficiency were studied in the range of 10–50°C. Figure 4 shows the characteristic temperature T_0 as a function of the cavity length. The curve has a shape typical of lasers with a narrow active region and separate electron and optical confinements [10]. In long-cavity diode lasers, T_0 is 40–60°C, which is lower than the values of this parameter for similar diodes on the GaAs substrate (T_0 = 100–200°C) [5]. However, even in short-cavity diode lasers, the effect of increasing the threshold current density on the maximum output optical power is insignificant compared to the contribution from the temperature dependence of the differential quantum efficiency (Fig. 3b).

Figure 4 presents the characteristic temperature T_1 as a function of the diode laser cavity length. This temperature is a parameter describing the temperature dependence of the differential quantum efficiency [9]:

$$\eta_d(T) = \eta_d(20°\mathrm{C})\exp[-(T - 20°\mathrm{C})/T_1]. \qquad (1)$$

The dependence of T_1 on the cavity length shows the opposite tendency as compared to that of T_0, which is inconsistent with the idea of making the cavity of a high-power diode laser longer. An important factor is the low value of T_1 in diode lasers based on InGaAsP/InP solid solutions. In lasers on GaAs substrates, this parameter reaches 300–1600°C, depending on the diode laser length [9]. As a consequence, the differential quantum efficiency falls dramatically with active region overheating both in a short-cavity InGaAsP/InP diode laser (Fig. 3b) and in a long-cavity one (Fig. 3a).

A study of the dependence of the reciprocal differential quantum efficiency on the diode laser cavity length at different temperatures yielded temperature dependences of α_i and η_i. These quantities are the internal optical loss (α_i) and internal quantum efficiency (η_i) in the well-known formula for the differential quantum efficiency

$$\eta_d = \eta_i \frac{\alpha_{\text{out}}}{\alpha_{\text{out}} + \alpha_i}. \quad (2)$$

Figure 5 shows the obtained temperature dependences of η_i and α_i. The internal quantum efficiency η_i is a characteristic of a laser HJ; beyond the lasing threshold η_i characterizes quantitatively the occurrence of current leakage and the existence of nonradiative recombination channels in an HJ and, naturally, depends on the active region temperature. In our opinion, the temperature sensitivity of η_i can be lowered by improving the design of a laser HJ.

The stimulated quantum efficiency defined by

$$\eta = (1/\tau_r)(1/\tau_r + 1/\tau_{nr})^{-1} \quad (3)$$

depends on the ratio of lifetimes of stimulated radiative (τ_r) and nonradiative (τ_{nr}) recombination processes and is close to unity beyond the generation threshold.

The internal optical loss increases with increasing temperature, with the percentage change corresponding to that observed in a similar dependence for lasers on a GaAs substrate [5]. Therefore, in our opinion, the influence of this change on η_i can be reduced by making the absolute value of α_i lower.

4. CONCLUSION

Mesastripe InGaAsP/InP diode lasers with wide contact were fabricated and studied. A cw optical output power P of 3 and 2.6 W and a pulsed power of 9 and 6.5 W were attained at $\lambda = 1.3$ and 1.5 μm, respectively. In cw operation, the temperature of the active region of the diode laser at maximum output power rises by 30–60°C relative to heatsink. Together with the internal optical loss and the series resistance of the laser structure, one more factor—the temperature dependence of the differential quantum efficiency—strongly affects the maximum output power of a diode laser. Because of the low value of T_1, this effect is most pronounced in InGaAsP/InP lasers.

5. ACKNOWLEDGMENTS

We thank N.Yu. Davidyuk and S.O. Slipchenko for the development of a procedure for measuring high-power laser radiation in the wavelength range of 1.3–1.65 μm and G.G. Zegrya for his helpful participation in discussions. The work was supported by the Russian Interbranch Scientific-and-Engineering Program “Physics of Solid Nanostructures” (project nos. 97-1035, 99-2038, and 99-2037).

REFERENCES

1. V. P. Evtikhiev, D. Z. Garbuzov, Z. N. Sokolova, *et al.*, Fiz. Tekh. Poluprovodn. (Leningrad) **19**, 1420 (1985) [Sov. Phys. Semicond. **19**, 873 (1985)]; Zh. I. Alferov, D. Z. Garbuzov, A. B. Nivin, *et al.*, Fiz. Tekh. Poluprovodn. (Leningrad) **19**, 456 (1985) [Sov. Phys. Semicond. **19**, 284 (1985)].
2. D. Z. Garbuzov, N. Yu. Antonishkis, A. D. Bondarev, *et al.*, IEEE J. Quantum Electron. **27**, 1531 (1991).
3. L. J. Mawst, A. Bhattacharya, J. López, *et al.*, Appl. Phys. Lett. **69**, 1532 (1996).
4. A. Al-Muhanna, L. J. Mawst, D. Botez, *et al.*, Appl. Phys. Lett. **73**, 1182 (1998).
5. M. R. Gokhale, J. C. Dries, P. V. Studenkov, *et al.*, IEEE J. Quantum Electron. **33**, 2266 (1997).
6. D. Z. Garbuzov, R. J. Menna, R. U. Martinelli, *et al.*, Electron. Lett. **33**, 1635 (1997).
7. S. Adachi, *Physical Properties of III–V Semiconductor Compounds* (Wiley, New York, 1992).
8. D. Botez, Appl. Phys. Lett. **74**, 3102 (1999).
9. L. J. Mawst, A. Bhattacharya, M. Nesnidal, *et al.*, Appl. Phys. Lett. **67**, 2901 (1995).
10. I. S. Tarasov, D. Z. Garbuzov, V. P. Evtikhiev, *et al.*, Fiz. Tekh. Poluprovodn. (Leningrad) **19**, 1496 (1985) [Sov. Phys. Semicond. **19**, 920 (1985)].
11. H. Temkin, D. Coblentz, R. A. Logan, *et al.*, Appl. Phys. Lett. **62**, 2402 (1993).
12. E. G. Golikova, V. A. Gorbylev, N. Yu. Davidyuk, *et al.*, Pis’ma Zh. Tekh. Fiz. **26** (6), 5 (2000) [Tech. Phys. Lett. **26**, 225 (2000)].
13. E. G. Golikova, V. P. Duraev, S. A. Kozikov, *et al.*, Kvantovaya Élektron. (Moscow) **22**, 85 (1995).

Translated by M. Tagirdzhanov

Semiconductors, Vol. 34, No. 7, 2000, pp. 857–860. Translated from Fizika i Tekhnika Poluprovodnikov, Vol. 34, No. 7, 2000, pp. 891–894.
Original Russian Text Copyright © 2000.

PERSONALIA

Zhores Ivanovich Alferov (dedicated to his 70th birthday)

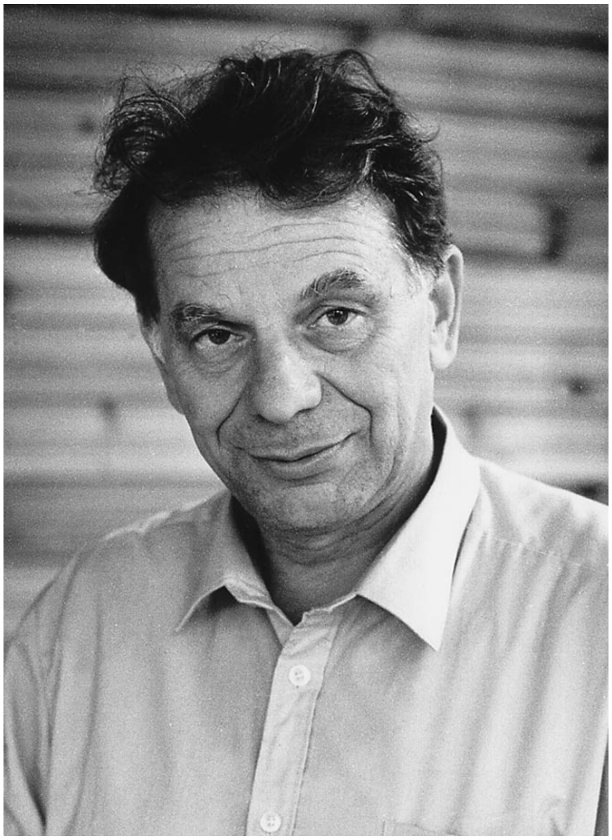

Zhores Ivanovich Alferov was born in Vitebsk. His father, Ivan Karpovich, was a participant in the October Revolution, commanded a cavalry regiment during the Civil War, then studied at the Industrial Academy and later became a founder of and a leading personality in the paper and pulp industry of the USSR.

In 1947, Zh.I. Alferov graduated from school with a gold medal. At that time, many young men and women wanted to enter institutions of higher education where the main subject was nuclear physics. Although Zh. Alferov, being a medalist, could have entered any institute, he followed the advice of his school teacher and chose electronics, which was Alferov's hobby during the last years at school. He received his higher education at the Leningrad Electrical Engineering Institute.

At the Institute, Alferov was an active member of the students' scientific society and studied the photoconductivity of bismuth telluride. In his third year at the Institute, he read the book *The Main Concepts of Modern Physics* by A.F. Ioffe, which had just been published. This book made a deep impression on Alferov, and his strongest desire became to work at the "academicians' school"—the Ioffe Physicotechnical Institute of the Academy of Sciences of the USSR (Phystech). This desire was realized in 1953 when Zh.I. Alferov graduated with distinction from the Institute and was given a work placement at the Phystech.

In the first half of 1950s, the Ioffe Institute, as the Phystech was called at that time, was posed with a specific problem that consisted in the development of semiconductor devices suitable for introduction into Soviet industry. Systematic physical studies of the new class of materials were started under the leadership of V.M. Tuchkevich. It was to Tuchkevich's laboratory that Zh.I. Alferov was assigned.

Tuchkevich's laboratory faced the important problem of obtaining single crystals of pure germanium (at that time, the latter was not produced by the USSR industry) and developing on its basis junction diodes and triodes. Zh.I. Alferov also became involved in solving this problem. The latter required deep insight into the physics of processes occurring in semiconductors and into the production technology for semiconductor materials. At that period, Alferov also had to work as an engineer when new products at the Elektrovypryamitel' plant in Saransk were being introduced.

Alferov was involved in the development of the first Soviet transistors; in 1954, Tuchkevich and Alferov were also the first in the USSR to develop high-power germanium devices, which found rapidly numerous technical applications in various branches of industry and in railway and urban transport.

On the basis of the complex of studies performed, for which Alferov received the first Government reward in 1959, he defended a candidate's dissertation that summed up his almost ten-year studies.

A correspondent of one newspaper once asked Alferov which quality he appreciated most in a scientist. Alferov answered, "The ability to choose a promising field of studies, boldness in this choice, and patience and persistence in these studies if there is no immediate success." These components of the creative process characterize the investigation strategy and research itself of Alferov. Such an approach became especially pronounced after the studies related to the development of high-power rectifiers had been completed.

Alferov faced the problem of choosing a further field of studies. The experience he had gained allowed him to start pursuing his own line of research. At that time, an idea of using heterojunctions in semiconductor technology was suggested. The development of a heterojunction-based perfect structure could bring about completely new designs in science and technology. This was understood by scientists in many foreign research centers, where active studies started.

The young Candidate of Science Alferov also recognized the importance of studies in the new promising field. In the early 1960s, he took an ambitious initiative—he decided to get down to the problem of heterojunctions in earnest—and, with a small group of enthusiasts, started research in this field, although he was dissuaded from doing this by many coworkers.

By 1967, in many publications in scientific journals and at numerous scientific conferences, the opinion that research in this field was without prospects was strongly expressed; it was based on the failure of numerous attempts to realize the seemingly promising idea. The cause of failures lay in the difficulties in producing an almost perfect junction and in identifying and obtaining the required materials for heterojunctions. Nevertheless, neither the opinions of experts nor the difficulties in his studies changed the choice made by Alferov.

GaAs and AlAs were suitable for an ideal heterojunction; however, AlAs was oxidized almost immediately if exposed to atmospheric air. It was necessary to choose another material. The latter was discovered at the same institute, in the laboratory headed by N.A. Goryunova. It happened to be the AlGaAs ternary compound. Thus, the GaAs/AlGaAs heteropair, which is now widely known in the world of microelectronics, was identified. In 1967, when the unfavorable verdict for heterojunctions was announced, Alferov and his coworkers fabricated almost ideal heterostructures in an AlAs–GaAs system and later the first semiconductor heterolaser that operated in the continuous-wave mode at room temperature.

A satisfactory solution to the heterojunction problem was promoted by the profound physical approach to the phenomena under study characteristic of Alferov, his broad grasp of a problem, the intuition that often helped him to find optimal alternatives, and, last but not least, his ability to interest a team of young coworkers in an extremely fascinating, albeit very difficult, problem.

Alferov's discoveries of ideal heterojunctions and new physical phenomena (i.e., the superinjection and electronic and optical confinement in heterostructures) made it possible to radically improve the parameters of most of the known semiconductor devices and develop basically new devices that were especially promising for applications in optoelectronics and quantum electronics.

Alferov summarized the new stage in studies of heterojunctions in semiconductors in his doctoral dissertation, which he successfully defended in 1970.

The true value of the works by Alferov was appreciated by international and Soviet science. In 1971, the Franklin Institute (USA) awarded him the prestigious Ballantine medal (called a "small Nobel Prize") founded as an award for outstanding accomplishments in physics. Later on, he received the highest award in the USSR, the Lenin prize (in 1972), and the Hewlett-Packard award of the European Physical Society followed.

Fundamental studies performed by Alferov formed the basis for a number of new scientific and technological lines of investigations. Some of these went beyond his laboratory and continue to be developed under the scientific guidance of Alferov in the institutes related to a particular branch of industry. A number of devices with heterojunctions (lasers, light-emitting diodes, the pump sources for solid-state lasers, optoelectronic displays, optical sources for traffic lights, photodetectors, and solar cells) were mastered before long by Soviet industry. Technologies of production of new types of high-power diodes and transistors and the heterostructure-based thyristors were also transferred to industry.

As far back as in 1939, a photovoltaic cell based on thallium sulfide with a conversion efficiency of about 1% was developed at the Phystech for technical purposes. Efforts concerned with the conversion of solar energy into electrical energy were also continued after World War II, because the need for autonomous energy converters became more urgent with time. The need for new power sources increased especially with the advance of space exploration. Here again, heterojunctions were found to be useful.

Using the technology of AlGaAs/GaAs-based high-efficiency radiation-resistant solar cells developed by Alferov in the 1970s, the world's first large-scale production of heterostructure-based solar cells for space applications was started at the NPO Kvant. One of these cells mounted in 1986 aboard the base module of the *Mir* space station operated during its entire service life without any significant decrease in power.

In the 1980s–1990s, Alferov and his coworkers continued their extensive studies of heterojunction-based solar cells, which resulted in the development of photovoltaic converters operating under concentrated (up to 10^3 times) solar radiation. The efficiency of the new generation of solar cells approached the theoretical limit and exceeded 30%. Such solar cells formed the basis for progress in the efforts in space and terrestrial solar-energy conversion at a new level.

Among the studies performed under the guidance of Alferov, most attention was paid to the search for new heterostructures, the investigation of physical processes at the interfaces between materials, and the use of heterostructures in the investigations of luminescence and size-quantization effects. The purely engineering development of new principles in the design of solid-state devices for electronics and integrated optics was not ignored either.

On the basis of ideal junctions suggested by Alferov in 1970, semiconductor lasers that were based on multinary InGaAs compounds and operated in a much wider spectral range than those based on an AlGaAs system were developed. These lasers found application as the emission sources in the fiber-optical links for long-distance communication.

As a result of studies of radiative recombination and photoelectric phenomena in heterostructures, Alferov found the conditions for obtaining a 100% internal quantum yield (i.e., the almost complete internal conversion of electrical energy into optical energy and vice versa), which opened new possibilities for developing the high-efficiency sources of coherent and spontaneous radiation. On the basis of these studies, in the mid-1970s, spontaneous-radiation sources were developed at the Phystech, in which, due to the reduction of optical losses in the crystal, it was possible to attain the highest ever values of external quantum yield of 45% in the infrared region of the spectrum and higher than 10% in the red region.

Studies of the generation, propagation, and transformation of the light wave in waveguide heterostructures resulted in the development of new approaches to the design of monolithic optoelectronic integrated circuits capable of efficiently controlling the light fluxes. The semiconductor-based line of research in integrated optics related to the studies by Alferov and his coworkers is now considered as one of the most promising in this field of physics, which is at the interface between modern optics and electronics.

Alferov attentively kept track of the newest progress in science and, already as the director of the Institute, founded the Center for the Study of Nanoheterostructures within the Phystech. At this Center, various technologies for obtaining heterostructures (such as liquid, metal-organic, and molecular-beam epitaxy) were developed and used with good results; this made it possible to develop a new generation of heterostructure-based optoelectronic devices. Among these devices are injection size-quantization lasers for infrared and visible regions of the spectrum with a record-breaking conversion efficiency, a single-mode laser with distributed feedback, picosecond lasers and photedetectors, and optoelectronic integrated circuits for ultrahigh-speed computers.

Beginning in 1993, one of the main lines of research at the Center became the fabrication and study of nanostructures with a lowered dimensionality: quantum wires and quantum dots. New methods for obtaining the self-organizing nanostructures with high crystalline perfection and high uniformity were suggested and implemented. The processes of capture, relaxation, and recombination of charge carriers in nanostructures were studied.

In 1993–1994, the world's first heterolasers based on structures with quantum dots or "artificial atoms" (narrow-gap nanodimensional inclusions of indium and gallium arsenides in the gallium arsenide matrix) were fabricated. In 1995, Alferov and coworkers demonstrated for the first time an injection laser that was based on quantum dots and operated in the continuous-wave mode at room temperature.

The widening of the spectral range of lasers based on quantum dots on GaAs substrates to the region in the vicinity of 1.3 μm was an event of fundamental significance; this region is important for applications in fiber-optical communication links. The first surface-emitting lasers that were based on quantum dots in an InGaN system, operated in the ultraviolet region of the spectrum, and were pumped optically at room temperature were developed. Thus, Alferov's studies laid a foundation for a basically new type of electronics that is based on heterostructures, has a very wide range of applications, and is known now as "band engineering."

One of the traditions at the Phystech was a close link with institutions of higher education, first of all, the Physicomechanical Department of the Leningrad Polytechnical Institute, from which young skilled graduates came to join the scientific community. In the 1950s, such a link became weaker. The abnormality of such a situation, where direct interaction between the academic institute and the institution of higher education was disrupted, became more and more evident to Alferov. In the last two decades, he, already a famous scientist, has used any opportunity to express in speech or in the press the necessity to return (of course, at a new level and on a larger scale) to the above tradition that has deteriorated but has been nevertheless fully justified in the case of Phystech.

In 1973, Alferov, in cooperation with academician V.M. Tuchkevich, used a continued connection with the Leningrad Electrical Engineering Institute and founded an optoelectronics department there, which became a basic department of this educational institute for the Physicotechnical Institute. In the following years, this department became one of the most popular and probably the best department of this type among those at Leningrad institutions for higher education. Its success was due to a highly qualified staff of professors and lecturers (including the experimentalists and theoreticians from the Phystech) whom Alferov recruited for these activities and also to his large personal contribution to this field, which was extremely important for the development of physics and electronics.

Following the example of the Leningrad Electrical Engineering Institute, several basic departments have also been founded at the Leningrad Polytechical Institute (LPI). In order to improve the organizational aspects of education, they soon joined to become the Physicotechnical Faculty of the LPI, and Alferov, who contributed immensely to the organization of this Faculty and paid persistent attention to it, became its permanent dean.

It is Alferov's opinion that prospective students for the Department should be selected in good time, taking into account their aptitudes for pursuits in physics, which become evident even during one's school days; such aptitudes should be encouraged and developed. Therefore, the next step involved the organization of a physicotechnical school based on the Phystech; Alferov and the members of the staff of the Institute have become quite frequent and welcome guests at this school. They actively participate not only in the educational process but also in the organization of physical Olympiads.

The erection of a new large building for the Physicotechnical Institute was completed last year. In this building, there is a Scientific–Educational Center with excellent lecture theaters, laboratories, and recreation areas, which include sports halls, a tennis court, and a swimming pool. There is also a small hotel for visiting lecturers. Here, a school, the basic department of the Leningrad Electrical Engineering Institute, and the physicotechnical department of the LPI are joined in a unified educational process. In order to realize his dream, Alferov had to make full use of his scientific authority and organizational abilities; in fact, it was not easy in our troubled times to obtain budgeting and organize the building of the Center. Only an enterprising person with excellent organizational skills and obsessed by a noble idea would be able to overcome all the difficulties.

Owing to the worldwide fame of the Ioffe Physicotechnical Institute and the activities of its director, the leading foreign and Russian scientists are not only frequent guests at this Institute but also active assistants and consultants in research. Therefore, it is not surprising that, on the initiative of Alferov and in order to improve and consolidate the links between scientific centers, the medal "To the Honorary Member of Staff of the Ioffe Physicotechnical Institute" was set up; 26 outstanding scientists have already been awarded this medal.

As an incentive to research and in order to raise the prestige of science and immortalize the memory of outstanding scientists that have worked at the Physocotechnical Institute, awards and medals named after A.F. Ioffe (the founder of the Institute), B.P. Konstantinov (a vice-president of the Academy of Sciences), and Ya.I. Frenkel' (an outstanding theoretician) were set up with the active participation of Alferov. Many participants of annual competitions of scientific works have become the recipients of these awards and medals.

In addition to scientific and pedagogical work at the Physicotechnical and Electrical Engineering Institutes, academician Alferov is engaged in scientific–managerial activities; he is a member of a number of scientific councils of the Russian Academy of Sciences and the Editor-in-Chief of the journal *Technical Physics Letters*. Alferov also actively participates in the activities of the European Physical Society.

The scientific works of Alferov are well known both in this country and abroad. He is the author and coauthor of more than 500 scientific publications (including three monographs) and more than 50 inventions.

It is fair to say now that there is an Alferov scientific school. There are 48 Candidates and 15 Doctors of Science among his followers.

Alferov celebrates his 70th birthday in the prime of his creative capabilities; he has thought out and planned a broad field of future research whose realization will undoubtedly lead to new achievements.

In the year of his anniversary, we wish Z.I. Alferov many happy returns of the day and new achievements for the benefit of Russian science and Russia.

We congratulate academician Zh.I. Alferov on awarding him the Russian Federation's Order "For Services to this Country" of the second degree and wish him further outstanding achievements in science.

Colleagues, friends,
and members
of the editorial board
of this journal